A ROUGH SURFACE MIXED LUBRICATION MODEL OF MACHINE COMPONENT INTERFACES WITH AN EXPERIMENTAL EVALUATION

by

Nolan Ryan Chu

A dissertation submitted to the Graduate Faculty of
Auburn University
in partial fulfillment of the
requirements for the Degree of
Doctor of Philosophy

Auburn, Alabama
May 6, 2023

Keywords: Rough Surface Elastic-Plastic Contact, Sinusoidal Asperity, Boundary Lubrication, Flow Factors, Shear Thinning, Thermal Heating

Approved by

Robert L. Jackson, Chair, Albert Smith Jr. Professor of Mechanical Engineering
Mark Hoffman, Assistant Professor of Mechanical Engineering
Jay Khodadadi, Alumni Professor of Mechanical Engineering
Kyle Schulze, Assistant Professor of Mechanical Engineering

ABSTRACT

This work develops a numerical methodology for predicting the performance of an automotive piston ring system by considering contact and lubrication mechanics. The rough surface contact mechanics and lubrication occurs on a scale much smaller than the size of the piston rings and therefore the key aspect of the model is an algorithm that solves simultaneously the multiple mechanisms at different scales. The finite element method will be used to model the mechanical deformations of the piston ring surfaces at large scales. The quasi-steady state model includes heat generation due to solid and viscous friction. This heat generation will then be used to predict the temperature rise and thermal effects in the lubricant and component. A statistical rough surface method that renders asperities as elastic-plastic wavy surfaces predicts the solid contact area. The modified Reynolds equation will be solved to consider the effects of mixed-hydrodynamic lubrication while using flow factors formulated for actual piston and ring surfaces. The lubricant viscosity depends both on temperature and shear rate. This will allow for the regimes of boundary, mixed and full-film lubrication to be considered. The model predicts friction for various loads and speeds that are then compared to experimental measurements. Although the contacts operate mostly in the mixed lubrication regime, the model and experiments show changes in friction with load, speed and temperature.

ACKNOWLEDGEMENTS

I would like to thank Ford Motor Company for funding this project as a part of the Ford University Research Program.

TABLE OF CONTENTS

LIST OF TABLES

LIST OF FIGURES

LIST OF SYMBOLS

A_n	Nominal contact area
A_r	Real contact area
$\overline{A}$	Single asperity contact area
ω	Interference between surfaces
ω_c	Critical interference
E	Elastic modulus
v	Poisson's ratio
E'	Effective elastic modulus
$\overline{F}$	Single asperity contact force
η	Asperity density
R	Asperity radius
σ	Composite root mean square (RMS) roughness of surfaces
σ_s	Root mean square (RMS) asperity height
ϕ	Distribution function for asperity heights (assumed to be Gaussian throughout this work)
m_2	Second spectral moment
m_4	Fourth spectral moment
α	Bandwidth parameter

ω_c	Critical interference between surfaces
S_y	Yield strength
λ	Wavelength of sinusoidal surface ($1/f$)
Δ	Amplitude of sinusoidal surface
$\overline{p}$	Average pressure over surface
p^*	Pressure required for complete elastic contact
A_p	Elastic-plastic contact area for single sinusoidal asperity
p^*_{ep}	Pressure required for complete elastic-plastic contact
Δ_c	Critical amplitude for elastic-plastic contact
G	Nondimensionalized gap between surfaces
g	Gap between surfaces
h	Surface separation or film thickness
ρ	Density of lubricant
μ	Dynamic viscosity of lubricant
p	Hydrodynamic pressure
q_x, q_z	Flow rate in axial and transverse directions
U_1, U_2	Velocity of surfaces in sliding direction
γ	Peklenik number in the principal direction
φ_s	Combined shear flow factor
φ_x, φ_z	Pressure flow factors
μ_k	Sliding friction coefficient due to rough surface contact
T_{room}	Room temperature (presumed to be 20°C)
T_m	Melting point of cylinder liner/piston ring

CHAPTER 1

INTRODUCTION

Reciprocating contacts often experience high friction because sliding speeds are low when motion reversal occurs. In a piston ring-cylinder liner system, this occurs at the top and bottom dead centers. Studies have shown that 20% of energy losses in internal combustion engines are associated with surface contact friction. The main source of these losses is the piston ring-cylinder liner and the piston skirt-cylinder liner (40% of this energy loss) [1,2]. Even a small reduction in friction will significantly reduce emissions and save fuel. The piston rings tightly seal the space between the cylinder liner and the piston skirt, which controls the lubricant distribution and heat transfer from the piston. However, the simultaneous sliding and sealing results in high friction losses. Studies have shown that up to 15% of fuel consumption is spent overcoming friction due to piston ring-cylinder liner contact [3]. While internal combustion engines will slowly be phased out, they will still most likely power vehicles for decades to come, especially in developing countries where adoption of electric vehicles will be slower [4]. In addition, certain applications and vehicles such as heavy trucks will consist mostly of combustion vehicles for longer. Thus, strategies to reduce frictional losses in the piston

ring-cylinder liner assembly remain essential [5]. However, the friction losses must first be quantified as it will be the parameter that determines the best solution.

This work's goal is to develop a numerical model for a cylinder wall-piston ring interface that considers lubrication and contact mechanics to evaluate system performance over the entire operating range. The iterative model will be able to predict the friction and possible failure dependent on operating conditions. For a given speed, load, and temperature, the lubrication model is combined with a contact mechanics model that accounts for flash temperature increases because of friction-generated heat. A finite element analysis determines the deformation of the piston ring due to the loads it carries. Lastly, the numerical model is verified by experimental measurements. While many models for the individual modules exist, there are few such models that combine all of these aspects at once.

To consider the effect of lubrication, the Reynolds equation is solved using flow factors, a method initially derived by Patir and Cheng [6] and then refined by Locker et al. [7] for the specific surfaces being studied. For the contact mechanics portion, the Greenwood-Williamson statistical model is applied to determine the load carried by rough surface contact. Because the base GW model only considers elastic contact, it is refined to include the effects of elastic-plastic deformation that often occurs. The GW-model also assumes a perfectly flat surface in contact with a surface with spherical asperities, so modifications were made to account for two rough surfaces in contact. Recent work by Chu et al. [8] revealed that models based on sinusoidal asperities provide

a better fit to deterministic models. Both models reflect the measured profiles of a cylinder wall and a piston ring and how they interact with each other.

The lubrication and contact mechanics models and a finite element analysis are coupled via shared boundary conditions and material properties that create a system of equations to solve using an iterative process until the predictions converge. The overall model predicts several parameters that can be applied to component design. Some of these are the portion of the load carried by the oil and by solid contact, the friction coefficient, and the temperature rise due to frictional forces.

CHAPTER 2

LITERATURE REVIEW

2.1 General Literature Review – Prior works on the Piston Ring – Cylinder Liner interface.

Many methods and techniques have been used in the past to predict the frictional losses of a piston ring – cylinder liner interface in an engine. This system includes several variables such as surface topography, transient lubrication, and exhaust flow rate that interact with each other. Prior works have generally focused on only one variable at a time. Furuhama and Sumi's [9] analysis of compression ring linings is one of the first investigations on the subject. Ma et al. [10] analyzed lubricant transport and found that cylinder liner surface and ring movement significantly influence the tribological behavior. Akalin and Newaz [11] analyzed the mixed lubrication regime using the Reynolds equation with flow factors. They found that hydrodynamic lubrication occurs during most parts of the stroke, but the friction coefficient increases greatly at top and bottom dead center when the sliding speed is too low for the lubricant to support much of the load. Their analysis did not calculate flow factors for a specific surface or consider

elastic-plastic asperity contact, nor did they perform experiments to validate their model. Jeng [12] analyzed the lubrication conditions at the ring contact surface. Furuhama and Sasaki [13] derived a new technique to measure friction forces for small engines. Previously this was a difficult task because they could not be isolated from much larger gas and inertia forces. Taking into account torsion, film thickness changes, and ring wear, Tian [14] studied piston ring dynamics numerically and experimentally.

In recent years several studies have focused on improving internal combustion engine efficiency. Morris et al. [15] optimized the piston ring to minimize the energy losses, incidence of asperity contact, and ring mass. Bewsher et al. [16] applied atomic force microscopy to measure the boundary asperity shear strength and thus calculate localized values of frictional losses on real engine components. Howell-Smith et al. [17] tested lubricant coatings and surface textures for friction reduction. They found that surface modifications of the liner at top dead center (TDC) reduces friction by creating additional lubricant reservoirs there. In turn, this increases the power output of the engine by up to 4%. Li et al. [18] found that laser finishing could reduce the friction coefficient and weight loss of an Al-Si alloy cylinder liner by removing the aluminum layer and exposing rounded edges of silicon particles.

Efficiency can also be improved by changing the surface texture. Senatore et al. [19] studied a bronze coating with different surface textures and found that an appropriate texture geometry improves the friction coefficient and wear. Wang et al. [20] tested the effects of dimples on brass discs. They found that only a small dimple pattern reduced

the friction – for large dimples the friction coefficient actually increased. Kligerman et al. [21] developed an analytical model for partial laser surface texturing to reduce the friction in the piston ring – cylinder liner system. They found an optimal percentage of the textured portion and dimple depth depending on operating conditions. Spencer [22] developed simulations to evaluate a cross hatched cylinder liner to reduce oil consumption, wear, and friction. Lu and Wood [23] observed an 82% reduction in piston ring – cylinder liner friction when texture grooves were normal to the sliding direction. Abril et al. [24] studied the effects of dimples and the honing groove in the cylinder liner. A slight increase in dimple density increased the minimum film thickness and reduced the friction force. Comparable increases in minimum film thickness could be obtained with deeper, larger dimples. Their honing groove analysis found that a 15 degree increase in honing angle reduced the friction coefficient by more than 14%. However, friction increased when the honing groove density was too high.

2.2 Rough Surface Contact

Contact between rough surfaces is an ubiquitous problem that can be applied to numerous phenomena such as friction, wear, and contact resistance. It can be modeled in various ways – statistical [25-28], fractal [29], multi-scale [30], and deterministic [31] models are just some of the methods employed. In the statistical model, mathematical parameters describing the surface are used to calculate probabilities and determine the

contact area and load. Fractal based models account for different scales of surface features that statistical models neglect. However, for a perfect fractal, the predicted contact area at the smallest scale is zero. The multi-scale model avoids this because it more accurately incorporates surface structure and deformation mechanics. Rather than approximate features, the deterministic model incorporates all of them in an analysis. However, this is frequently too computationally expensive to be feasible. Thus, faster methods (statistical, multi-scale) are more commonly used instead.

Henrich Hertz was one of the first researchers in the field of contact mechanics. His solution of a parabola deforming elastically in contact with a flat surface can be applied to cylindrical or spherical contact [32]. However, he did not consider frictional or yielding effects. The single asperity, or raised point on a surface, solution can be expanded by incorporating a roughness model that describes the surface's topography.

One such expansion is the statistical model by Greenwood and Williamson [25] (GW model). They considered the interaction between a perfectly flat, rigid plane and a plane covered with spherical asperities of varying heights. They assumed that asperities behave independently of each other and that deformation is limited to the asperities. However, they only assumed elastic contact, so other models were subsequently derived when yielding occurs at larger loads. Jackson and Green (JG) [27] derived a statistical elastic-plastic deformation model in which they established the load required for plastic deformation. Other models were proposed by Chang, Etsion, and Bogy (CEB) [26] and by Kogut and Etsion (KE) [28] that incorporate the effects of plasticity. As contact

pressure increases, the internal stress within asperities increases as well. This results in yielding and plastic deformation. At the critical interference, ω_c, the material is assumed to yield. The JG model, while it includes varying fully plastic pressure not captured by the KE model, is limited to small deformations where the contact radius is no more than 41% of the radius of curvature. Wadwalker et. al. [33] extended the model for larger contact radii, but asperities may behave like isolated spheres rather than peaks at higher loads.

Statistical models are reliable and easily implemented, but shortcomings exist. Those previously described assume a homogenous radius of curvature over an entire region, neglect the effects of different scales of features, and do not couple the deformation between asperities and the substrate. Bush et. al. [34] developed a statistical model that accounts for variable asperity radius, but they still assumed negligible asperity interaction. Ciavarella et al. developed a model that accounts for lateral asperity interaction [35]. Afferrante et al. followed up with a coalescing asperity model, while Vakis expanded it below the mean asperity height [36-37]. These works are similar to the wavy asperity model that includes lateral asperity interaction used here, but they do not address the existence of features at different scales.

Majumdar and Bhushan (MB) [29] created a fractal model for rough surface contact by applying the Weierstrauss-Mandelbrot (WM) function to multiple levels of roughness. However, a surface may not have a spectrum that strictly follows the fractal equation. Ciavarella et al. [38] solved the 2D W-M fractal-rigid flat interface using a stacked

asperity assumption and an elastic sinusoidal model derived by Westergaard [39]. Morag and Etsion [40] attempted to improve the model by allowing the asperity contacts to exit the elastic regime and become plastic as load increases, but the fractal models are still arguably deficient in other ways. The usage of the fractal geometry for describing real rough surfaces is still debated, and it is questionable to use them in a rough surface contact model [40-46]. In fact, it has been shown in elastic and elastic-plastic contact that a true fractal surface in contact will have zero contact area and infinite pressure [47,48]. There are also other families of models based on diffusion and fractal geometries, but it is unclear or impossible to employ different single asperity models within them. For these reasons, this work does not consider a fractal-based model.

To overcome the limitations of the GW model and predict a realistic area of contact, the multi-scale model was developed by Jackson and Streator [29] (JS). Their model builds off Archard's [49] "protuberance upon protuberance" concept in which the Hertzian sphere was expanded by including hemispheres of smaller radii on it. As loads increase, the surfaces come into complete contact at the smallest scales and begin compressing at larger scales. Archard's theory predicted a linear relationship between area and force and that rougher surfaces would only flatten with larger force. Jackson and Streator refined Archard's model so it could be applied to real surfaces [29]. They made the following assumptions: smaller asperities are stacked on larger asperities, load is distributed equally over all asperities on each scale, total load does not depend on scale, and the contact area is limited to that of the scale below. They applied the Johnson,

Greenwood, and Higginson piecewise solution [50] for perfectly elastic 3D sinusoidal contact and connected the equations. To consider roughness, the surface was converted using a discrete Fourier transform into a series of sine waves of known frequency and amplitude [29].

The JS model was subsequently modified using results from Krithivasan and Jackson [51], who analyzed a finite element model of a sinusoidal asperity. Like the JG model, a critical value below which contact remains perfectly elastic exists. Because interference is not calculated, the critical values are found in terms of force. Chu et al. [8] found this model to be inadequate for predicting the surface separation given the load, so this work does not consider a multi-scale model. Other recent works have also sought to incorporate the effect of coatings [52] size-dependent properties [53] (especially material strength), and tangential loading or friction [54–56] and even wear or surface damage [57].

Idealistically, deterministic models solve rough surface contact without making any significant simplifying assumptions (in contrast the mathematical and statistical models are already discussed). A review and summary of some deterministic rough surface contact modelling methods is provided in Liu et al. [31]. Later, Liu et al. [59] used the finite element method with plastic deformation and the simplex algorithm to consider cylindrical and 2-D rough surface contact in plane strain. Somewhat different from other works, several researchers [60–62] used a semi-analytical boundary element-based approach to solve the elastic-plastic problem. Finite elements were used by Pei et al. [63]

and Sahoo and Ghosh [64] to consider the contact of self-affine fractal elastic-plastic surfaces. The rough surfaces of a microelectromechanical system in contact were considered by Liu et al. [65] using the finite elements. The finite element deterministic modeling methodologies were discussed by Thompson [66,67] in order to predict the thermal contact resistance. A deterministic finite element model was compared to a hybrid analytical model by Megalingam and Mayuram [68]. More recently, Wang et al. [69] and An et al. [70] implemented an elastic-plastic finite element deterministic model of measured rough surfaces and sought to refine the mesh toward a converged solution. Although all of these models are referred to as deterministic, they still make many assumptions and contain errors in their predictions. In many cases they have not reached mesh convergence.

2.3 Hydrodymanic Lubrication

To calculate the hydrodynamic load in modeling viscous flow of lubricant between the cylinder wall and the piston ring, the Reynolds Equation is used. It is a second order partial differential equation derived from the Navier-Stokes equations assuming a Newtonian fluid, negligible inertia and body forces, negligible pressure variation across the film, laminar flow, and negligible curvature [71]. It can take many forms depending

on the physical mechanisms involved in the system. The general form for a thin Newtonian fluid is given by

$$\frac{\partial}{\partial x}\left(\frac{\rho h^2}{12\mu}\frac{\partial p}{dx}\right)+\frac{\partial}{\partial z}\left(\frac{\rho h^2}{12\mu}\frac{\partial p}{dz}\right)=\frac{\overline{U}}{2}\frac{\partial \rho h}{\partial x}+\frac{\partial \rho h}{\partial t}. \quad (2.1)$$

While this form assumes laminar flow, it can be derived for different operating conditions as well. Ng and Pan derived a version for incompressible turbulent flow using the linearized turbulent theory [72]. Peiran and Shizhu derived another version for non-Newtonian thermal elasto-hydrodynamic lubrication [73]. Mitsuya et. al. tried to incorporate roughness and slip past the asperities [74]. Wu built on this model and applied it to the compressible flow equation [75]. In the model presented here, statistical flow factors that account for various surface roughness in the full-film lubrication regime have been added.

Flow Factors are a method to determine roughness effects on lubrication flow in any of the three regimes: full film lubrication, mixed lubrication, and boundary lubrication. These regimes are depicted in Figure 2.1.

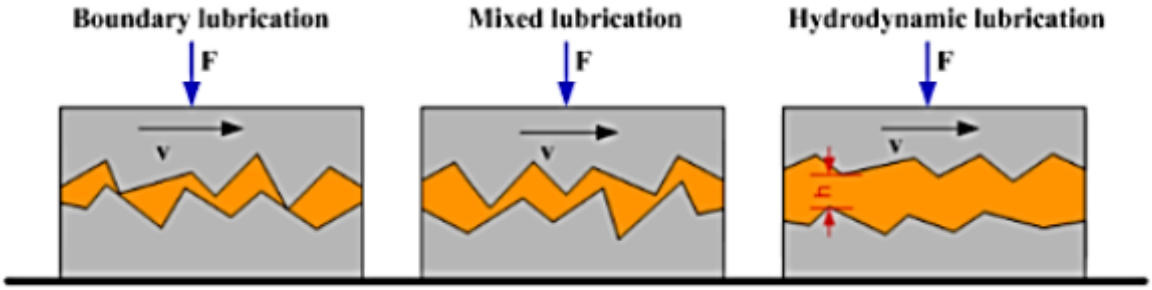

Figure 2.1: Lubrication Regimes [76]

Boundary lubrication, which is characterized by high surface abrasion and wear, is on the left side. On the right side, the lubricant separates the surfaces sufficiently such that no solid contact occurs. The lubrication regimes can be categorized by the Stribeck curve, a plot of friction coefficient against the dimensionless bearing number, shown in Figure 2.2. It is used to determine transitions between flow regimes.

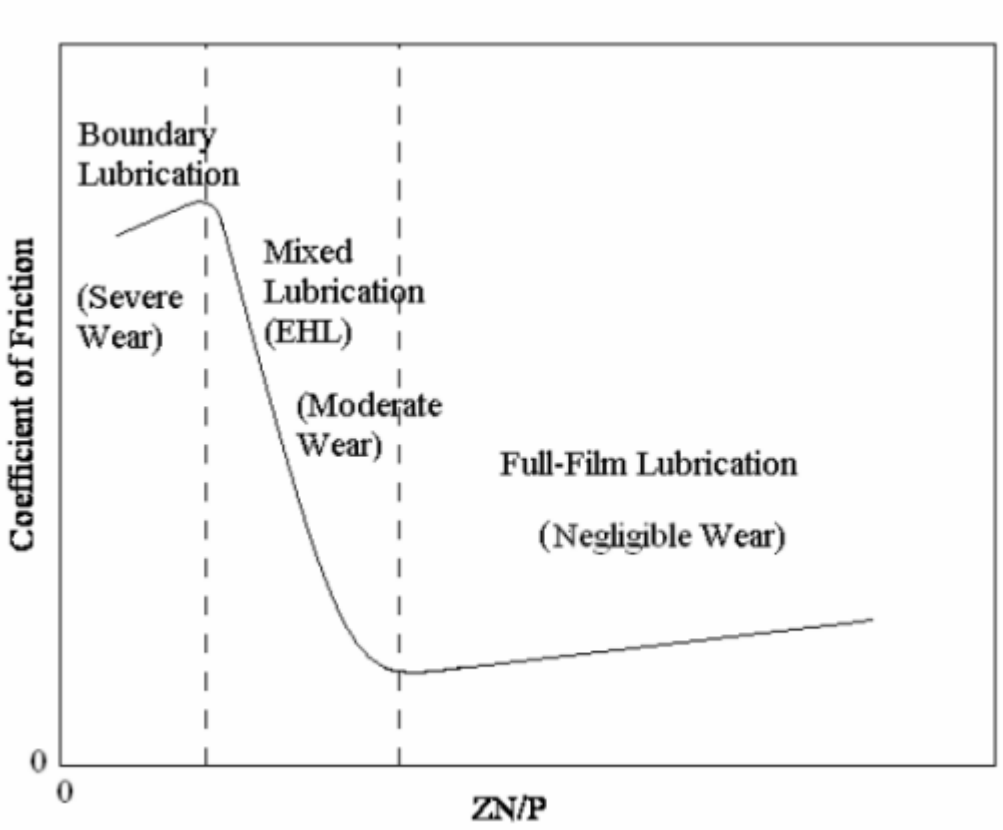

Figure 2.2: Sample Stribeck Curve [77]

Lubricants interact at both the macroscopic and the microscopic scales; the latter is especially important for the surfaces. Using the Reynolds equation to determine the pressure at each asperity is possible akin to a deterministic contact model, but it becomes computationally unfeasible for a sufficiently large surface resolution. Flow past individual asperities is too computationally and numerically difficult to model, so the simpler method of flow factors added to the Reynolds equation is used instead. Patir and Cheng [6] were the first to determine the effects of surface roughness on flow between

three-dimensional surfaces. They derived statistical flow factors added to the Reynolds equation as follows:

$$\frac{\partial}{\partial x}\left(\varphi_x \frac{\rho h^2}{12\mu}\frac{\partial p}{dx}\right)+\frac{\partial}{\partial z}\left(\varphi_z \frac{\rho h^2}{12\mu}\frac{\partial p}{dz}\right)=\frac{\overline{U}}{2}\frac{\partial \rho h}{\partial x}+\frac{\partial \rho h}{\partial t}+\frac{\partial \varphi_s}{\partial x}. \qquad (2.2)$$

This modified Reynolds equation produces a more accurate solution that accounts for microscopic surface features. In this equation, φ_z and φ_x measure the flow resistance across asperities in the flow direction and the transverse direction respectively, while φ_s measures lubricant transport due to shear effects. The flow factors depend on the film thickness, the RMS surface roughness, and the Peklenik number, γ. This number can be calculated from auto-correlation functions derived from the surface topography [78].

The flow factors calculated by Patir and Cheng were based off a statistically generated surface whose asperities were purely transverse, isotropic, or purely longitudinal. However, their flow factors are not totally accurate for a real surface that is not perfectly Gaussian. Other researchers tried methods to improve upon Patir and Cheng's work to find a more accurate model for specific cases. Wilson and Marsault derived an alternate form of the Reynolds equation applicable for high contact area ratios [79]. Peeken et. al. investigated flow factors for sintered bearing surfaces [80]. Hu and Zheng considered different boundary conditions and numerical methods to calculate flow factors but still considered theoretical surfaces [81]. Morales-Espejel derived a transformation to calculate flow factors for a non-Gaussian surface from their

counterparts for a Gaussian surface [82]. Sahlin et al. devised a new way to calculate flow factors that accounts for contact mechanics and used measured surfaces to do so [83]. Their results agreed with those of Patir and Cheng for longitudinal asperities but differed substantially for cross-hatched surfaces. Others applied various numerical and analytical methods [84-86]. The methodology used here is similar to work by Leighton et. al. [87], who derived surface specific flow factors for a piston ring-cylinder liner interface.

Previous studies of surface roughness effects on lubrication flow was mostly limited to stochastic concepts such as those first introduced by Tzeng and Saibel [88]. Patir and Cheng [6, 89] derived a new method based on numerically solving the Reynolds equation over a randomly generated surface and calculating an average equation from flow quantities. Their method assumes that rough surface heights are a perfect Gaussian distribution though. This work uses the flow factors Locker et al. [7] derived for an actual cross-hatched cylinder wall by combining stochastic concepts with Peklinik's signal processing theory [78].

CHAPTER 3

MODULE METHODOLOGY

The overall piston ring model is divided into a rough surface contact module and a lubrication module with sub modules for finding the frictional force and its effects on the system temperature. This chapter describes the modules in greater detail.

3.1: Rough Surface Contact

This work uses the Greenwood-Williamson statistical model [25] as a base for predicting the effects of rough surface contact. The equations to find the total contact load and area are

$$P(h) = A_n \eta \int_h^\infty \overline{P}(z-h)\phi(z)\,dz. \tag{3.1}$$

$$A(d) = A_n \eta \int_d^\infty \overline{A}(z-h)\cdot\phi(z)\cdot dz \tag{3.2}$$

P is the total contact force, A_n is the nominal area of contact (neglecting roughness), h is the mean surface separation, η is the areal asperity density, and ϕ is the asperity height distribution. Asperities are assumed to be homogenous and evenly distributed; their RMS (root mean square) height is σ_s. In early versions of the model, the spectral moment

approach used by McCool [90] was employed to calculate η, ϕ, and σ_s. From raw surface data spectral moments can be calculated using

$$m_2 = \frac{1}{N}\sum_{n=1}^{N}\left(\frac{dz}{dx}\right)_n^2 \tag{3.3}$$

and

$$m_4 = \frac{1}{N}\sum_{n=1}^{N}\left(\frac{d^2z}{dx^2}\right)_n^2, \tag{3.4}$$

where N is the number of points at which the surface height is measured. Because the analyzed surfaces are three-dimensional, moments were calculated along two orthogonal directions then averaged (the surfaces were assumed to be isotropic). They were used to calculate the statistical quantities:

$$\eta = \frac{m_4}{6\pi\sqrt{3}m_2} \tag{3.5}$$

$$R = 0.375\sqrt{\frac{\pi}{m_4}} \tag{3.6}$$

$$\sigma_s = \sqrt{\sigma^2 - \frac{0.0003717}{\eta^2 R^2}} \tag{3.7}$$

Note that σ is the rms height of the entire surface. To determine whether the surface was Gaussian in nature, the bandwidth parameter was calculated in both dimensions using

$$\alpha = m_4\left(\frac{\sigma}{m_2}\right)^2. \tag{3.8}$$

If its value exceeded 1.5, the surface was assumed to be sufficiently Gaussian in that direction to confidently use the G-W model. In a previous work [91], it was found that many surfaces are too far removed from a Gaussian distribution for a real value of σ_s to

be calculated. Thus, an alternate method of deriving the statistical parameters was developed. Asperities were manually counted by scanning the surface profile and identifying points whose height was higher than any of the 8 surrounding points. Kalin et al. found that using this deterministic approach results in different values of the statistical parameters compared to the spectral moments method [92]. The radius of curvature of each asperity was calculated in 2 orthogonal directions using

$$r_x = \frac{\left[1+\frac{dh}{dx}\right]^{\frac{3}{2}}}{\frac{d^2h}{dx^2}} \tag{3.9}$$

and

$$r_y = \frac{\left[1+\frac{dh}{dy}\right]^{\frac{3}{2}}}{\frac{d^2h}{dy^2}}. \tag{3.10}$$

The two values were averaged to estimate asperity's radius of curvature r. This parameter was calculated for every asperity, and then it was averaged to find R for all the asperities. The asperity density η was found by dividing the number of asperities counted by the area scanned. The original G-W model assumes elastic Hertz contact and a constant value of R. Different equations are used here because this work assumes the asperities are sinusoidal in nature and the loads are large enough for yielding to occur. The following relations were used to convert the asperity radius and density to frequency and amplitude:

$$f = \sqrt{\frac{\eta}{2}}, \tag{3.11}$$

$$\Delta = \frac{1}{4R(f\pi)^2}. \tag{3.12}$$

For a single $\lambda \times \lambda$ wavy asperity area to reach complete elastic contact the pressure required is given by

$$p^* = \sqrt{2}\pi E' f \Delta, \tag{3.13}$$

where

$$\frac{1}{E'} = \frac{1-\nu_1^2}{E_1} + \frac{1-\nu_2^2}{E_2} \tag{3.14}$$

Assuming an average contact pressure of $\bar{p}$ and letting

$$P_e = \frac{\overline{p}}{p^*}, \tag{3.15}$$

the following asymptotic solutions were found by Johnson, Greenwood, and Higginson [50]:

$$\left(\overline{A}_{JGH}\right)_1 = \pi\lambda^2 \left[\frac{3P_e}{8\pi}\right]^{\frac{2}{3}} \tag{3.16}$$

for small values of P_e and

$$\left(\overline{A}_{JGH}\right)_2 = \frac{\lambda^2}{2}\left(1 - \frac{3}{2\pi}\left[1 - P_e\right]\right) \tag{3.17}$$

when P_e approached unity.

Jackson and Streator [30] fitted a polynomial combining these equations using experimental data from Johnson et. al [50]

$$\widetilde{A} = \begin{cases} \left(\overline{A}_{JGH}\right)_1 \left(1 - P_e^{0.51}\right) + \left(\overline{A}_{JGH}\right)_2 P_e^{1.04}, P_e < 0.8 \\ \left(\overline{A}_{JGH}\right)_2, P_e \geq 0.8 \end{cases}$$

(3.18)

These equations neglect asperity yielding, so the elastic-plastic model developed by Krithivasan and Jackson [51] is used instead. They derived an expression for the contact area above which elastic-plastic contact occurs. This was derived from spherical contact, so this work uses a model developed by Jackson et. al. [93] that computes the critical interference above which elastic-plastic relations are used. That expression from Ghaednia et al. [94] is

$$\Delta_c = \frac{\sqrt{2} S_y}{E' f \pi \left[3e^{-\frac{2}{3}(\nu+1)} + 2\left(\frac{1-2\nu}{1-\nu}\right)\right]}. \tag{3.19}$$

Using this value of critical interference, the following equation was fitted to the FEM data of Krithivasan and Jackson [51] that links the pressures required for complete contact under elastic and elastic-plastic loading:

$$\frac{P^*_{ep}}{p^*} = 0.992^{\left[\left\{\frac{\Delta}{\Delta_c}\right\}^{\frac{10}{3}\left(\frac{\Delta}{\Delta_c}\right)^{-0.39} + \frac{9}{4}\nu^4 + 0.64} - 1 \right]}. \tag{3.20}$$

The contact area for low loads is found using

$$A_p = 2\left(\frac{A_c}{2}\right)^{\frac{1}{1+d}} \left(\frac{3\overline{p}}{4Cf^2 S_y}\right)^{\frac{d}{1+d}}, \tag{3.21}$$

where

$$d = 3.8\left(\frac{E' f \Delta}{S_y}\right)^{0.11}. \tag{3.22}$$

The equation that links the contact area for low and high loads is

$$\overline{A} = A_p\left(1 - P_{ep}^{\ 1.51}\right) + \left(\overline{A}_{JGH}\right)_2 P_{ep}^{\ 1.04}. \tag{3.23}$$

In this equation, $\left(\overline{A}_{JGH}\right)_2$ is calculated by replacing P_e with P_{ep} in Equation 3.16.

To apply sinusoidal asperities to the GW model, the surface separation needs to be calculated. Rostami and Jackson [95] derived expressions by averaging the surface separation from a finite element model. Their fitted equations are

$$G = \left(1 - \sqrt{P_e}\right)^{2.5} \tag{3.24}$$

for elastic contact and

$$G = \left(1 - P_{ep}^{\ A_1 P_{ep} + A_2}\right)^{2.5} \tag{3.25}$$

for elastic-plastic contact. In these equations,

$$G = \frac{g}{\Delta}, \tag{3.26}$$

$$A_1 = -0.08 \ln B^*, \tag{3.27}$$

$$A_2 = \frac{1}{15}\left(B^* - 1\right)^{0.44} + 0.99^{0.41\left\{B^* - 1\right\}} - 0.5, \tag{3.28}$$

and

$$B^* = \frac{\Delta}{\Delta_c}. \tag{3.29}$$

The integrals in Equation 3.1 and 3.2 were numerically evaluated for a range of surface separations. To find the corresponding load, Equation 3.24 for elastic contact or Equation 3.25 for elastic-plastic contact was solved numerically for the pressure, which was subsequently multiplied by the nodal area.

3.2 Fluid Lubrication Model

The piston ring-cylinder wall interface is not exclusively boundary lubrication; fluid film lubrication plays an integral role in the overall system behavior. To calculate the hydrodynamic lift, the modified Reynolds equation is employed. The original Reynolds equation was derived from the Navier-Stokes equations for the assumptions of incompressible thin film steady state flow of a Newtonian fluid. For smooth surfaces the Reynolds equation is

$$\frac{\partial}{\partial x}\left(\frac{h^2}{12\mu}\frac{\partial p}{dx}\right)+\frac{\partial}{\partial z}\left(\frac{h^2}{12\mu}\frac{\partial p}{dz}\right)=\frac{\overline{U}}{2}\frac{\partial h}{\partial x}+\frac{\partial h}{\partial t} \tag{3.30}$$

The left hand side of the Reynolds equation represents 2D Poiseuille flow due to a pressure gradient in the direction of fluid motion. The first term on the right hand side of the equation represents velocity driven (Couette) flow due to a velocity gradient normal to the fluid's motion. The last term of the equation is the squeeze film term – it represents the time-dependent variation of film thickness. This work neglects squeeze film effects, but they could be considered in a future version of the model.

3.2.1 Flow Factor Derivation and Reasoning

Since the Reynolds equation assumes smooth surfaces, it needs to be modified for surface roughness. Patir and Cheng [6] first developed a flow factor method that models rough surfaces as smooth; Locker et al. [7] refined them for the piston ring and cylinder wall studied here.

Consider a control volume of length Δx, width Δz, and height h(z,x,t). The local film thickness can be written as

$$\frac{\partial h}{\partial t} = -\left(\frac{q_{x+\Delta x} - q_x}{\Delta x} + \frac{q_{z+\Delta z} - q_z}{\Delta z} \right) \tag{3.31}$$

or

$$\frac{\partial h}{\partial t} = -\left(\frac{\partial q_x}{\partial x} + \frac{\partial q_z}{\partial z} \right) \tag{3.32}$$

for the limiting case of an arbitrarily small control volume. The local flow rates per unit width are defined as

$$q_x = -\frac{h^3}{12}\frac{\partial p}{\partial x} + \frac{\overline{U}}{2}h \tag{3.33}$$

and

$$q_z = -\frac{h^3}{12}\frac{\partial p}{\partial z}. \tag{3.34}$$

The average flow rates can be defined as

$$\bar{q}_x = \frac{1}{\Delta z}\int_z^{z+\Delta z}\left(-\frac{h^3}{12}\frac{\partial p}{\partial x} + \frac{\overline{U}}{2}h \right) dz \tag{3.35}$$

and

$$\bar{q}_z = \frac{1}{\Delta x}\int_x^{x+\Delta x} -\frac{h^3}{12}\frac{\partial p}{\partial z} dx. \tag{3.36}$$

The pressure and shear flow factors are defined such that the average flow rates become

$$\bar{q}_x = -\varphi_x \frac{h^3}{12}\frac{\partial p}{\partial x} + \frac{\overline{U}}{2}h + \frac{U_1 - U_2}{2}\sigma\varphi_s \tag{3.37}$$

and

$$\bar{q}_z = -\varphi_z \frac{h^3}{12}\frac{\partial p}{\partial z}. \tag{3.38}$$

The average flow rates can be used to modify the Reynolds equation as follows:

$$\frac{\partial}{\partial x}\left(\varphi_x \frac{h^2}{12\mu}\frac{\partial p}{dx}\right)+\frac{\partial}{\partial z}\left(\varphi_z \frac{h^2}{12\mu}\frac{\partial p}{dz}\right)=\frac{\overline{U}}{2}\frac{\partial h}{\partial x}+\frac{U_1-U_2}{2}\sigma\frac{\partial \varphi_s}{\partial x} \tag{3.39}$$

To obtain the pressure flow factors two 1D Poiseuille flows are assumed. The following boundary conditions are assumed: the pressure takes known values of P_A and P_B at x = 0 and x = L_x respectively, the pressure is periodic normal to the flow, and the local film thickness remains finite. In the x-direction, equations 3.35 and 3.37 are set to be equal. Solving that equation for the flow factor results in

$$\varphi_x = \frac{\frac{1}{\Delta z}\int_z^{z+\Delta z}\left(-\frac{h^3}{12}\frac{\partial p}{\partial x}\right)dz}{\frac{h^3}{12}\frac{\partial p}{\partial x}} \tag{3.40}$$

A similar procedure is followed in the z-direction using equations 3.36 and 3.38 to obtain

$$\varphi_z = \frac{\frac{1}{\Delta x}\int_x^{x+\Delta x}\left(-\frac{h^3}{12}\frac{\partial p}{\partial z}\right)dx}{\frac{h^3}{12}\frac{\partial p}{\partial z}} \tag{3.41}$$

Following this methodology, Locker et al. [7] averaged flow factors over the entire surface.

The shear flow factor relates the effects of neighboring asperities in terms of pure shear and accounts for the chance of cavitation at the trailing edge of each asperity. Each individual surface was assumed to be sliding separately against a smooth surface with no pressure induced gradient. Roughness effects are obtained through a similar surface

discretization to the pressure flow factor derivation. The shear flow factor for each surface can be written as

$$\Phi_s = \frac{2}{L_x L_z} \int_0^{L_x} \int_0^{L_z} \left(\frac{-\frac{h^3}{12\mu} \frac{\partial p}{\partial x} dz dx}{(U_1 - U_2)\sigma} \right) \tag{3.42}$$

The combined shear flow factor is convoluted through each surface's variance ratio:

$$V_{ri} = \left(\frac{\sigma_i}{\sigma} \right)^2 \tag{3.43}$$

Equations 3.42 and 3.43 are now combined to write the shear flow factor as

$$\varphi_s = \left(\frac{\sigma_1}{\sigma} \right)^2 \Phi_{s,1} + \left(\frac{\sigma_2}{\sigma} \right)^2 \Phi_{s,2} \tag{3.44}$$

Locker et al. [7] fitted the flow factors to empirical equations:

$$\varphi_x = 2.48 \left(\frac{h}{\sigma} \right)^{-1.777} + 1 \tag{3.45}$$

$$\varphi_z = 1 - 0.4824 e^{-0.2477\left(\frac{h}{\sigma}\right)} \tag{3.46}$$

For the surfaces being studied, φ_x and φ_z are related through the film thickness, roughness, and surface anisotropy index as

$$\varphi_x \left(\frac{h}{\sigma}, \gamma \right) = \varphi_z \left(\frac{h}{\sigma}, \frac{1}{\gamma} \right) \tag{3.47}$$

Later in the model's development, additional flow factors from [89] were added to account for surface roughness in the shear stress calculation. Defining $z = \frac{h}{3\sigma}$:

If $z > 1$:

$$\phi_f = \frac{35}{32} z \left[\left(1-z^2\right)^3 \ln\left(\frac{z+1}{z-1}\right) + \frac{z}{15}\left[66 + z^2\left(30z^2 - 80\right)\right]\right] \tag{3.48}$$

Otherwise,

$$\phi_f = \frac{35}{32} z \left[\left(1-z^2\right)^3 \ln\left(\frac{z+1}{300}\right) + \frac{1}{60}\left[-55 + z\left(132 + z\left(345 + z\left(-160 + z\left(-405 + z\left(60 + 147z\right)\right)\right)\right)\right)\right]\right] \tag{3.49}$$

$$\Phi_{fs} = \begin{matrix} A_3 H^{\alpha_4} e^{-\alpha_5 H + \alpha_6 H^2}, 0.5 < H < 7 \\ 0, H \geq 7 \end{matrix} \tag{3.50}$$

$$\varphi_{fs} = \left(\frac{\sigma_1}{\sigma}\right)^2 \Phi_{fs,1} + \left(\frac{\sigma_2}{\sigma}\right)^2 \Phi_{fs,2} \tag{3.51}$$

where H is the dimensionless surface separation (h/σ). Values of coefficients are given in Table 3.1.

Equation 3.39 is solved numerically using an iteration scheme.

3.2.2 Shear Rate, Pressure, and Temperature dependence of Viscosity

Because early versions of the model predicted that the system operated mostly in the hydrodynamic regime with relatively high shear rates, a shear thinning model was introduced. A version of the Carreau model adapted from Jang, Khonsari, and Bair [96] was introduced as follows:

$$\mu_{eff} = \mu_2 + \left(\mu_1 - \mu_2\right)\left(1 + \left(\frac{\mu_1 U}{hG}\right)^2\right)^{\frac{n-1}{2}} \tag{3.52}$$

In this equation, G and n are material dependent constants. The placeholder values of 10 kPa for G and 0.8 for n were initially selected, but later versions of the model fitted

curves to measured data to derive them. However, said data was only provided for two distinct temperatures: 60 and 100°C. Initially it was presumed that they would suffice (while not being 100% accurate) for the base temperatures of 50 and 120°C, while the average was used for an 80°C starting temperature. Early versions of the model set μ_2 to 0 and performed a least squares regression to find G and n. Eventually it was realized that the curve fit would have to be generated at one of the temperatures for which data was given as attempts to interpolate between the values failed. Therefore, a single fit was done at a temperature of 60°C. Tables 3.1 and 3.2 list the lubricant's shear thinning data. In these tables, the first two measurements were conducted with a Cone and Plate Viscometer, while the other values were measured by a Tapered Bearing Simulator Viscometer and modified relative to ASTM D6616.

Table 3.1: Lubricant Viscosity Dependence on Shear Rate, 100°C

Shear Rate (1/s)	μ (Pa*s)
1000	0.0072
10000	0.006735
10000	0.00661
100000	0.00596
1000000	0.00603
3500000	0.00548

Table 3.2: Lubricant Viscosity Dependence on Shear Rate, 60°C

Shear Rate (1/s)	μ (Pa*s)
1000	0.02
10000	0.01921
10000	0.01971
100000	0.01777
1000000	0.01601
3500000	0.01537

Figure 3.1 shows the fit to the shear thinning data, and Table 3.3 shows the values of *G* and *n*. It was presumed that the coefficients remained valid for different temperatures.

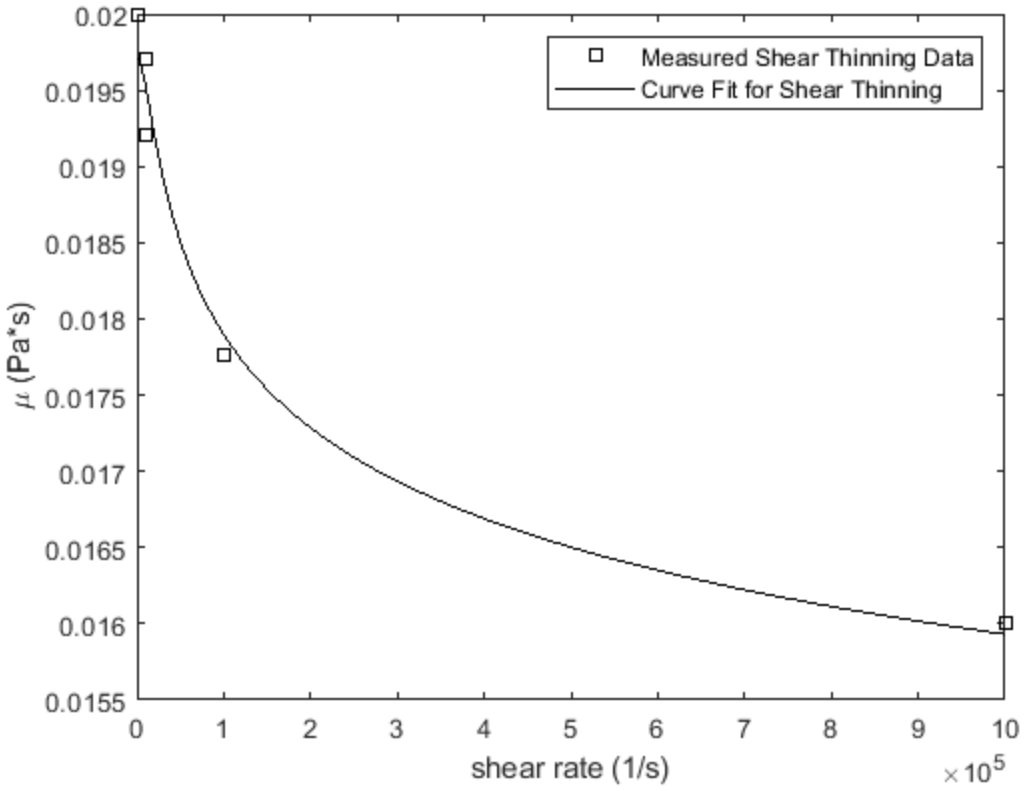

Figure 3.1: Final Shear Thinning Fit at 60°C

Table 3.3: Coefficients Used in Equation 3.48

G (Pa)	299
n	-0.0254

Initially the model was executed using a constant viscosity, but to improve the comparison with experimental data it was subsequently revised to incorporate pressure viscosity effects. At high pressures, the lubricant's resistance to flow increases until solidification occurs at a sufficiently high pressure. This model uses the Barus equation to account for increased viscosity under pressure.

$$\mu = \mu_0 e^{\xi P} \tag{3.53}$$

Table 3.4 lists the values used for the pressure viscosity coefficient.

Table 3.4: Pressure Viscosity Coefficient Values of the Lubricant

Temperature (°C)	ξ (Pa*s)
25	$2.05*10^{-8}$
100	$1.248*10^{-8}$

With only two values provided, the pressure viscosity coefficient was assumed to vary linearly with temperature. If the temperature was beyond the range of the provided values, the closer value was used without modification. Figure 3.2 shows the effects of pressure on viscosity for a temperature of 100 °C when applied to the model. The pressure viscosity dependence appears to be an important factor to include, particularly in the hydrodynamic regime. Neglecting viscosity changes due to pressure resulted in a small decrease in the predicted friction coefficient at higher speeds and smaller changes at lower speeds where rough surface contact carries a majority of the load.

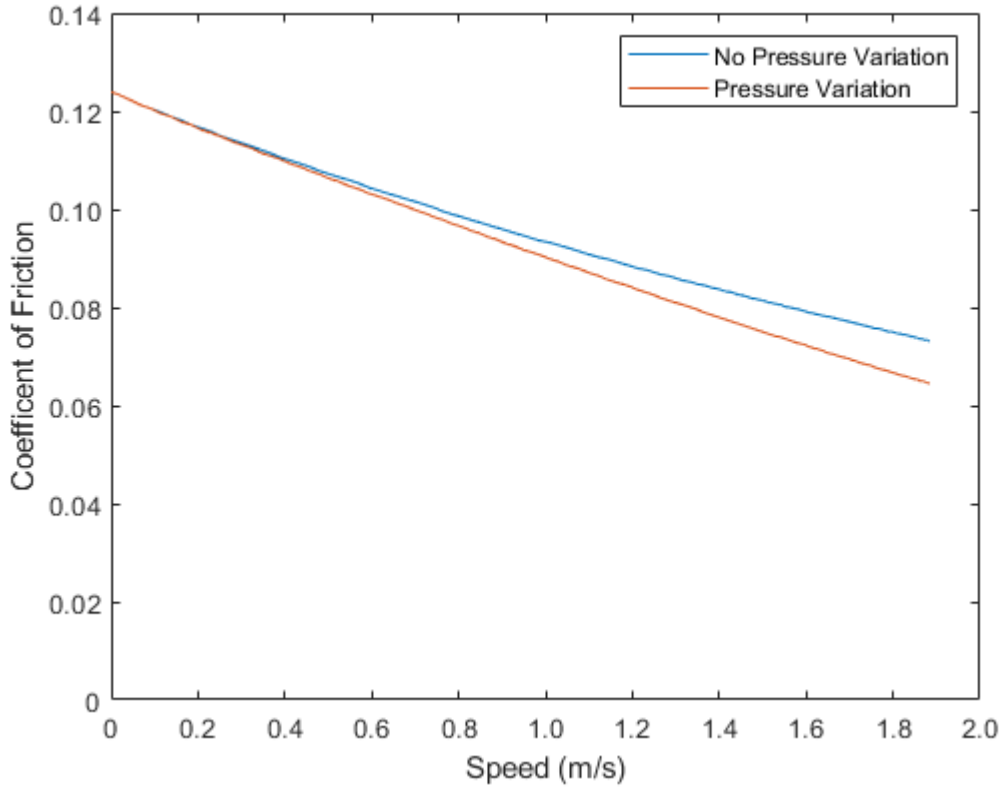

Figure 3.2: Viscosity Pressure Effects on Predicted Friction Coefficient

Once frictional heating was incorporated, the effects of increased temperature on viscosity also needed to be added to the model. As the temperature increases, the intermolecular forces that resist flow of a liquid decrease. The Roelands equation was used to adjust the viscosity.

$$\frac{\mu}{\mu_0} = \frac{\mu_\infty}{\mu_0} 10^{G_0\left(1+\frac{t_m}{135}\right)^{-S_0}} \tag{3.54}$$

Figure 3.3 illustrates the viscosity fit as a function of temperature.

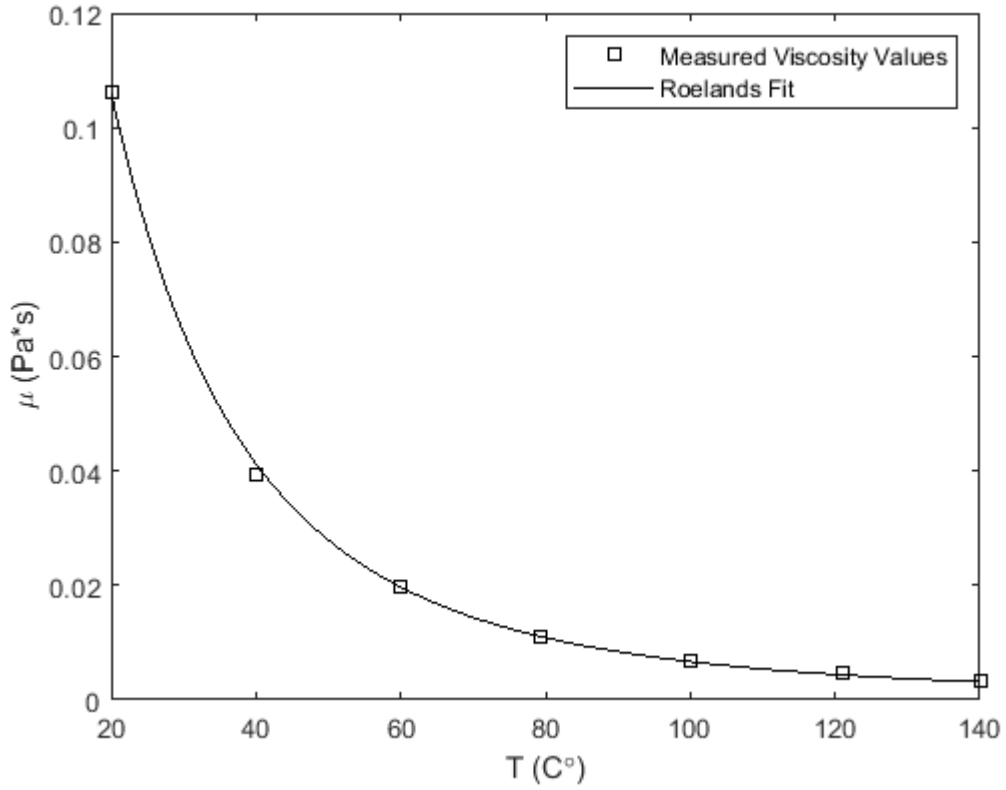

Figure 3.3: Created Fit for Temperature Dependent Viscosity Variation

3.3 Predicting the Frictional Force

This model relies on Amonton's Law of Friction,

$$F_f = F_{contact}\mu_k \tag{3.55}$$

to predict the frictional force due to solid contact. Initially, the value of μ_k was guessed and assumed to be independent of load. However, the model did not match the experimental measurements very well. One possible reason is that it did not consider friction behaviors observed for elastic-plastic contacts. A mechanism to decrease the

friction coefficient with load (which has been observed and predicted by various researchers) needed to be added [97-100]. The first attempt to improve the model was taken from Cohen et al. [97]

$$\mu_s = \left(0.26 + \frac{0.43}{\psi}\right)\left(F^*_n\right)^{0.0095\psi - 0.09} \tag{3.56}$$

where the plasticity index ψ is given by

$$\psi = \frac{2E'}{\pi C S_y}\sqrt{\frac{\sigma_s}{R}} \tag{3.57}$$

This model considers friction to be due to asperity micro-welding, and sliding occurs only after the entire contact area has yielded. Friction coefficient decreases as load (and plasticity) increase. However, Equation 3.49 is not valid for $\psi > 8$. In that case, a different equation derived by Li, Etsion, and Talke [98] must be used instead.

$$\mu_s = \left(0.26 + 0.32e^{-0.34\psi^{1.19}}\right)\left(F^*_n\right)^{-\exp\left(-1.9\psi^{0.4}\right)} \tag{3.58}$$

After this equation gave an even higher predicted friction coefficient, another equation for friction coefficient was evaluated based off the Etsion model:

$$\mu_s = \mu_{\max}\left[1 + 1.23\exp\left(-0.34\psi^{1.19}\right)F^{*\,-\exp\left(-1.9\psi^{0.4}\right)}_n\right] \tag{3.59}$$

μ_{max} is a parameter that can be set just like μ_k in Equation 3.48.

Unfortunately, this model predicted an increase in friction coefficient as load increased; friction coefficient is observed to be inversely proportional to load. Thus, a new simplified model was formulated from experimental data and evaluated (see Chapter 7).

$$\mu = 0.33F^{-0.2} \tag{3.60}$$

In this equation, the friction coefficient only depends on the overall load measured in Newtons. However, it could be adapted so it could include the nondimensionalized load. Based on FEM results from Wang et al. [99] and a sample of results applying the model using Equation 3.53 (see Figures 7.6 – 7.11), the following expression was derived.

$$\mu = \mu_{\max} - 0.085F_n^* \tag{3.61}$$

Once again μ_{max} can be varied; its initial value was 0.175. After doing some curve fitting to experimental data with a baseline temperature of 80°C (see Chapter 5), the following equation was proposed.

$$\mu = \mu_{\max} - 0.2F_n^* \tag{3.62}$$

Initially μ_{max} was set to 0.153, but it was increased to 0.1565 as that resulted in a better comparison to experimental data.

To determine the friction due to fluid motion, Newton's Law of Viscosity was initially used.

$$\tau = \mu \frac{du}{dy} \tag{3.63}$$

Later versions of the model added shear factors that reflect the surface roughness and used the following equation to calculate viscous shear stress instead:

$$\tau = \mu \frac{U_2 - U_1}{h}\left(\phi_f \pm \phi_s\right) \pm \frac{h}{2}\frac{\partial p}{\partial x} \tag{3.64}$$

The frictional force can then be calculated by multiplying the shear stress by the area on which it is applied.

3.4 Incorporating Temperature Adjustments into the Model

Due to the high friction coefficient in boundary lubrication, a large amount of heat can be generated, especially when the load is large. This is known as flash temperature. The following equation can be used to calculate the generated heat.

$$Q = \mu F V \tag{3.65}$$

The heat depends on the total frictional force and the velocity – higher speeds and/or loads will result in a greater amount of heat generated. That manifests itself in a temperature increase of the system as given by Equations 3.62 for a moving surface and 3.63 for a stationary surface [101].

$$T - T_0 = \frac{Q}{4.56rk\sqrt{0.66 + Pe}} \tag{3.66}$$

$$T - T_0 = \frac{Q}{4rk} \tag{3.67}$$

Based off an analogy with electrical current, Equations 3.62 and 3.63 can be combined for the case in which neither surface is adiabatic [71]:

$$Q = 4rk_1\left(T - T_0\right) + 4rk_2\left(T - T_0\right) \tag{3.68}$$

Equation 3.64 assumes a low sliding speed for both surfaces but can be easily adapted if either surface is sliding rapidly. Solving it for the temperature change results in

$$T - T_0 = \frac{Q}{4.56rk\sqrt{0.66 + Pe} + 4rk} \tag{3.69}$$

To calculate all the quantities, the thermal diffusivity and conductivity of the ring and liner must be known. There are multiple ways to incorporate frictional heating: either the temperature change of the system as a whole can be considered, or the temperature could be calculated at specific points. It was quickly discovered that the former option would not be feasible.

3.5 Summary

Different modules are employed and tested in the integrated piston ring model to compare its predictions to experiments. They incorporate the effects of rough surface contact using wavy asperities; hydrodynamic lubrication with flow factors to account for roughness; speed, pressure, and temperature dependence on viscosity, friction coefficient dependence on normal load, and heat generation due to frictional forces. The influence and effectiveness of these modules will be discussed in future chapters.

CHAPTER 4

COMBINING THE INTEGRATED LUBRICATION AND SOLID CONTACT MODELS

4.1 Coding the Mixed Lubrication Elastic-Plastic Model and Integrating Abaqus Outputs

The combined effects of the oil hydrodynamic pressure and surface contact pressure need to be considered in modeling the cylinder wall – piston ring interface. Procedures for finding these pressures are detailed in Chapter 3. They are superimposed on every side of the piston ring to find the overall force on the system. To improve the model, deformations are incorporated by coupling the combined model to a finite element analysis performed in Abaqus. Initially, a very simple axisymmetric model using the mesh shown in Figure 4.1 was created, as the only goal at the time was to make sure Abaqus could read the forces calculated from running the lubrication and contact models in MATLAB®.

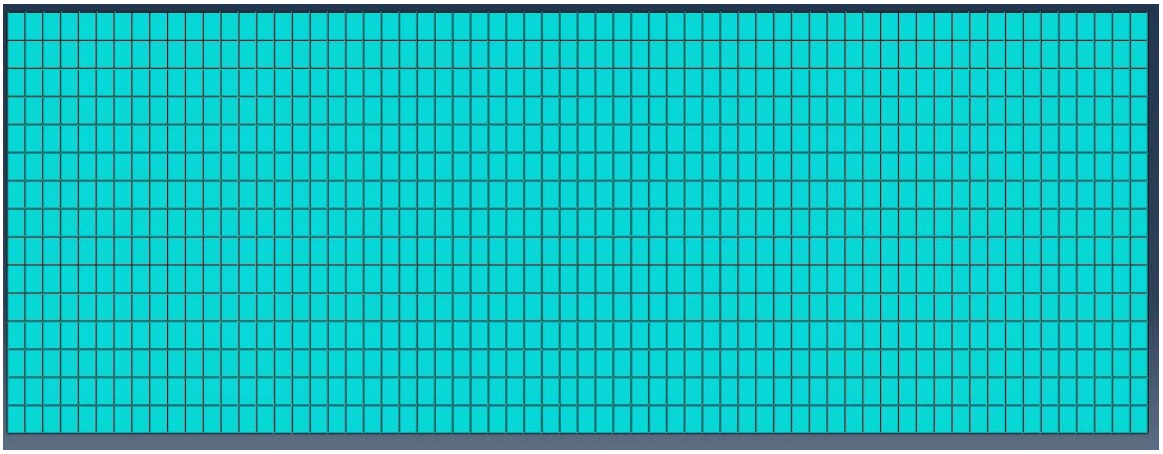

Figure 4.1: Initial Mesh of Piston Ring

The abaqus2matlab toolbox [102] is used to allow the MATLAB® program to read the displacements from the finite element analysis to determine the new ring profile for the next iteration. Once it was demonstrated that MATLAB® and Abaqus could communicate with each other, the piston ring was refined to reflect the actual geometry; the mesh and the geometry are shown in Figures 4.2-4.3.

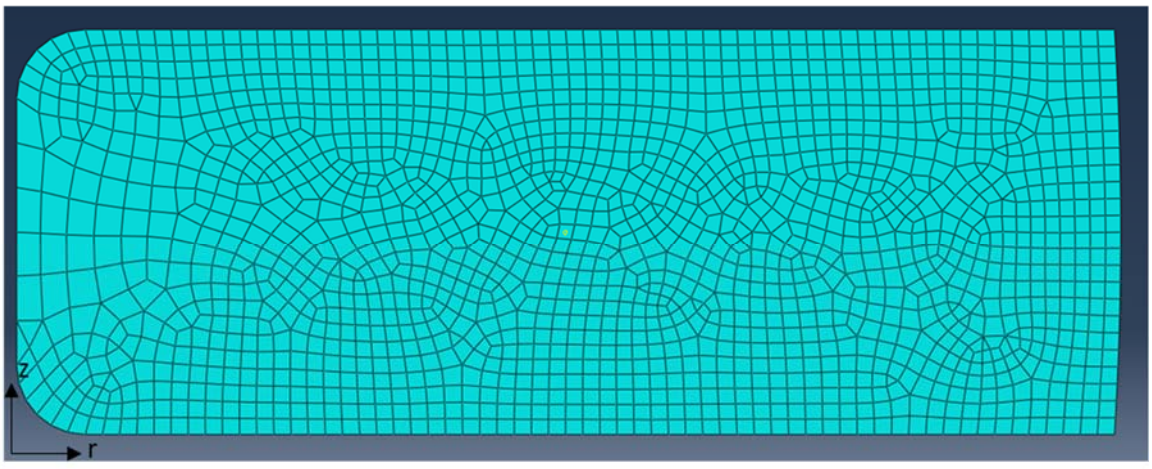

Figure 4.2: Final Mesh of Piston Ring

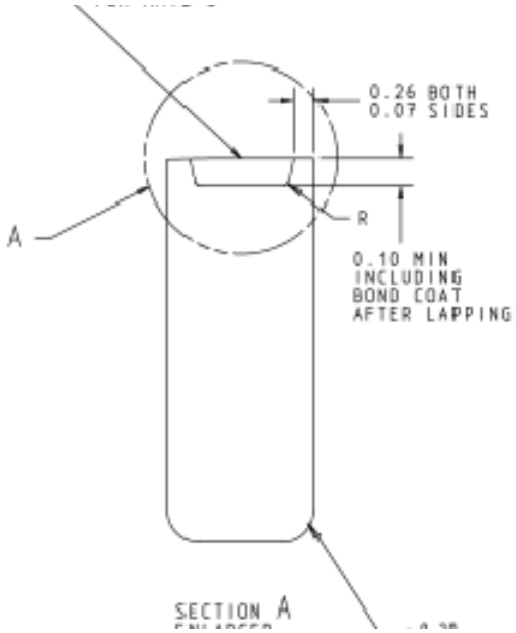

Figure 4.3: Schematic of Ring Geometry

For baseline predictions, the piston ring was assumed to slide over the following range of speeds: 0.0009 m/s to 0.9 m/s, which is based on typical speeds of an actual piston head. The lubricant temperature was held at 100 °C, and the sliding friction coefficient was taken to be 0.10. A 424 kPa pressure was applied to the inside of the ring as shown in Figure 4.4 (left side of figure).

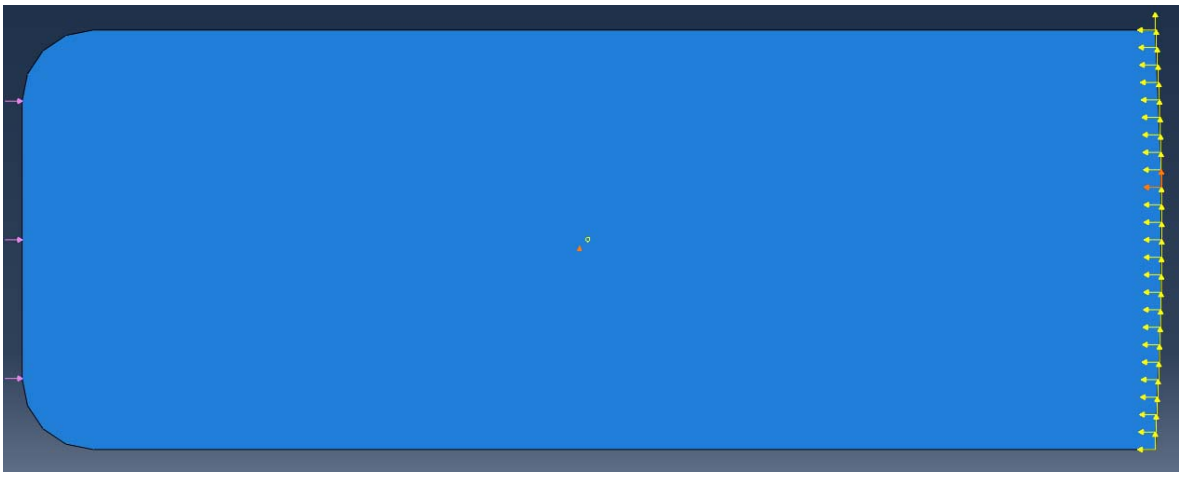

Figure 4.4: Loads and Pressures on the Ring

The flowchart for running the model is given in Figure 4.5.

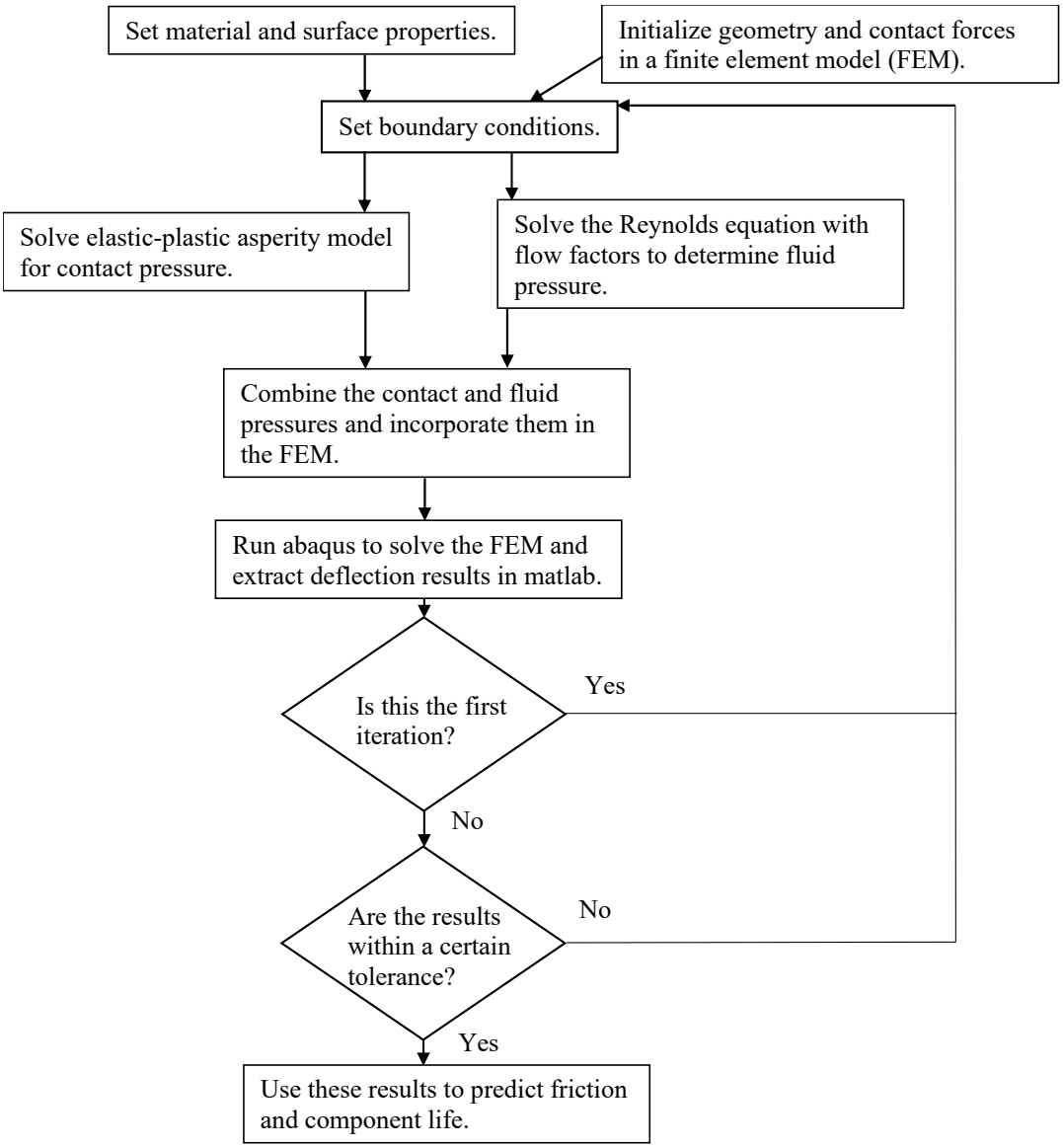

Figure 4.5: Initial Flowchart of Model

Boundary conditions include lubricant pressures on the edges of the ring (open to atmosphere in the experiments [see Chapter 5]), the base temperature, the applied load,

and the range of speeds analyzed. Sliding speed is assumed to vary sinusoidally – three different average speeds were analyzed: 0.3 m/s, 0.6 m/s, and 1.2 m/s. Figure 4.6 shows how the speed varies as a function of time.

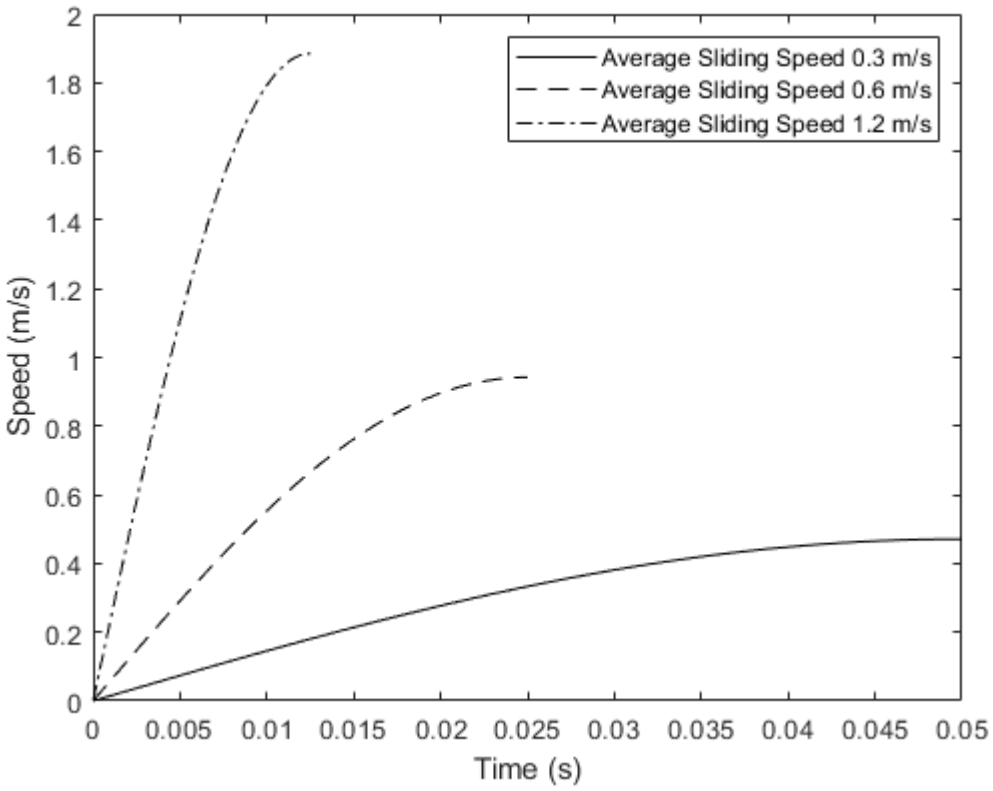

Figure 4.6: Converting Speed to Time

At higher average sliding speeds, the piston ring reaches its maximum speed faster and spends less time at lower speeds where boundary lubrication would likely occur. The density and the kinematic viscosity vary with temperature. Table 4.1 lists their values.

Table 4.1: Available Properties of Lubricant

Temperature (°C)	η (mm^2/s)	ρ (g/cm^3)
-40	22000	
-20	2200	
-17.8		871.2
0	422	
20	125	848.6
21.1		847.8
40	47.17	835.7
49.4		830.9
60	23.9	824.5
79.4	13.7	812.9
93.3		804.5
100	8.698	800.5
121	5.84	787.9
140	4.3	776.5

Using Equation 4.1, the dynamic viscosity can be calculated from the data in Table 4.1.

$$\mu = \eta\rho \quad (4.1)$$

Figure 4.7 shows the temperature dependent density variation.

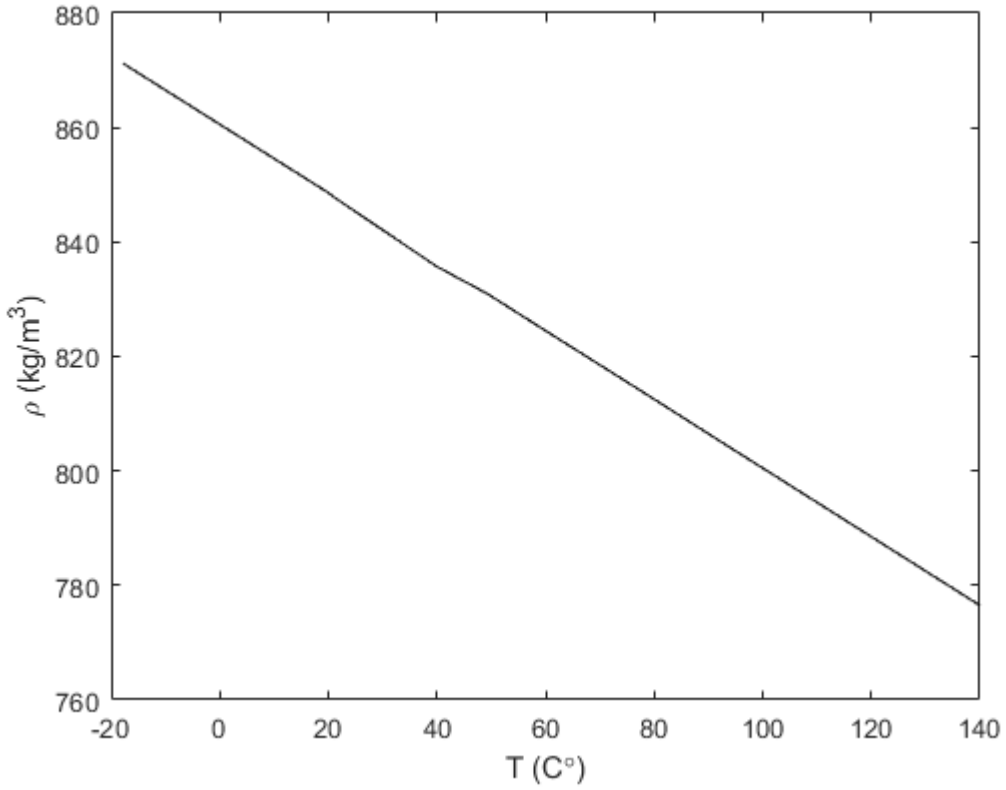

Figure 4.7: Density Variation with Temperature

Initially when the model temperature was held at a constant, the closest temperature for which viscosity and density were given were used. For other operating temperatures, curve fits were generated to determine the viscosity or density. The figure above suggests a linear fit is highly suitable for the density variation, but a look at Figure 3.4 suggests that a fit to Equation 3.51 is required to predict the viscosity given the temperature.

When applying the contact and fluid pressures to the ring (Figure 4.3), they needed to be converted to forces. This was done by calculating the area of a node on the outside of the

ring. This surface was treated as a rectangle with dimensions depicted in Figure 4.8 below.

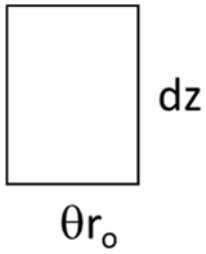

Figure 4.8: Area of a Single Node

The angle was calculated as follows:

$$\theta = \cos^{-1}\left(\frac{2r_0^{\,2} - 0.017}{2r_0^{\,2}}\right) \quad (4.2)$$

where r_0 is the outside radius of the piston ring, 0.0463 m. For the edge nodes, the value of the node spacing dz is halved.

On the other side of the ring, the applied load (50, 100, or 150 N) was converted to a pressure using the contact area on the inside. This mimics the loads applied in the experiment and those experienced in an actual engine. Combining the applied load on the inside with the contact and fluid pressures on the outside gives an equation that relates net axial force and surface separation. The location of the ring was numerically solved for a net zero axial force. The contact and hydrodynamic forces that solve the equilibrium equation are written in an abaqus input file that creates the mesh shown in

Figure 4.2 and applies the loads shown in Figure 4.4. The input file is then run in Abaqus, and the toolbox abaqus2matlab [102] is used to transfer the displacements back to MATLAB®. These displacements are then used to alter the piston ring profile, and the process is repeated until convergence is reached.

4.2 Early Model Results and Validation Attempts

Version 1 of the model does not incorporate temperature changes based on the friction force. It predicts the load carried by the asperities and the load carried by the lubricant for a range of speeds. The results are shown in Figures 4.9-4.14 for four specific speeds and a range of speeds to confirm the model works properly. In each case the load is the placeholder load stated on Page 55.

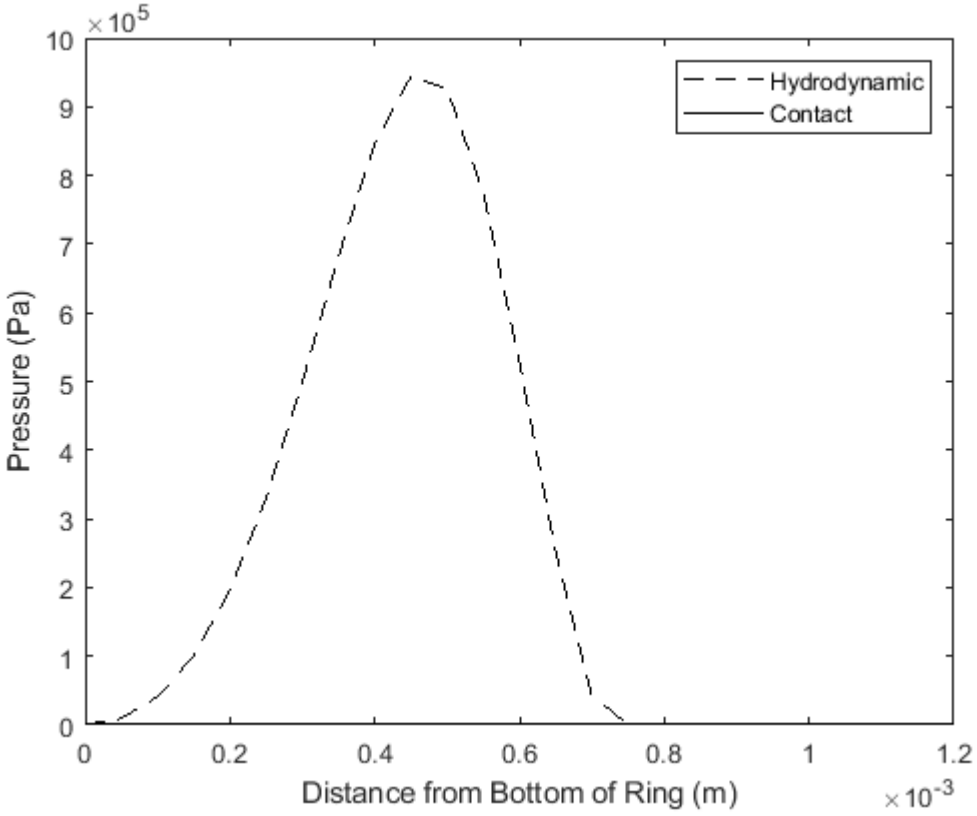

Figure 4.9: Pressure Distribution for a Speed of 0.9 m/s, Model Version 1

This suggests hydrodynamic lift completely separates the surfaces at a sliding speed of 0.9 m/s and that rough surface contact can be neglected completely.

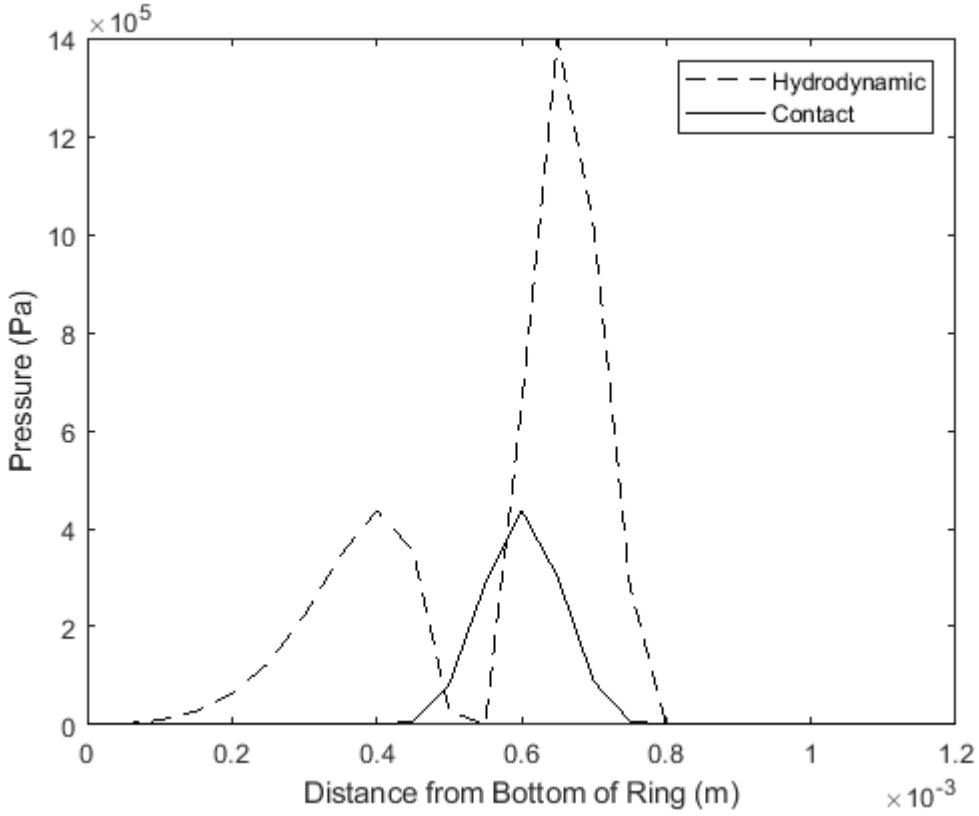

Figure 4.10: Pressure Distribution for a Speed of 0.09 m/s, Model Version 1

For the slower sliding speed of 0.09 m/s, the lubricant still carries most of the load. However, surface roughness begins to play a role as the peak contact pressure is roughly 35% of the maximum hydrodynamic pressure.

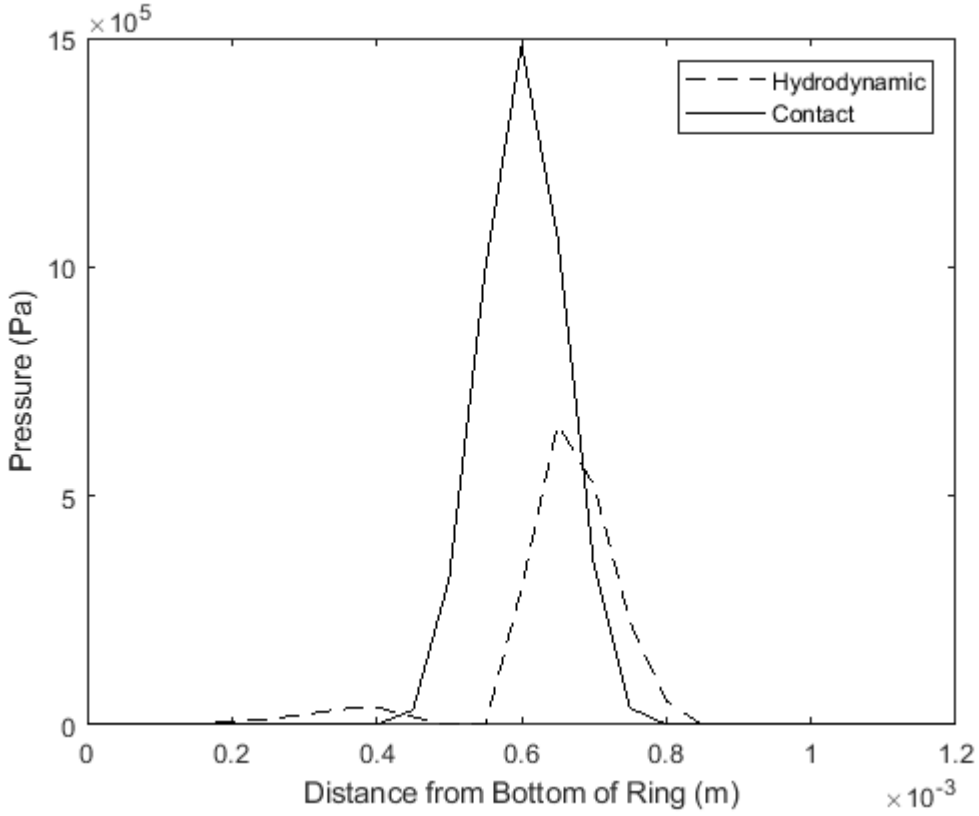

Figure 4.11: Pressure Distribution for a Speed of 0.009 m/s, Model Version 1

For the even slower sliding speed of 0.009 m/s, surface contact begins to carry most of the load, but the lubricant still carries a significant portion.

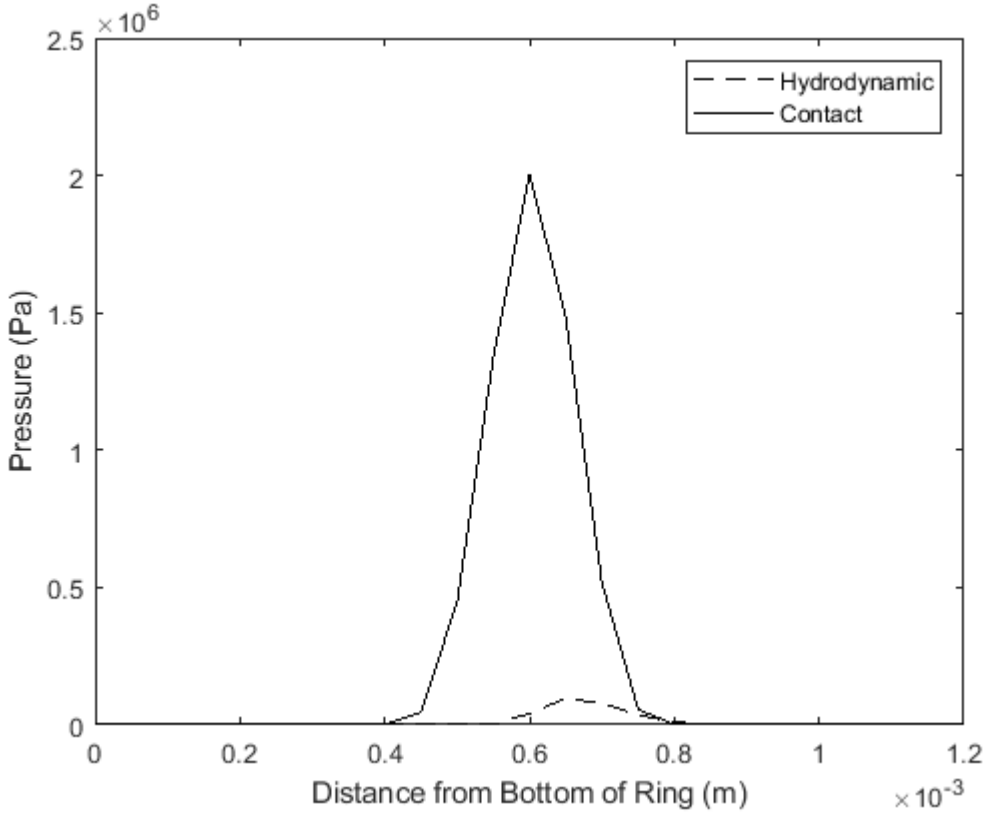

Figure 4.12: Pressure Distribution for a Speed of 0.0009 m/s, Model Version 1

For the slowest sliding speed considered, the lubricant cannot support much of the load; its effects are largely negligible.

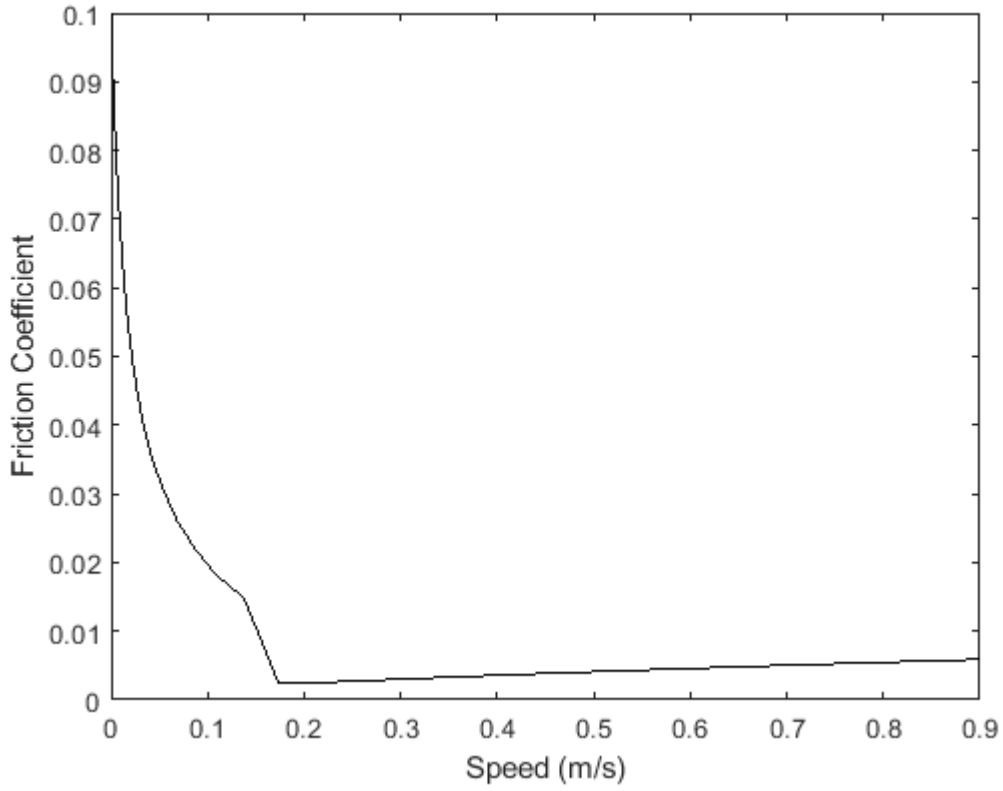

Figure 4.13: Stribeck Curve, Model Version 1

The model predicts a high friction coefficient at very low sliding speeds. However, it seems that the predicted friction coefficient drops erratically at sliding speeds between 0.1-0.2 m/s. This indicates that revisions will likely be needed.

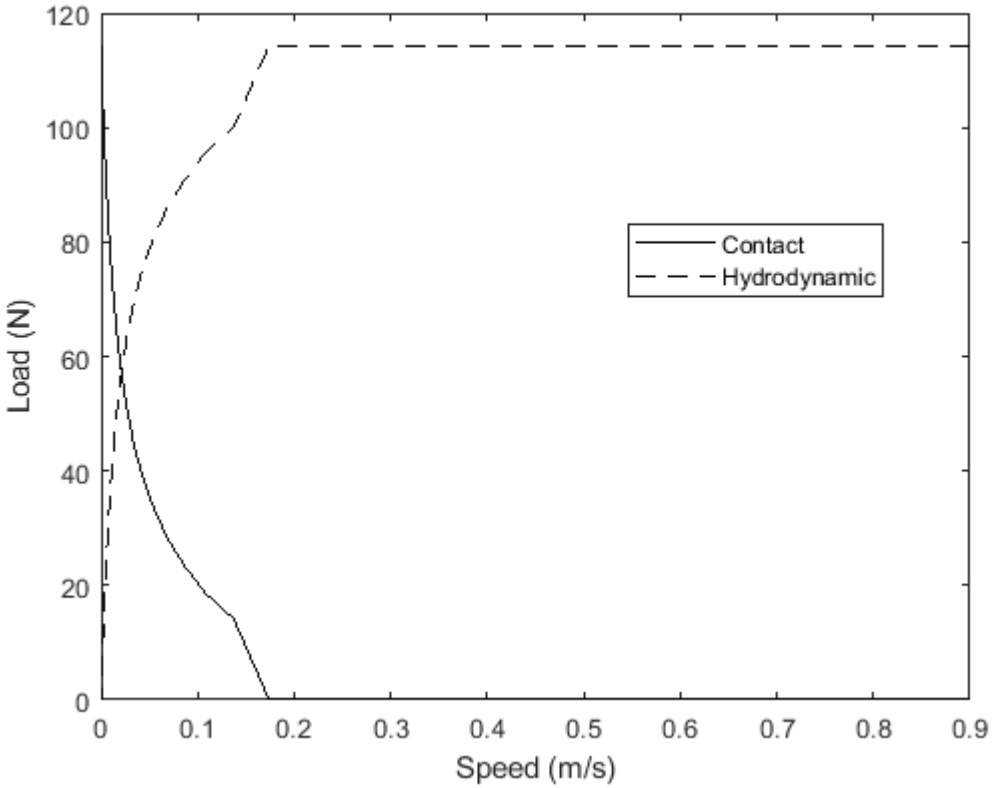

Figure 4.14: Load Carrying Distribution

Figure 4.14 shows how the model predicts the load is carried at different speeds. At the fastest piston speeds, the lubricant carries the entire load. This coincides with the slow increase in predicted friction coefficient as speed increases under the fully hydrodynamic regime as shear force increases (Equation 3.60). As the speed decreases, the contact pressure increases because the oil cannot carry as much of the load. The system remains in the boundary lubrication regime only for very low speeds and quickly transitions to the hydrodynamic regime. The average friction coefficient is 0.0155. This is a very low value, and the trend is nowhere close to the experimental measurements. An attempted

solution was to modify the sliding friction coefficient from 0.1 to 0.25. However, did not appreciably increase the predicted friction coefficent; Figure 4.14 depicts the new Stribeck Curve with only that friction parameter changed.

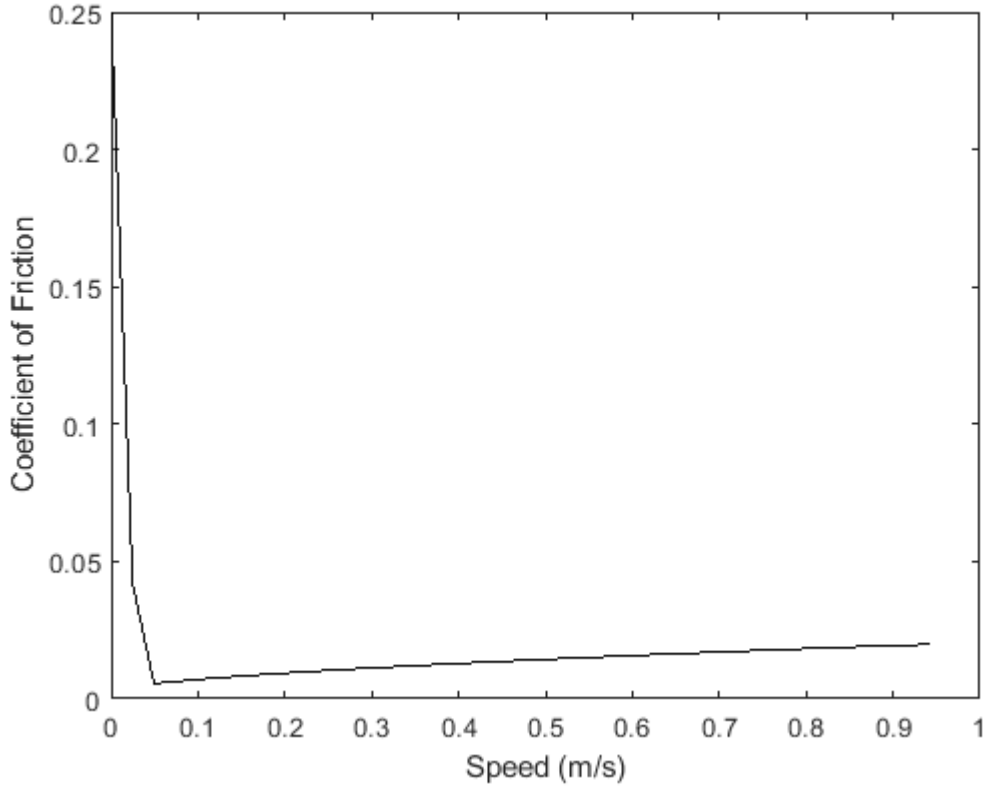

Figure 4.15: Stribeck Curve for the Revised Dry Friction Value

From Figure 4.15, the overall trend remains very similar – for almost the entire quarter cycle the ring operates in the hydrodynamic regime. In fact, it appears that the ring enters the hydrodynamic regime at an even slower speed. While the quarter cycle average

friction coefficient increased to a value of 0.0198, it was clear that the model needed substantial revisions. It still did not incorporate any temperature adjustments.

4.3 Establishing Model Convergence Criteria and Improving the Model's Estimations

A closer inspection at the code revealed significant errors: the only convergence requirement was for the pressure on the outside of the ring, which was quickly satisfied due to forces being balanced. The deformations were not mapped correctly either, and the shear flow factor equation was inaccurate.

The criteria were revised as follows: the hydrodynamic and contact pressures were checked at each node to see if they changed by more than a certain amount, and the shear force percentage change could not exceed a certain value, say 0.05% relative to the previous iteration. Table 4.2 shows how the predicted friction coefficient for a sliding speed of 0.09 m/s and a load of 150 N was affected by choice of maximum pressure change.

Table 4.2: How a Nodal Pressure Change Tolerance Affected Model Predictions

Maximum Allowed Pressure Change Between Iterations	Final Predicted Coefficient of Friction
1 MPa	0.0575
100 kPa	0.065
10 kPa	0.065

In the latter two cases, convergence was not reached very quickly. While looking at the data, it was observed that the shear force converged to a very low value. Figure 4.16 shows the trend.

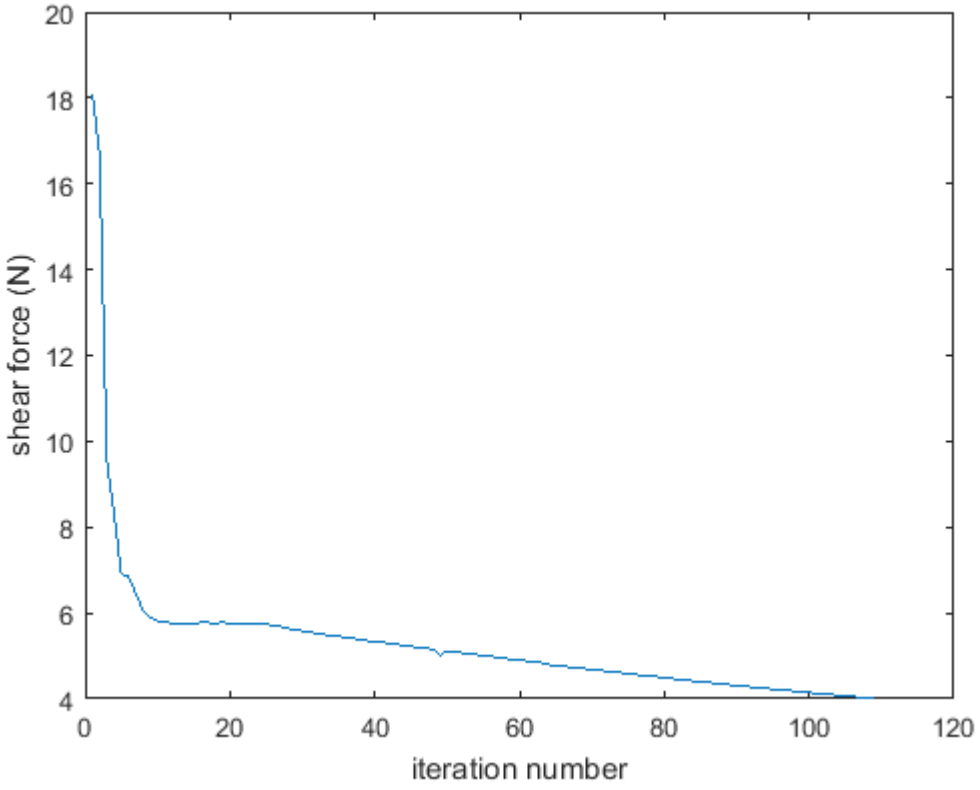

Figure 4.16: Shear Force Convergence for Model Version 2

Two notable observations can be made: the number of iterations required for convergence and the instability of the decreasing shear force trend. With over 100 iterations required, the program would not be feasible to run because it would take too long to predict the friction for a range of speeds. The other noteworthy issue was the fact that shear force was almost continually decreasing. However, this was not seen as a

problem at the time. An observation of the predicted pressures revealed that the contact pressure was an order of magnitude smaller than hydrodynamic pressure. While the lubricant's contribution to the total shear force was minimal, it was desired to correct the contact model first. Based on the difficulties with using spectral moments to calculate surface parameters, those values were recalculated by manually inspecting the surfaces for asperities. Details of this method are explained in Chapter 3. Table 4.3 lists the parameters that were used in the model.

Table 4.3: Surface Parameters

R (μm)	16.05
η (asperities/m^2)	1.803×10^{10}
σ_s (μm)	0.5126

Figures 4.17 and 4.18 show model Version 2's predictions using the revised set of surface parameters.

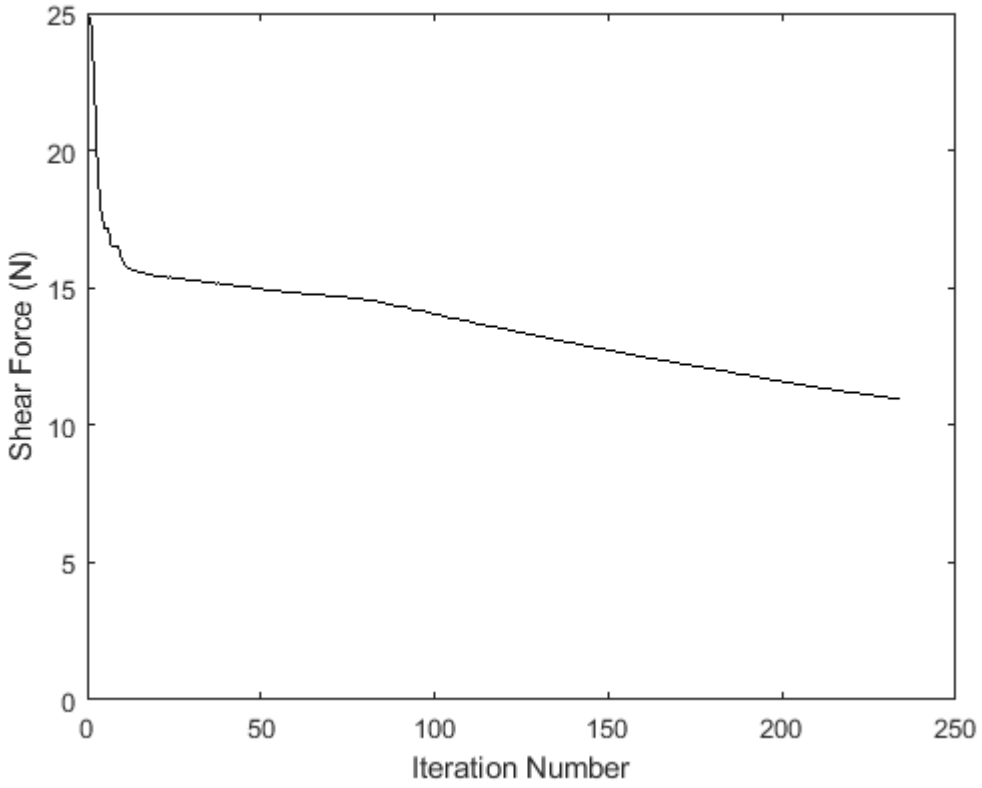

Figure 4.17: Shear Force Convergence with New Surface Parameters

While the revised model increased the predicted shear force, the trend of slowly decreasing shear force persisted.

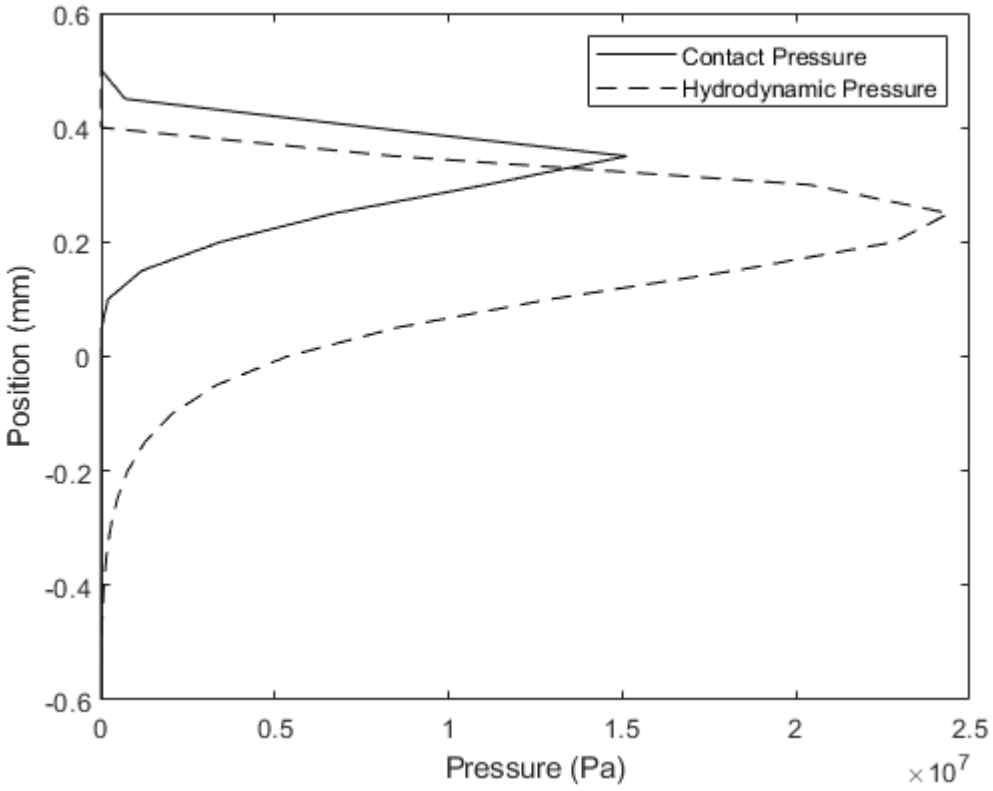

Figure 4.18: Model Version 3 Predicted Pressure Profiles

While the predicted pressures and friction were higher, the model took more than twice as long to converge. With over 240 iterations required for a single velocity, it was clear new convergence criteria had to be developed. The requirement for pressure changes at individual nodes was dropped, and only a 0.05% change in shear force was retained. The load remained at 150 N. Figure 4.19 shows the model's predicted friction coefficient.

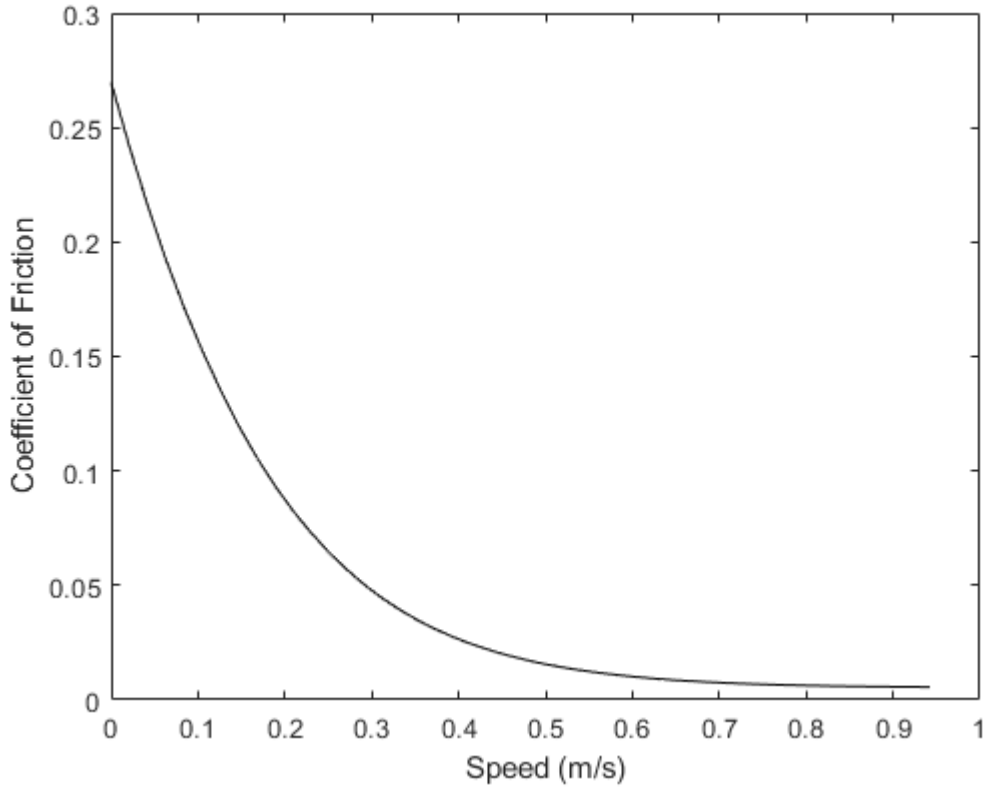

Figure 4.19: Model Version 3 Predicted Friction Coefficient

Model Version 3 predicts a quarter cycle average friction coefficient of 0.036. This is still a very low value compared to experimental measurements, so the model needed more revisions. This suggests that the model is missing important mechanisms or implementing them incorrectly. The predicted friction coefficients for higher piston speeds was below 0.01, which suggested frictional force due to the lubricant was nearly negligible compared to measured values. Since it appeared the model was over-predicting the hydrodynamic lift, shear thinning model was added to the overall model; details are given in Chapter 3. Figures 4.20-4.22 summarize the overall model predictions once shear thinning was incorporated.

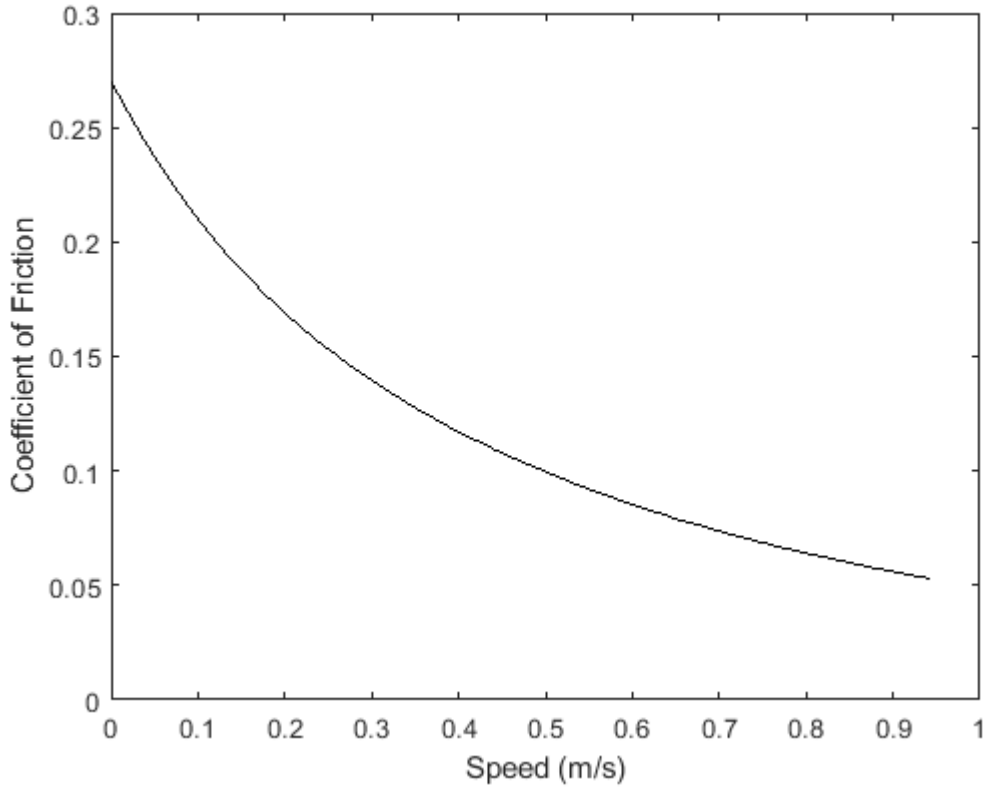

Figure 4.20: Model Predicted Friction Coefficient with Shear Thinning

The quarter cycle average friction coefficient is 0.10. This is roughly 2.78 times higher compared to the previous version of the model.

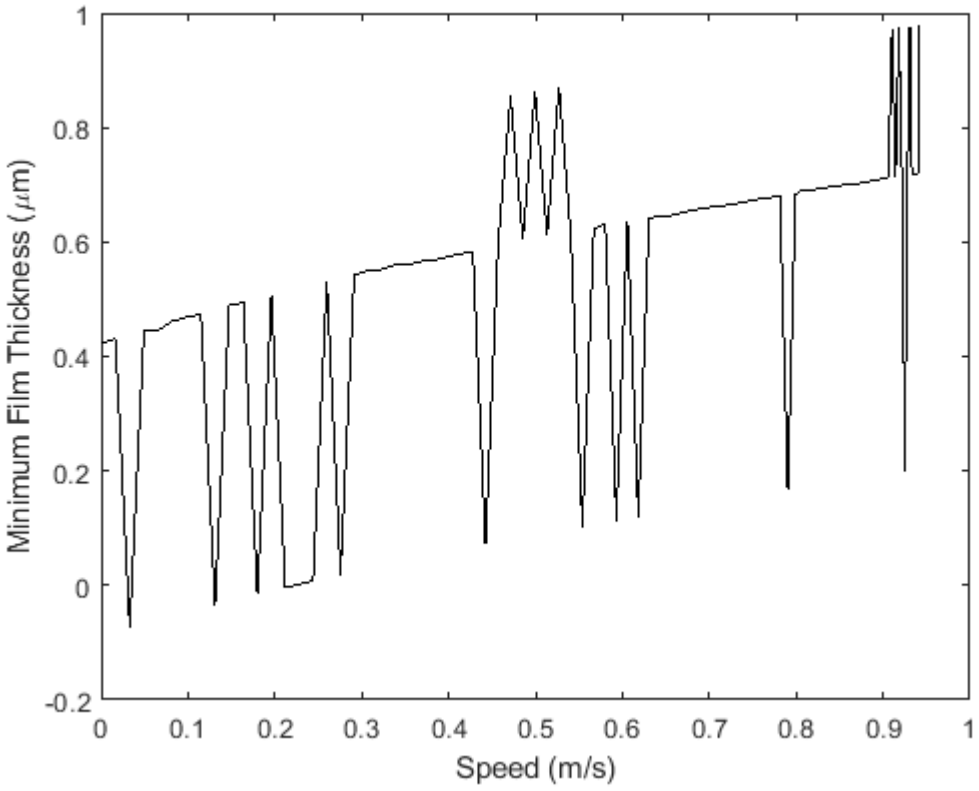

Figure 4.21: Model Version 4 Predicted Minimum Film Thickness

However, a look at Figure 4.21 reveals that the model has not converged. The minimum film thickness should not be fluctuating that much. This indicates that the convergence criteria are too lenient.

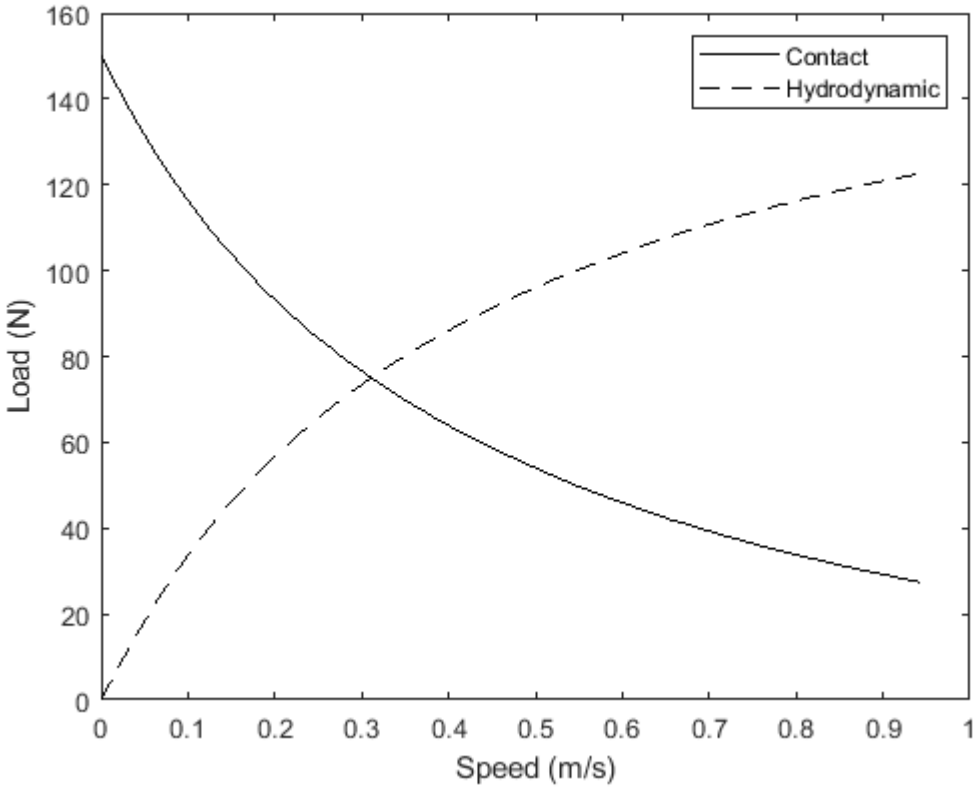

Figure 4.22: Model Version 4 Predicted Load Distribution

The oil no longer carries the entire load at higher speeds, which means the model has not yet entered the hydrodynamic regime at the maximum speed unlike previous versions that lack the effects of shear thinning. While more rigorous convergence criteria were being devised to rectify this in the next version of the model, the current version was run for an average sliding speed of 0.3 m/s to gauge how it performed at different speeds. The load remained at 150 N. The friction coefficient variation for this different average speed is depicted in Figure 4.23.

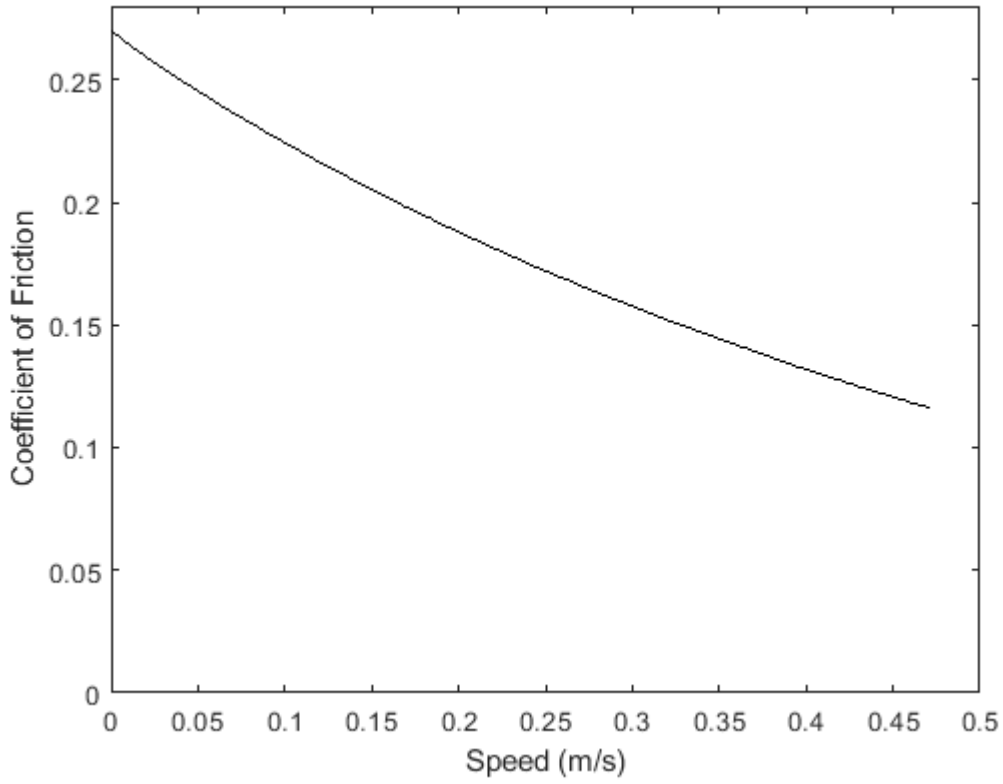

Figure 4.23: Model Version 4 Predicted Friction Coefficient, Average Speed 0.3 m/s

The predicted average friction coefficient is 0.163 for this version of the model. This is a much higher value compared to the case with an average speed of 0.6 m/s. The dry friction coefficient was reduced to 0.21; results are shown in Figures 4.24 and 4.25.

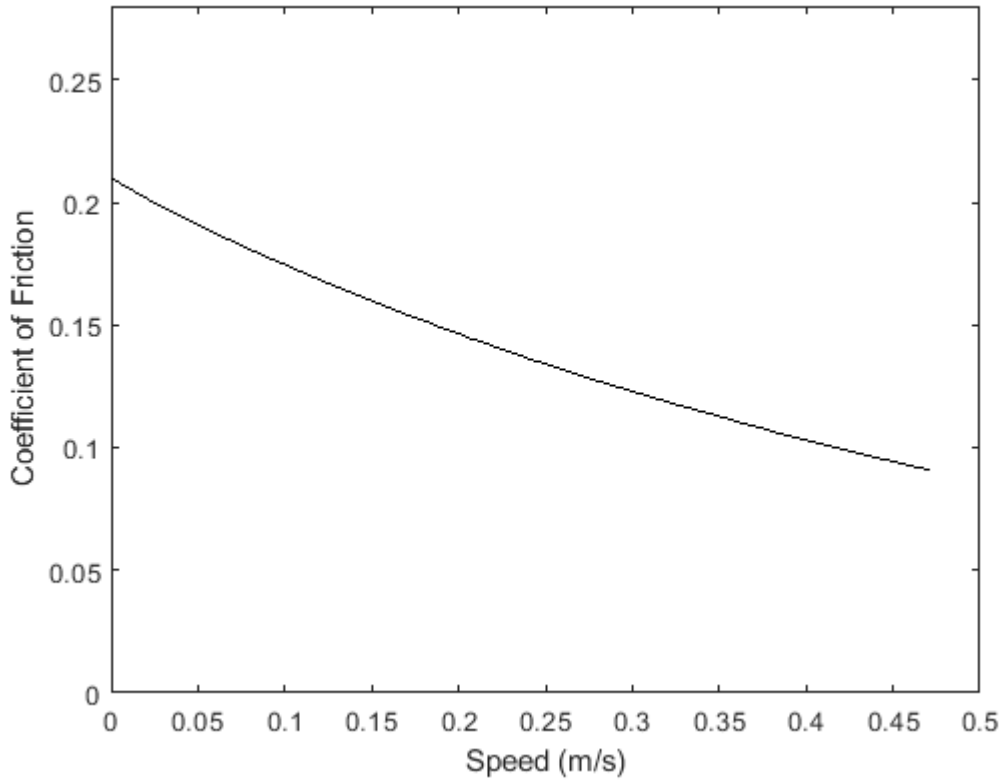

Figure 4.24: Model Predicted Friction Coefficient, Average Speed 0.3 m/s, Assumed Dry Friction Coefficient 0.21

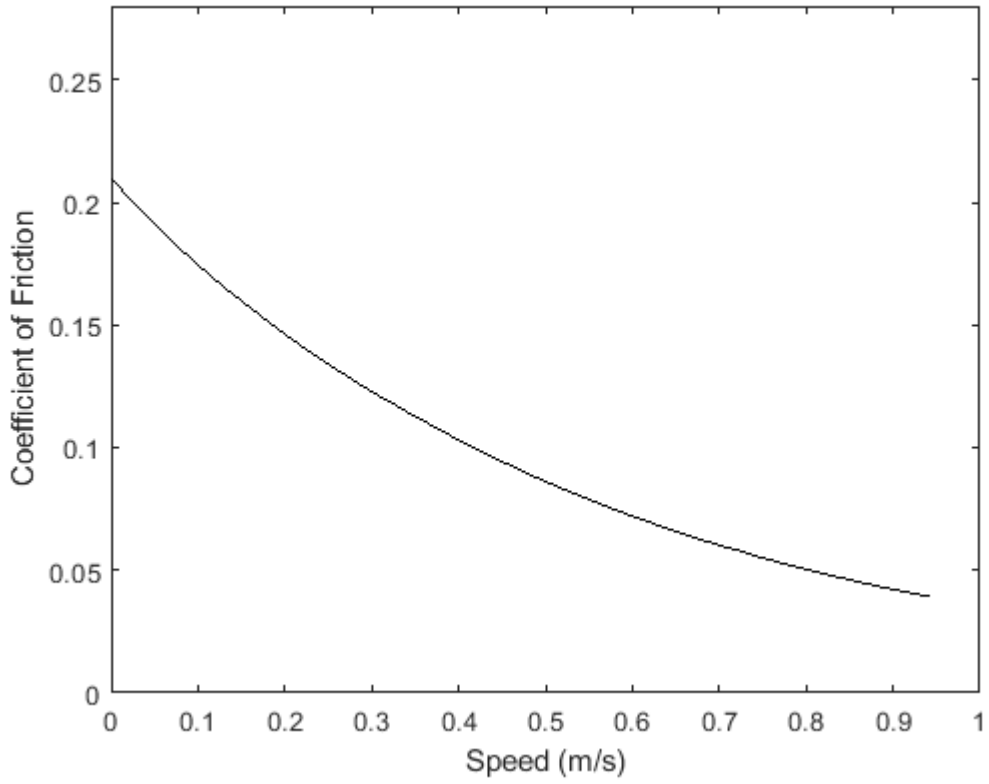

Figure 4.25: Model Predicted Friction Coefficient, Average Speed 0.6 m/s, Assumed Dry Friction Coefficient 0.21

As shown in Figures 4.24 and 4.25, the quarter cycle average friction coefficients decreased to 0.127 and 0.083 for average running speeds of 0.3 m/s and 0.6 m/s respectively. These seemed to be reasonable values; however, there was still substantial variation over the range of speeds analyzed. The results should be taken with a grain of salt because the non-physical fluctuations in minimum film thickness had not been rectified. The code was modified further, and those refined results are presented and

discussed in Chapter 6. Table 4.4 summarizes different versions of the model tested so far.

Table 4.4: Tested Versions of Model so Far

Version Number	Assumed Dry Friction Coefficient	Determination of Surface Parameters	Shear Thinning
1	0.1	Spectral Moments	Not Present
2	0.25	Spectral Moments	Not Present
3	0.27	Manually Count and Measure Asperities	Not Present
4	0.27	Manually Count and Measure Asperities	Present
5	0.21	Manually Count and Measure Asperities	Present

CHAPTER 5

MEASURING THE FRICTION COEFFICIENT VIA A RECIPROCATING TEST

Model predictions are ultimately meaningless without experimental data to support and verify them. For this reason, the model is compared to the results of a reciprocating test of a production ring sliding along a cast iron liner. Measurements were produced by using a Phoenix Tribology TE77 High Frequency Friction Machine. This test apparatus is widely used in the literature for measuring piston ring against cylinder liner friction [103-104]. An image of this machine is shown in Figure 5.1.

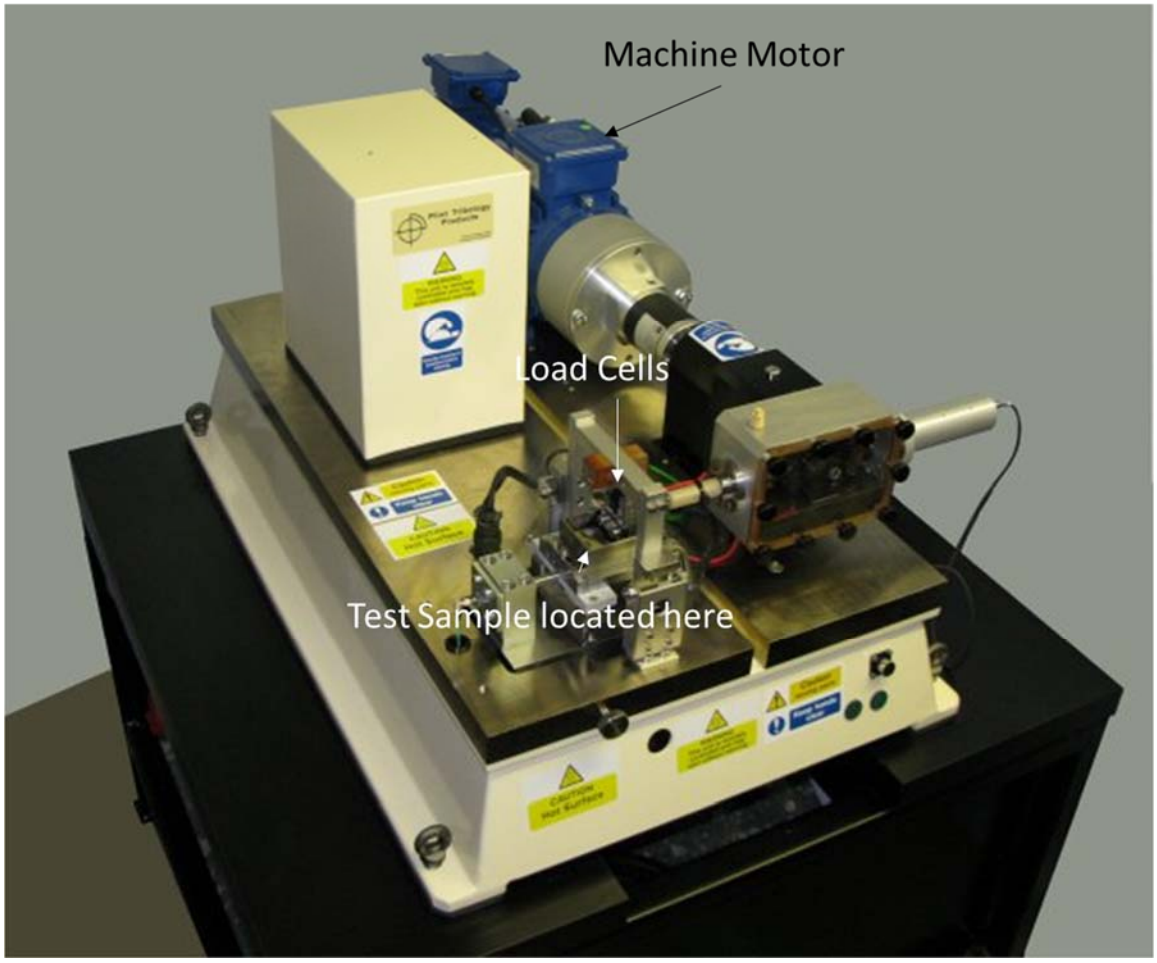

Figure 5.1: Phoenix Tribology TE77 High Frequency Friction Machine [105]

Before each set of runs, the cylinder liner and piston ring were cleaned using hexane in an ultrasonic bath. Enough SAE 5W-20 oil to cover the specimen was added to the test chamber shown in Figure 5.2.

Figure 5.2: Experimental Setup

Four different combinations of piston ring and cylinder liner were run: production ring on cast iron liner, production ring on PTWA3 (a ~0.3 mm thick coating made of low carbon ally steel deposited on aluminum using plasmas transfer wire arc) coated liner, and two different DLC coated rings on cast iron liner. Due to a lack of unused piston rings and cylinder liners, the components had previously been tested. However, the cylinder liners were in reasonably good condition. After testing one of the DLC coated rings, the wear was much more severe than before the test, so the cylinder liner was replaced with one that was not as worn. For each combination, the oil temperature was set to either 30, 50, 80, or 120°C and maintained by a PID (proportional-integral-derivative) controller. The sliding frequency was set to 2, 5, 10, or 20 Hz with a stroke length of 15 mm. These

sliding frequencies correspond to average sliding speeds of 0.12, 0.3, 0.6, and 1.2 m/s respectively. Figure 5.3 shows the velocity as a function of time.

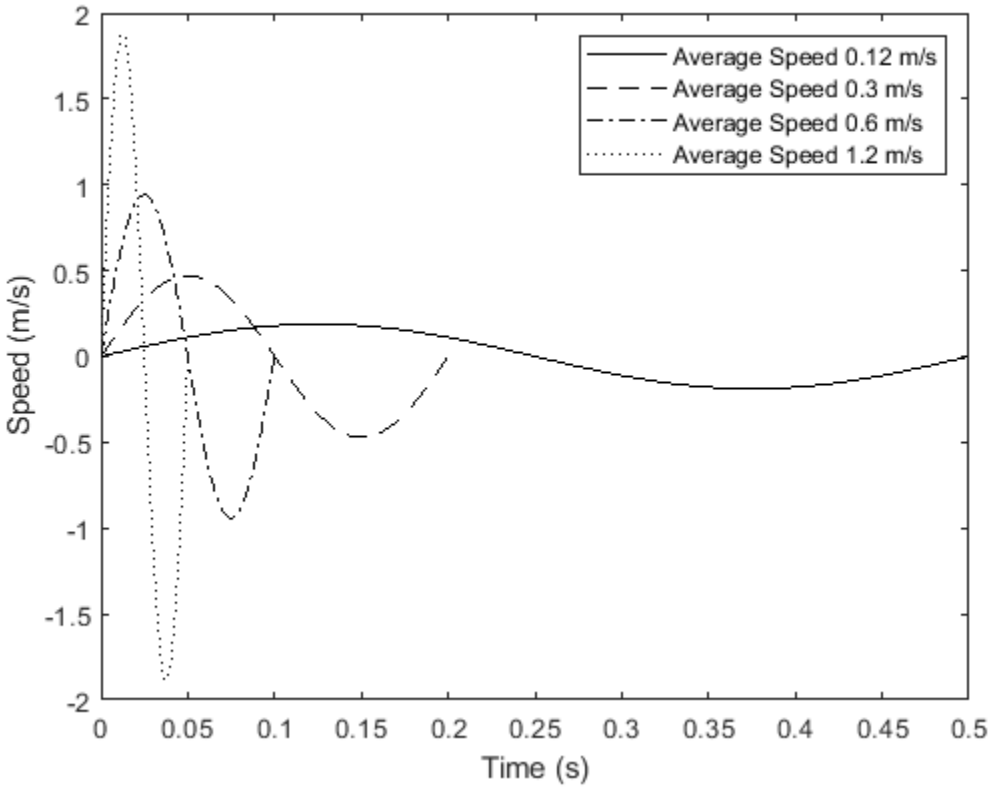

Figure 5.3: Time Dependence of Velocity for a Single Cycle

The applied load was either 50, 100, or 150 N. For each temperature/frequency/load combination, the machine was allowed to run for 10 minutes to eliminate transient effects. Friction data was then taken for 10 seconds at a rate of 5000 samples per second. This was done three times so the data would be more robust. Data from the runs are shown in Figures 5.4-5.9. While only one average sliding cycle is shown for each, that cycle reflects the average of every cycle across the three runs. As the model was only compared to the production ring on cast iron liner, the figures exclusively focus on

measurements with those two components. For the 10 Hz, 30°C, 150 N combination, data from one of the tests (Figure A.27) was not deemed suitable and excluded from the averages.

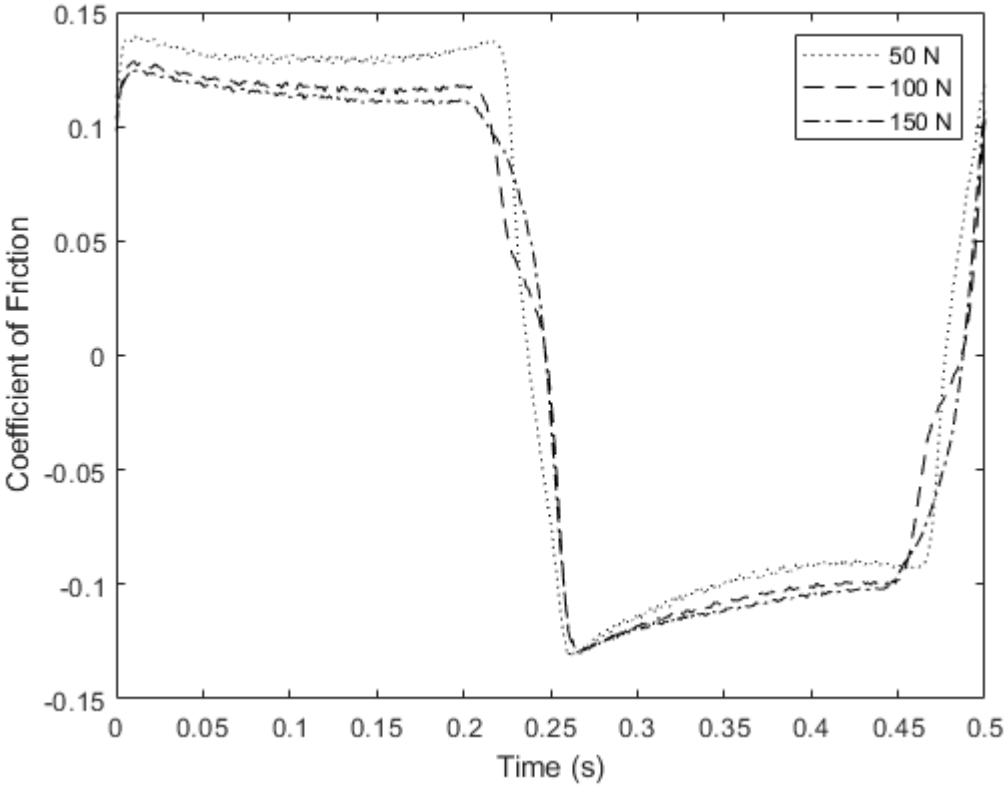

Figure 5.4: Averaged Experimental Measurements at 30°C and 2 Hz for One Cycle

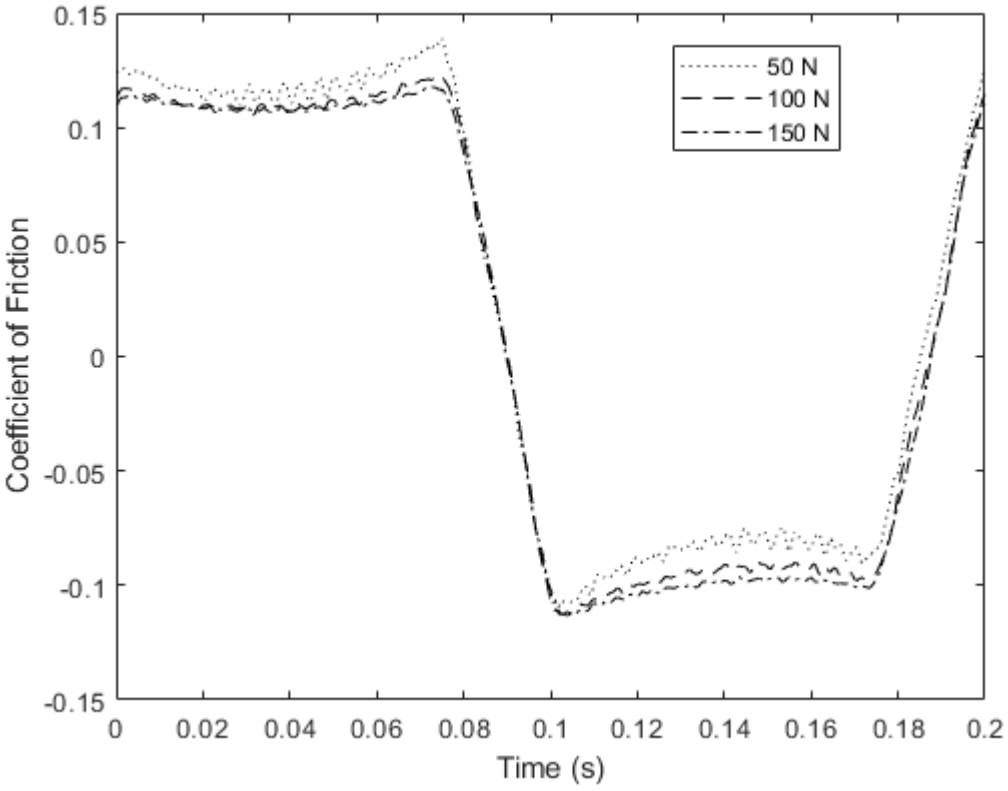

Figure 5.5: Averaged Experimental Measurements at 30°C and 5 Hz for One Cycle

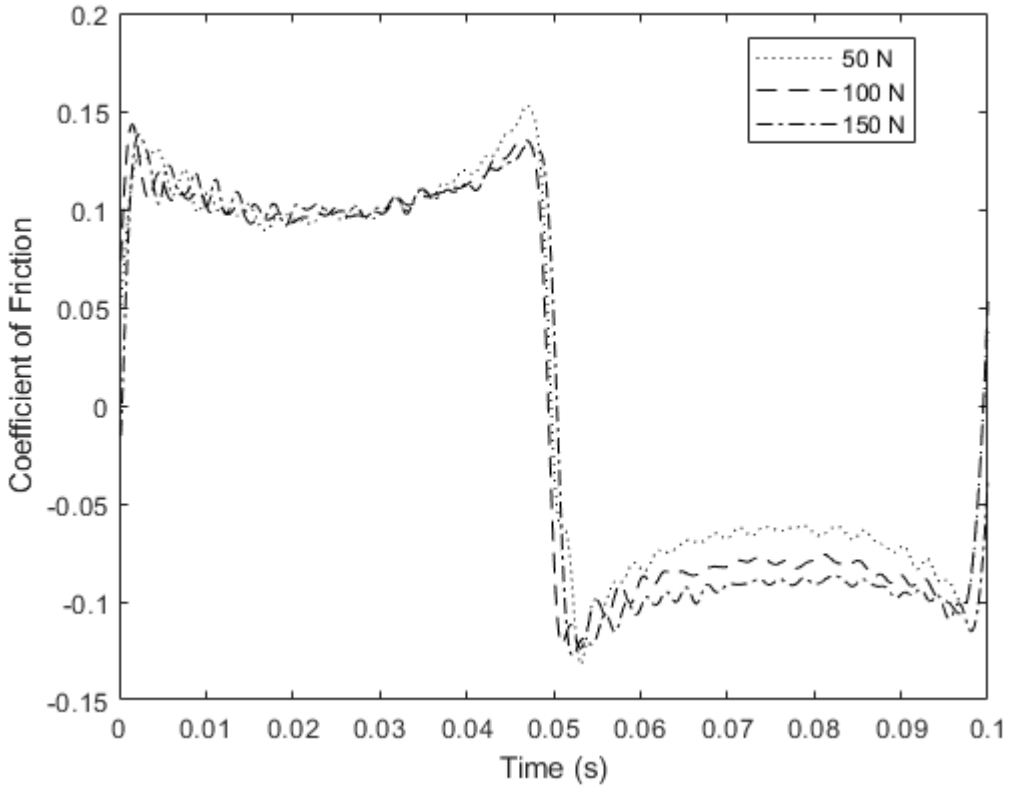

Figure 5.6: Averaged Experimental Measurements at 30°C and 10 Hz for One Cycle

Based off Figures 5.4-5.6, the friction coefficients were observed to decrease with increasing speed and load. However, load did not have as large of an influence on the friction coefficient at higher speeds. Generally, as speed increases the fluid lift increases and less solid friction occurs. This results in friction decreasing with speed as seen in the Stribeck Curve (Figure 2.2). The relationship with load is potentially happening because of increased elastic-plastic contact at higher loads – yielded asperities will not be able to resist sliding as much relative to elastic contact [97-98]. Another reason is that the oil could be heating up at higher speeds due to the larger frictional force. This decreases the

lubricant's load carrying capacity and results in more load (and friction) carried by the asperities.

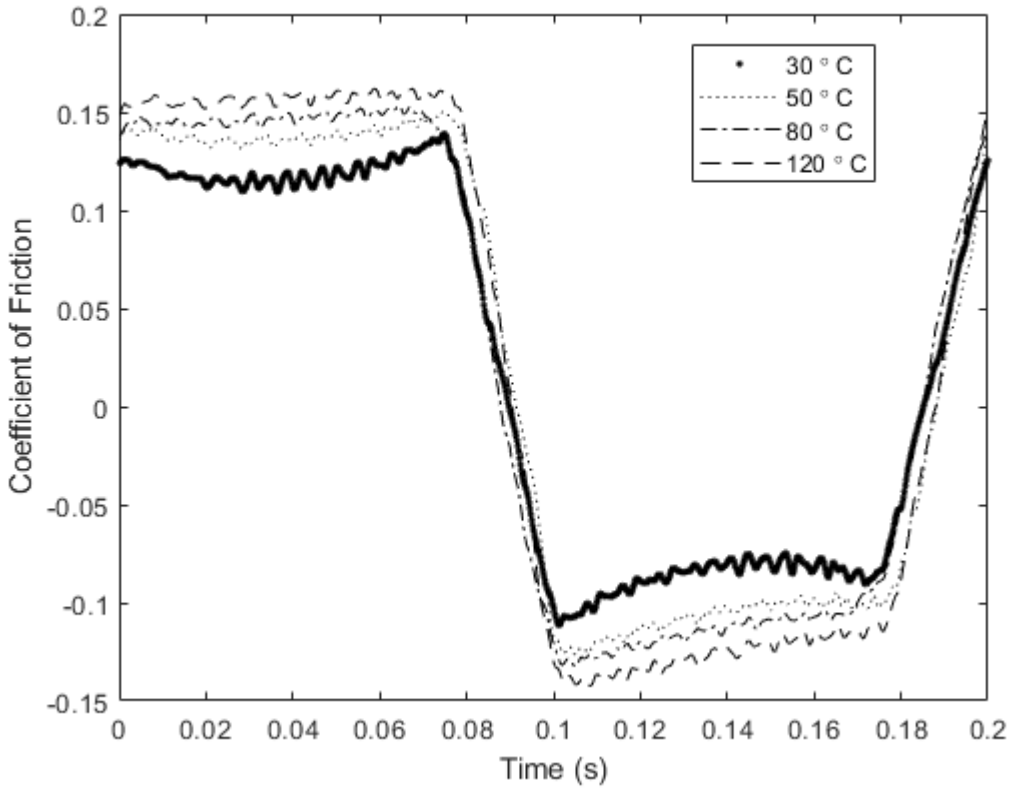

Figure 5.7: Averaged Experimental Measurements at 5 Hz and 50 N for One Cycle

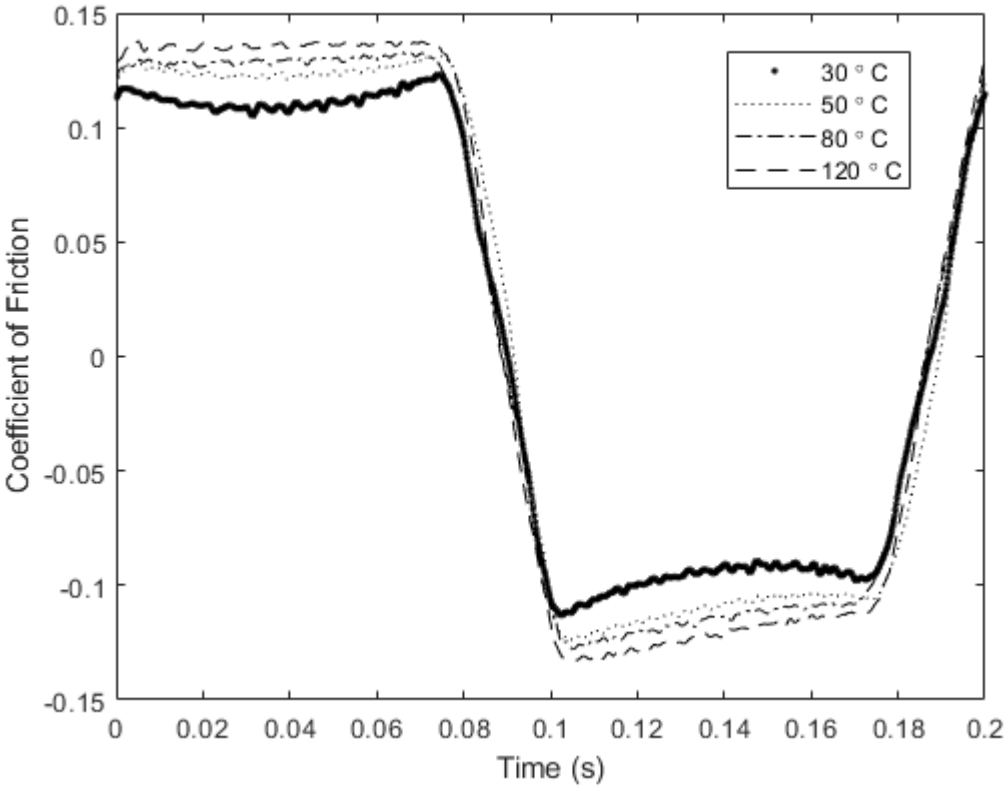

Figure 5.8: Averaged Experimental Measurements at 5 Hz and 100 N for One Cycle

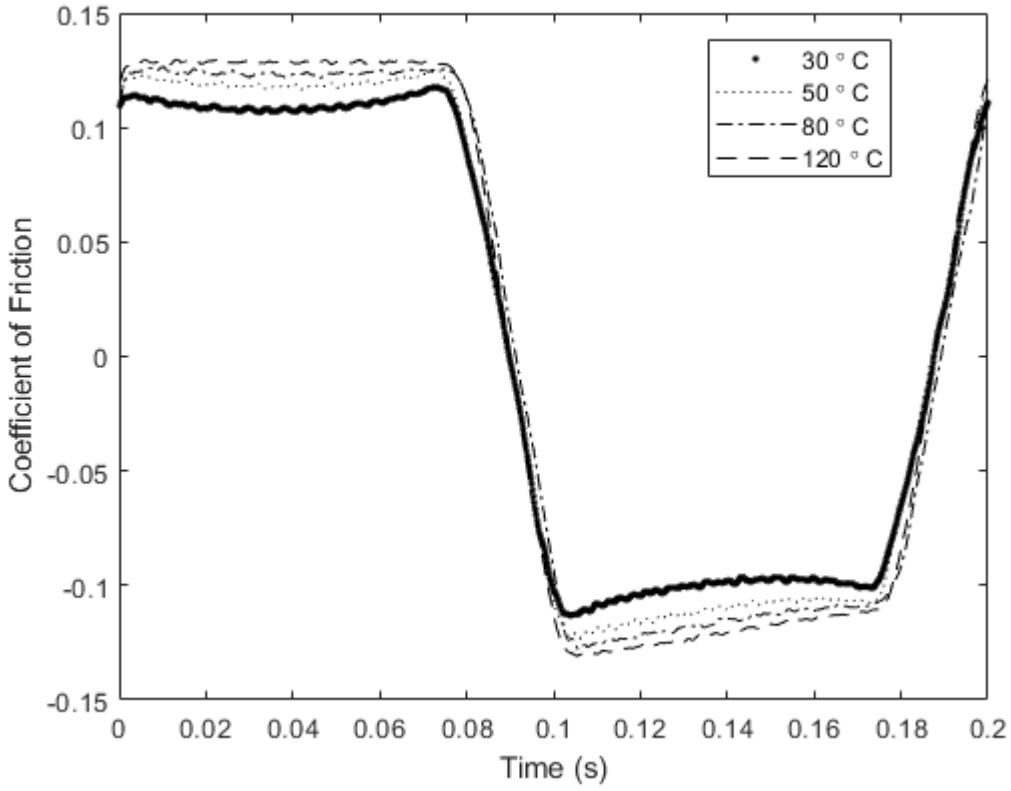

Figure 5.9: Averaged Experimental Measurements at 5 Hz and 150 N for One Cycle

Examining Figures 5.7 - 5.9, higher friction coefficients were observed as the temperature increased. Perhaps this is because the lower viscosities at higher temperatures mean a lesser flow resistance and a loss of load carrying capacity. For the reverse half of the stroke, the friction coefficient magnitude was observed to decrease across the entire stroke at higher temperatures.

Possible sources of error during the experiments include minor variations in applied load and lubricant temperature during the test. There was also a lack of precision in setting the speed – the data shown in Figures 5.4, 5.5, and 5.7-5.9 does not align perfectly

across all the tests. Measurements at 20 Hz were deemed to be too unrepeatable due to excess vibration, and later versions of the model are not compared to them.

Tables 5.1 and 5.2 summarize the average measured friction coefficients for the forward half of the stroke. These values were calculated by averaging every point in time during the repeating tests whose friction coefficient value was at least 10% of the maximum observed during its test. As seen in Figures 5.4-5.9, the friction coefficients for the backwards half of the stroke exhibit different trends. For this reason, those values are excluded from the averages.

Table 5.1: Average Measured Friction Coefficient, Average Sliding Speed 0.3 m/s

	50 N	100 N	150 N
30 °C	0.1226	0.1130	0.1102
50 °C	0.1386	0.1239	0.1183
80 °C	0.1451	0.1270	0.1215
120 °C	0.1542	0.1325	0.1250

Table 5.2: Average Measured Friction Coefficient, Average Sliding Speed 0.6 m/s

	50 N	100 N	150 N
30 °C	0.1107	0.1064	0.1074
50 °C	0.1293	0.1176	0.1177
80 °C	0.1394	0.1255	0.1189
120 °C	0.1477	0.1300	0.1248

Tables 5.3 and 5.4 show the standard deviation for the experimental measurements. These values were calculated by using every data point that is part of the averages in Tables 5.1 and 5.2 and determining their deviations from the overall average.

Table 5.3: Standard Deviation of All Measurements, Average Sliding Speed 0.3 m/s

	50 N	100 N	150 N
30 °C	0.0175	0.0132	0.0126
50 °C	0.0147	0.0130	0.0129
80 °C	0.0145	0.0135	0.0135
120 °C	0.1542	0.1325	0.1250

Table 5.4: Standard Deviation of All Measurements, Average Sliding Speed 0.6 m/s

	50 N	100 N	150 N
30 °C	0.0250	0.0180	0.0155
50 °C	0.0182	0.0141	0.0139
80 °C	0.0174	0.0145	0.0135
120 °C	0.0179	0.0152	0.0139

CHAPTER 6

DEBUGGING AND REFINING THE MODEL USING EXPERIMENTAL DATA

6.1 Continuing to Refine a Basic Model

Modifying the convergence criteria to eliminate significant, unphysical variations in minimum film thickness seen in Figure 4.20 resulted in a relaxation factor added to the model to assist convergence. They were believed to be due to numerical errors. Difficulties were observed in reaching convergence when a minimum film thickness criteria was added to make the sliding speed-minimum film thickness plot linear in nature. It was believed that deformations were implemented too quickly, so a relaxation factor (which is used to prevent instabilities in iterative calculations) proportional to the iteration number was introduced. While testing various initial relaxation factors for a stationary ring wide variations were observed in the minimum film thickness; the largest value was 50% greater than the smallest value. This meant the final ring profile differed depending on the initial value of the relaxation factor. The model still predicted the same frictional force; however, for a moving ring the predicted friction force varied by about 10-15% between the largest and smallest values. Eventually it was decided to set the relaxation factor equal to 0.05 times the iteration number until a limiting value of 1 was

reached. At higher speeds, continued difficulties meant the relaxation factor was reduced to 0.02 times the iteration number. Ultimately the following convergence criteria were proposed: the relaxation factor reached 1, the frictional force did not change by more than 0.05%, and the minimum film thickness changed by no more than 5%. Figures 6.1-6.6 show the convergence of shear force and minimum film thickness over several iterations for two different piston speeds.

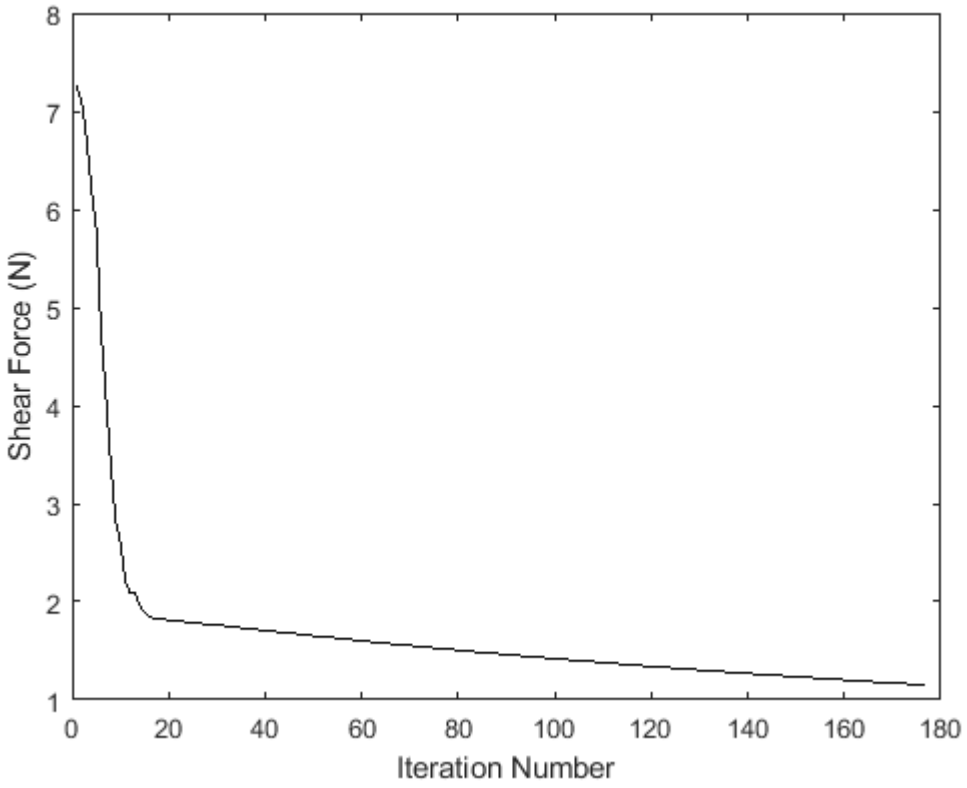

Figure 6.1: Shear Force Convergence for a Sliding Speed of 0.8243 m/s

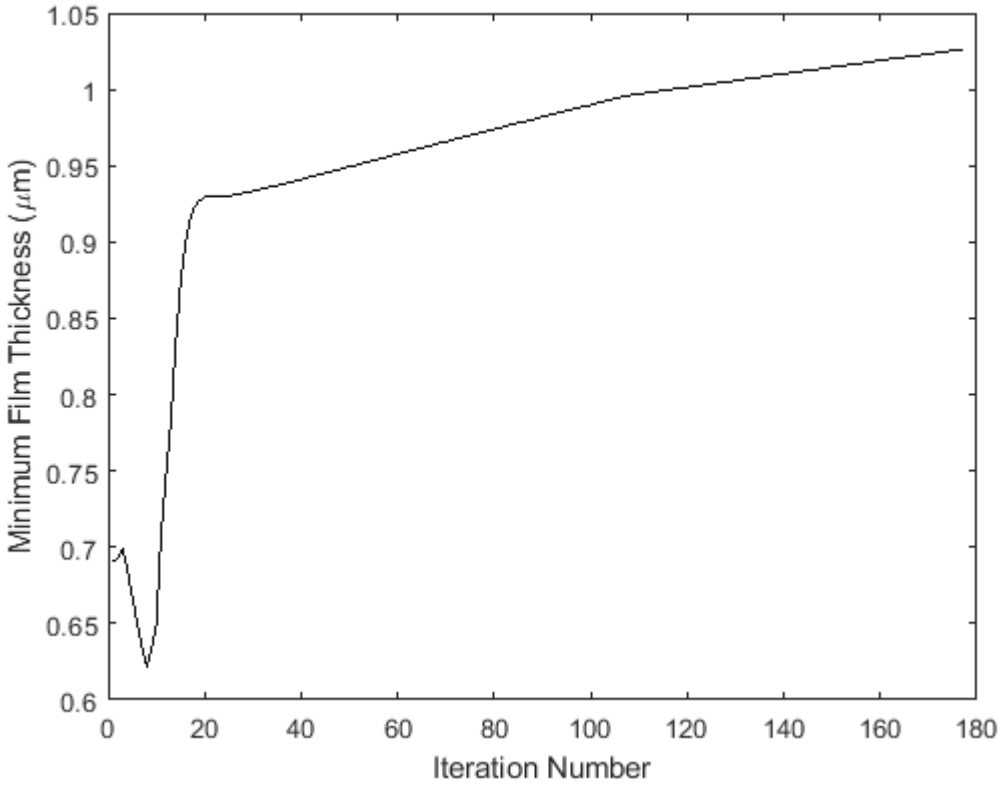

Figure 6.2: Minimum Film Thickness Convergence for a Sliding Speed of 0.8243 m/s

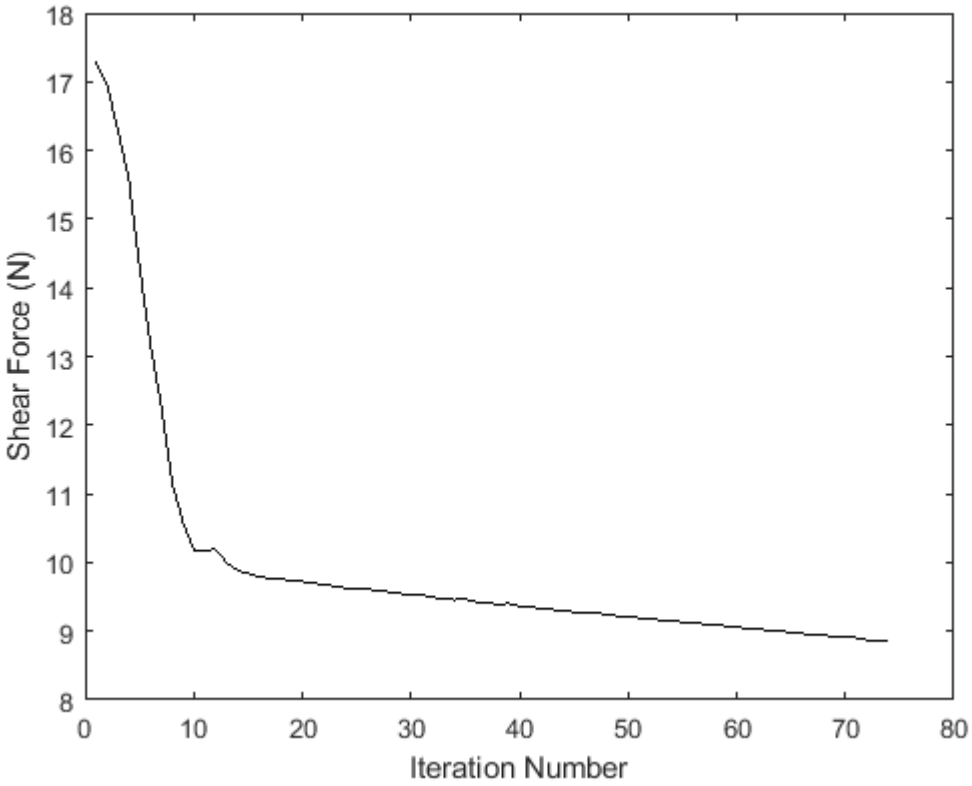

Figure 6.3: Shear Force Convergence for a Sliding Speed of 0.3378 m/s

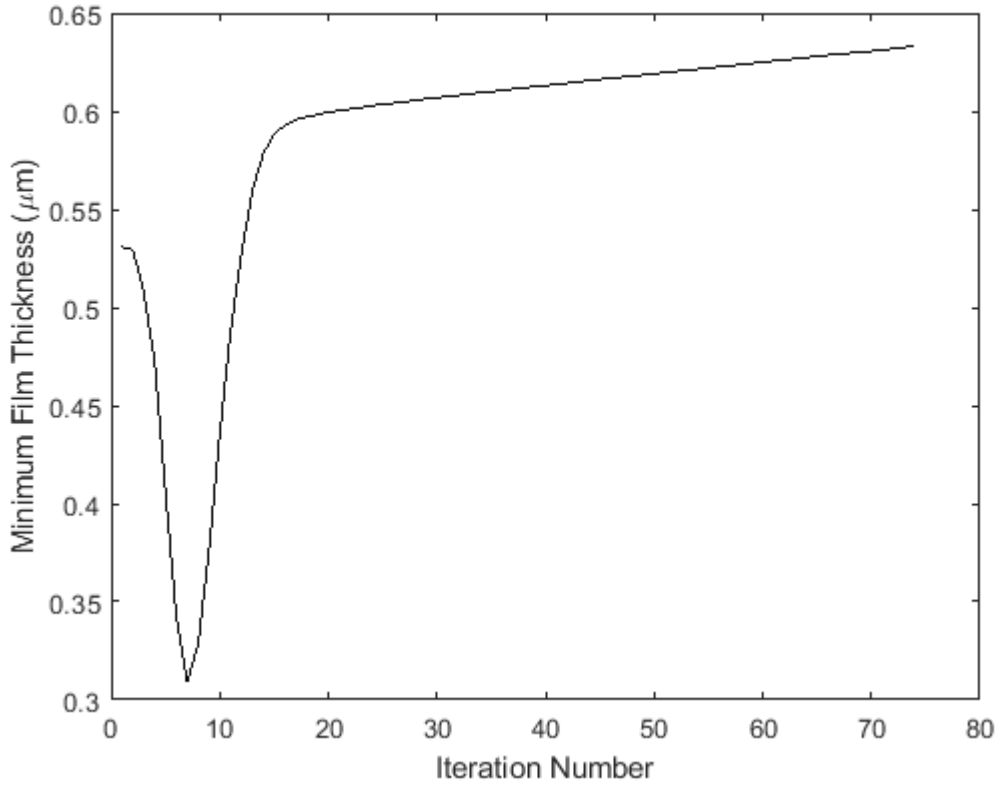

Figure 6.4: Minimum Film Thickness Convergence for a Sliding Speed of 0.3378 m/s

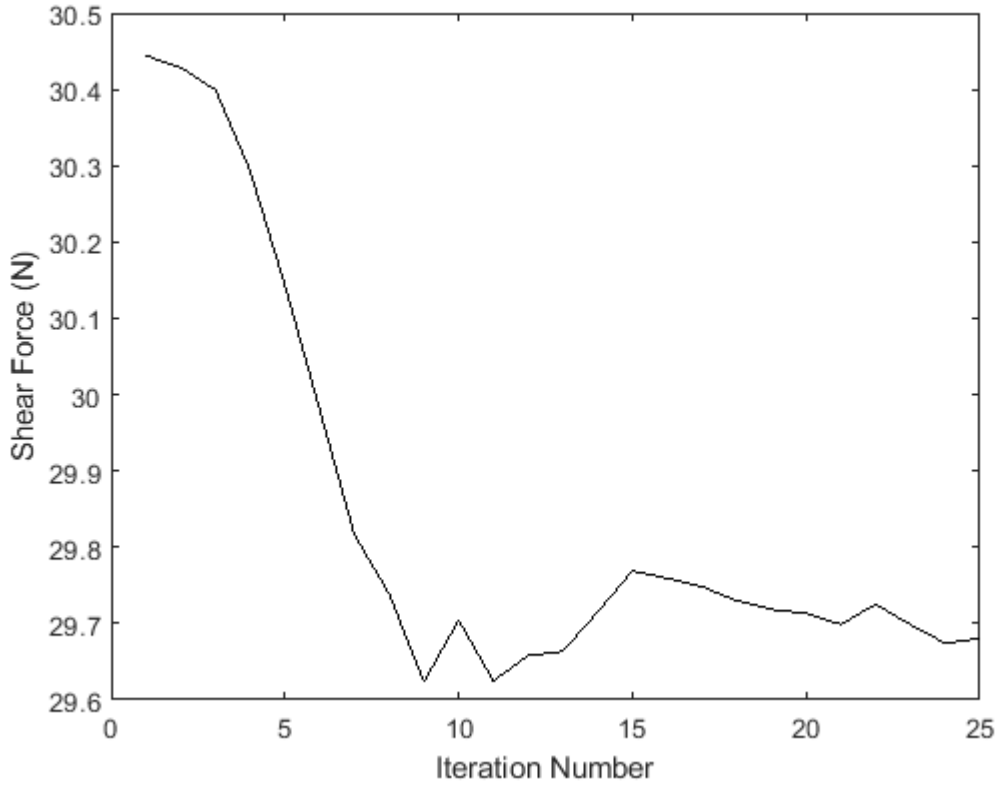

Figure 6.5: Shear Force Convergence for a Sliding Speed of 0.0164 m/s

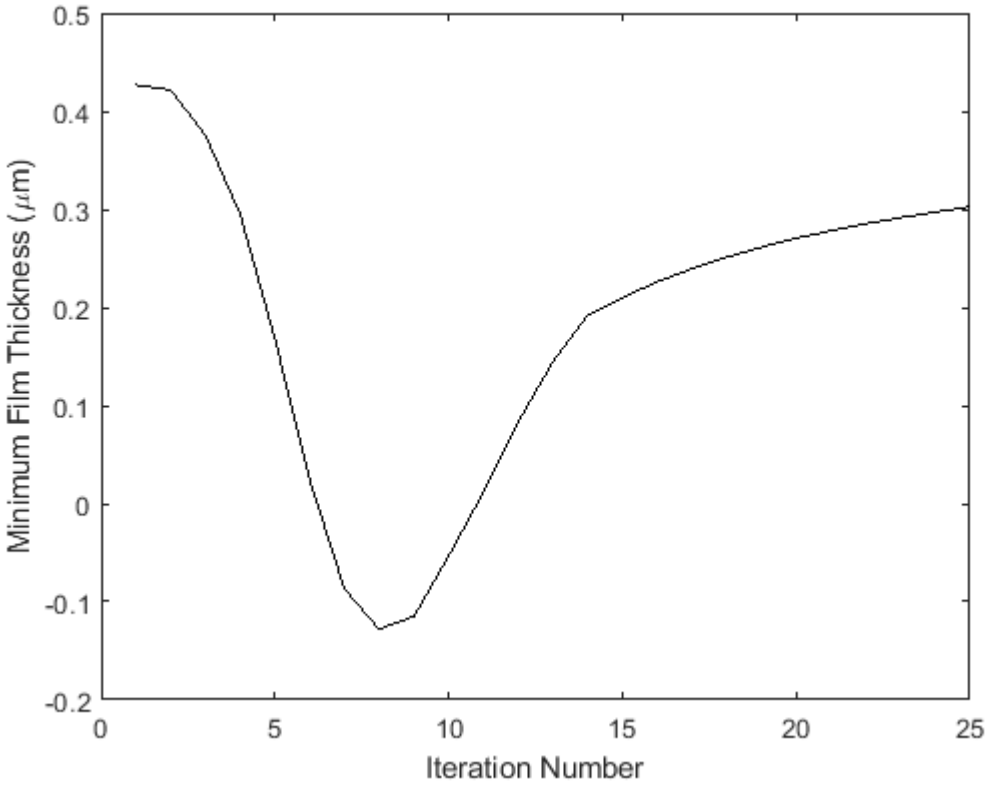

Figure 6.6: Minimum Film Thickness Convergence for a Sliding Speed of 0.0164 m/s

Based on these results, the code seemed to reach convergence relatively quickly for low speeds, but it still took 25 iterations. For higher speeds convergence took even longer: more than 70 iterations for a medium sliding speed and nearly 180 for a fast sliding speed. Even then the model might not have truly converged considering that the shear force and minimum film thickness continue to change in the same direction between late iterations. Considering the 12 different load/temperature combinations that were tested in Chapter 5 the program would take hours to run a single case. The minimum film thickness behaved similarly across the 3 speeds tested: it sharply decreased for the first 8 iterations, then increased almost as rapidly for the next ~6

iterations before leveling off and increasing very slowly until convergence was reached according to the criteria. While the shear force leveled off quickly at the slowest speed, the trend at faster speeds was identical what was observed in Figures 4.15 and 4.16: the shear force decreased very slowly. Based on the erratic nature of the minimum film thickness, the piston ring profiles were examined for each iteration to determine how to further improve the code. Figures 6.7-6.9 show the final profiles for the 3 speeds analyzed here.

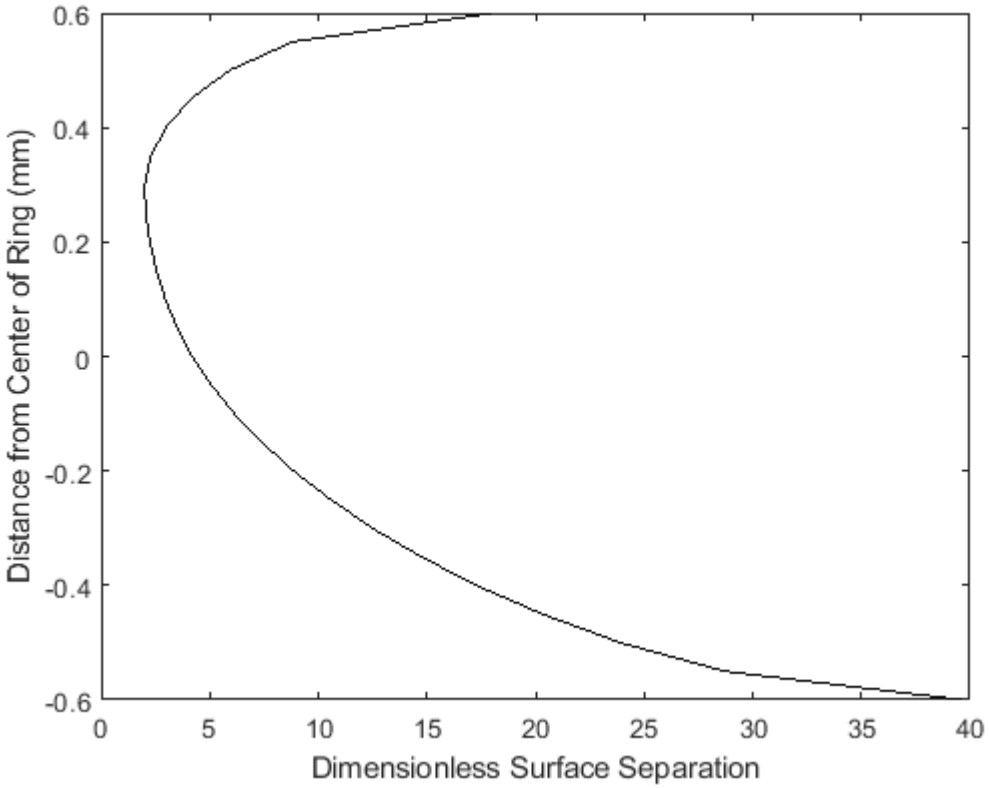

Figure 6.7: Piston Ring Profile for a Sliding Speed of 0.8243 m/s

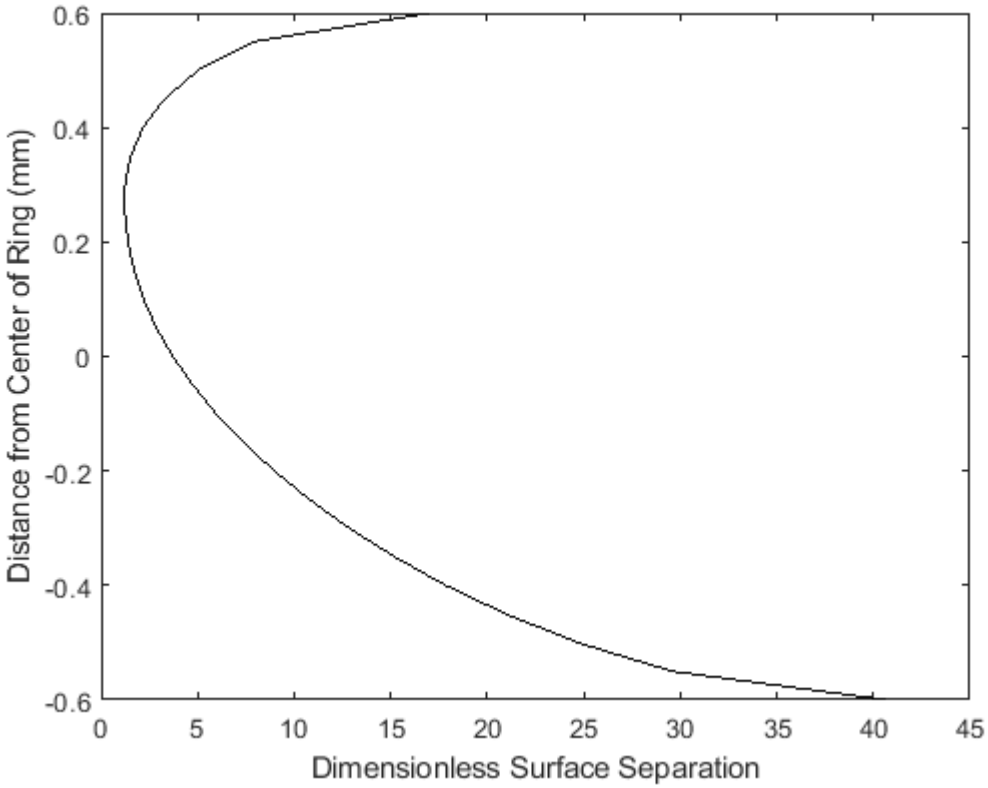

Figure 6.8: Piston Ring Profile for a Sliding Speed of 0.3378 m/s

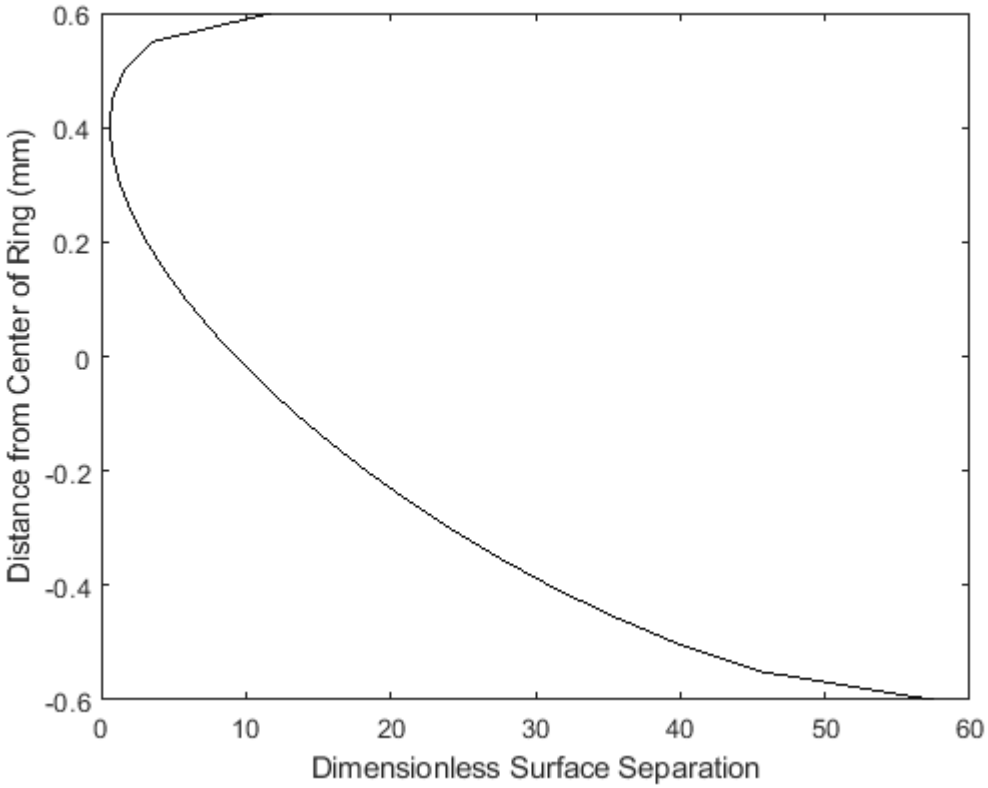

Figure 6.9: Piston Ring Profile for a Sliding Speed of 0.0164 m/s

All 3 piston ring profiles share a similar shape – the ring experiences major tilting due to friction on it; a ring profile without tilt would appear symmetric. The deformations are less extreme at higher speeds where solid contact carries less of the load and contributes less to the total frictional force. The model was tested using the same parameters from Figure 4.22, only with different convergence criteria. Figures 6.10 and 6.11 show the results.

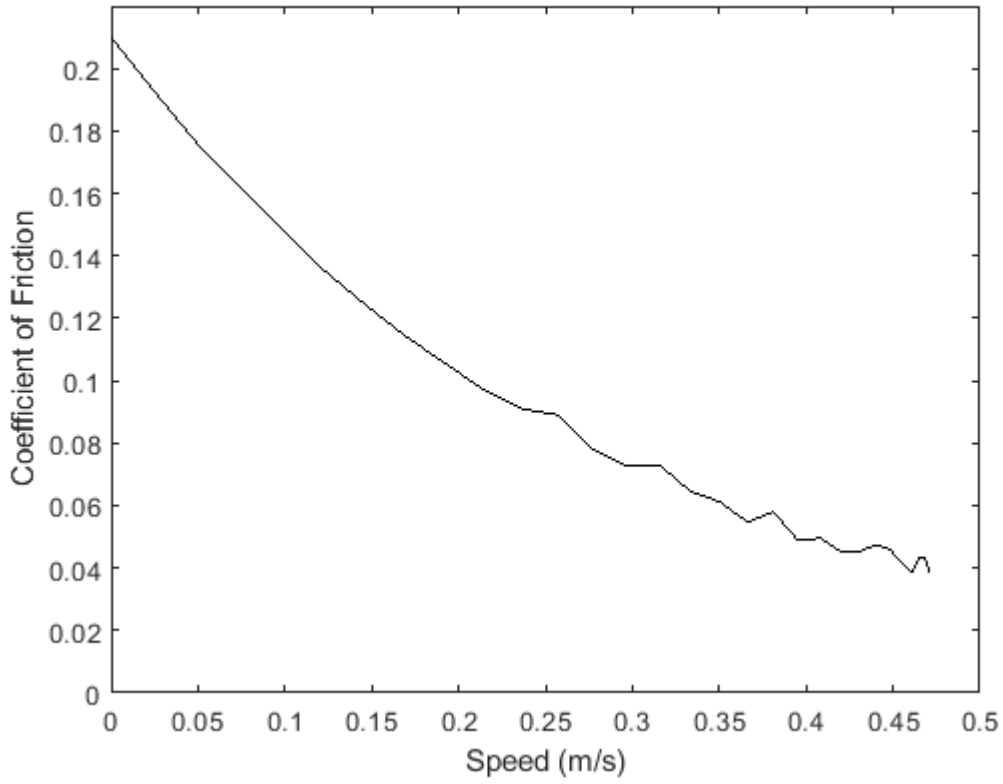

Figure 6.10: Model Version 6 Predicted Friction Coefficient, Average Speed 0.3 m/s, Assumed Dry Friction Coefficient 0.21, Initial Relaxation Factor 1/3

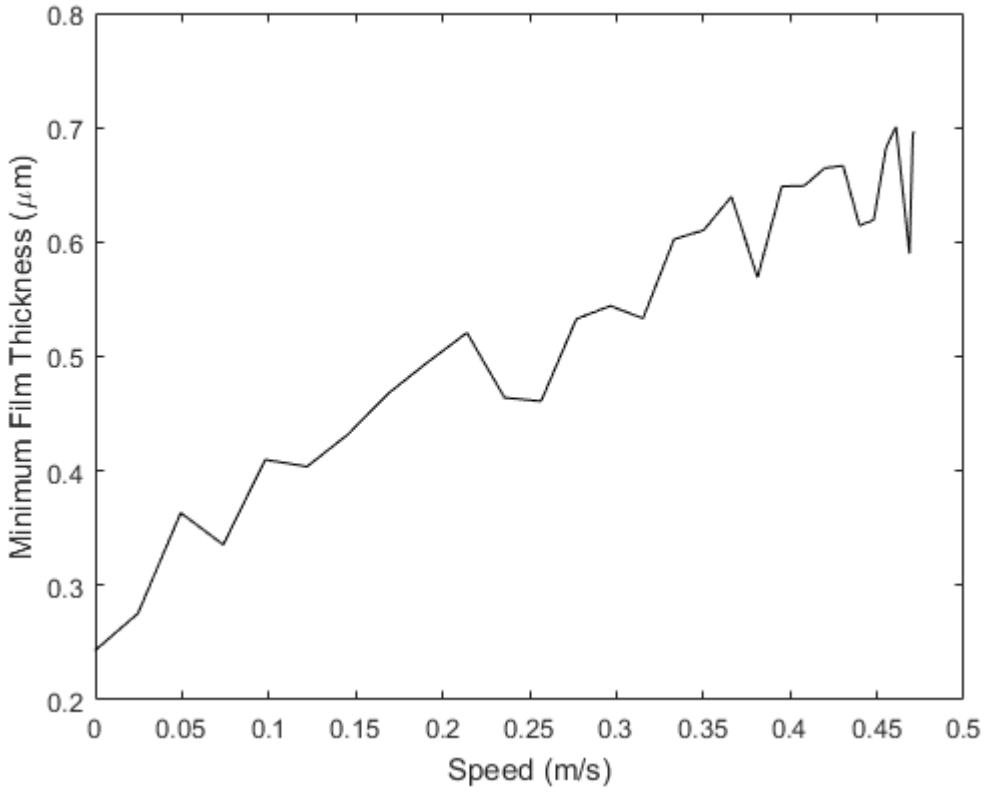

Figure 6.11: Model Version 6 Predicted Minimum Film Thickness, Average Speed 0.3 m/s, Assumed Dry Friction Coefficient 0.21, Initial Relaxation Factor 1/3

While the minimum film thickness never dropped below zero, the model still predicts significant variations from a linear trend. The quarter cycle average friction coefficient was 0.0836. In other words, only changing the initial relaxation factor decreased the predicted friction by 33%. This indicated serious problems existed with the model, but those remained undiscovered for a few months. To increase the predicted friction, the assumed dry friction coefficient was increased to 0.35. Figures 6.12 and 6.13 show the effect of this single change on the model.

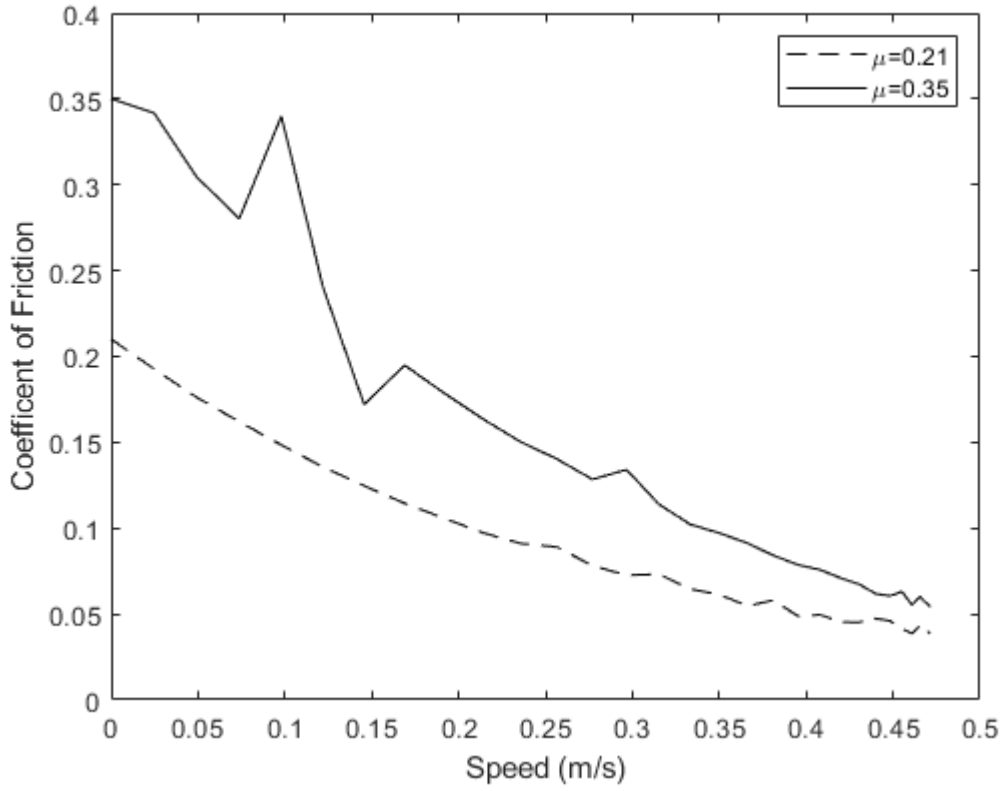

Figure 6.12: Model Version 7 Predicted Friction Coefficient Comparison, Average Speed 0.3 m/s, Initial Relaxation Factor 1/3

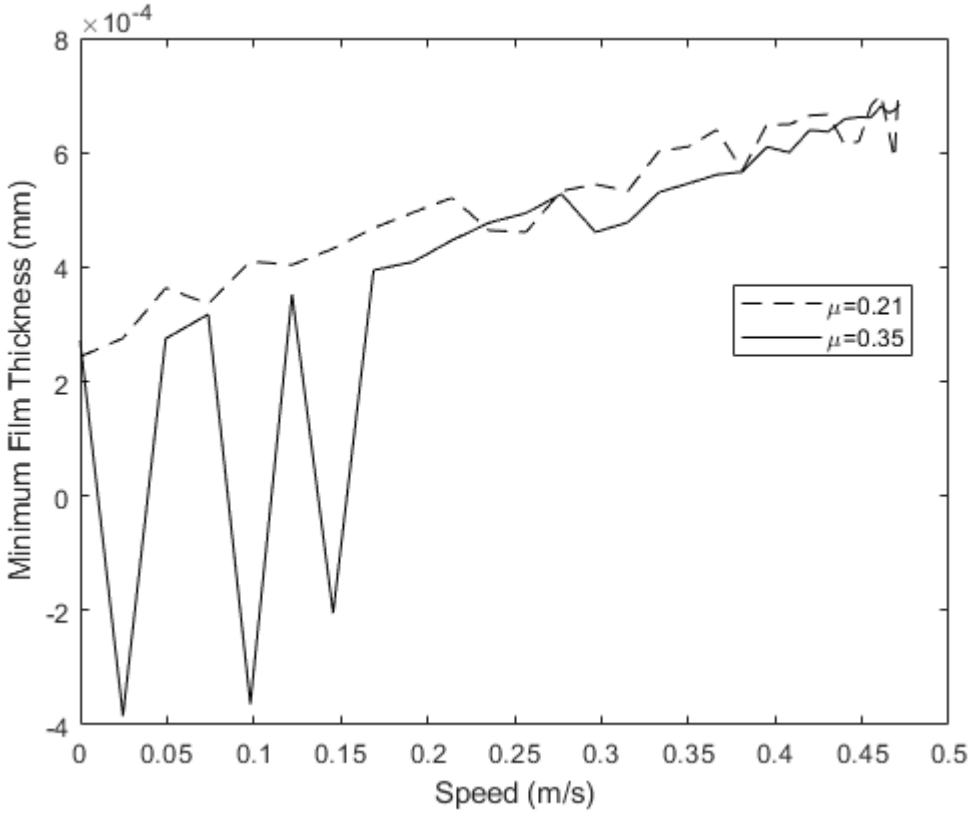

Figure 6.13: Model Version 7 Predicted Minimum Film Thickness, Average Speed 0.3 m/s, Initial Relaxation Factor 1/3

When the dry friction coefficient was increased to 0.35, the quarter cycle average friction coefficient increased to 0.139. This was more than 60% higher than the previous model. While the predicted friction increased over the entire range of speeds considered, there was much greater variation at low speeds (which was thought to be numerical error). A look at the minimum film thickness plot reveals severe problems – the model predicts a negative film thickness, which means the ring penetrates the liner. To determine whether the model's problems existed solely with the transition between the boundary and the

hydrodynamic regimes, the average speed was increased to 0.6 m/s. Figures 6.14 and 6.15 show the model's predictions with a faster range of speeds included.

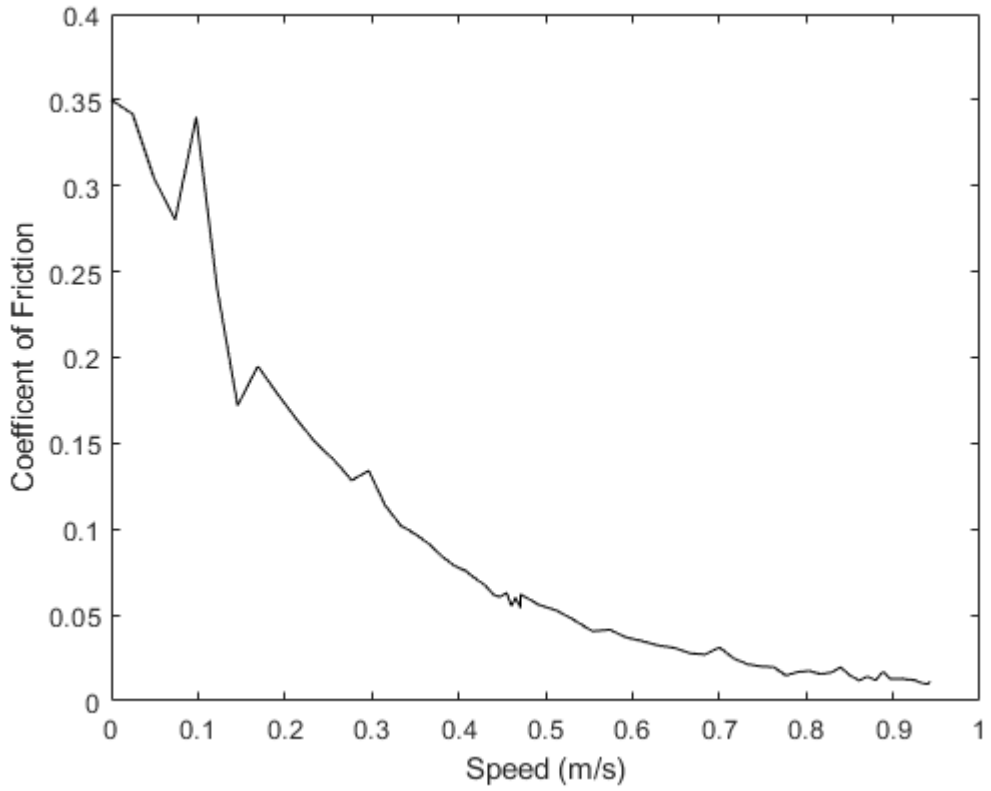

Figure 6.14: Model Version 7 Predicted Friction Coefficient, Average Speed 0.6 m/s, Initial Relaxation Factor 1/3, Assumed Dry Friction Coefficient μ=0.35

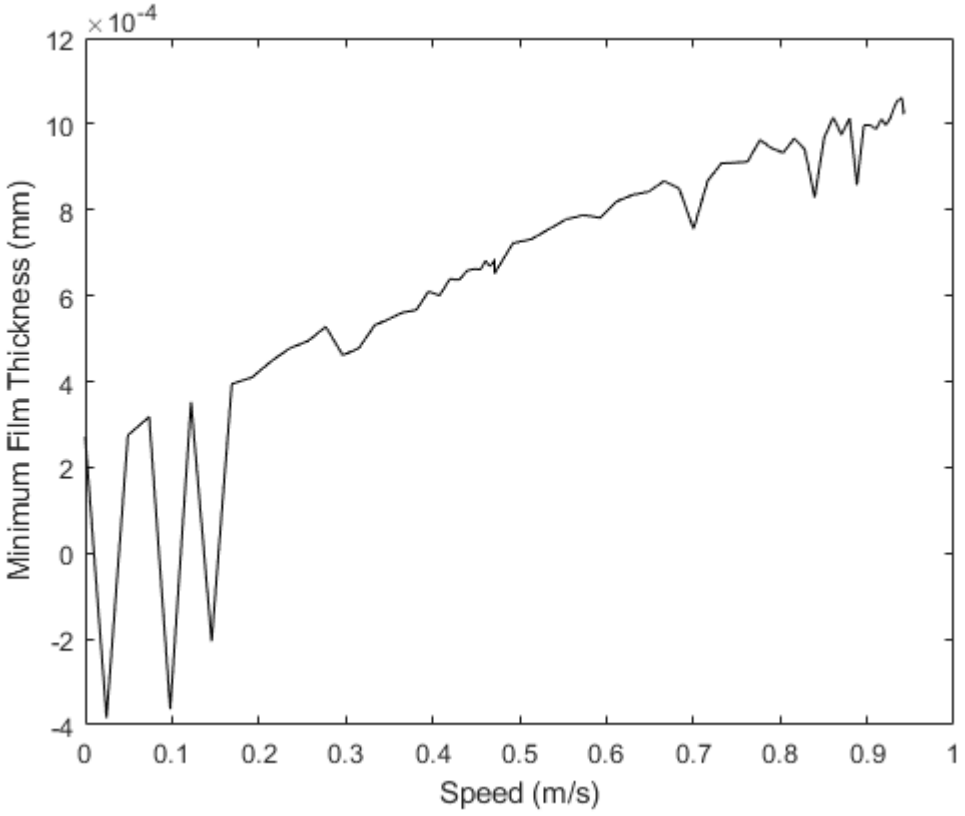

Figure 6.15: Model Version 7 Predicted Minimum Film Thickness, Average Speed 0.6 m/s, Initial Relaxation Factor 1/3, Assumed Dry Friction Coefficient μ=0.35

When the dry friction coefficient was increased to 0.35, the quarter cycle average friction coefficient was 0.072. For the faster speeds, the model predicted a very low friction coefficient as hydrodynamic load dominated. The concerning variations in minimum film thickness and predicted friction coefficient still existed, and the model took dozens of iterations to converge for certain speeds. The friction coefficient variation profile did not match the experiments at all. To help resolve potential issues with the ring profile, the dry friction coefficient was reduced to 0.18; it could be changed later if convergence

improved. An inspection of the code revealed that the placeholder values of G and n were still being used in Equation 3.45. Even though using the data at 100 °C would not provide a perfect fit, it was still deemed to be better than continuing to run the model with placeholder values. Figures 6.16 and 6.17 show how this changed the model's predictions.

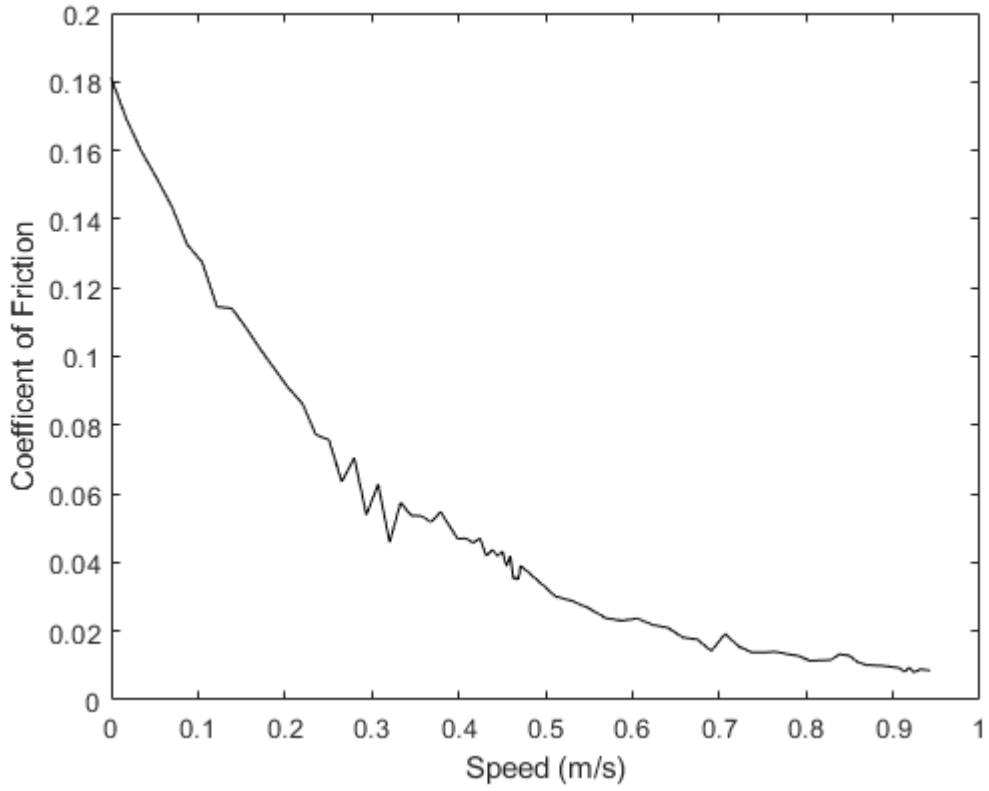

Figure 6.16: Model Version 8 Predicted Friction Coefficient with Shear Thinning Fit #1 Implemented

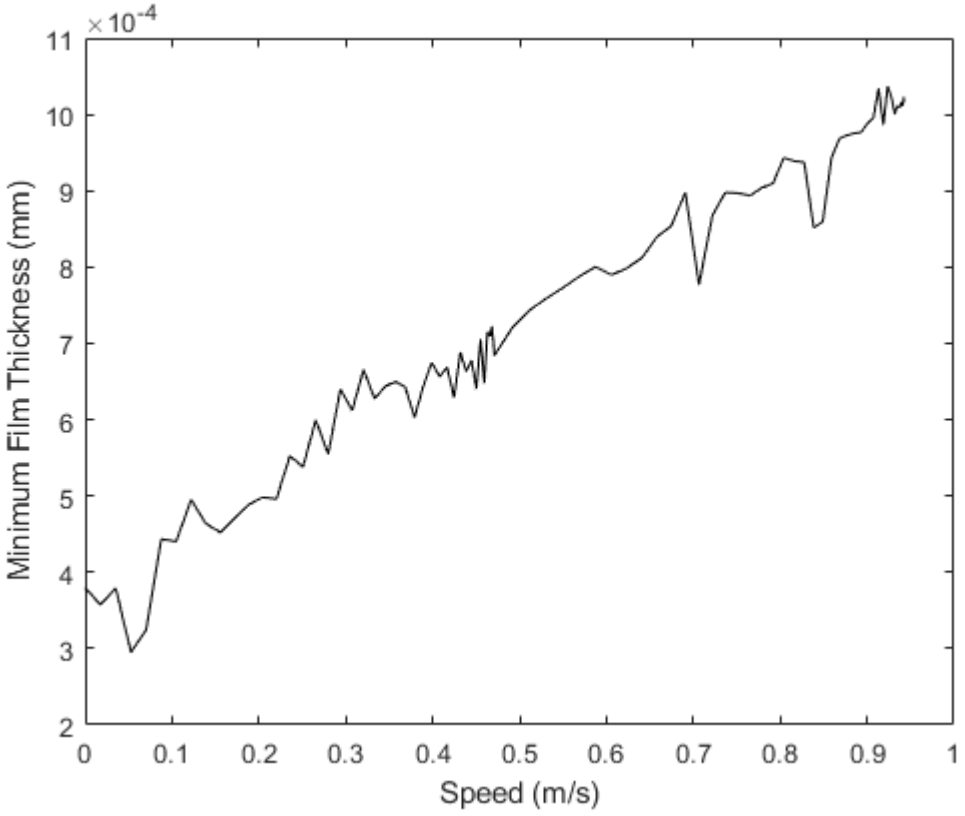

Figure 6.17: Model Version 8 Predicted Minimum Film Thickness with Shear Thinning Fit #1 Implemented

As expected, based off Figure 6.16 the model predicts a lower friction coefficient at low speeds. It was suspected the higher friction forces contributed to excessive deformation of the ring and the resultant negative film thickness, which the model no longer predicts. However, variations remain in the model's predictions of friction coefficient and minimum film thickness. This suggests that the model has not truly converged. To try to determine what was happening, the model was set to predict the friction coefficient for

the single speed of 0.05 m/s. Figures 6.18 and 6.19 show how the shear force and the friction coefficient changed with each iteration.

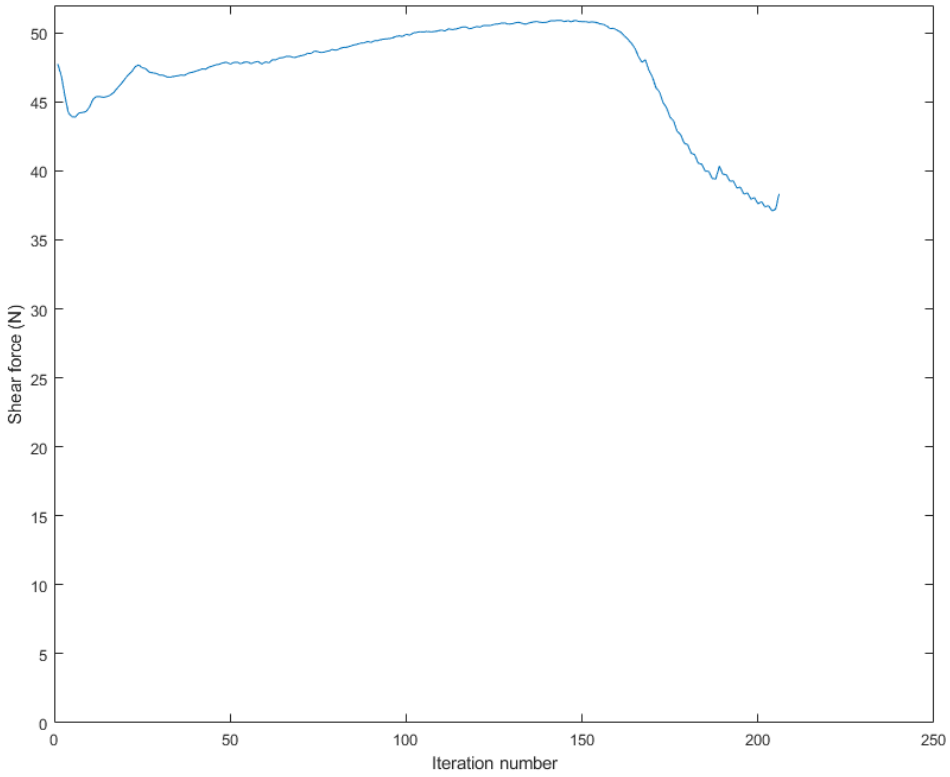

Figure 6.18: Variation of Shear Force over Several Iterations, Sliding Speed 0.05 m/s

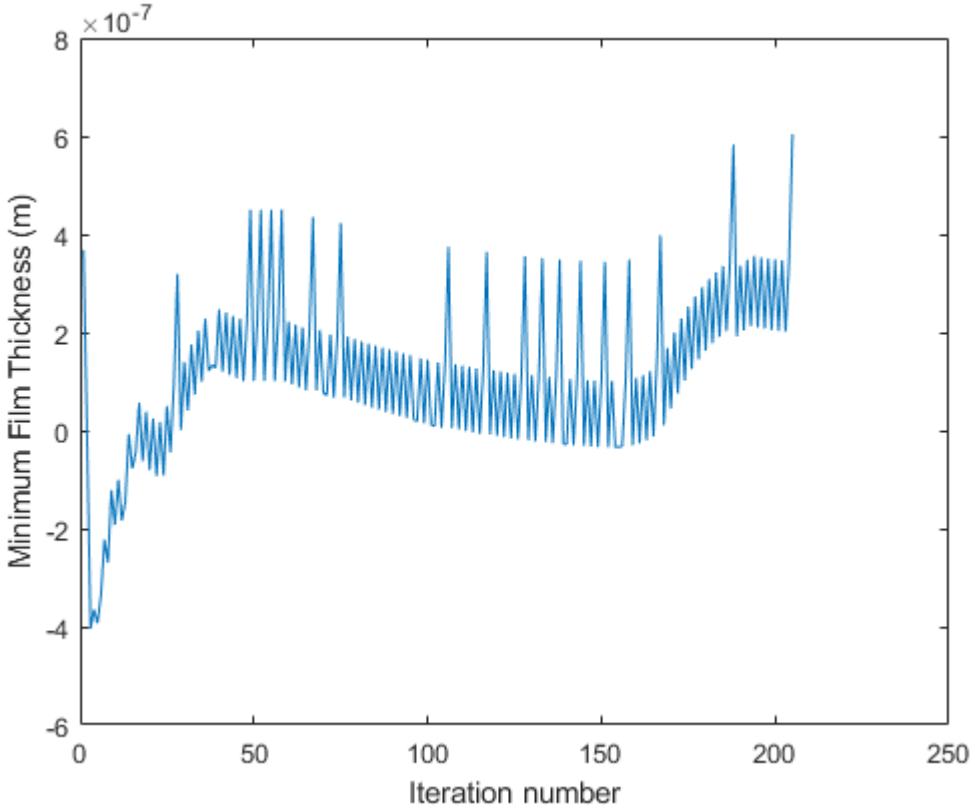

Figure 6.19: Variation of Minimum Film Thickness over Several Iterations, Sliding Speed 0.05 m/s

Looking at Figure 6.18, the shear force did not gradually decrease. It varied enough such that convergence was not reached. Of greater concern was the complete lack of a trend in variation of minimum film thickness. Based on all prior model predictions, two things were occurring: the model underpredicted the shear force due to the lubricant, or the model was predicting a transition to the hydrodynamic regime at too low a speed. A shear flow factor (Equation 3.46) was added that reflects the surface roughness, and the

dry friction coefficient was reset to 0.15. Figure 6.20 compares this model with the previous version.

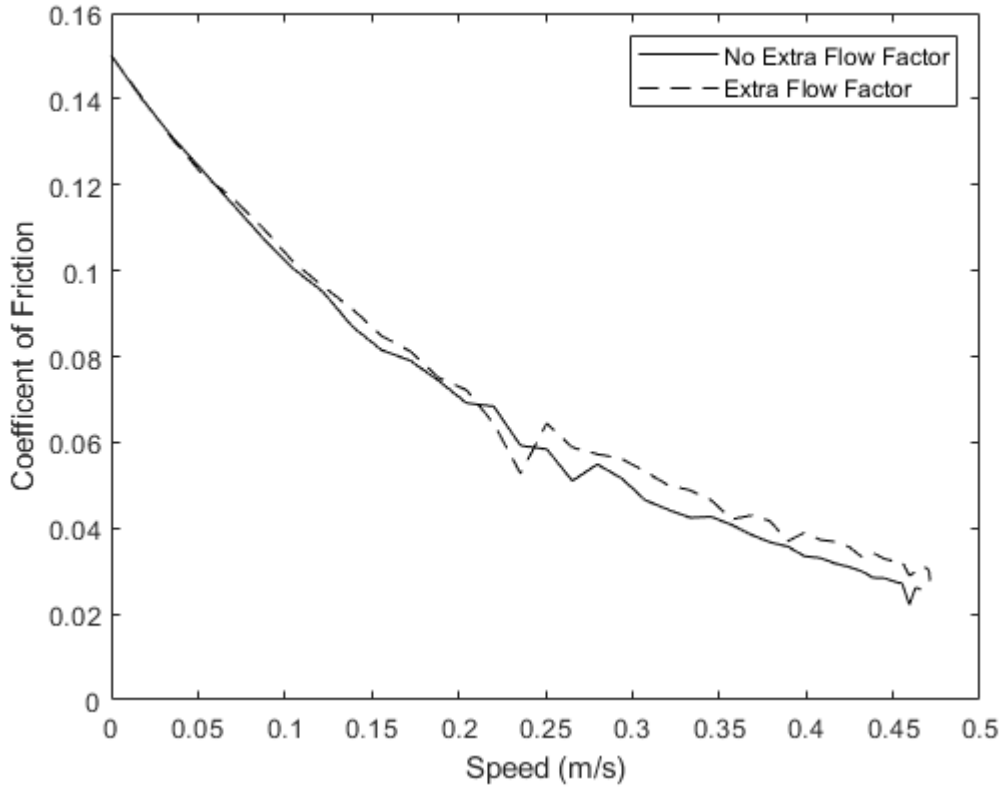

Figure 6.20: Model Version 9 with and Without an Extra Shear Flow Factor

Looking at the above figure, it appears that the addition of the extra shear flow factor does not really affect the model's predictions – the predicted friction coefficient is only slightly higher at faster speeds. Note that variations from a general decreasing trend remain – even though such oscillations exist in the experimental data, they are more pronounced in the model prediction. A closer look at the code revealed a huge problem: the deformations were cumulative rather than applied to the undeformed profile. That

explains the results of a convergence test in which the relaxation factor was varied both for a stationary ring and for a ring with a sliding speed of 0.1 m/s. In those tests, the number of iterations required to achieve convergence varied greatly because the differing relaxation factors resulted in different sets of deformations applied to the ring. In turn, this resulted in variations in piston ring profile and thus predicted friction force for the same temperature/load/speed combination. Figures 6.21 shows the predicted deformation from a single iteration.

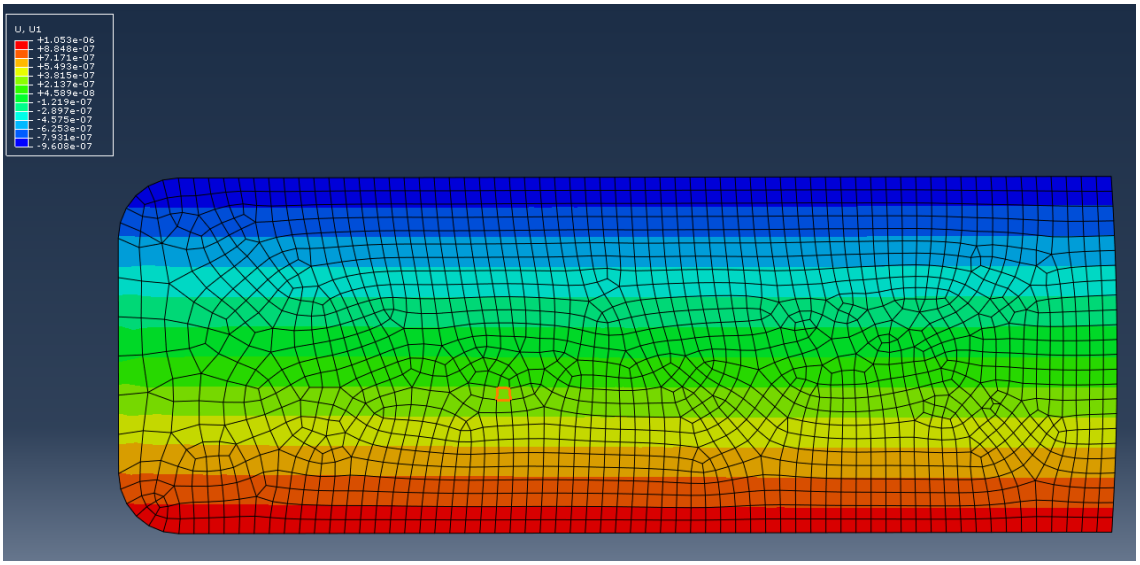

Figure 6.21: Predicted Axial Deformation (m) for a Single Iteration of the Model

While the deformation for a single iteration is small, bear in mind that prior versions of the model required dozens (or hundreds) of iterations to reach convergence.

6.2 Predictions with the Basic Model

Because of the temperatures at which shear thinning data was given, the temperature was decreased to 80 °C. The relaxation factor was removed; it could always be reinstated if convergence problems still existed. As there were problems reaching convergence at higher loads in the final version of the model, the relaxation factor was set at a constant value of 0.2. The requirement for it to be unity was removed. Figure 6.22 shows the model's predicted friction coefficient assuming an average sliding speed of 0.3 m/s.

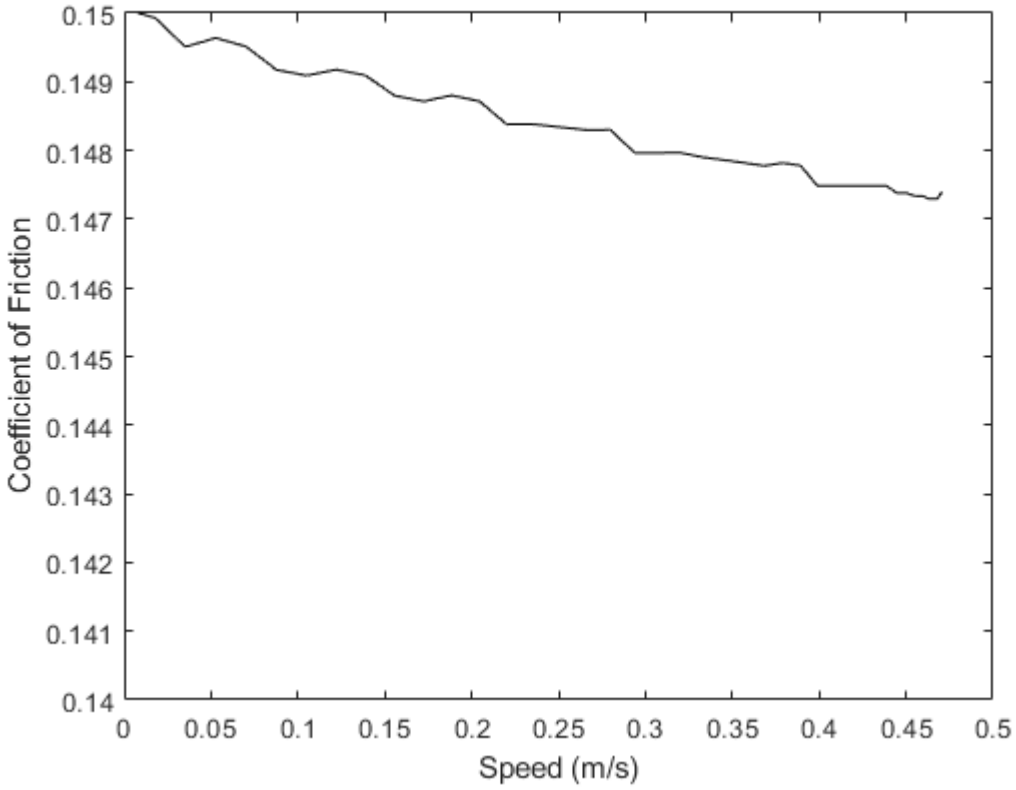

Figure 6.22: Model Version 10 Predicted Friction Coefficient, Temperature 80 °C, Average Sliding Speed 0.3 m/s, 150 N Load

The variation in predicted friction coefficient dropped sharply after fixing the problem with the deformation implementation discussed on the previous page. The average predicted friction coefficient was 0.148 with very little variation but a slight decreasing trend. The model predicts boundary lubrication over the entire range of speeds, a stark contrast to prior versions. Some small variations remain; this was believed to be numerical error because similar trends were observed from the measurements. Because the predicted trend more closely matched the experimental results, the model was extended to average speeds of 0.6 and 1.2 m/s. Table 6.1 summarizes these predictions and compares them to the experimental measurements.

Table 6.1: Average Friction Coefficients for Model Version 10 and the Experiments, 150 N Load

Average Speed (m/s)	Model Predicted Average Friction Coefficient	Average Measured Friction Coefficient
0.3	0.148	0.121
0.6	0.147	0.119
1.2	0.144	0.107

Figures 6.23-6.25 show the comparisons between the model and the experiments.

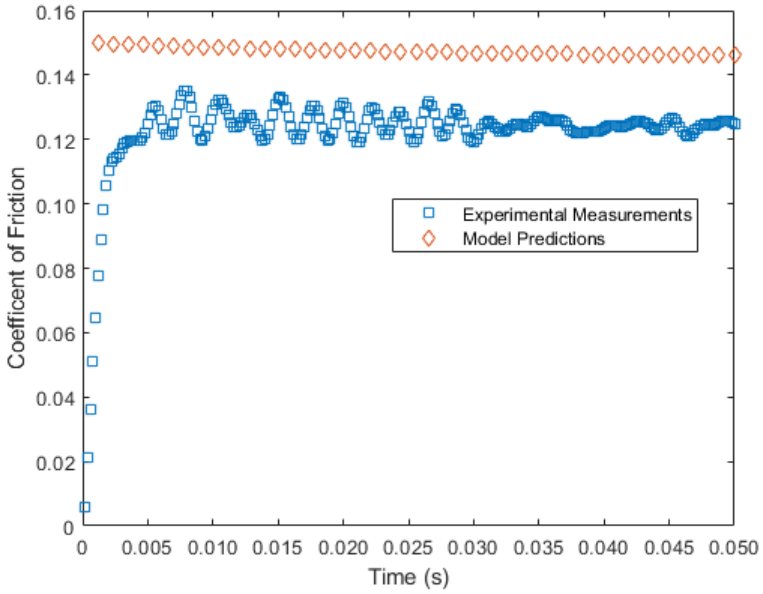

Figure 6.23: Model Version 10 Comparison to Experiment, Average Sliding Speed 0.3 m/s

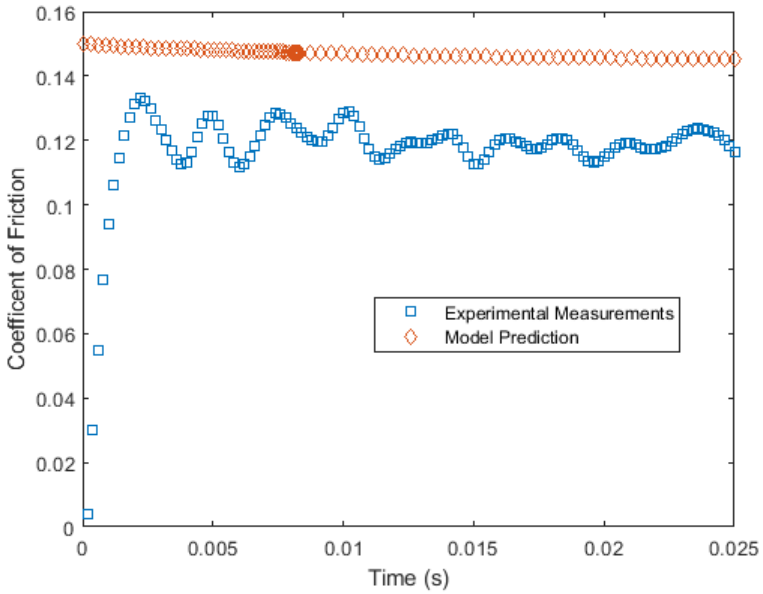

Figure 6.24: Model Version 10 Comparison to Experiment, Average Sliding Speed 0.6 m/s

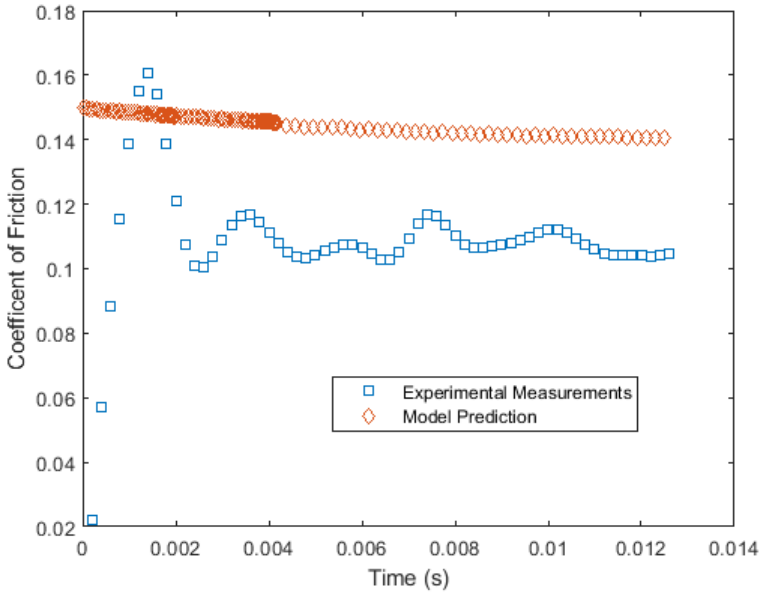

Figure 6.25: Model Version 10 Comparison to Experiment, Average Sliding Speed 1.2 m/s

As can be seen from the plots, the model overestimates the friction coefficient relative to the experiments. It is especially weak at predicting transient effects that occur when the sliding velocity changes direction. In these regions, mechanical play or ring rotation might cause the contacts to stick briefly, behaviors this model neglects. This could be corrected by changing the value of μ and hopefully finding a single value or function that would work for all speed/load/temperature combinations.

Based on the initial comparison and some samples of the experimental data, μ was set to 0.124. Figures 6.26-6.28 show how the model compares to the measurements. However, temperature influence has not yet been discussed.

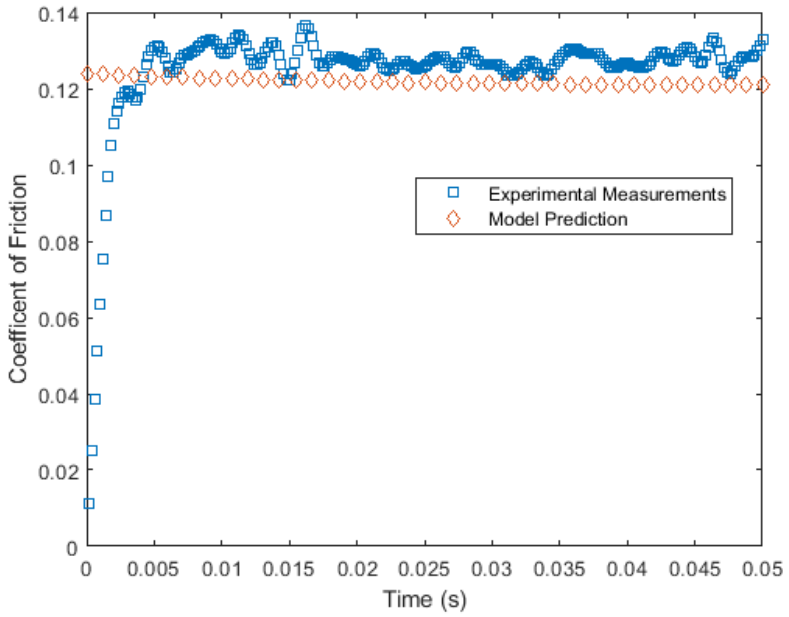

Figure 6.26: Model Version 11 Comparison to Experiment, Average Sliding Speed 0.3 m/s

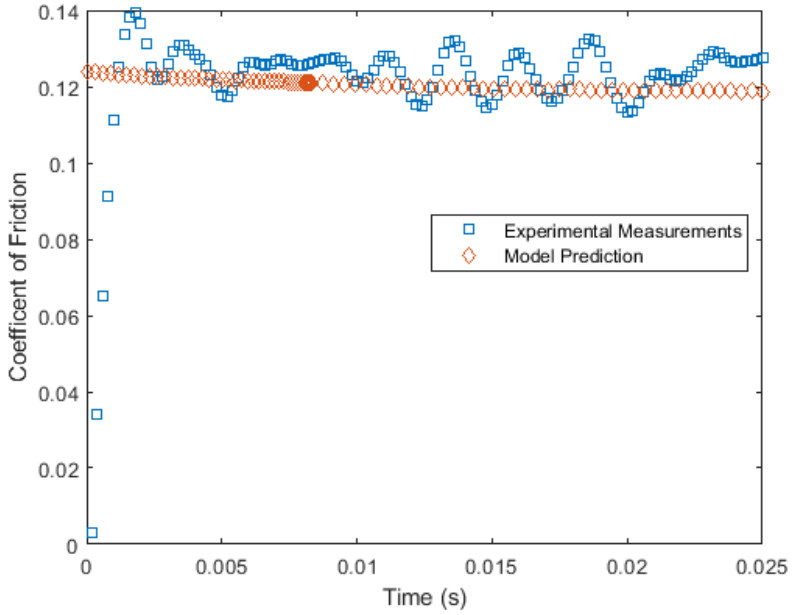

Figure 6.27: Model Version 11 Comparison to Experiment, Average Sliding Speed 0.6 m/s

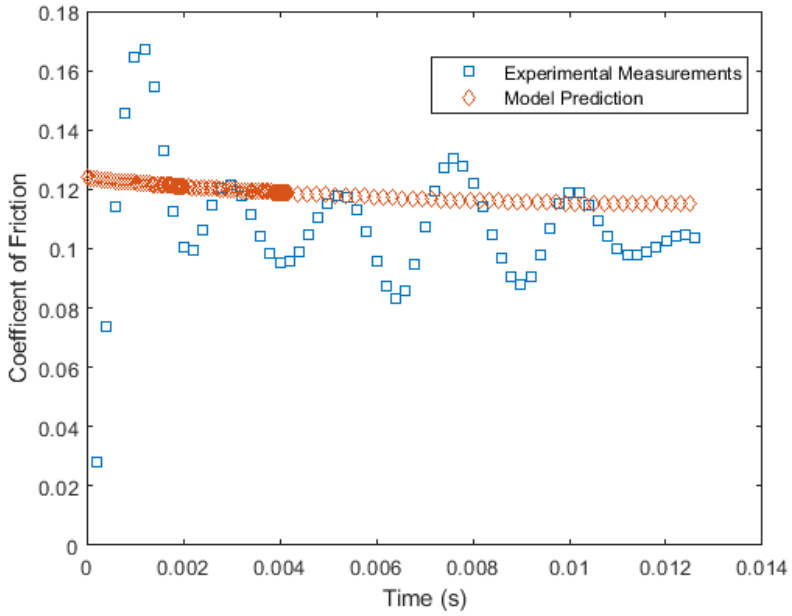

Figure 6.28: Model Version 11 Comparison to Experiment, Average Sliding Speed 1.2 m/s

Figures 6.26-6.28 illustrate a close match between model and experiment that lesser for increasing piston speed. Buoyed by this success, further comparisons were done for different loads and temperatures. Tables 6.2-6.5 compare the model's predictions of friction coefficient with the overall experimental averages.

Table 6.2: Average Friction Coefficients for Model Version 11 and the Experiments, 80 °C, 150 N

Average Speed (m/s)	Model Predicted Average Friction Coefficient	Average Measured Friction Coefficient
0.3	0.122	0.121
0.6	0.119	0.119
1.2	0.115	0.114

Table 6.3: Average Friction Coefficients for Model Version 11 and the Experiments, 120 °C, 150 N

Average Speed (m/s)	Model Predicted Average Friction Coefficient	Average Measured Friction Coefficient
0.3	0.121	0.125
0.6	0.118	0.125
1.2	0.113	0.120

Table 6.4: Average Friction Coefficients for Model Version 11 and the Experiments, 50 °C, 150 N

Average Speed (m/s)	Model Predicted Average Friction Coefficient	Average Measured Friction Coefficient
0.3	0.122	0.118
0.6	0.121	0.118
1.2	0.119	0.106

Table 6.5: Average Friction Coefficients for Model Version 11 and the Experiments, 50 °C, 100 N

Average Speed (m/s)	Model Predicted Average Friction Coefficient	Average Measured Friction Coefficient
0.3	0.122	0.114
0.6	0.120	0.118
1.2	0.118	0.106

These results suggested that the model needed a fundamental change – for a temperature of 50 °C, the model overestimated the friction coefficient by a greater value than at the higher temperatures. A closer inspection of Tables 6.3-6.5 reveals how little the

temperature change affected the model's predictions at the time. The friction coefficients were highest at low sliding speeds and high temperatures, which suggests that hydrodynamic lubrication still does not influence the model results enough. Recall from the Stribeck Curve that increases in either viscosity or velocity move contact towards the mixed lubrication regime and lower friction coefficients. It was clear the model would have to be further improved to reflect the effects of base temperature changes. An inspection of the code also revealed an incorrect viscosity value being used; it was 10 times greater than the true value.

6.3 Viscosity Pressure Dependence

To address the smaller than measured friction coefficient variation with speed, the viscosity now varied with pressure instead of remaining a constant. Figures 6.29 and 6.30 show how the revised model compares to the old version of the model and the measurements for a load of 50 N and a temperature of 80 °C. The procedure to find the pressure viscosity coefficient is detailed in Chapter 3.

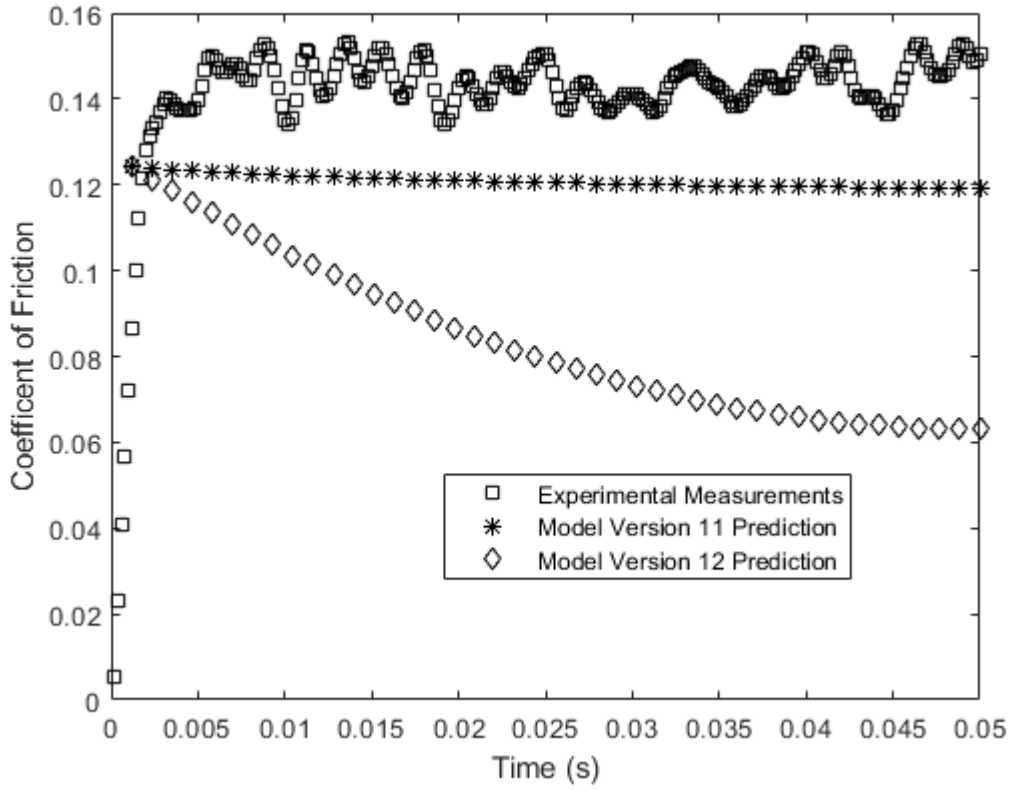

Figure 6.29: Model Versions 11 and 12 Compared to Experiment, Average Sliding Speed 0.3 m/s

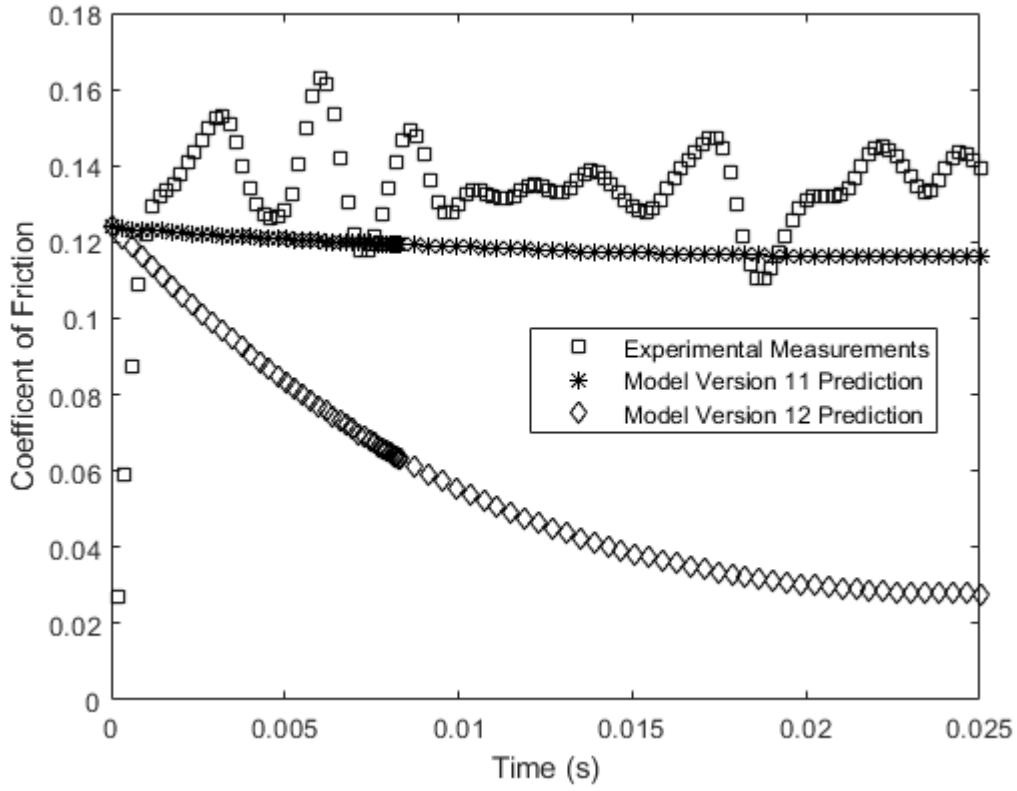

Figure 6.30: Model Versions 11 and 12 Compared to Experiment, Average Sliding Speed 0.6 m/s

Correcting the value of viscosity used and incorporating the Barus equation in the model resulted in a much lower friction coefficient compared to the previous version. In addition, the trend in predicted friction coefficient did not look as smooth as it did when the wrong viscosity value was used. The average friction coefficients are summarized in Table 6.6.

Table 6.6: Average Friction Coefficients for Model Versions 11 and 12 and the Experiments, 80 °C, 50 N

Average Speed (m/s)	Model Version 12 Predicted Average Friction Coefficient	Model Version 11 Predicted Average Friction Coefficient	Average Measured Friction Coefficient
0.3	0.084	0.121	0.145
0.6	0.056	0.119	0.139

The model now predicts a substantial decrease (27%) in average friction coefficient at higher speeds not too far removed from the measured percentage change. However, the model was unable to make any predictions at speeds higher than 1.6 m/s because the Reynolds code did not converge. This was because the Reynolds coefficients were not calculated correctly; their values were too small. A modification to the code rectified this, and Figure 6.31 illustrates how this impacts the split between contact and hydrodynamic forces for an average speed of 0.6 m/s.

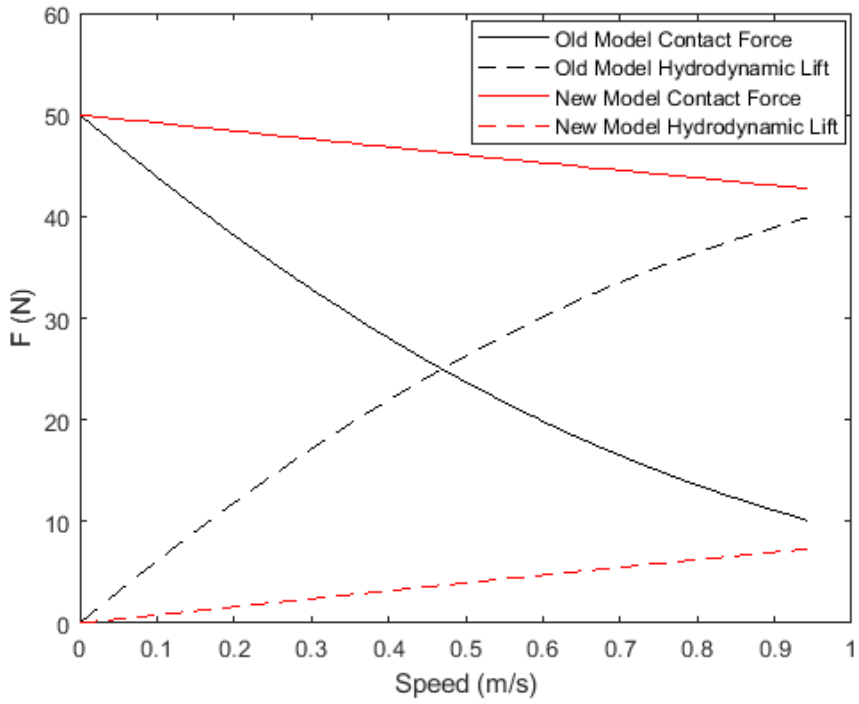

Figure 6.31: Breakdown of Load Type Before and After Correcting Reynolds Coefficients, Average Sliding Speed 0.6 m/s

The smaller calculated Reynolds coefficients resulted in the model predicting greater hydrodynamic lift at higher speeds (up to 80% of the load carried by the fluid). On the other hand, it predicts that surface contact will still carry more than 80% of the load at the faster speed with the corrected Reynolds coefficients. Figures 6.32-6.33 show how the last 3 models compare to the experiments for a load of 50 N and a temperature of 80 °C.

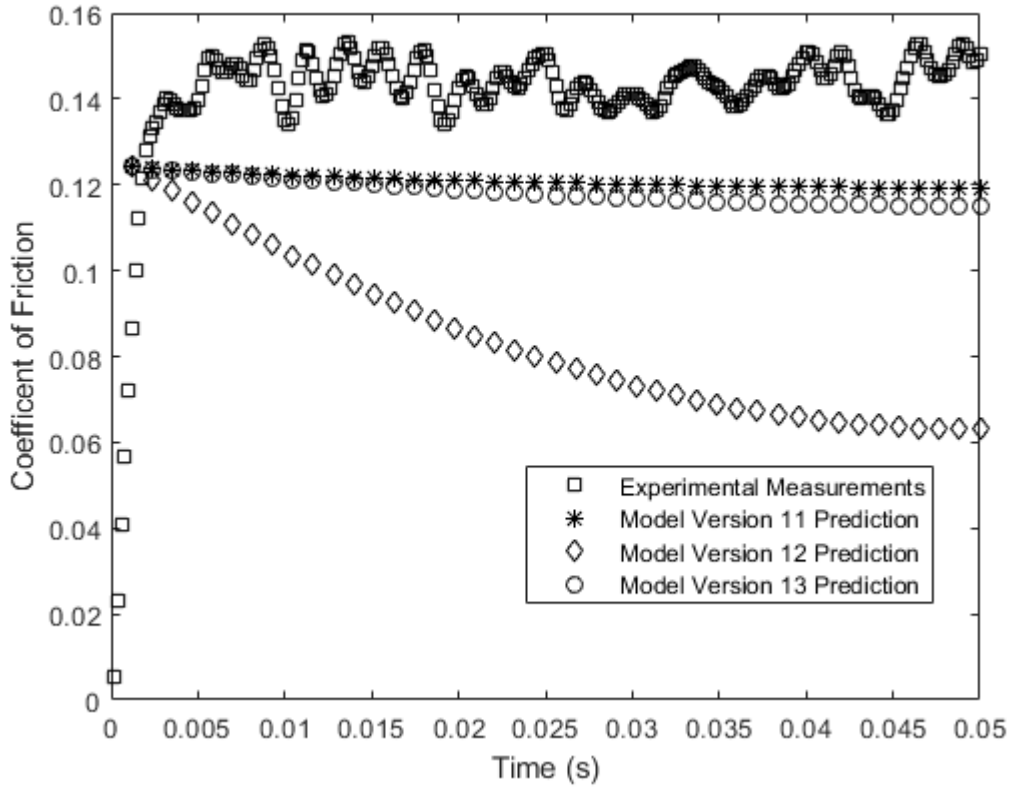

Figure 6.32: Model Versions 11, 12, and 13 Compared to Experiment, Average Sliding Speed 0.3 m/s

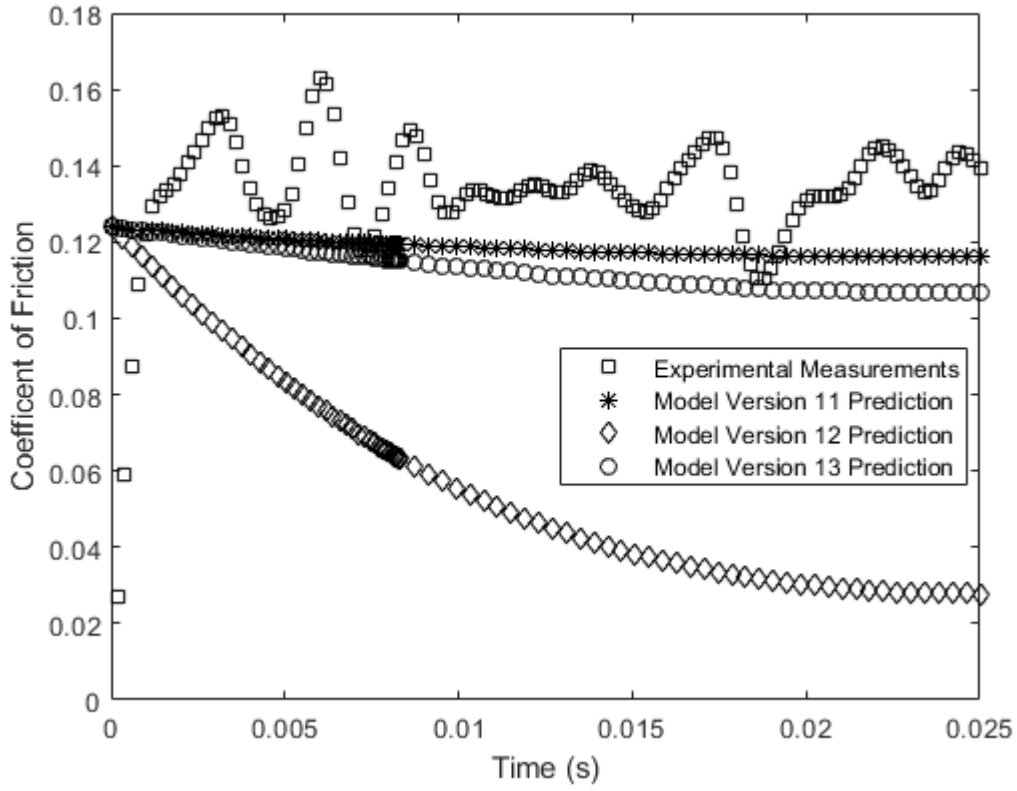

Figure 6.33: Model Versions 11, 12, and 13 Compared to Experiment, Average Sliding Speed 0.6 m/s

The updated model now predicts a similar trend to the 11th version – underestimating relative to the measured coefficient of friction, but something that could be easily rectified for a single temperature-load combination by adjusting the assumed value of μ to 0.154. Figures 6.34 and 6.35 show how the model now compares to the experiments for the same load and temperature.

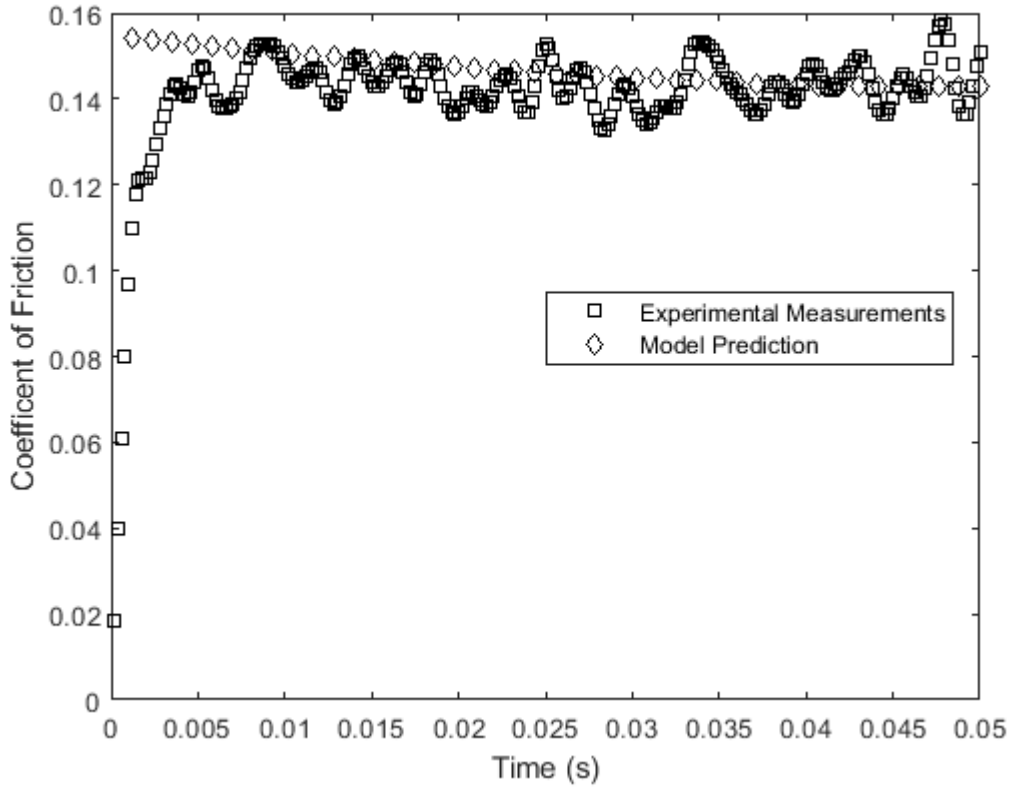

Figure 6.34: Model Version 14 Compared to Experiment, Average Sliding Speed 0.3 m/s

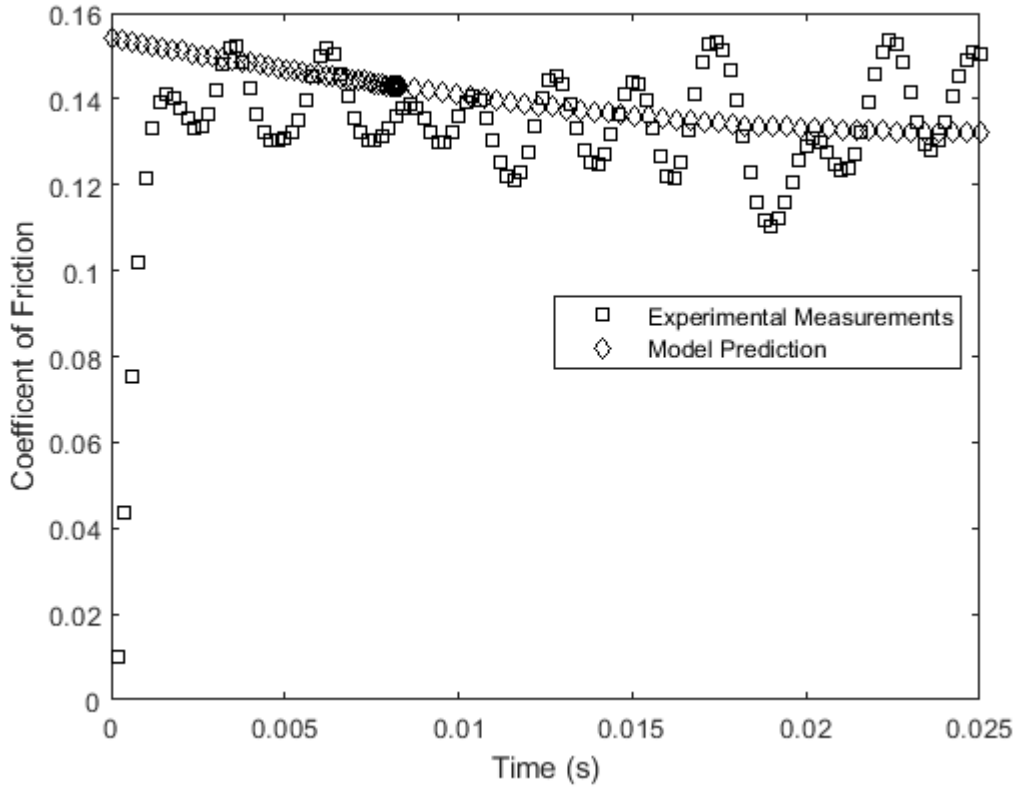

Figure 6.35: Model Version 14 Compared to Experiment, Average Sliding Speed 0.6 m/s

The model compares very favorably to the experiment; the predicted average friction coefficient is 0.147 for an average speed of 0.3 m/s and 0.140 for an average speed of 0.6 m/s. However, it needs to closely match the experimental data for other loads and temperatures too. Figures 6.36-6.41 show how it fares for other loads and temperatures.

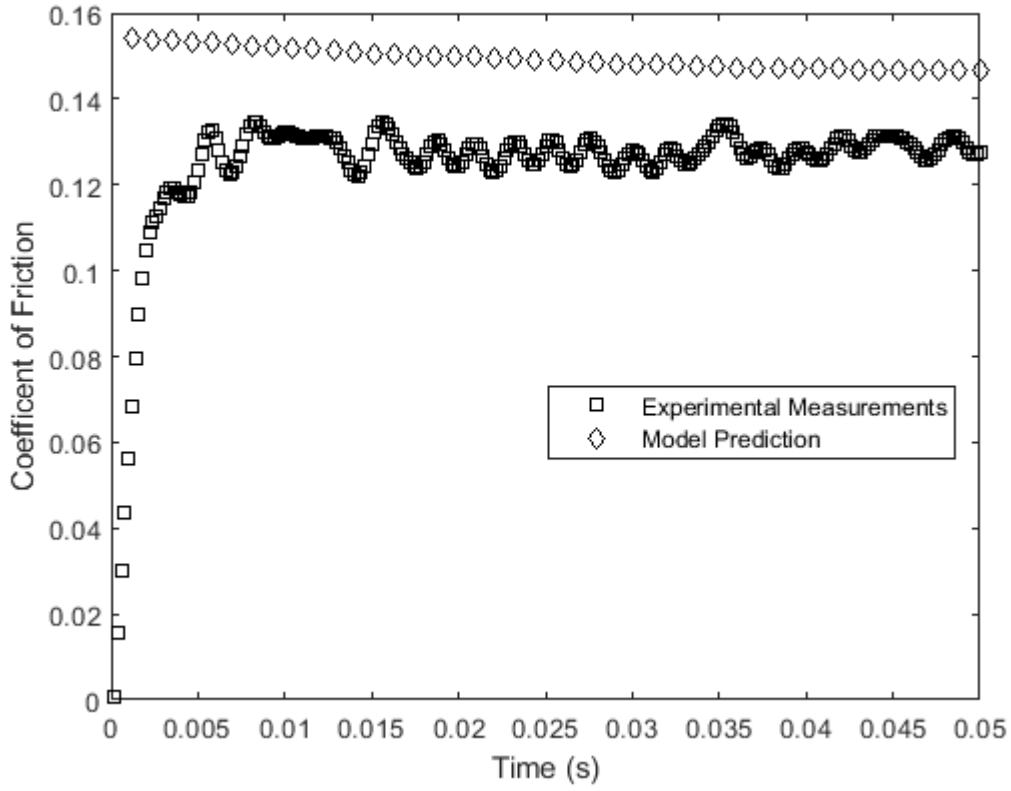

Figure 6.36: Model Version 14 Compared to Experiment, Average Sliding Speed 0.3 m/s, Applied Load 100 N, Temperature 80 °C

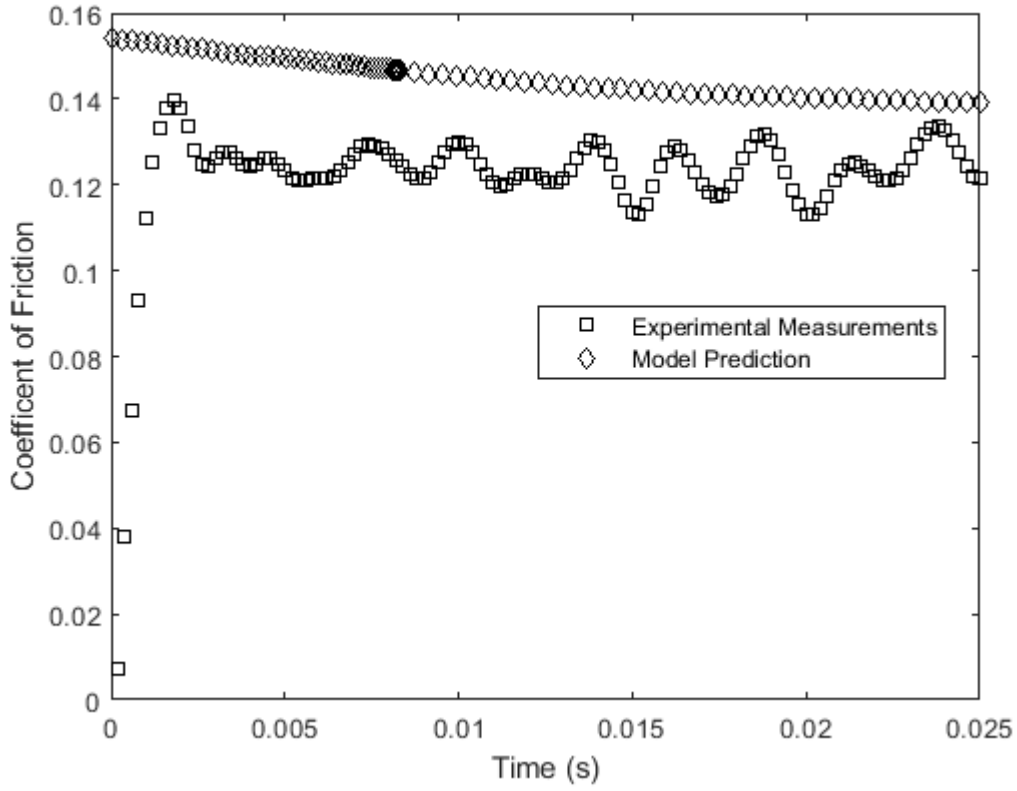

Figure 6.37: Model Version 14 Compared to Experiment, Average Sliding Speed 0.6 m/s, Applied Load 100 N, Temperature 80 °C

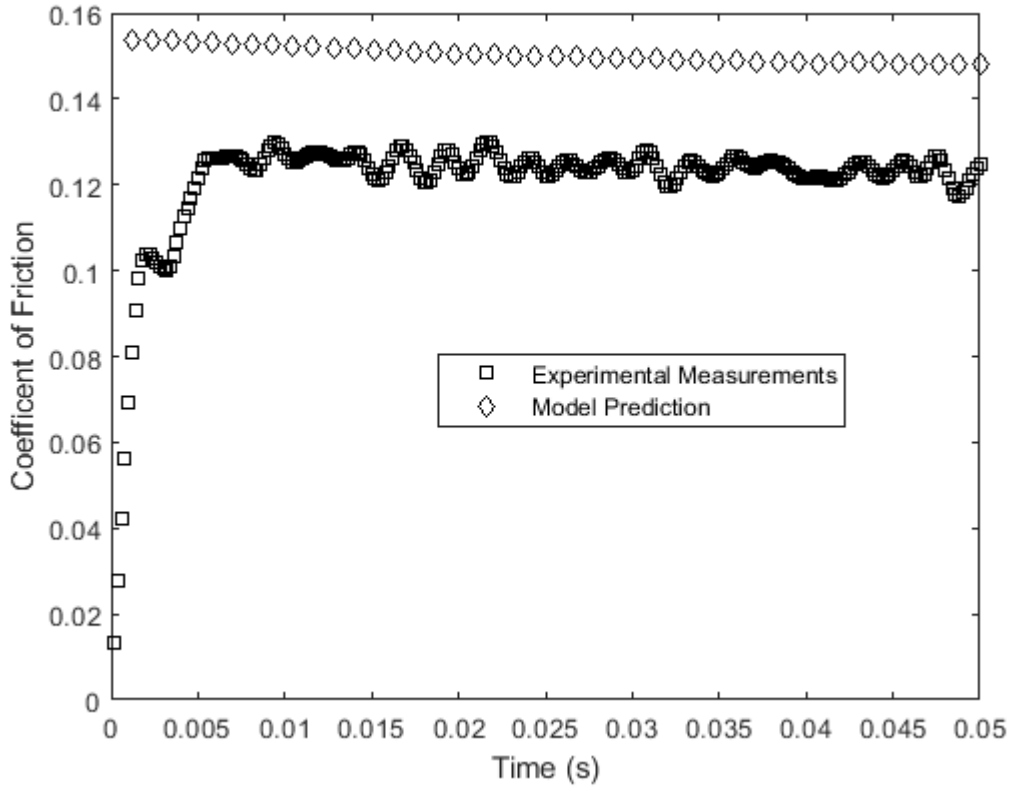

Figure 6.38: Model Version 14 Compared to Experiment, Average Sliding Speed 0.3 m/s, Applied Load 150 N, Temperature 80 °C

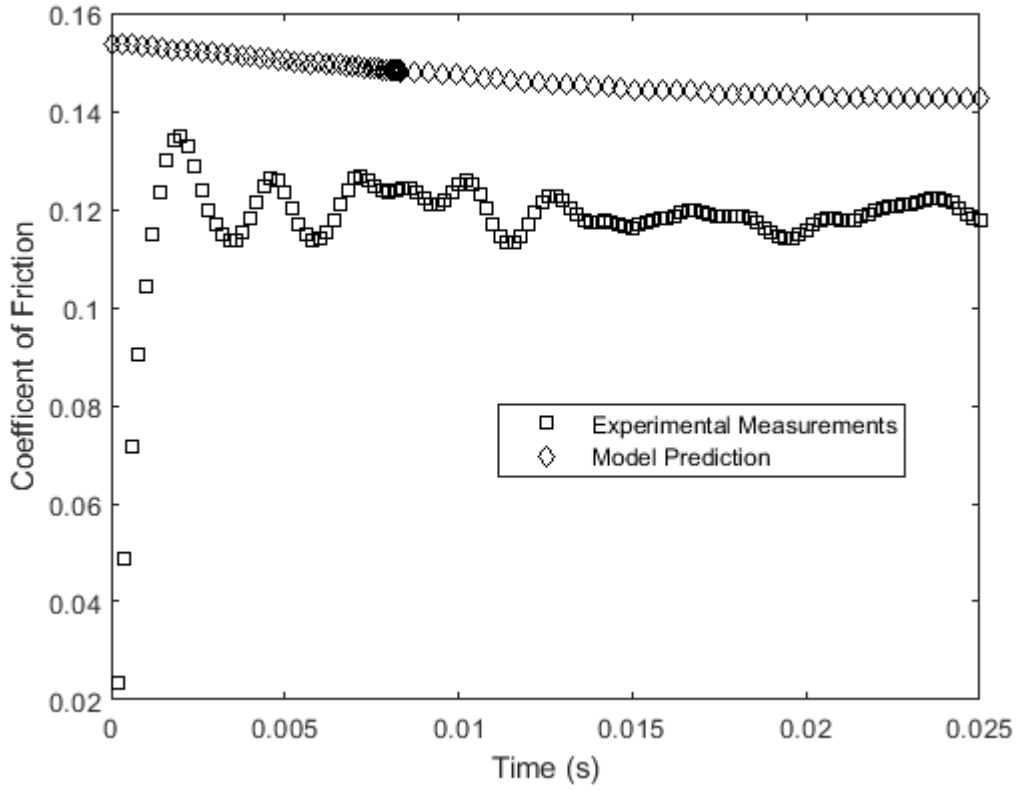

Figure 6.39: Model Version 14 Compared to Experiment, Average Sliding Speed 0.6 m/s, Applied Load 150 N, Temperature 80 °C

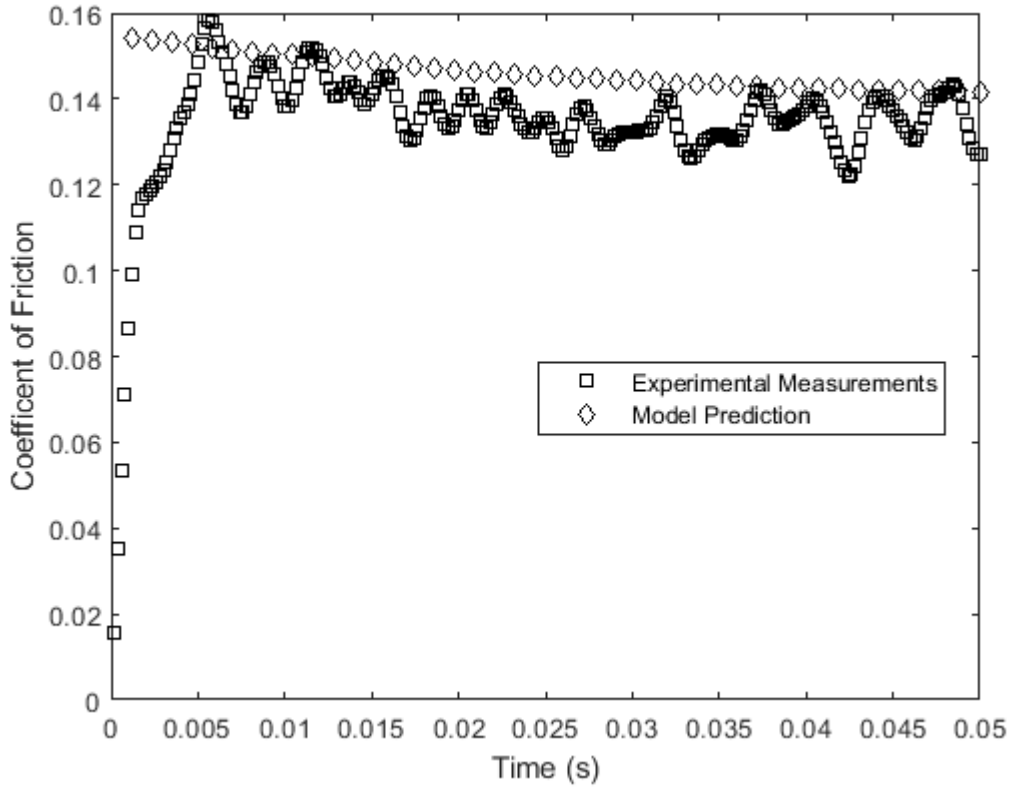

Figure 6.40: Model Version 14 Compared to Experiment, Average Sliding Speed 0.3 m/s, Applied Load 50 N, Temperature 50 °C

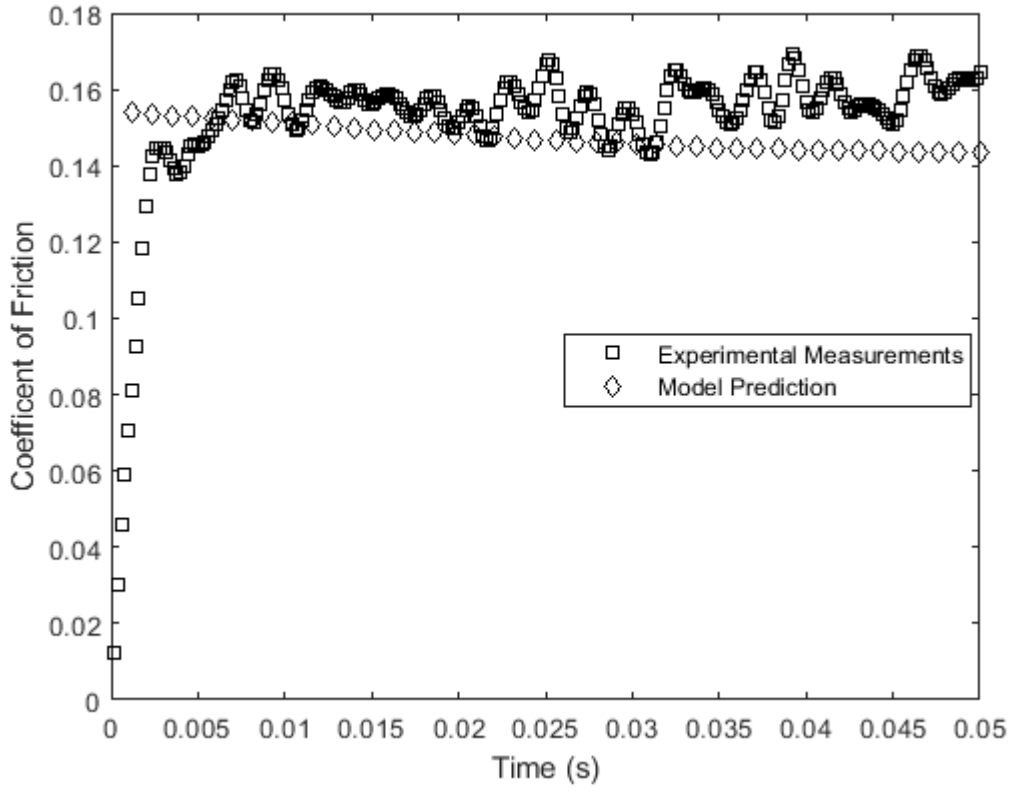

Figure 6.41: Model Version 14 Compared to Experiment, Average Sliding Speed 0.3 m/s, Applied Load 50 N, Temperature 120 °C

The model still compares reasonably well to the experiments for a 50 N load. However, it does not capture the effects of a different applied load as there is poor agreement with the 100 N and 150 N cases. It would need to be substantially revised to do so.

Table 6.7 summarizes the recent model versions and what changes were made between each version.

Table 6.7: Tested Model Versions (Continued from Table 4.3)

Model Version Number	Significant Change(s) from the Previous Version
6	The initial relaxation factor was set to 1/3.
7	The assumed dry friction coefficient was increased to 0.35 from 0.21.
8	The shear thinning fit used interpolation from measured data instead of placeholder coefficients.
9	A new shear flow factor that reflects surface roughness was added to the Reynolds Equation, and the dry friction coefficient was decreased to 0.15.
10	Deformations were now properly applied to the ring; previously, they were additive between iterations. This resulted in unrealistic ring profiles.
11	The assumed dry friction coefficient was set to 0.124.
12	A pressure dependence on viscosity was added.
13	A typo that caused the model to calculate the Reynolds coefficient incorrectly was fixed.
14	The assumed dry friction coefficient was set to 0.154.

CHAPTER 7

CONTACT FRICTIONAL FORCE DEPENDENCE ON LOAD MAGNITUDE

In many of the tests, lower friction coefficients were observed for higher loads. Two mechanisms could be accounting for this. First, the friction from fluid shearing is less dependent on normal load and could result in this trend. However, boundary lubrication dominates most of the cases. Therefore, the model was substantially revised so it can account for changes in friction coefficient when load increases. Initially the friction model adopted from Cohen et. al. [97] as shown in Equation 3.47. Figure 7.1 shows the result using this model and the results of the previous version for a load of 150 N at a temperature of 80 °C and an average speed of 0.3 m/s.

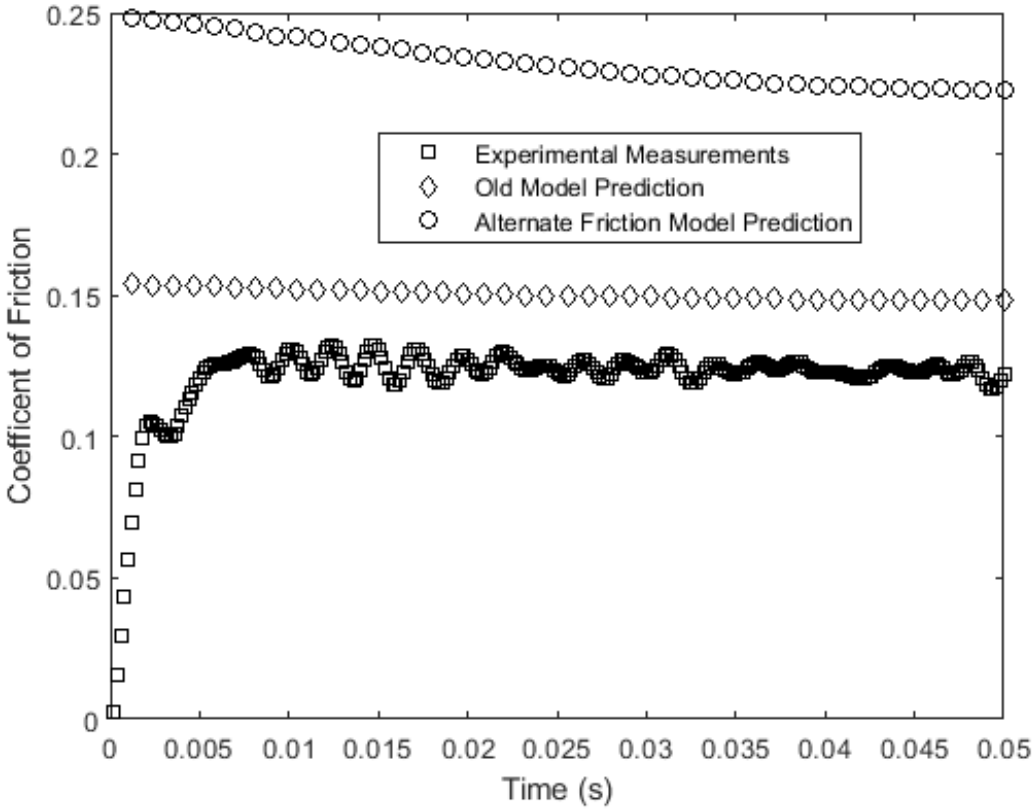

Figure 7.1: Model Versions 14 and 15 Compared to Experiment, Average Sliding Speed 0.3 m/s, Applied Load 150 N, Temperature 80 °C

This model was less effective than the previous version – it predicted an average friction coefficient of 0.232. The plasticity index, which had not been previously calculated, was added to the code. Its value was 17, well beyond the values of ψ for which Eq. 3.49 had been derived. Figure 7.2 shows the effect of replacing Eq. 3.49 with 3.51.

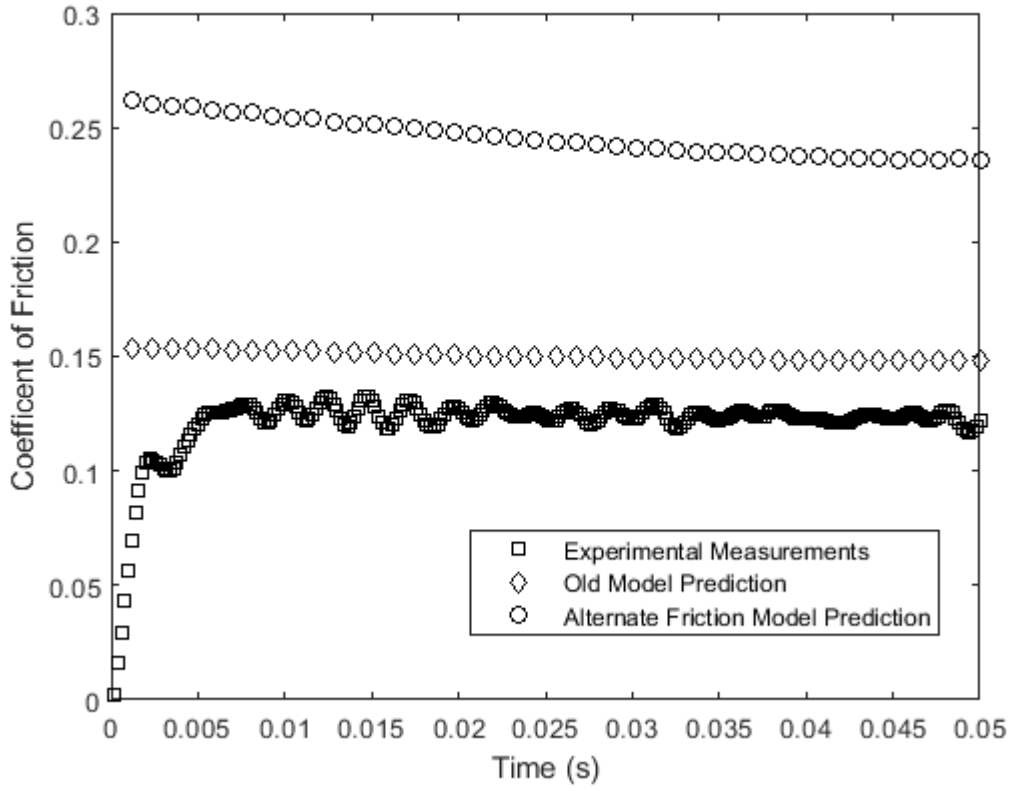

Figure 7.2: Model Versions 14 and 16 Compared to Experiment, Average Sliding Speed 0.3 m/s, Applied Load 150 N, Temperature 80 °C

The model now predicts an even higher friction coefficient (0.246) relative to the experiments. However, those equations are for static friction, meaning that slipping does not occur. An entirely different equation would have to be tried. Initially attempts to use Equation 3.52 did not work. With μ_{max} initially set to 1.25, Figure 7.3 illustrates a sample piston ring profile.

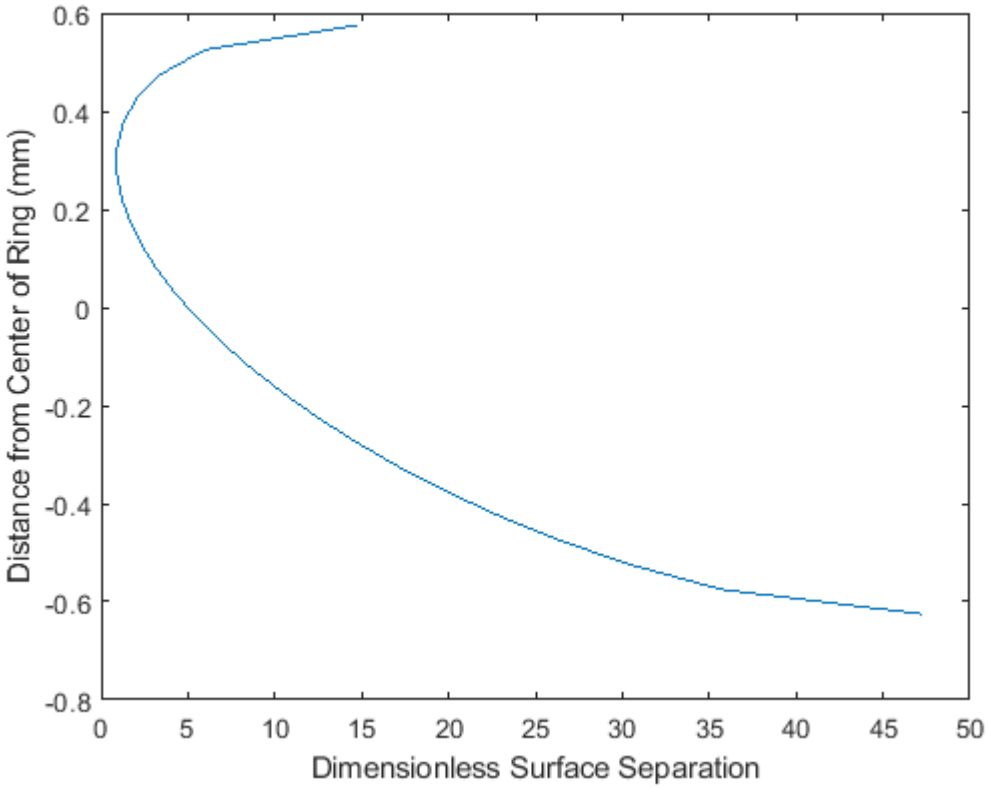

Figure 7.3: Predicted Piston Ring Profile when Using Equation 3.52

The highly deformed profile brought back memories of the convergence issues that were explained in Chapter 6. This time, the shear forces were found to be unusually high – roughly the same magnitude as the load. Two different values of μ_{max}, 0.125 and 0.25, were selected, and the model was run using the same temperature, load, and average speed. Subsequently, the load was reduced to 100 N to see how the model would handle a load variation. Figures 7.4 and 7.5 show how the models compare to the experiments.

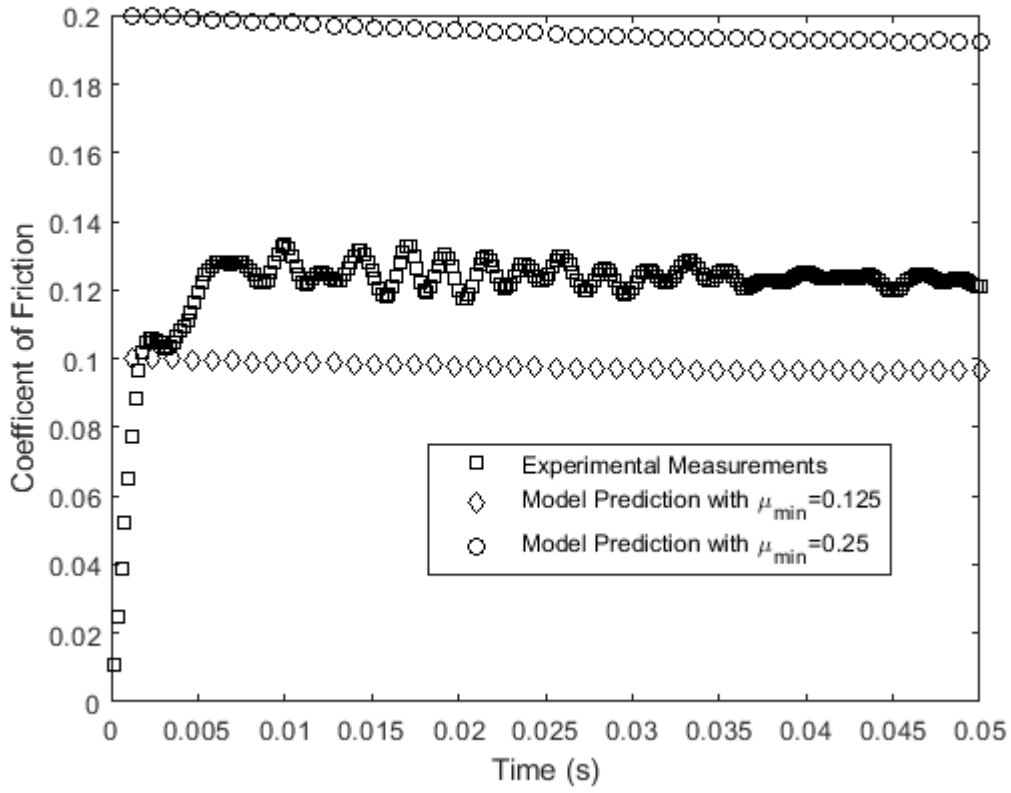

Figure 7.4: Model Comparisons to Experiment using Equation 3.52, Average Sliding Speed 0.3 m/s, Applied Load 150 N, Temperature 80 °C

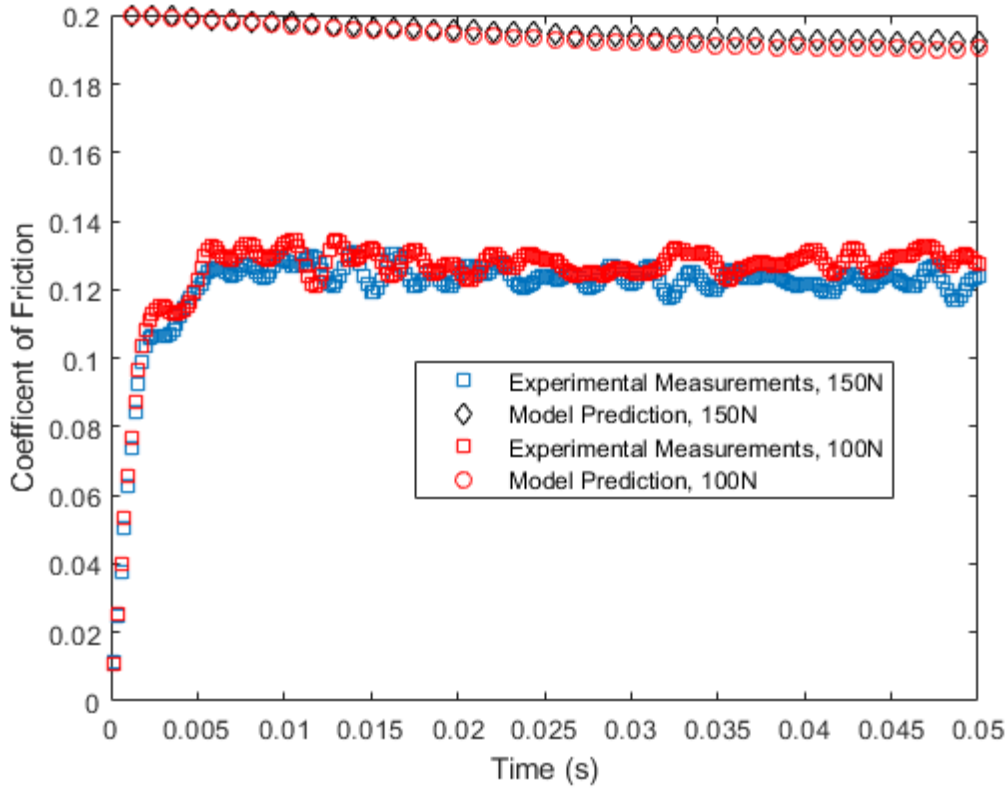

Figure 7.5: Model Comparisons to Experiment using Equation 3.52, Average Sliding Speed 0.3 m/s, Varied Applied Load, Temperature 80 °C, μ_{max} = 0.25

None of the models predicted the friction coefficient very well. While this could have been rectified by changing the value of μ_{max}, Figure 7.5 reveals a different trend: the model predicts an increase in friction coefficient as load increases, but a lower friction coefficient was observed when the load was increased. Thus, Equation 3.52 was discarded, and the model was tested using a simpler model for the dry friction coefficient that does not depend on the local load (Equation 3.53). Figures 7.6 – 7.11 show how the

model compares to the measurements with the simpler model for various temperatures and loads.

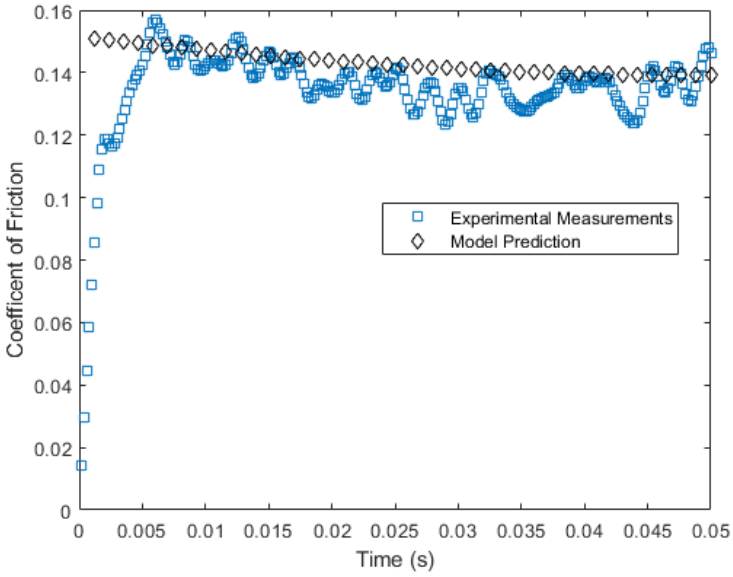

Figure 7.6: Model Comparison to Experiment using Equation 3.53, Average Sliding Speed 0.3 m/s, 50 N load, Temperature 50 °C

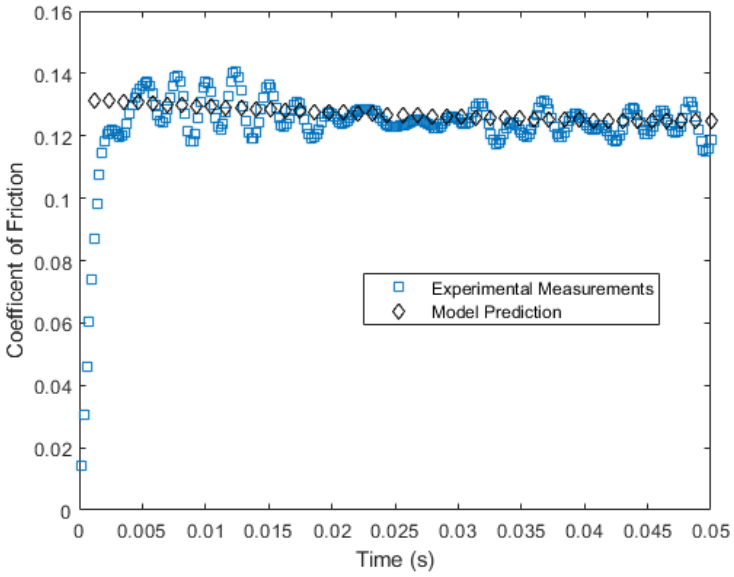

Figure 7.7: Model Comparison to Experiment using Equation 3.53, Average Sliding Speed 0.3 m/s, 100 N load, Temperature 50 °C

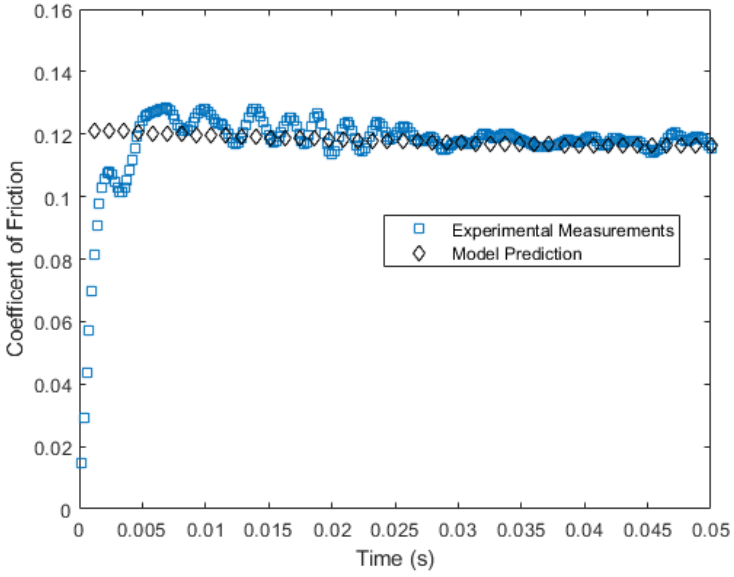

Figure 7.8: Model Comparison to Experiment using Equation 3.53, Average Sliding Speed 0.3 m/s, 150 N load, Temperature 50 °C

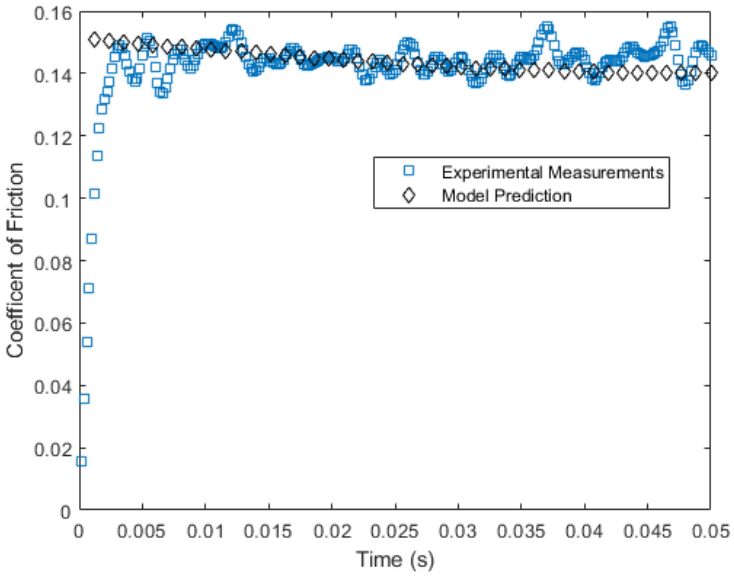

Figure 7.9: Model Comparison to Experiment using Equation 3.53, Average Sliding Speed 0.3 m/s, 50 N load, Temperature 80 °C

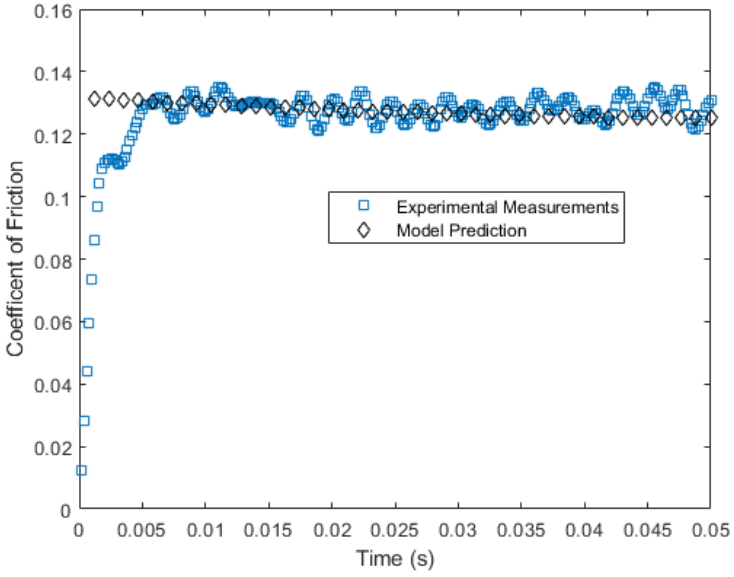

Figure 7.10: Model Comparison to Experiment using Equation 3.53, Average Sliding Speed 0.3 m/s, 100 N load, Temperature 80 °C

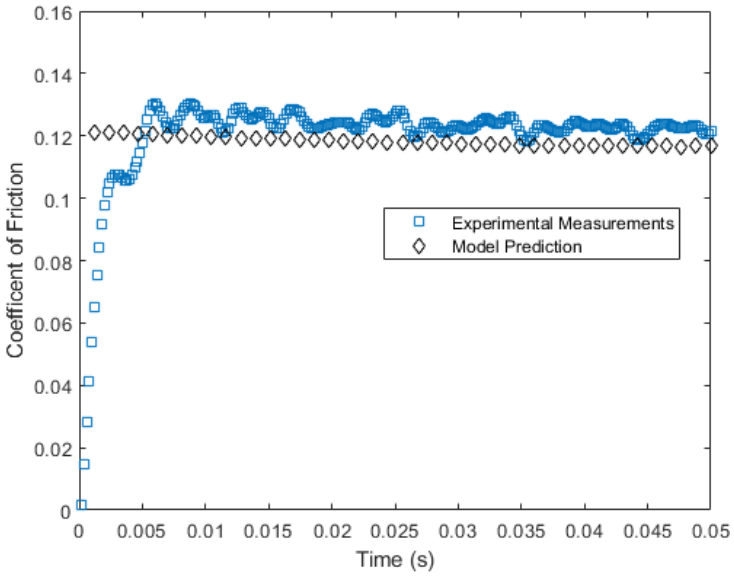

Figure 7.11: Model Comparison to Experiment using Equation 3.53, Average Sliding Speed 0.3 m/s, 150 N load, Temperature 80 °C

While the model predicts a good fit for different temperatures and loads, different speeds were not tested. Using these results and an analysis by Wang et. al. [99] considering friction in elastic-plastic rough surface contact, Equation 3.54 was derived. It became the new dry friction model employed; initially μ_{max} was set to 0.175. As always, it could be adjusted if necessary. Figures 7.12 and 7.13 depict the model's predictions against the measured friction coefficients using Equation 3.54 for a load of 100 N and two different temperatures.

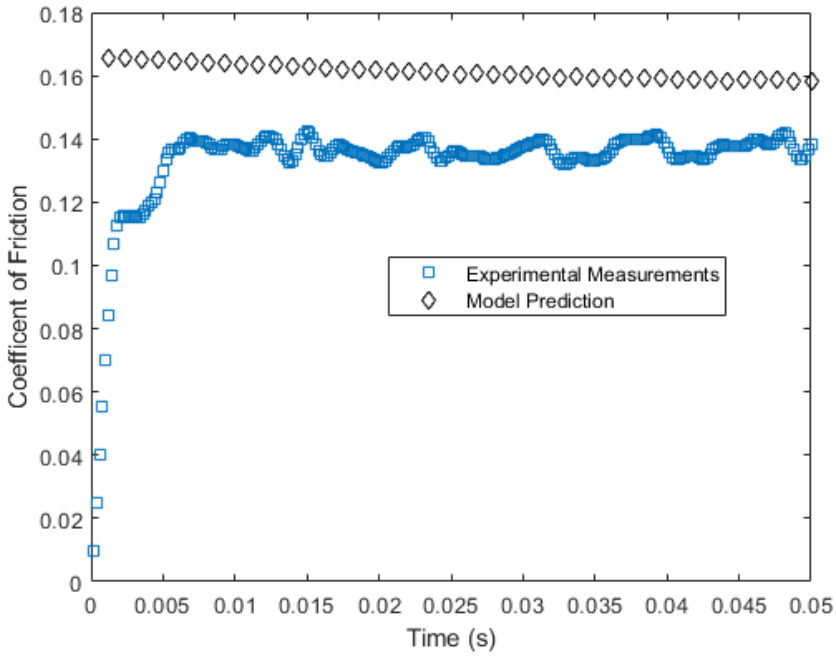

Figure 7.12: Model Comparison to Experiment using Equation 3.54, Average Sliding Speed 0.3 m/s, Temperature 120 °C

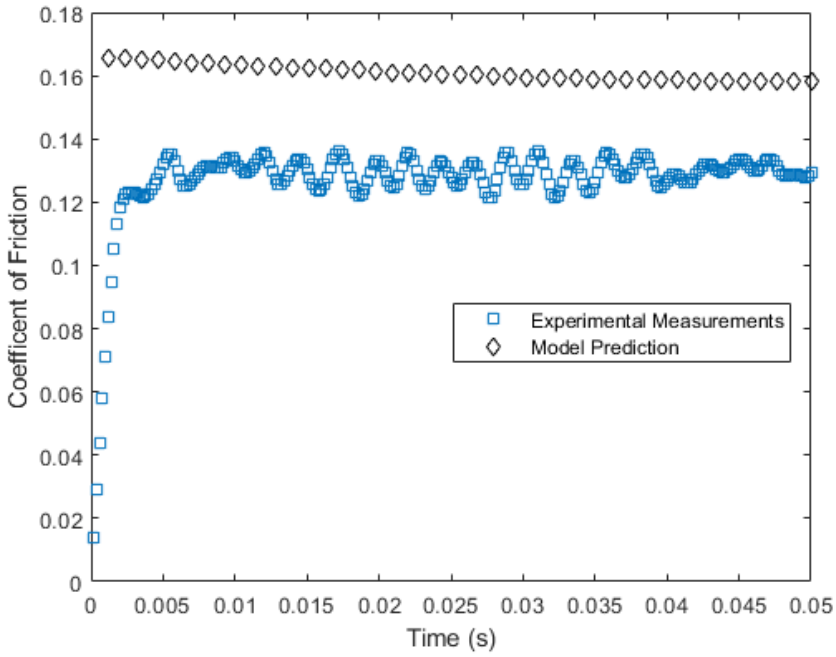

Figure 7.13: Model Comparison to Experiment using Equation 3.54, Average Sliding Speed 0.3 m/s, Temperature 80 °C

While the model overestimates the friction coefficient, that could be remedied by decreasing μ_{max} to a lower value such as 0.144. Figures 7.14 and 7.15 show how this affects the model's comparison with the experiment for the same load and temperatures.

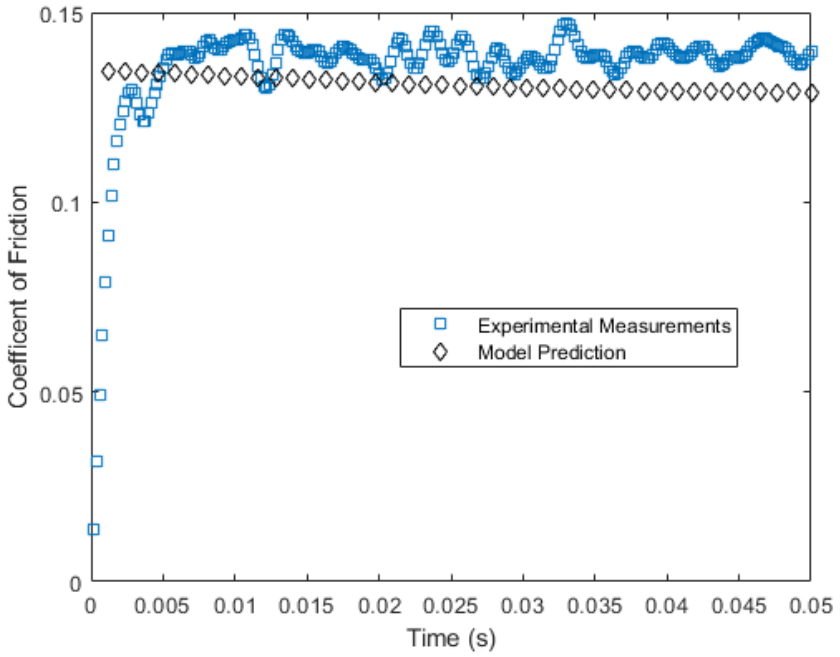

Figure 7.14: Model Comparison to Experiment using Equation 3.54, Average Sliding Speed 0.3 m/s, Temperature 120 °C

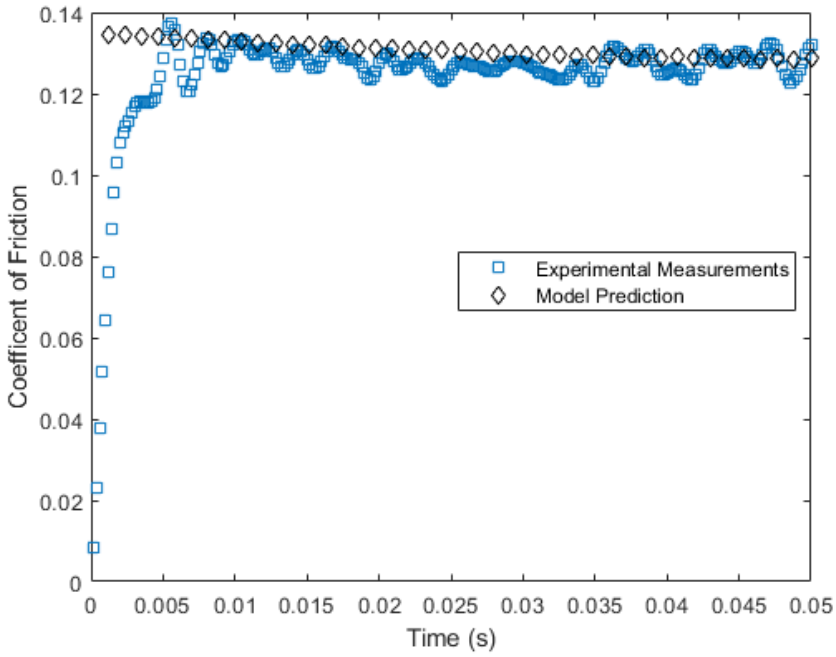

Figure 7.15: Model Comparison to Experiment using Equation 3.54, Average Sliding Speed 0.3 m/s, Temperature 80 °C

This appears to be a close match to the experiments, but further tests were run to see how well the model handled changes in applied load. Figures 7.16 – 7.19 compare the model's predictions to the measurements for loads of 150 N and 50 N.

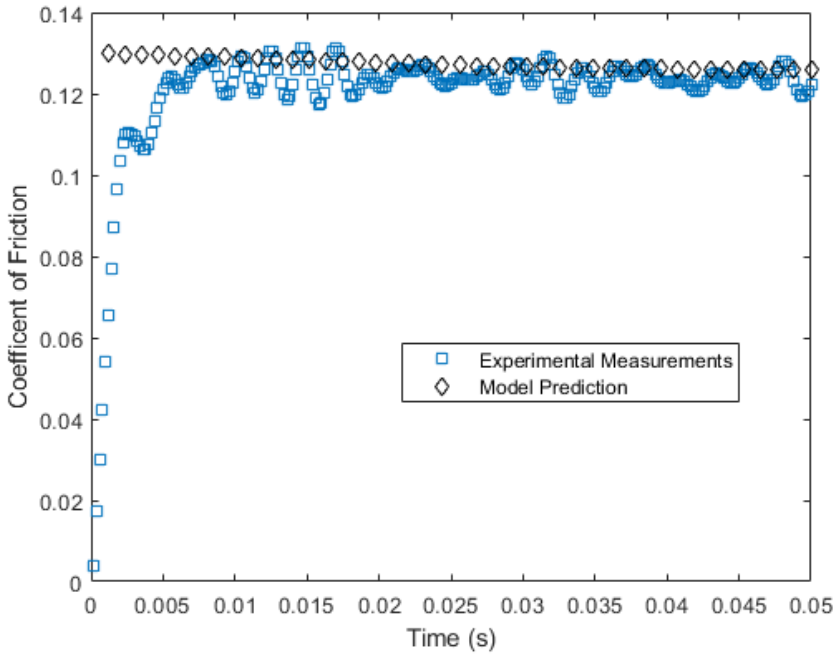

Figure 7.16: Model Comparison to Experiment using Equation 3.54, Average Sliding Speed 0.3 m/s, Temperature 120 °C, Applied Load 150 N

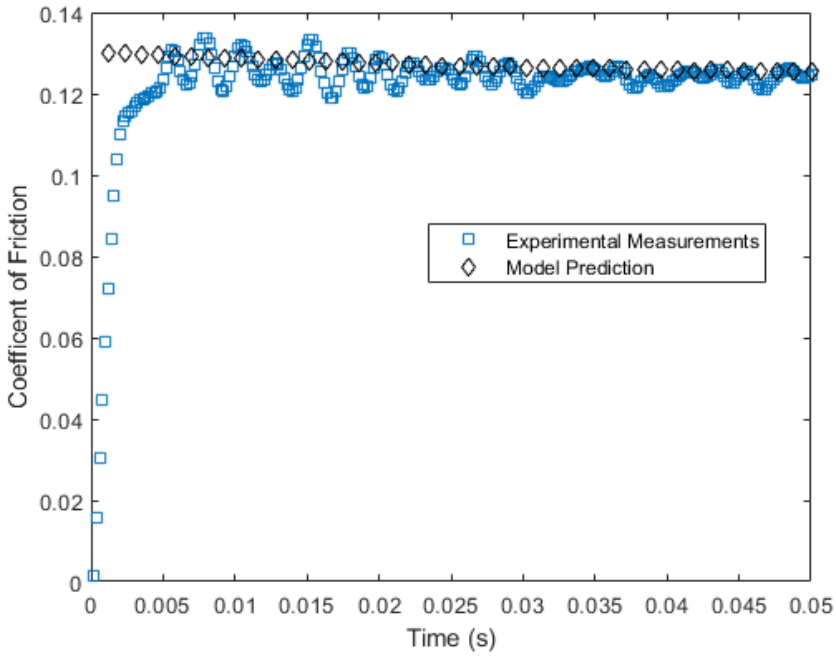

Figure 7.17: Model Comparison to Experiment using Equation 3.54, Average Sliding Speed 0.3 m/s, Temperature 80 °C, Applied Load 150 N

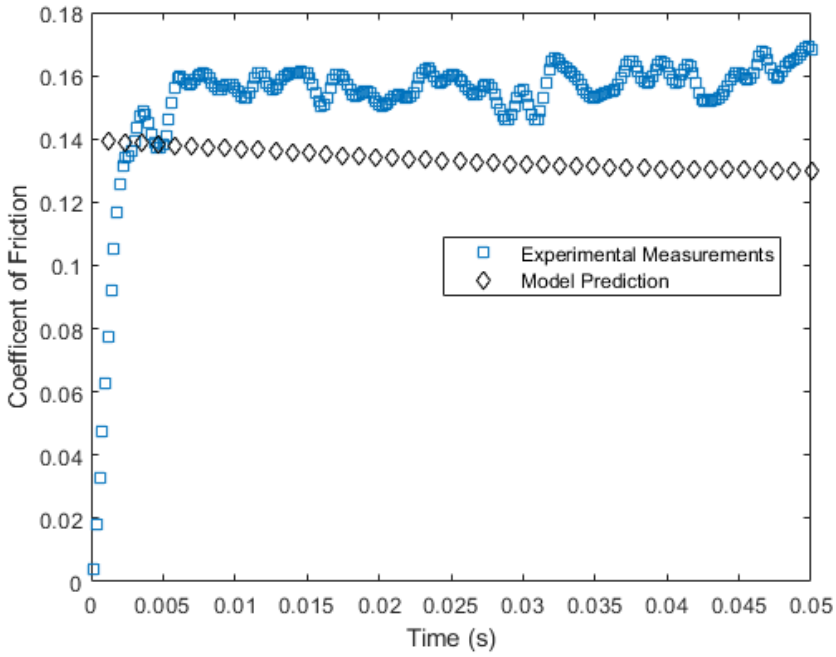

Figure 7.18: Model Comparison to Experiment using Equation 3.54, Average Sliding Speed 0.3 m/s, Temperature 120 °C, Applied Load 50 N

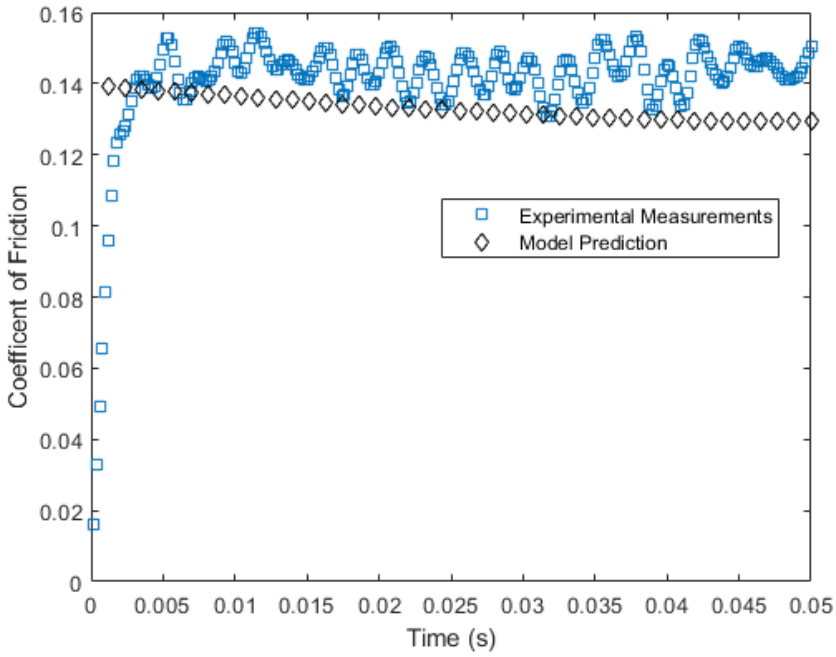

Figure 7.19: Model Comparison to Experiment using Equation 3.54, Average Sliding Speed 0.3 m/s, Temperature 80 °C, Applied Load 50 N

The model also provides a close match for a 150 N load, but it underestimates the friction coefficient for a 50 N load. Because of those problems, two new models were proposed for the contact friction coefficient based off Equation 3.54.

$$\mu = \mu_{\max} - \mathrm{e}^{0.085 F_n^*} \tag{7.1}$$

$$\mu = \mu_{\max} - 0.085 (F_n^*)^{0.72} \tag{7.2}$$

For these equations, μ_{max} was set to be 0.155. Table 7.1 summarizes their predicted friction coefficients.

Table 7.1: Model Predicted Average Friction Coefficients, Average Sliding Speed 0.3 m/s, Temperature 80 °C

Dry Friction Coefficient Calculated Using	Predicted Friction Coefficient with a 50 N Load	Predicted Friction Coefficient with a 150 N Load
Equation 7.1	0.1471	0.1492
Equation 7.2	0.1382	0.1295

Based on these results, Equation 7.1 was discarded. The results using Equation 7.2 were compared to the measurements (see Table 7.2 and Figure 7.20 below).

Table 7.2: Measured and Predicted Average Friction Coefficients, Average Sliding Speed 0.3 m/s, Temperature 80 °C Using Equation 7.2

	50 N	**100 N**	**150 N**
Experiments	0.1464	0.1282	0.1227
Model	0.1382	0.1341	0.1295
Percent Error	5.9	-4.4	-5.3

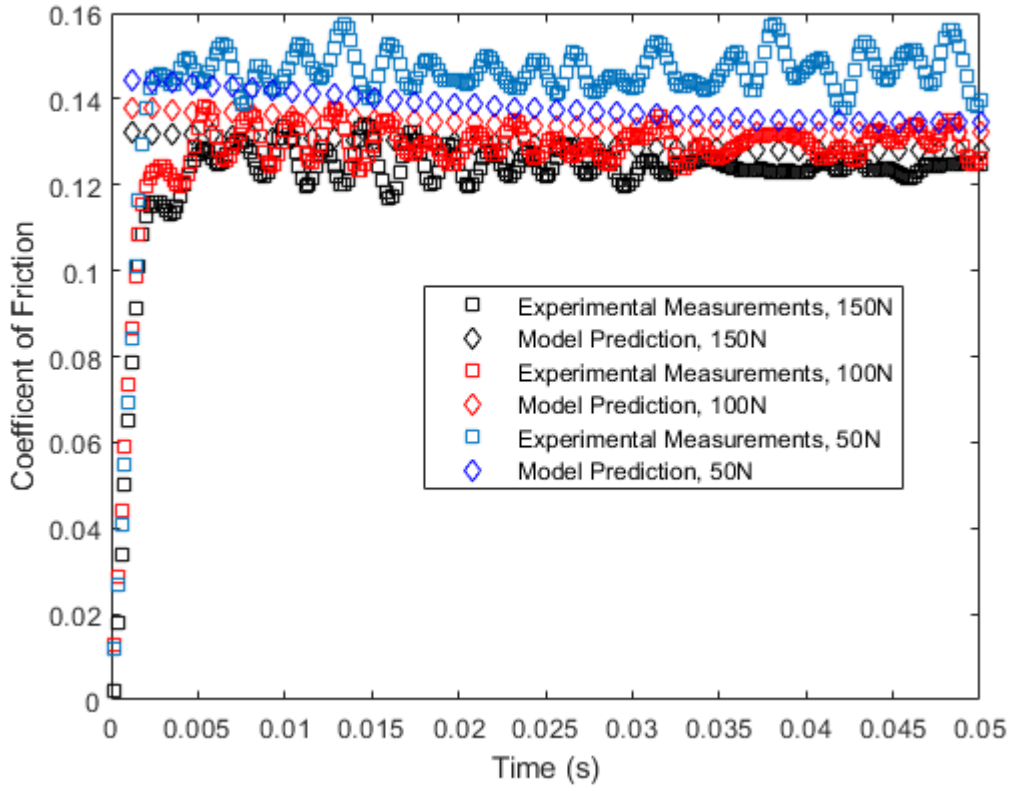

Figure 7.20: Model Comparison to Experiment using Equation 7.2, Average Sliding Speed 0.3 m/s, Temperature 80 °C

The model predicted a larger drop in friction coefficient that what was observed. A new model was proposed after fitting the average friction coefficient to the average contact pressure for the given loads. This would become the basis off which only minor variations would be made (Equation 3.55). Once again, the model predictions were compared to the measured values (see Figure 7.21).

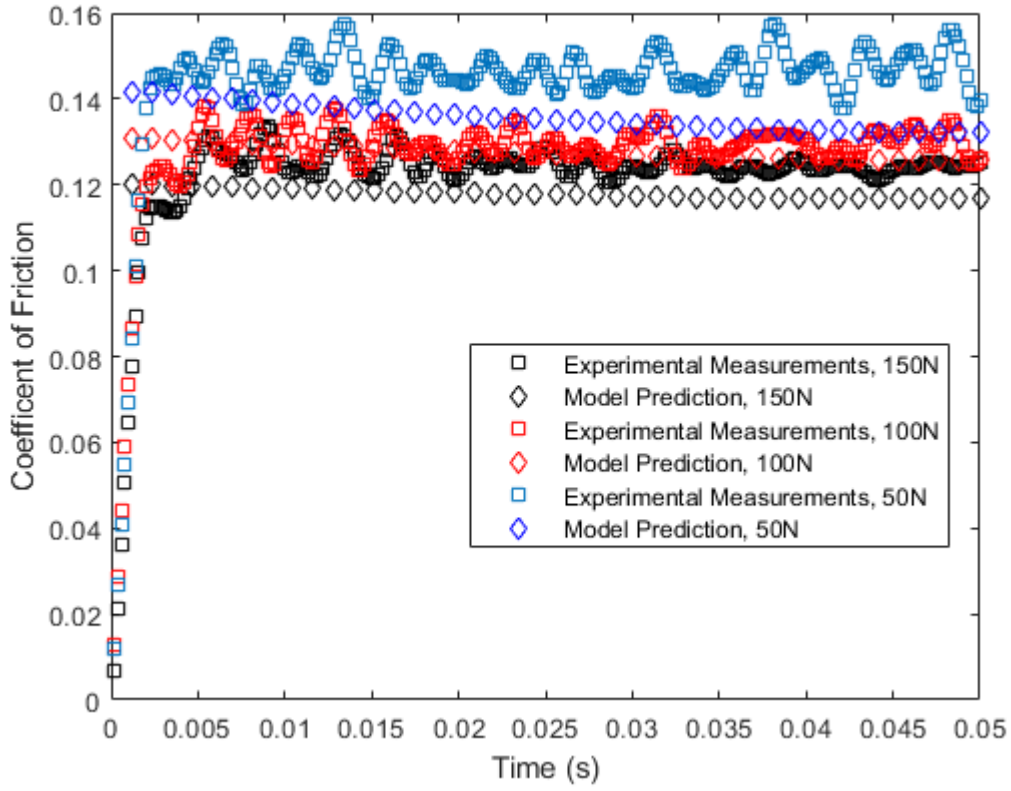

Figure 7.21: Model Comparison to Experiment using Equation 3.55, Average Sliding Speed 0.3 m/s, Temperature 80 °C

While the model underestimates the friction coefficient, that could be remedied by increasing μ_{max} to 0.1565. While this would result in a close fit for a single temperature, it needed to work well for other temperatures as well.

CHAPTER 8

INCORPORATING FLASH TEMPERATURE ADJUSTMENTS

Due to the high friction coefficients observed, a significant amount of heat is generated by the sliding piston ring. This heat can appreciably increase the temperature of the lubricant and decrease its viscosity. Flash temperature theory has been known for thousands of years, but only in the last century has it become a major factor in designing machinery [106]. With the addition of temperature changes to the model, the flowchart (Figure 4.1) describing the process needs to be revised. Figure 8.1 depicts the revised flowchart that now accounts for temperature changes.

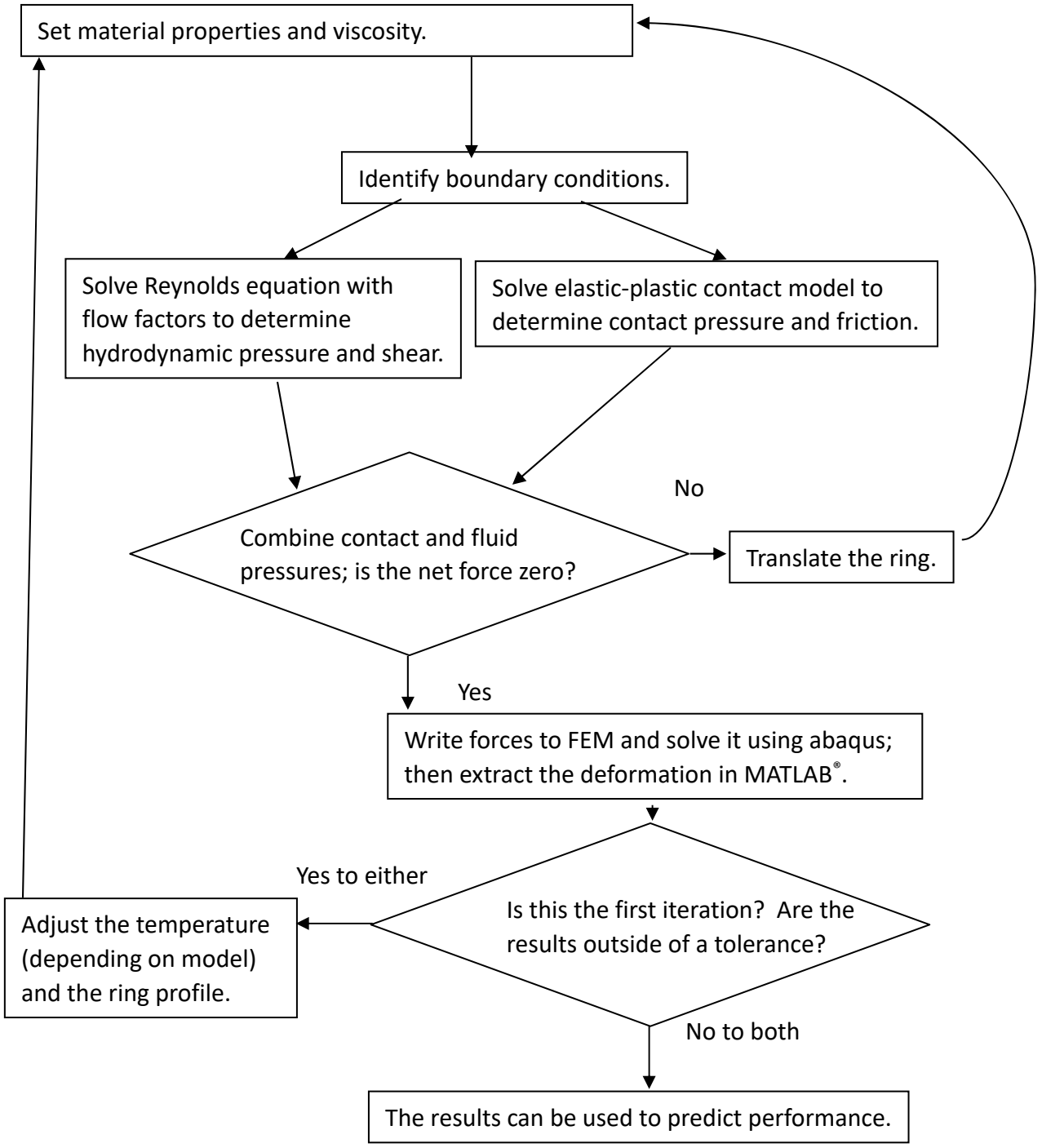

Figure 8.1: Revised Model Flowchart That Accounts for Temperature Changes

There were some early problems trying to implement the flash temperature adjustments. For a 100 N load, the model predicted an average friction coefficient of 0.135, but it also predicted a temperature increase of 2270 K at a single asperity. Below is the sample calculation using Equation 3.62 that resulted in such a high prediction.

$$T - T_0 = \frac{100\text{ N}\left(0.471\text{ m/s}\right)\left(0.156\right)}{4.56\left(1.6\times10^{-5}\text{ m}\right)\left(46.4\ \frac{W}{m^2}\right)\sqrt{0.66+0.255}} = \frac{7.35}{0.00324}\text{ or } 2270\text{ K}$$

It was assumed that all of the heat was transferred to the ring. The model was quickly revised to account for heat transfer to both the ring and the liner. A retest still found the predicted temperature to be unreasonably high as shown in Figure 8.2.

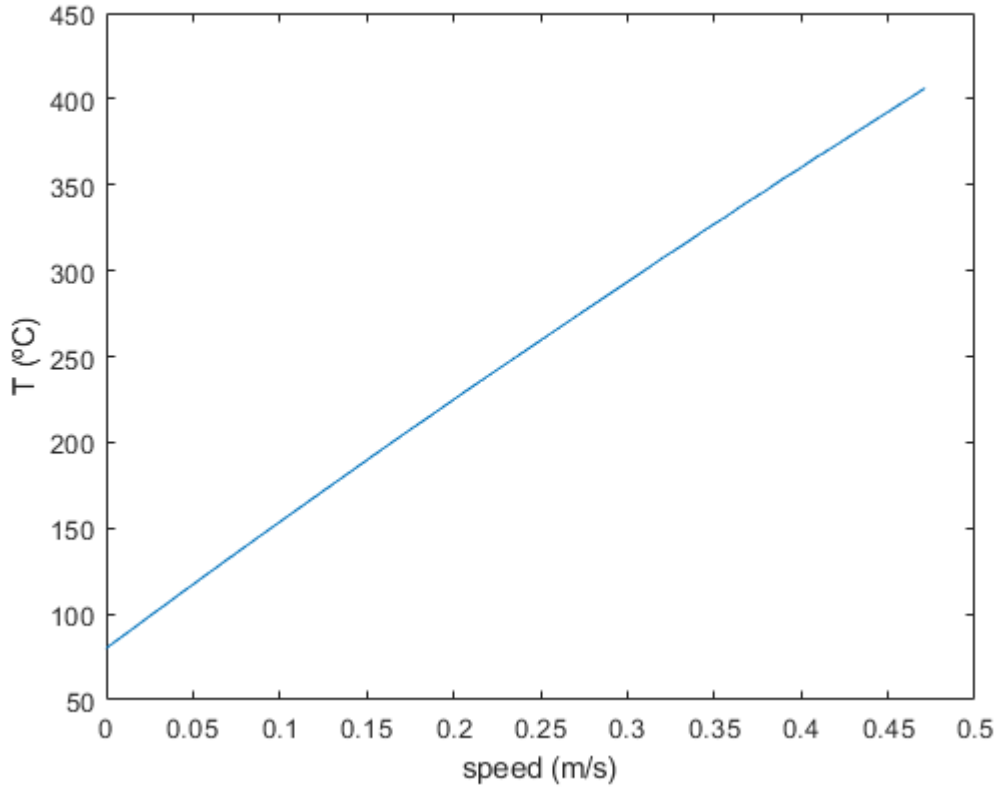

Figure 8.2: Flash Temperature Prediction, Average Sliding Speed 0.3 m/s, Base Temperature 80 °C, Applied Load 100 N

The final predicted temperature is well beyond the upper limit at which lubricant properties were given. While even higher flash temperatures were observed by Suzuki and Kennedy [107], they only considered the unlubricated contact of a sapphire slider and a thin film magnetic disk. In either case, the model would have to be substantially revised to accommodate heat flowing away from the contact points. It was quickly discovered that the load was distributed over several asperities, but the contact area only reflected a single asperity. Figure 8.3 shows the model's predicted temperature increase

using Equation 3.65 for 2 different loads when the contact area was expanded to match the FEM's mesh size.

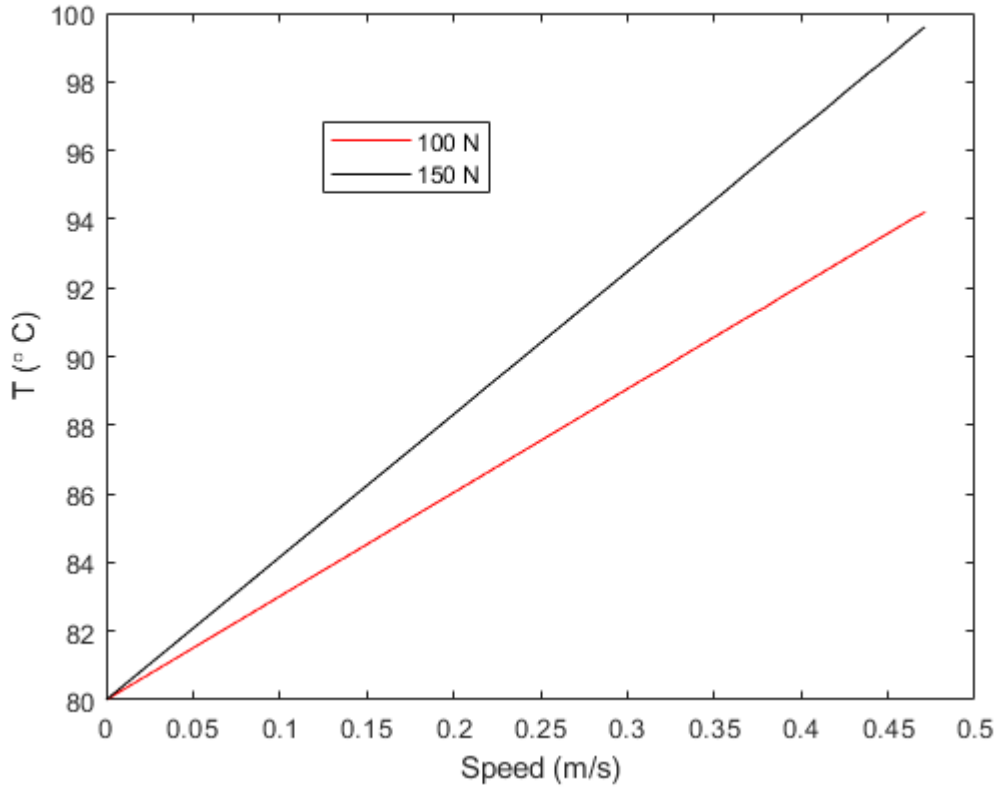

Figure 8.3: Flash Temperature Prediction, Average Sliding Speed 0.3 m/s, Base Temperature 80 °C

Note that the temperature increased more for the higher load because the frictional force was higher. Figure 8.4 shows the model's predicted friction coefficient after accounting for frictional heating (which decreases lubricant viscosity) compared to the measurements.

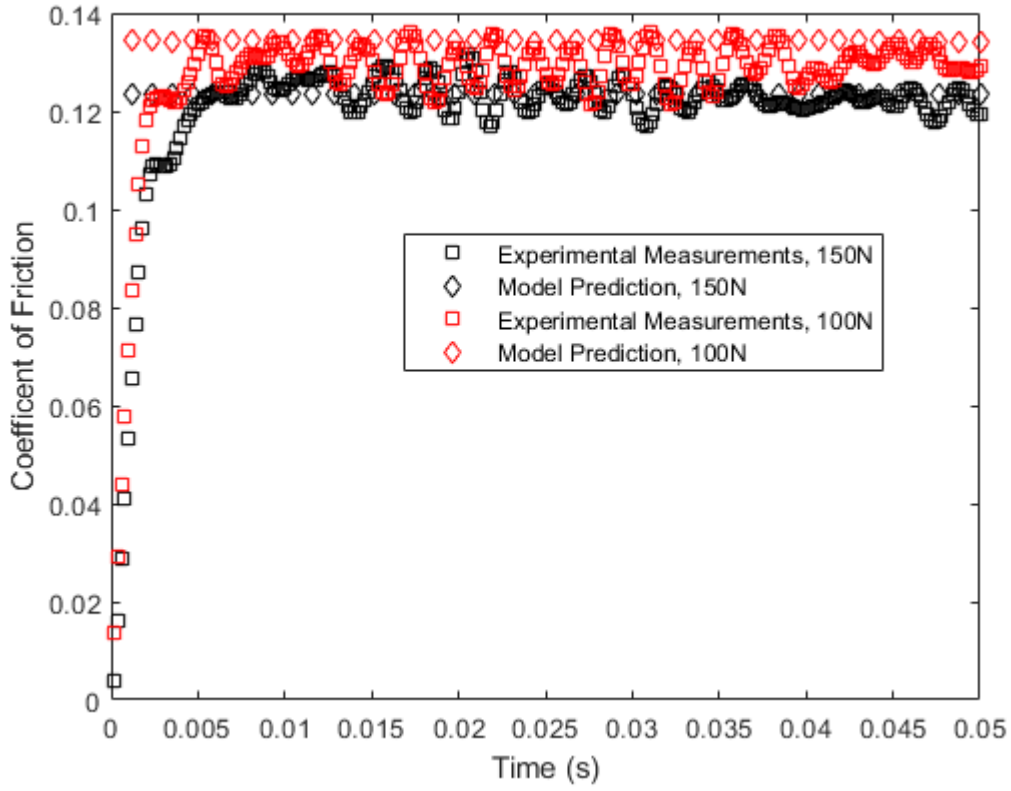

Figure 8.3: Model Comparisons to Experiments Flash Temperature Adjustment, Average Sliding Speed 0.3 m/s, Base Temperature 80 °C

While the model's predicted friction coefficient very closely matched the experiments, it was found that the flash temperature adjustments did not change the model predictions by a significant amount. Figure 8.4 shows the differences in predicted friction coefficient with the previous version of the model which predicted a negligible temperature increase.

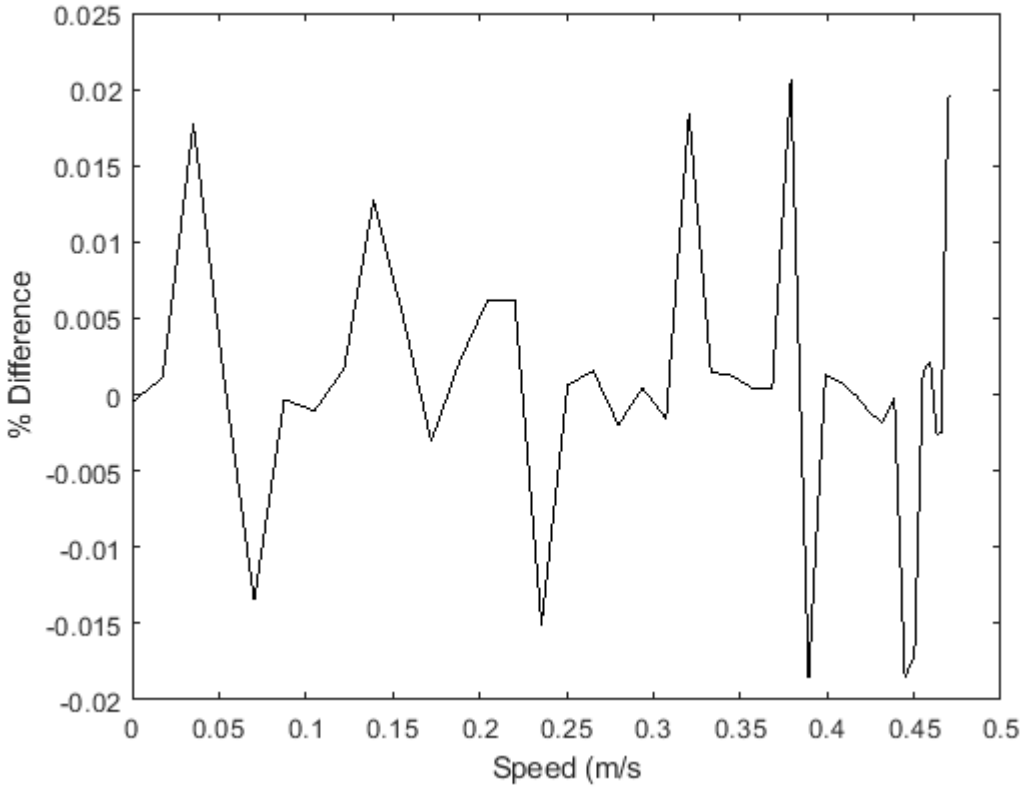

Figure 8.4: Percent Difference in Predicted Friction Coefficient When Flash Temperatures Were Incorporated for the First Time

Since changing the temperature did not really affect the results, it was decided to take a second look at the shear thinning model. A typo was found in the iterative calculation of viscosity, and it was discovered that the results of a least squares regression being performed were nowhere close to the actual curve. Figure 8.5 illustrates how erroneous the shear thinning fit was.

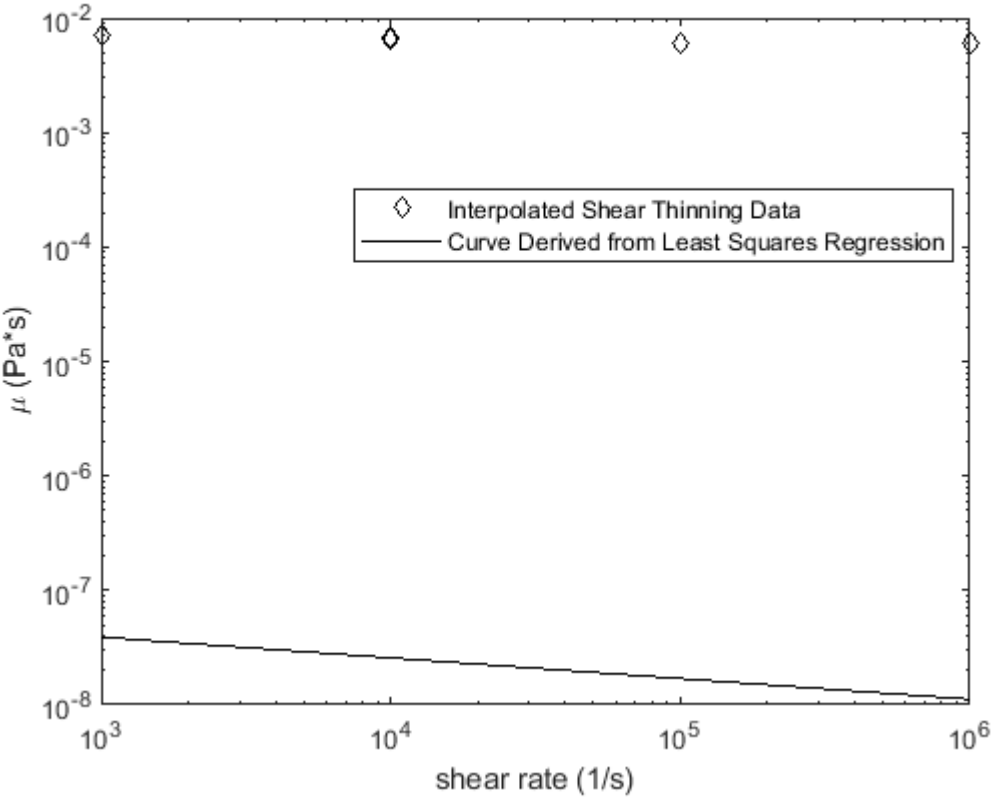

Figure 8.5: First Attempt at a Shear Thinning Fit, Base Temperature 80 °C

An attempt was made to perform a least squares regression that calculated G, n and μ_2, but this also failed. Several proposed curve fits were generated assuming $\mu_2 = 0$ in Equation 3.48. Figures 8.6 and 8.7 and Tables 8.1-8.2 summarize their results.

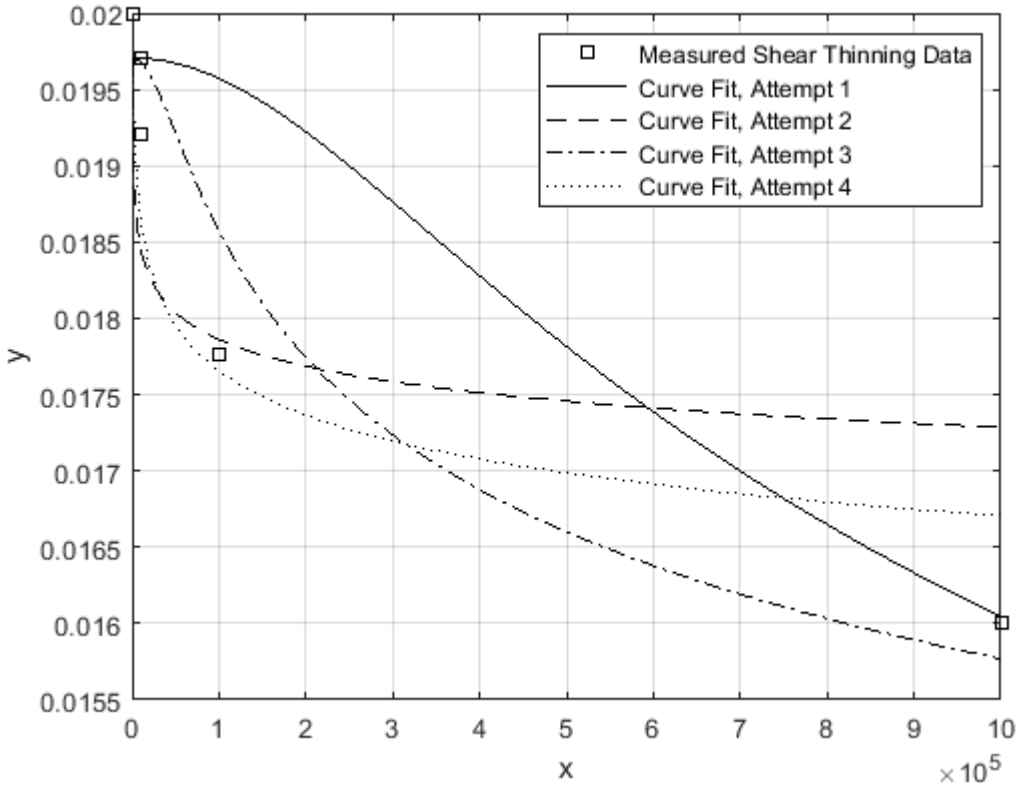

Figure 8.6: Attempts at a Shear Thinning Fit to Equation 3.48, Base Temperature 60 °C

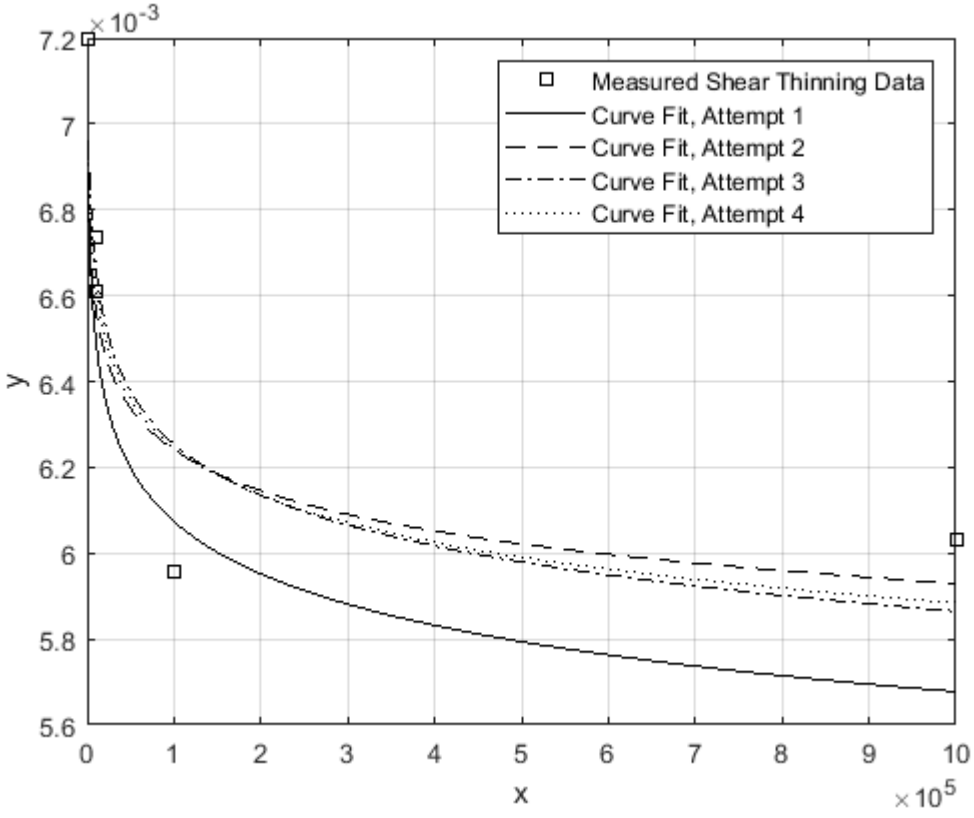

Figure 8.7: Attempts at a Shear Thinning Fit to Equation 3.48, Base Temperature 100 °C

Table 8.1: Results of Shear Thinning Fits to Equation 3.48 at 60 °C

Attempt	Initial Guess for *G* (Pa)	Initial guess for *n*	*G* (Pa)	*n*
1	0.323	0.506	7286	-0.097
2	1	-0.4	1.964	-0.0071
3	1000	-0.4	999.8	-0.037
4	20	-0.4	20.31	-0.012
5	300	-0.4	299	-0.0254

Table 8.2: Results of Shear Thinning Fits to Equation 3.48 at 100 °C

Attempt	Initial Guess for *G* (Pa)	Initial guess for *n*	*G* (Pa)	*n*
1	0.755	0.01	6.854	-0.0157
2	0.755	-0.01	5.19	-0.0124
3	10	-0.01	18.71	-0.0156
4	10	-0.4	10.32	-0.0139

While better than the least squares regression fit used previously, most of the shear thinning fits still did not accurately capture the trend of the measured values. Attempt 5 for a temperature of 60 °C worked very well, however (Figure 3.2). With the revised shear thinning fit in place, the model could now be properly run with the flash

temperature adjustment. Figures 8.8 and 8.9 show how the model compares to the experiments with and without the flash temperature adjustment.

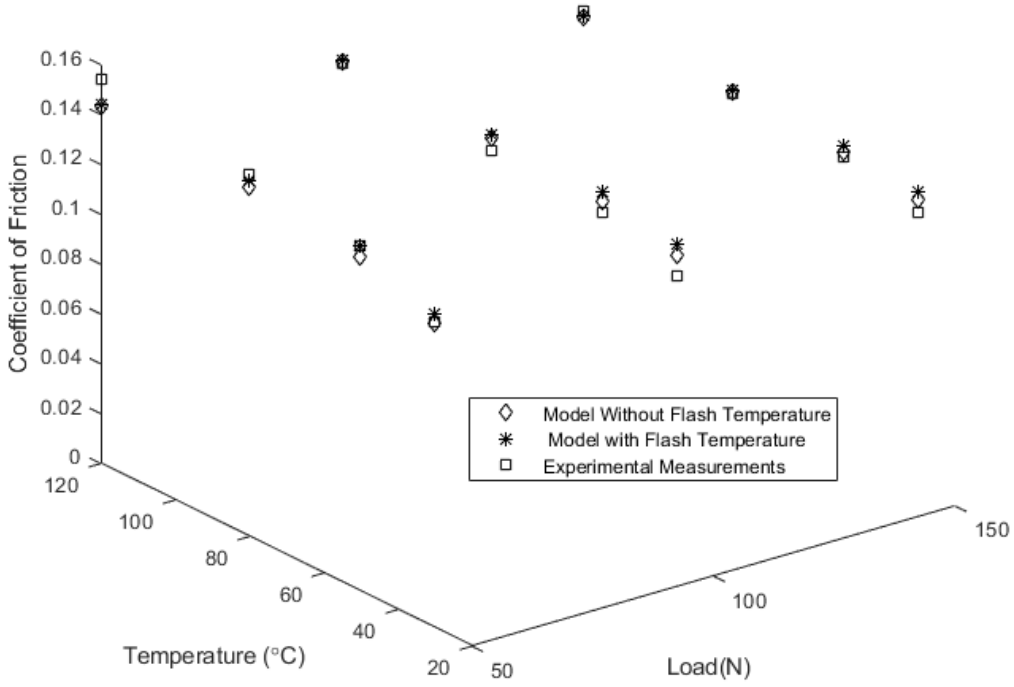

Figure 8.8: Overall Model Comparisons to Experiments, Average Speed 0.3 m/s

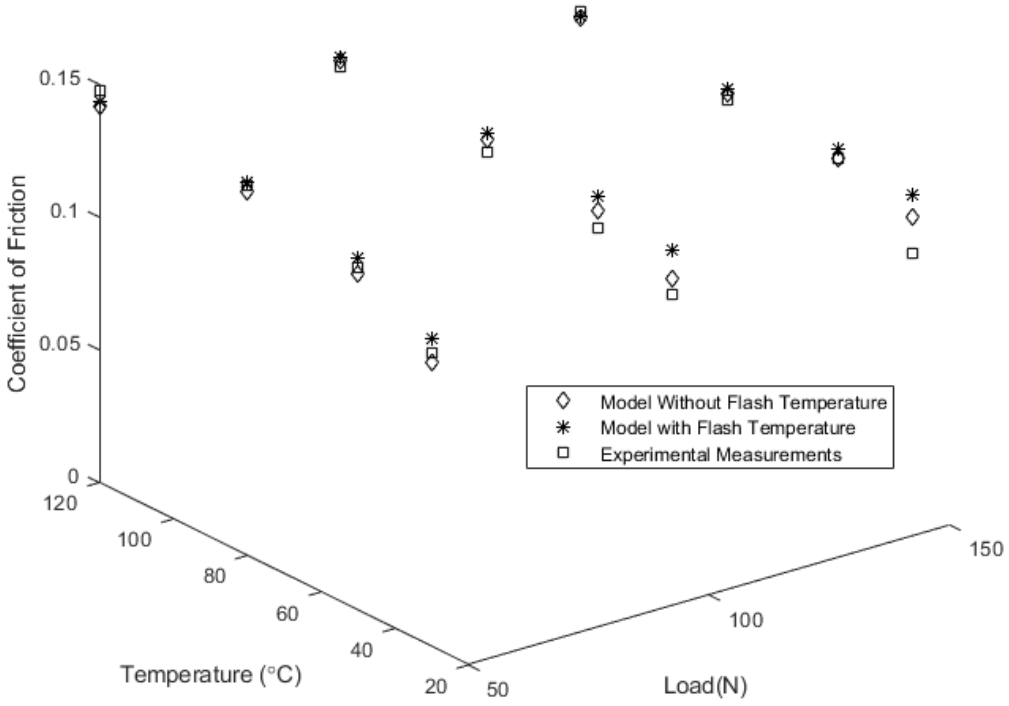

Figure 8.9: Overall Model Comparisons to Experiments, Average Speed 0.6 m/s

The overall average model error is shown in Table 8.3.

Table 8.3: Average RMS Error of Models Compared to Experiment

Average Speed (m/s)	0.3	0.6
No Flash Temperature Adjustment	0.00149	0.00114
Flash Temperature Adjustment	0.00182	0.00215

Based on the results it seems as though the flash temperature model predicts a larger friction coefficient on average relative to the experiments for most of the cases considered and that the adjustments decrease the model's overall accuracy. One element that it did not incorporate was the reduction in metals' yield strength as the temperature increases modeled by Johnson and Cook [108]. This would result in the surfaces becoming more liquid-like and less resistant to flow, meaning that the predicted dry friction coefficient would decrease. It was proposed that another adjustment could be made to the flash temperature model. The dry friction coefficient is modified based on the melting temperature of the contacting solid:

$$\mu = \mu_0 \left(1 - T^*\right) \tag{8.1}$$

$$T^* = \frac{T - T_{room}}{T_m - T_{room}} \tag{8.2}$$

T_m is the melting point, while the room temperature T_{room} was taken to be 20 °C. The friction coefficient predicted by the previous model is μ_0.

The model was rerun with these adjustments. Figures 8.10-8.33 show the models comparisons for each speed/temperature/load combination, while Figures 8.34-8.35 show the overall comparisons.

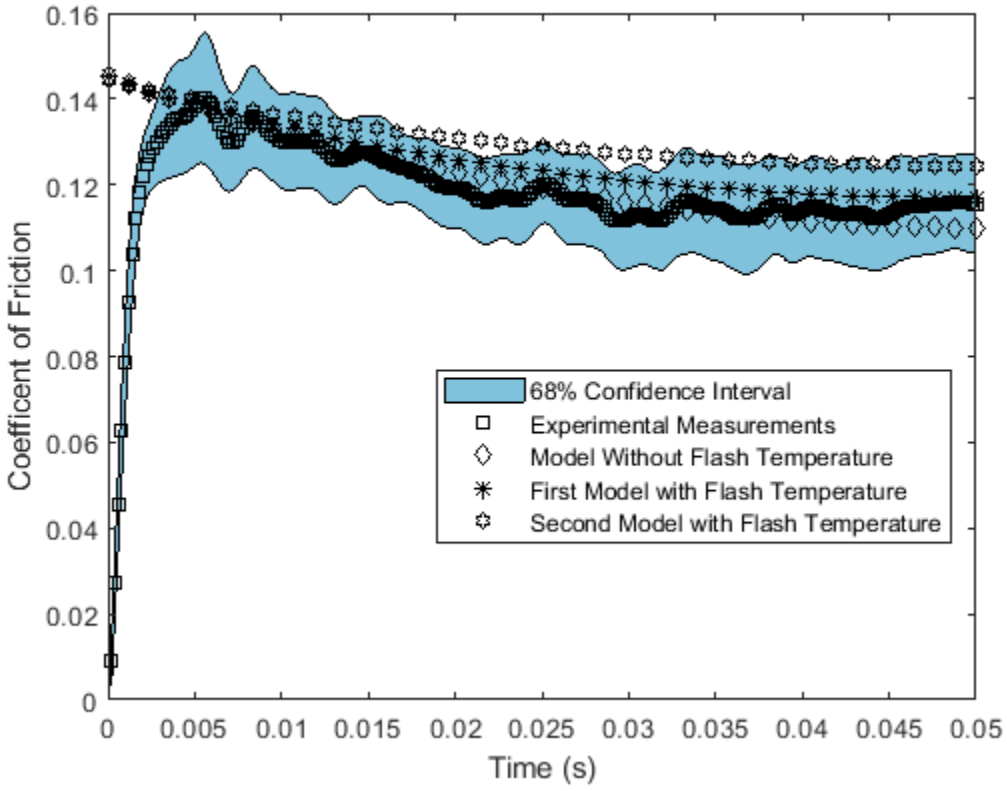

Figure 8.10: Model Comparisons to Experiments, Average Speed 0.3 m/s, Base Temperature 30 °C, 50 N Load

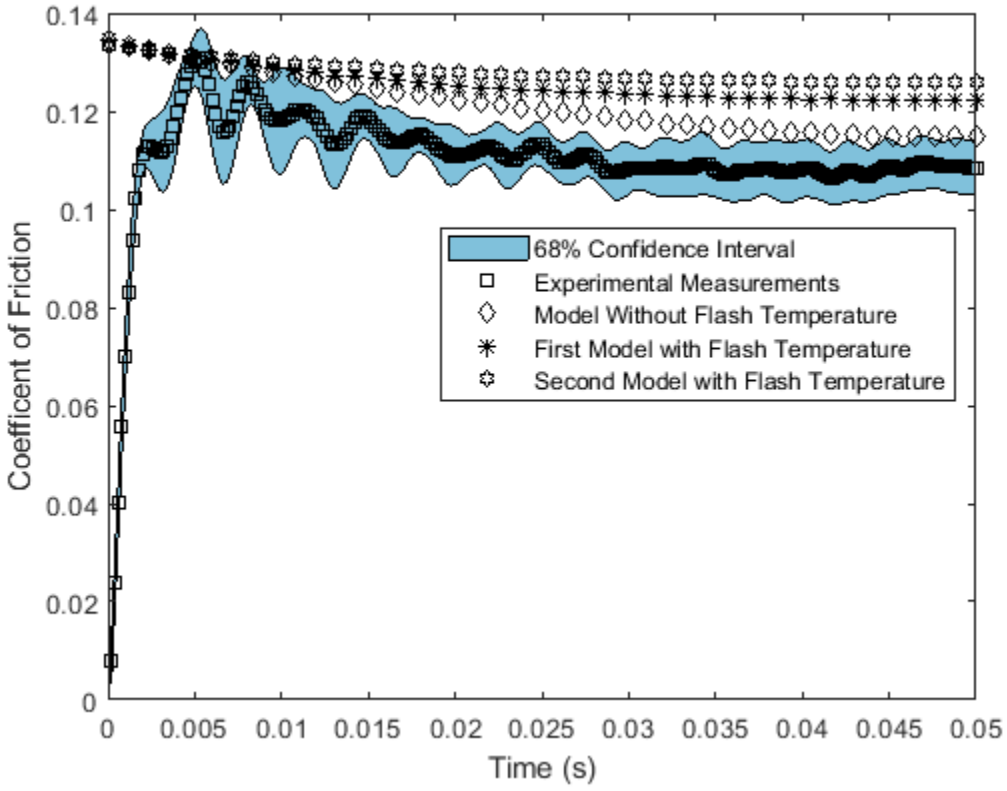

Figure 8.11: Model Comparisons to Experiments, Average Speed 0.3 m/s, Base Temperature 30 °C, 100 N Load

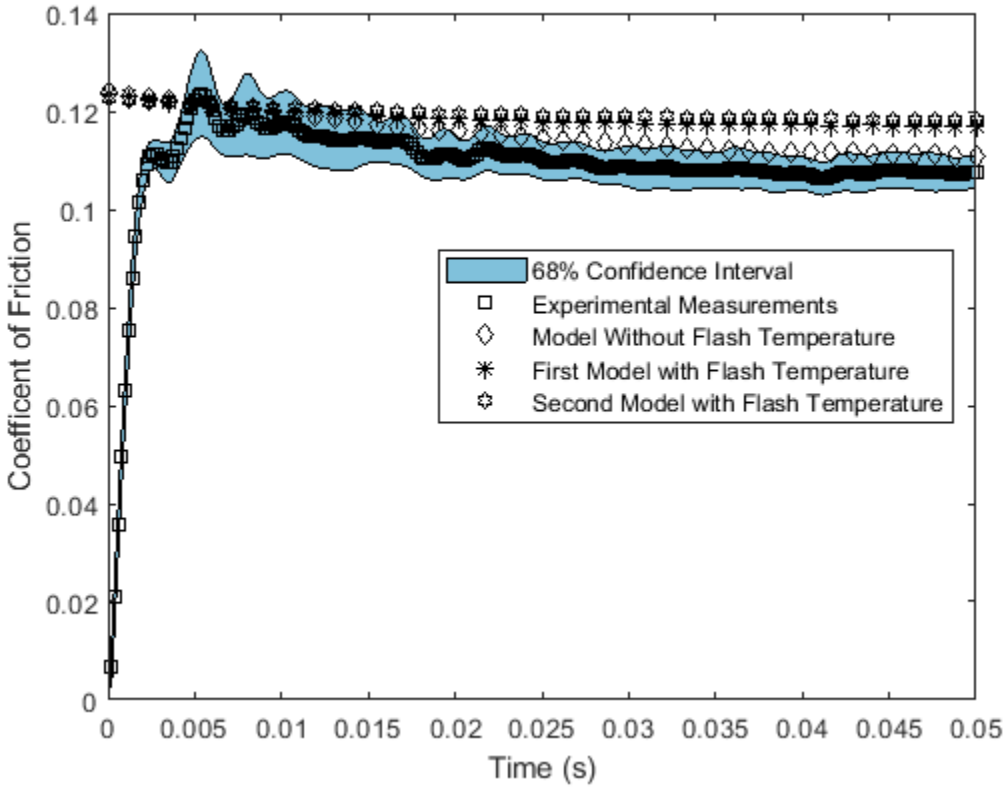

Figure 8.12: Model Comparisons to Experiments, Average Speed 0.3 m/s, Base Temperature 30 °C, 150 N Load

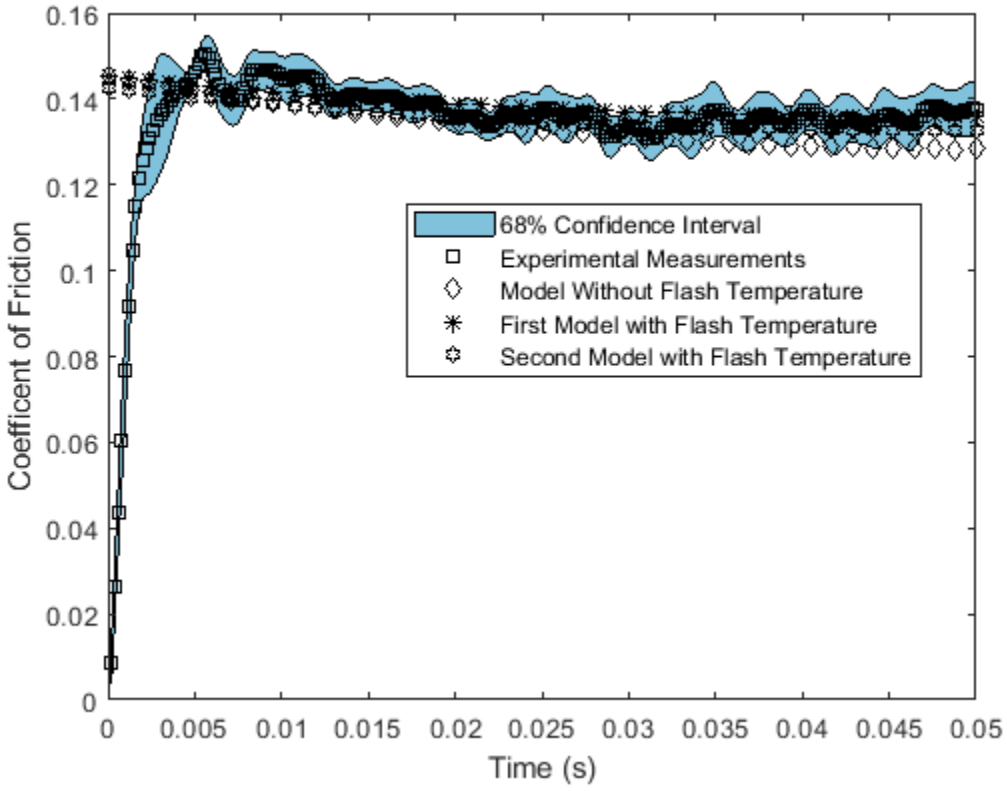

Figure 8.13: Model Comparisons to Experiments, Average Speed 0.3 m/s, Base Temperature 50 °C, 50 N Load

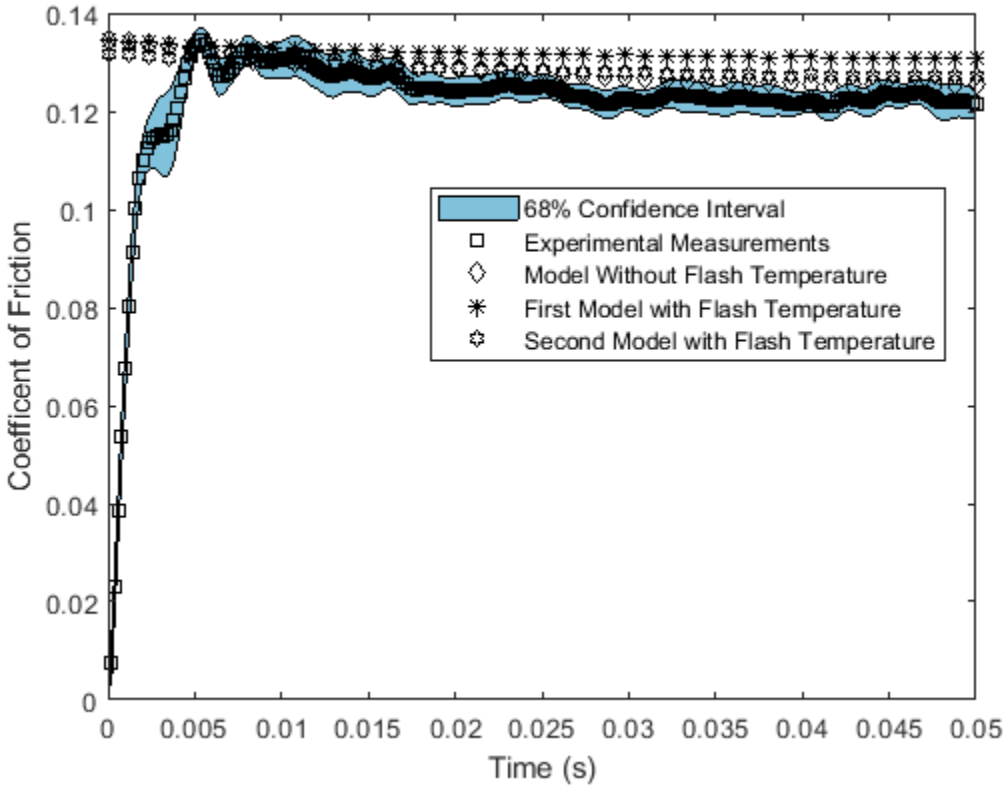

Figure 8.14: Model Comparisons to Experiments, Average Speed 0.3 m/s, Base Temperature 50 °C, 100 N Load

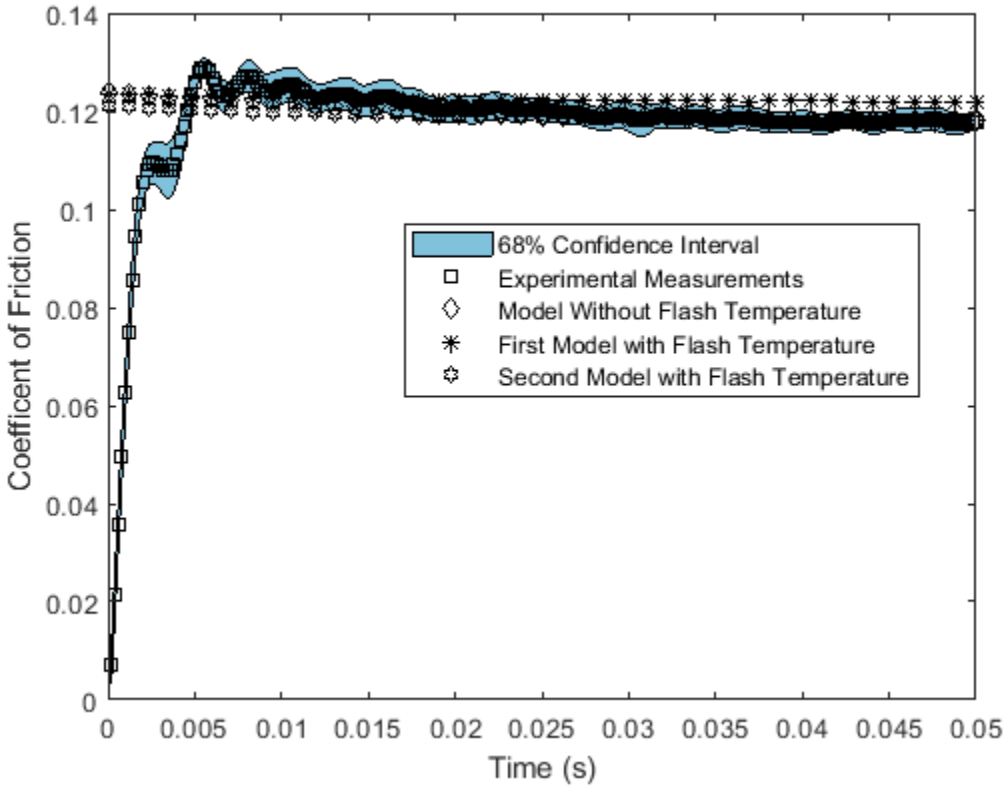

Figure 8.15: Model Comparisons to Experiments, Average Speed 0.3 m/s, Base Temperature 50 °C, 150 N Load

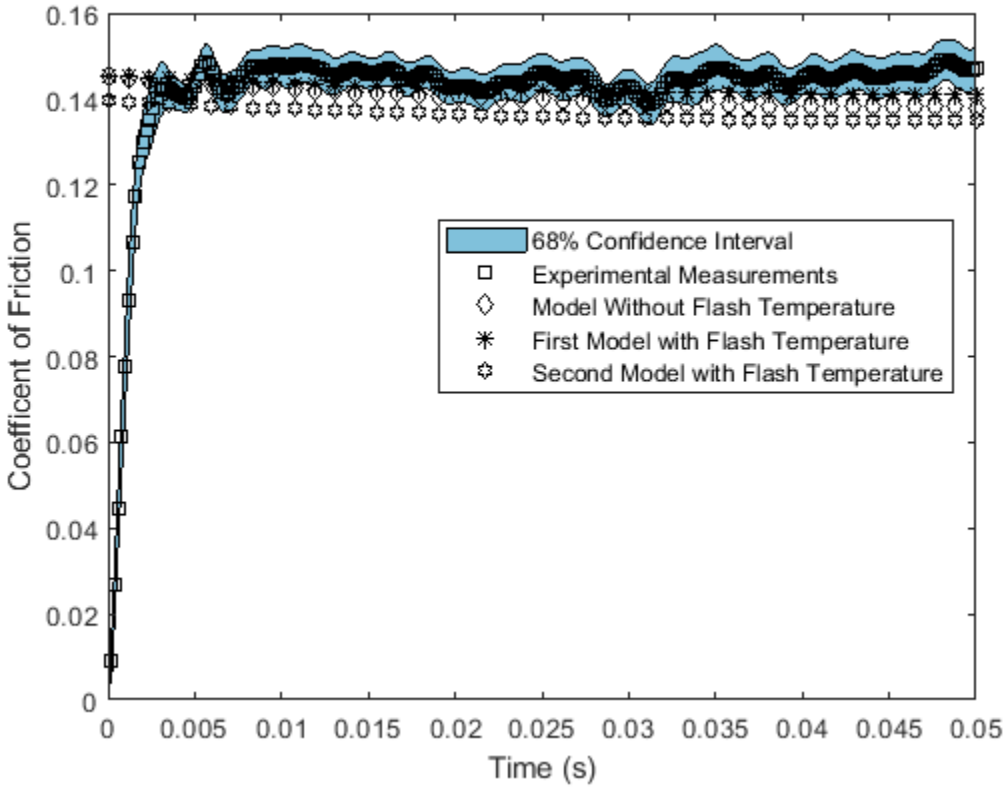

Figure 8.16: Model Comparisons to Experiments, Average Speed 0.3 m/s, Base Temperature 80 °C, 50 N Load

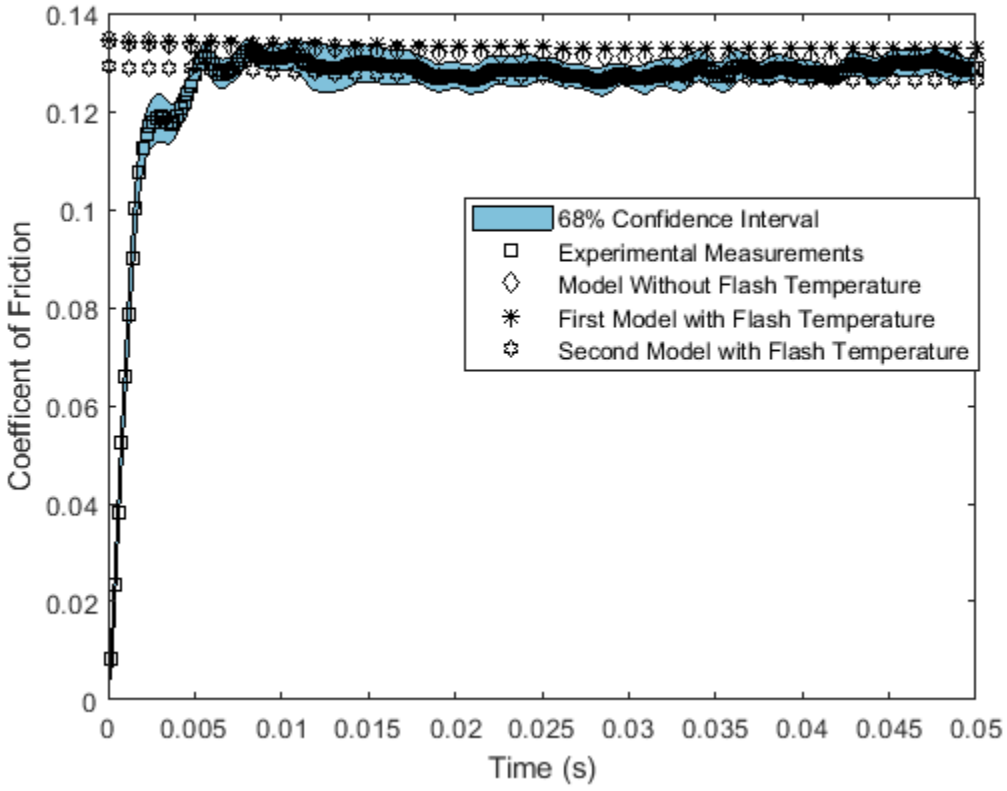

Figure 8.17: Model Comparisons to Experiments, Average Speed 0.3 m/s, Base Temperature 80 °C, 100 N Load

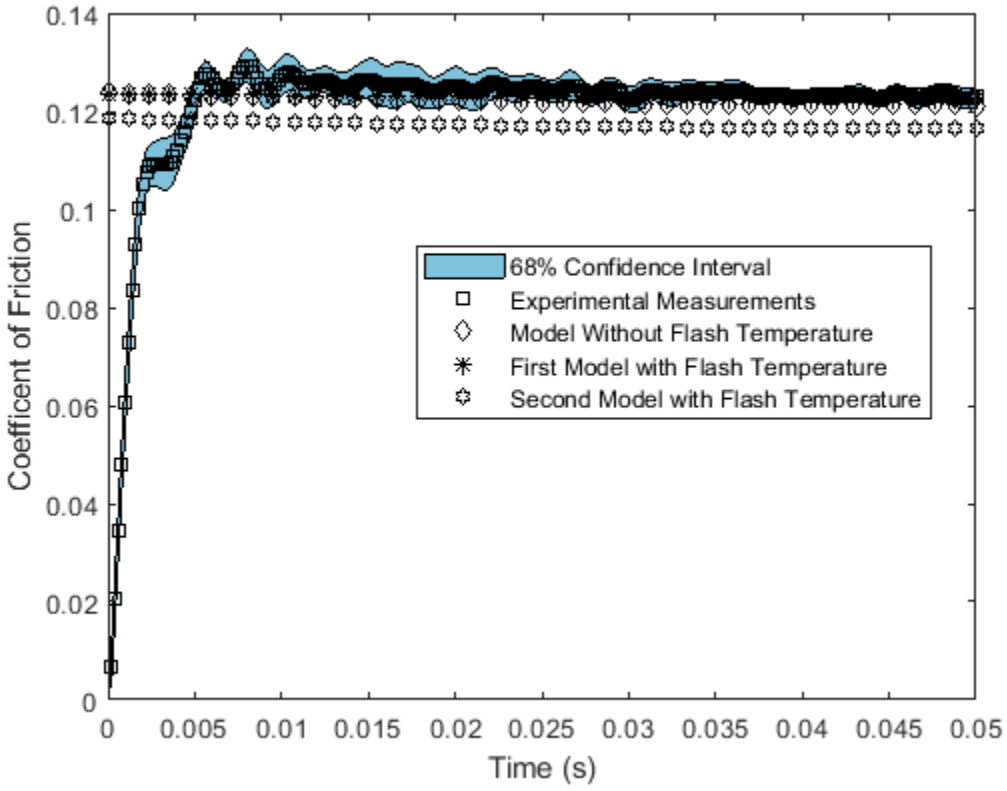

Figure 8.18: Model Comparisons to Experiments, Average Speed 0.3 m/s, Base Temperature 80 °C, 150 N Load

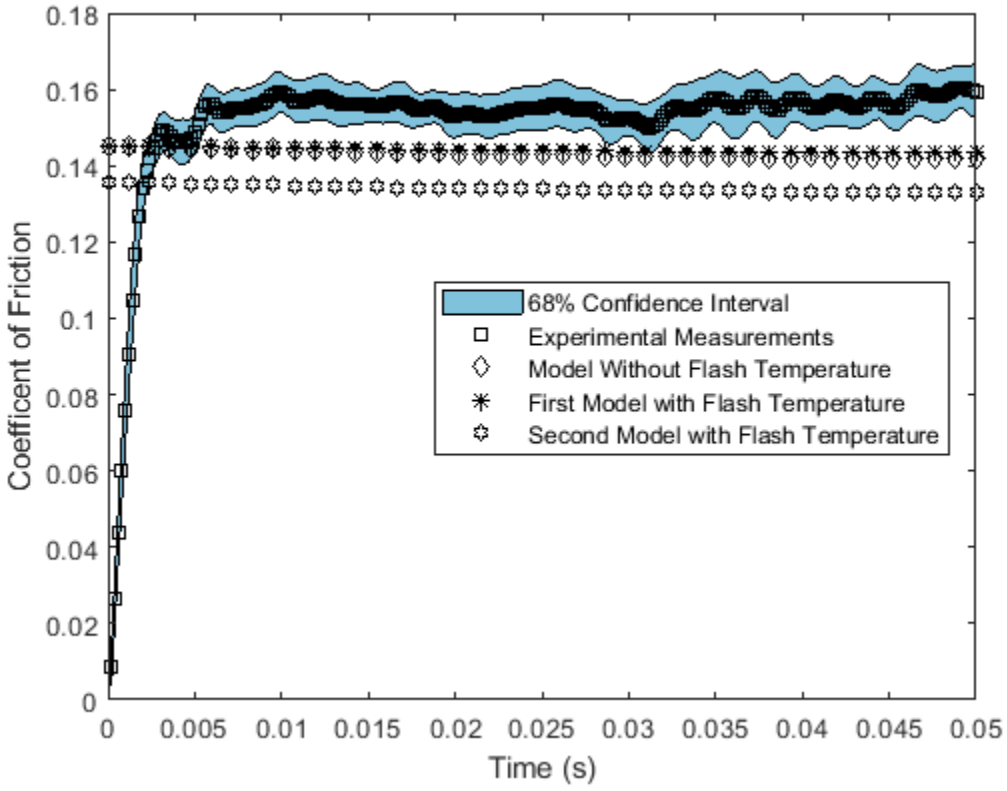

Figure 8.19: Model Comparisons to Experiments, Average Speed 0.3 m/s, Base Temperature 120 °C, 50 N Load

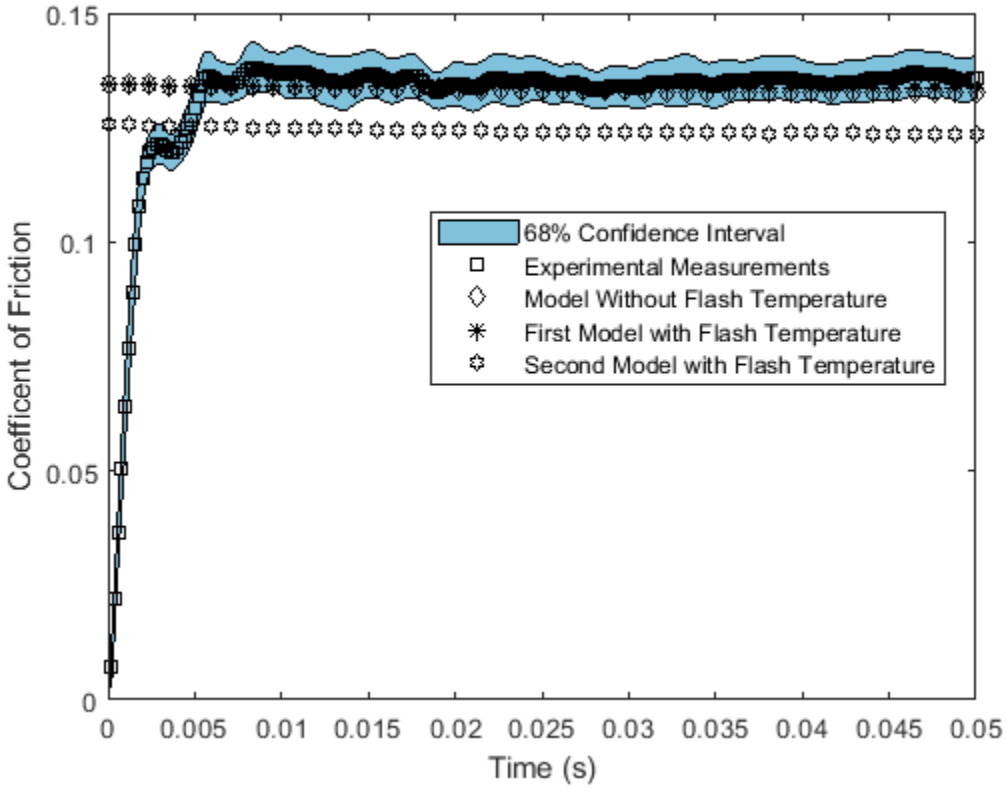

Figure 8.20: Model Comparisons to Experiments, Average Speed 0.3 m/s, Base Temperature 120 °C, 100 N Load

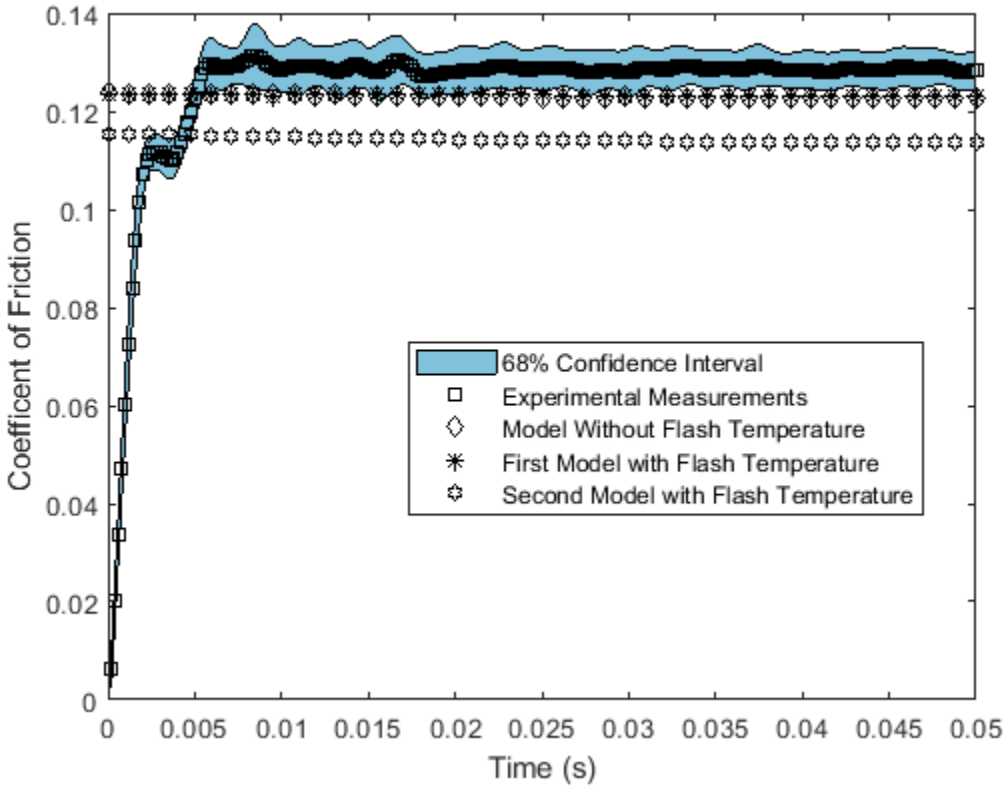

Figure 8.21: Model Comparisons to Experiments, Average Speed 0.3 m/s, Base Temperature 120 °C, 150 N Load

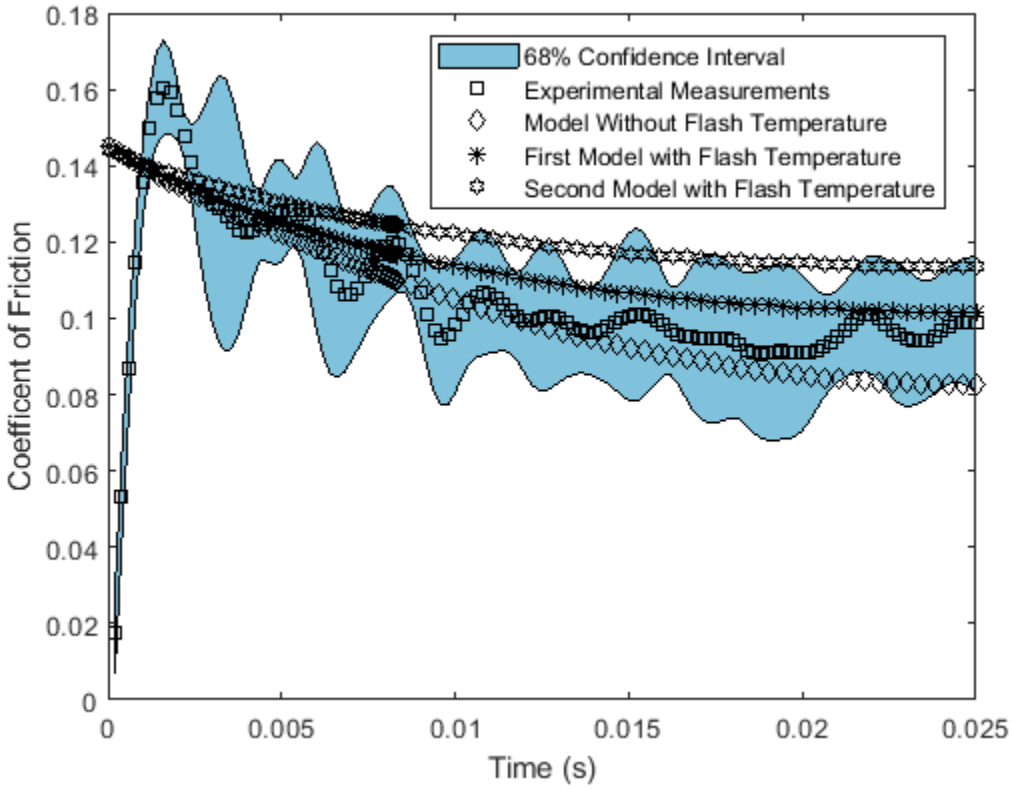

Figure 8.22: Model Comparisons to Experiments, Average Speed 0.6 m/s, Base Temperature 30 °C, 50 N Load

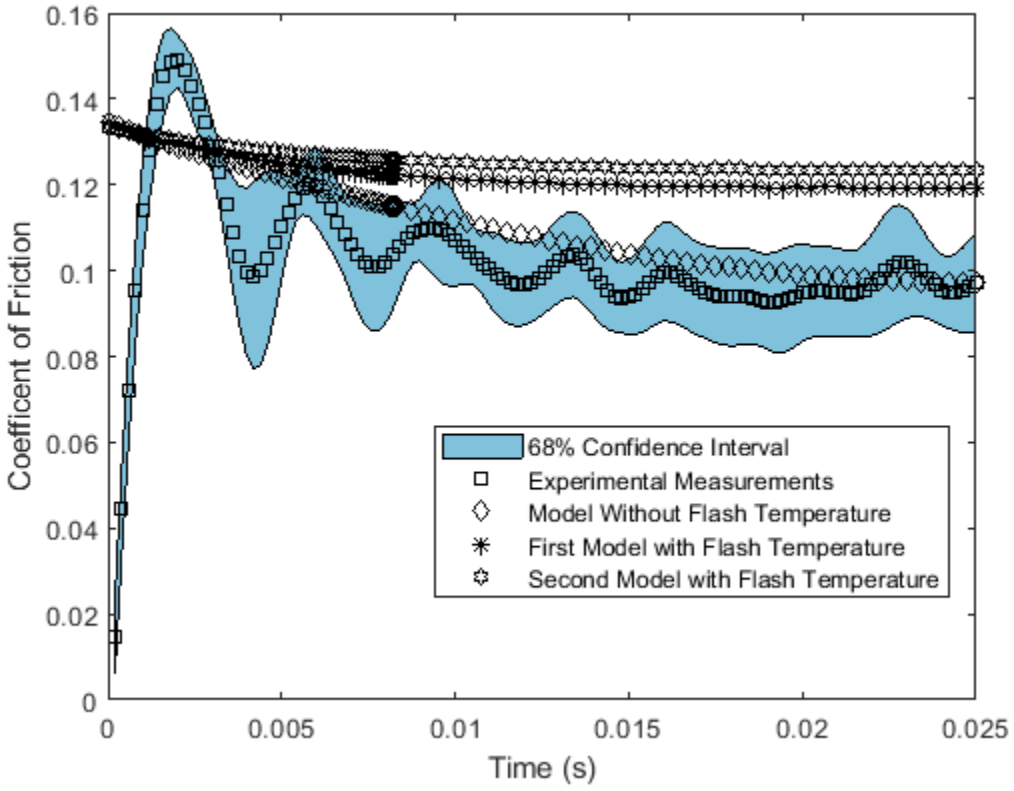

Figure 8.23: Model Comparisons to Experiments, Average Speed 0.6 m/s, Base Temperature 30 °C, 100 N Load

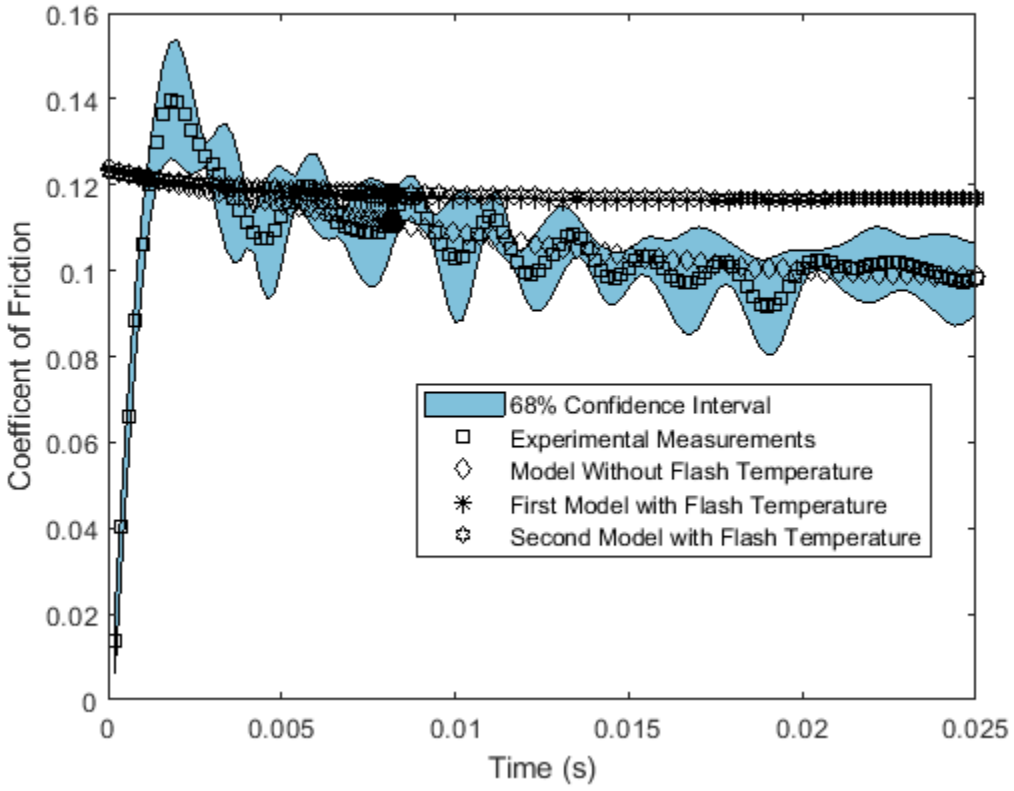

Figure 8.24: Model Comparisons to Experiments, Average Speed 0.6 m/s, Base Temperature 30 °C, 150 N Load

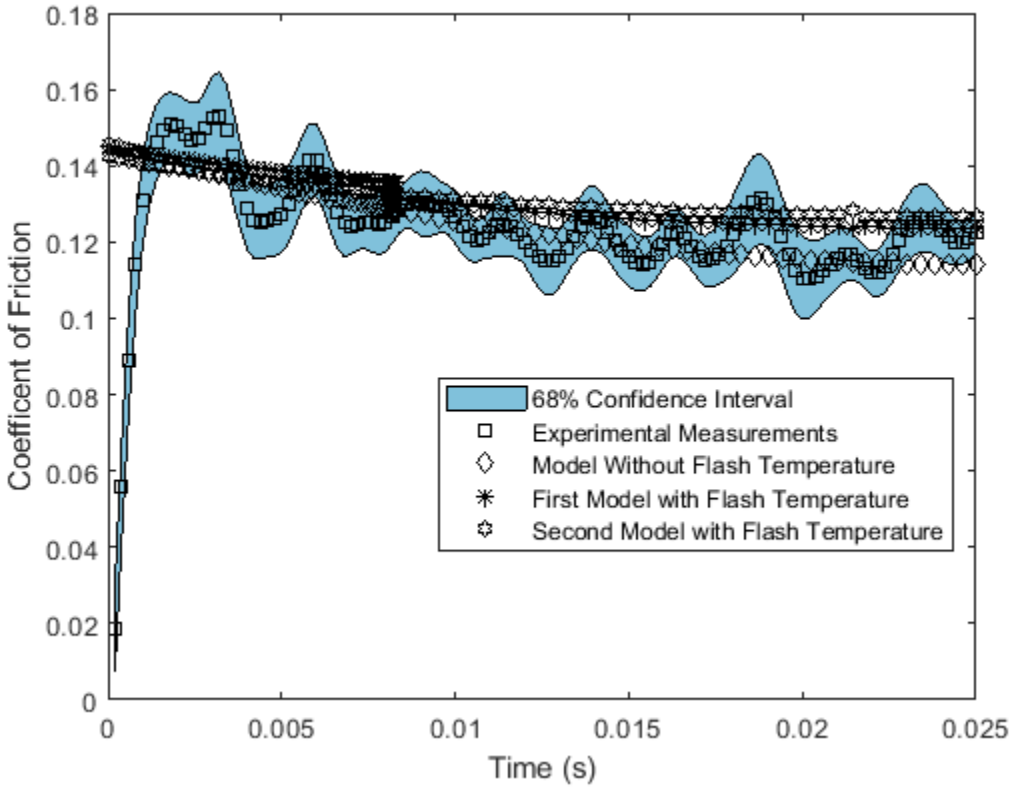

Figure 8.25: Model Comparisons to Experiments, Average Speed 0.6 m/s, Base Temperature 50 °C, 50 N Load

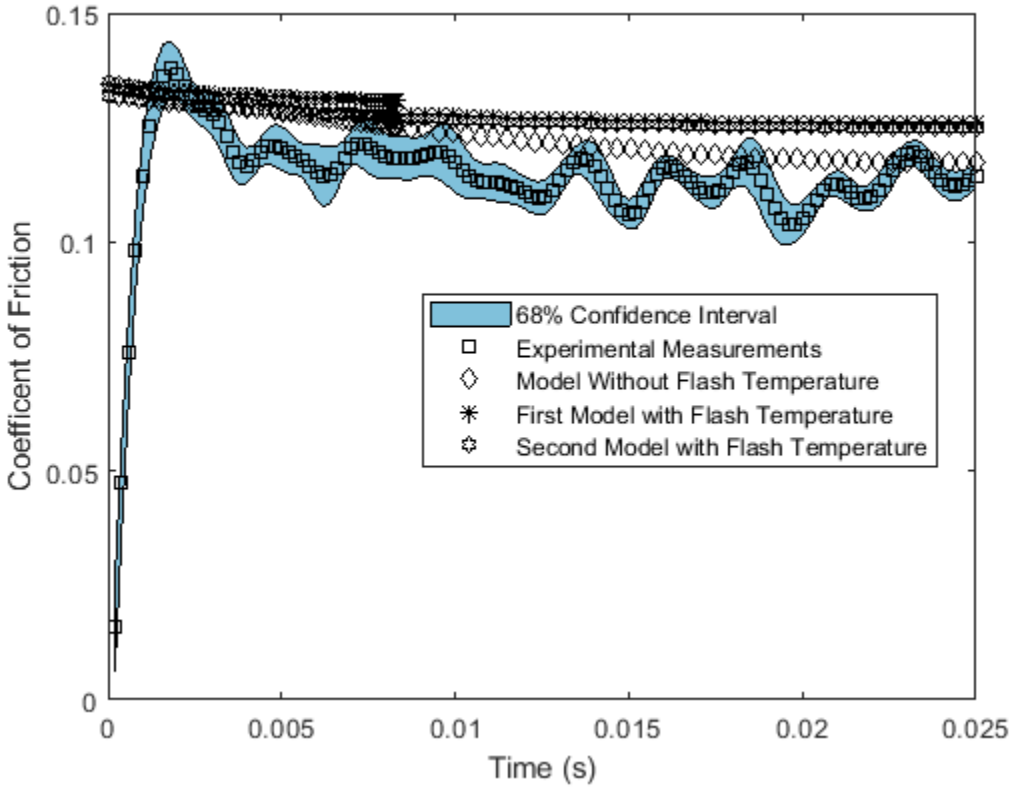

Figure 8.26: Model Comparisons to Experiments, Average Speed 0.6 m/s, Base Temperature 50 °C, 100 N Load

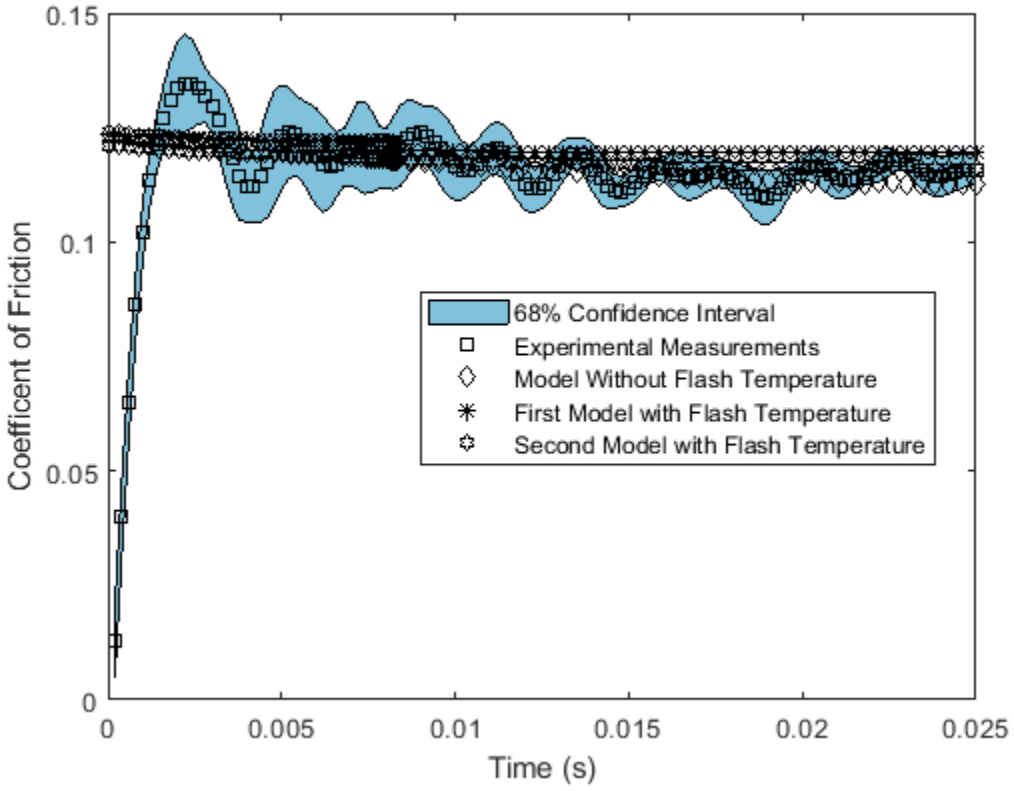

Figure 8.27: Model Comparisons to Experiments, Average Speed 0.6 m/s, Base Temperature 50 °C, 150 N Load

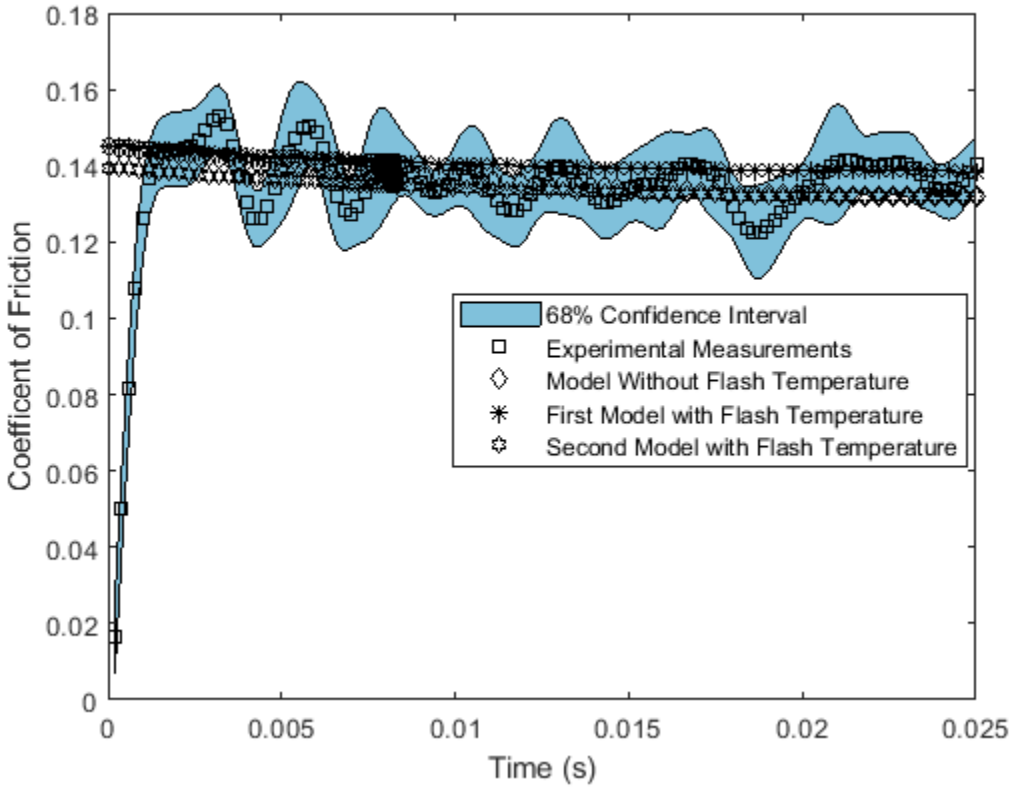

Figure 8.28: Model Comparisons to Experiments, Average Speed 0.6 m/s, Base Temperature 80 °C, 50 N Load

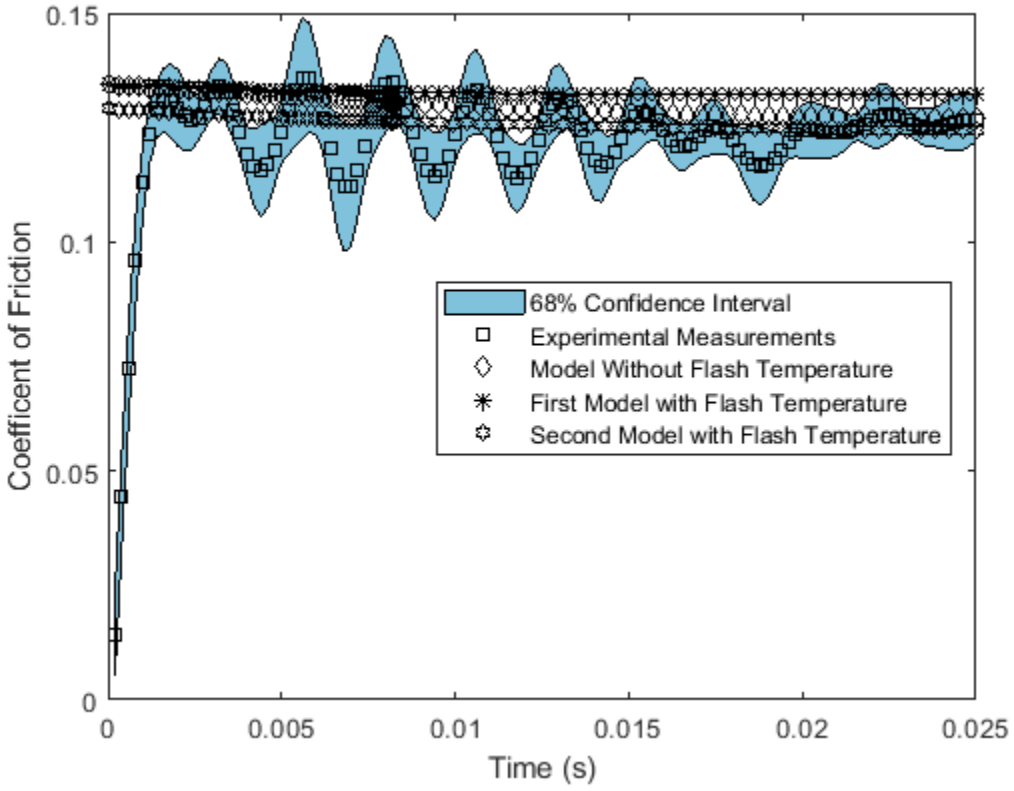

Figure 8.29: Model Comparisons to Experiments, Average Speed 0.6 m/s, Base Temperature 80 °C, 100 N Load

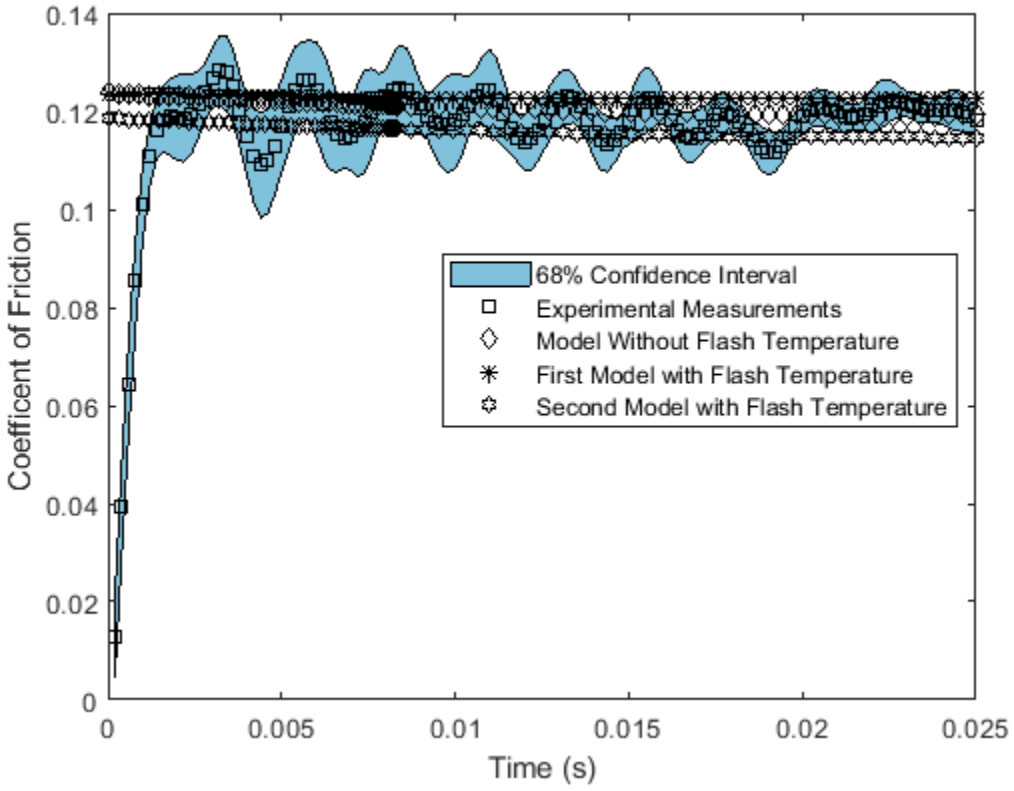

Figure 8.30: Model Comparisons to Experiments, Average Speed 0.6 m/s, Base Temperature 80 °C, 150 N Load

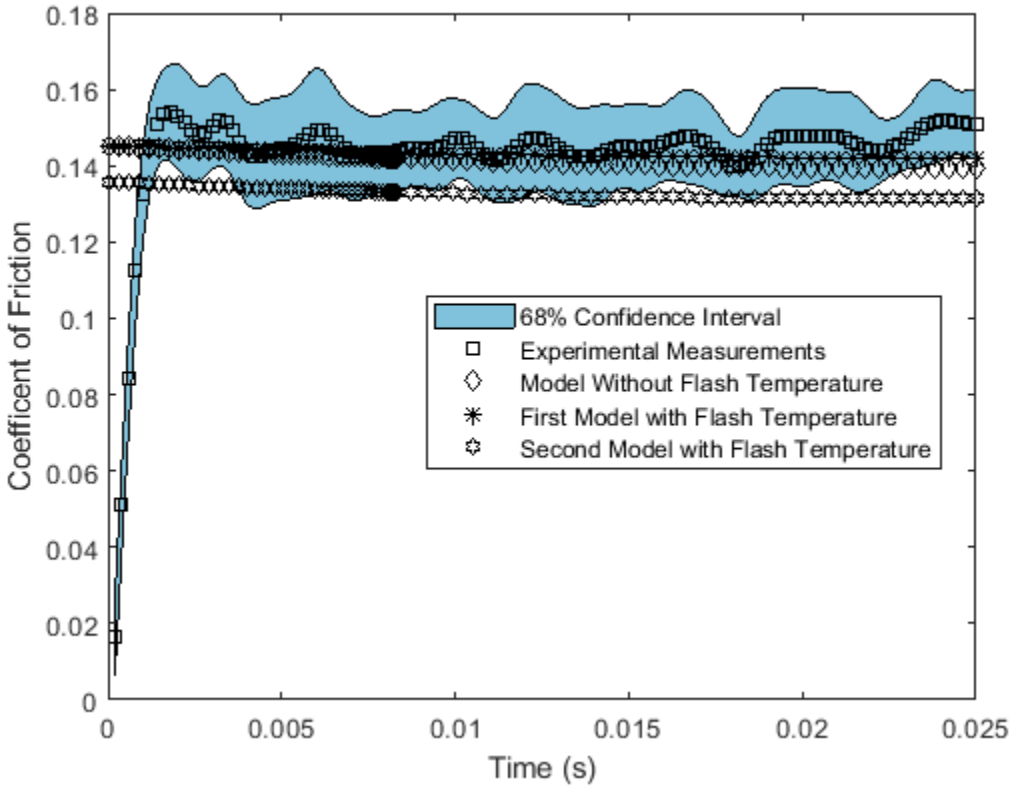

Figure 8.31: Model Comparisons to Experiments, Average Speed 0.6 m/s, Base Temperature 120 °C, 50 N Load

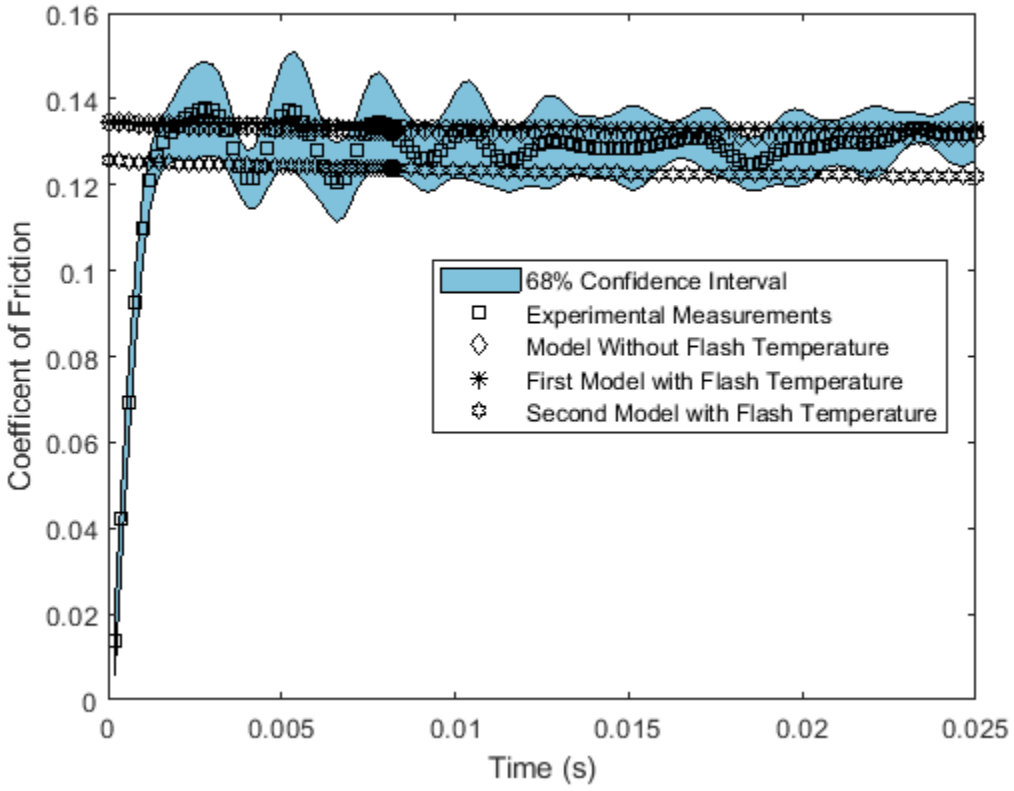

Figure 8.32: Model Comparisons to Experiments, Average Speed 0.6 m/s, Base Temperature 120 °C, 100 N Load

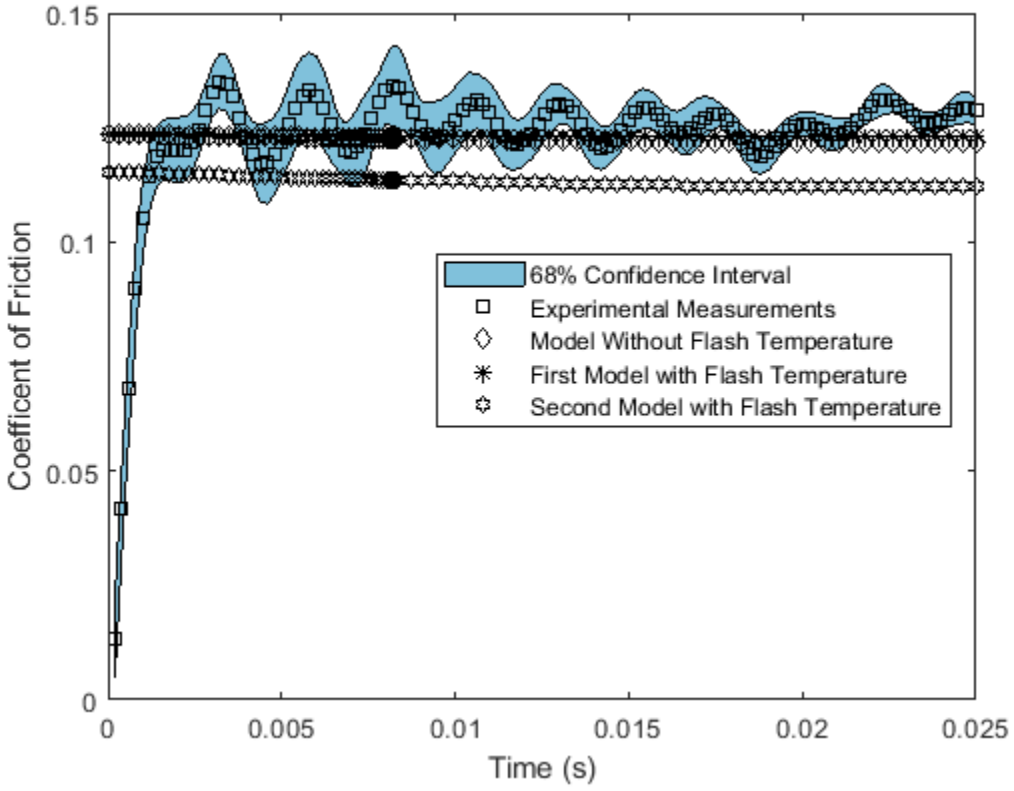

Figure 8.33: Model Comparisons to Experiments, Average Speed 0.6 m/s, Base Temperature 120 °C, 150 N Load

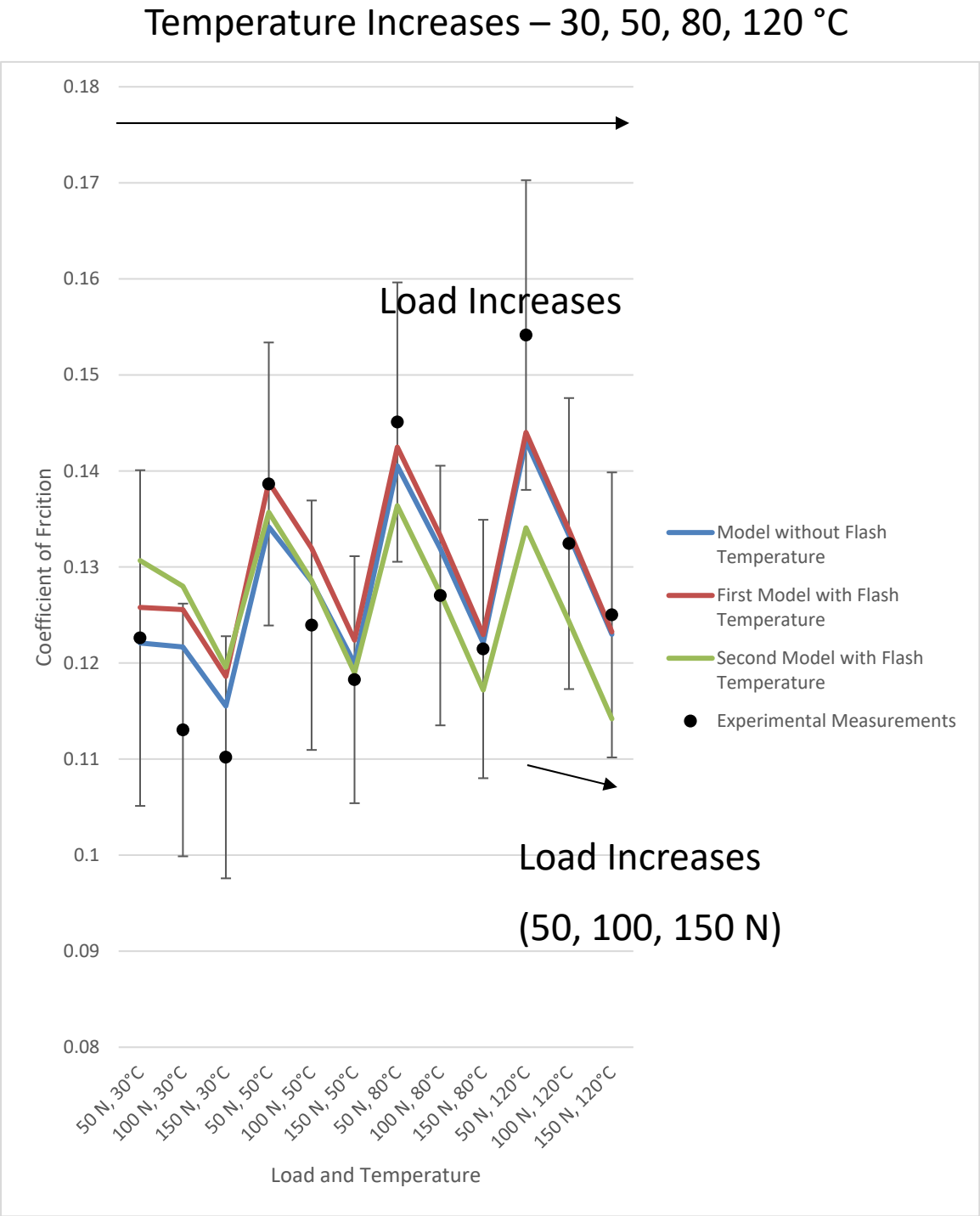

Figure 8.34: Overall Model Comparisons to Experiments, Average Speed 0.3 m/s

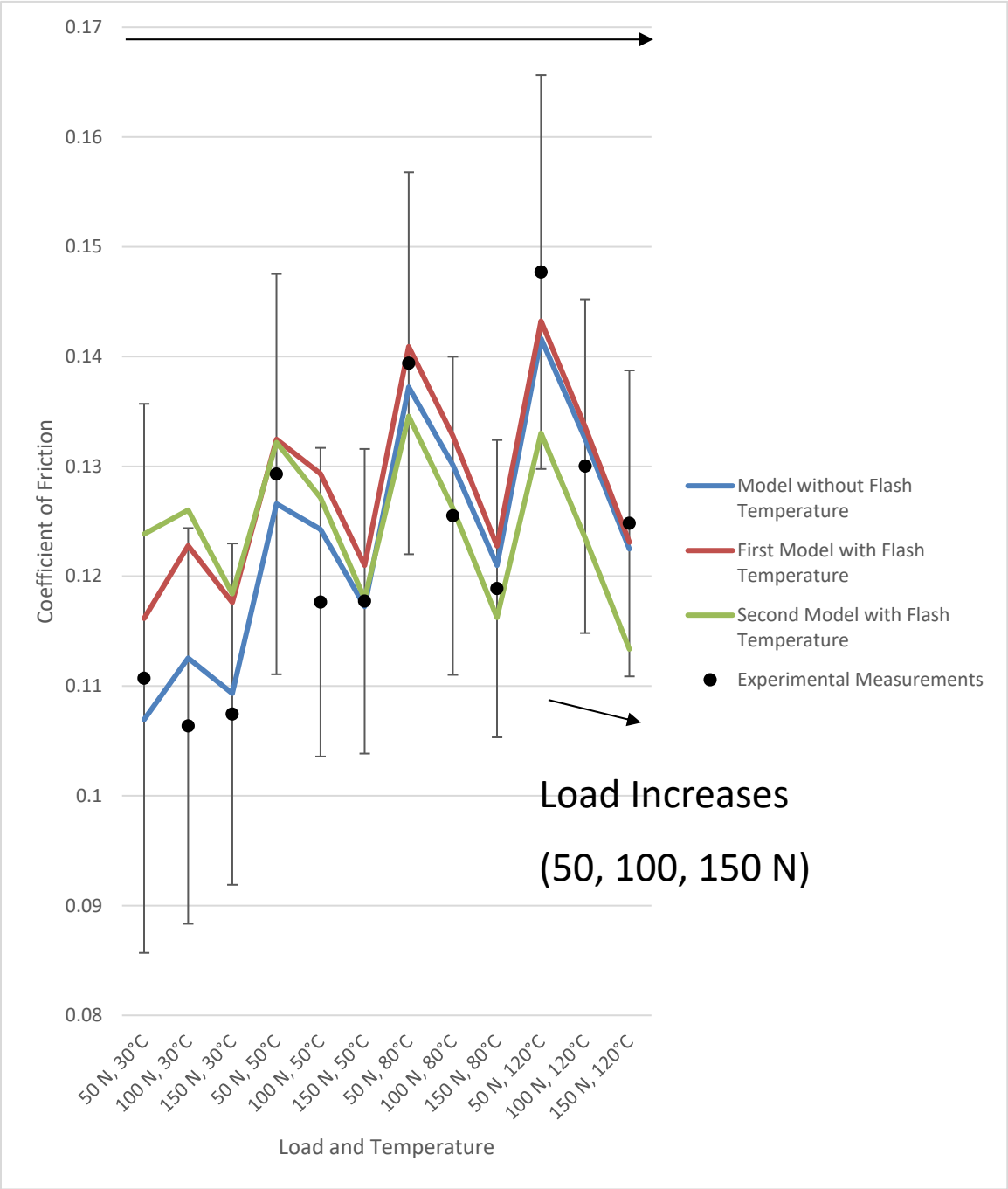

Figure 8.35: Overall Model Comparisons to Experiments, Average Speed 0.6 m/s

Overall there is good agreement between the models and the experiments. The largest differences occur at the extremities of load and speed. In particular, the second flash temperature model is the only one that predicts a friction coefficient more than 1 standard deviation away from the experimental averages for any temperature/speed/load combination. Larger standard deviations within the experiments were generally observed at lower values of temperature and load, which suggests that those measurements are not as repeatable due to small fluctuations in those values being more pronounced. At the faster speed the small variations in measured friction coefficient increased in magnitude. These were observed to be sufficiently large for an average speed of 1.2 m/s such that those data sets were not deemed consistent enough for a good comparison to the model. Tables 8.4 and 8.5 compare the average friction coefficient for the experiment and the models.

Table 8.4: Average Coefficient of Friction for a Mean Piston Speed of 0.3 m/s

Data Set	Friction Coefficient
Experimental Measurements	0.1275
Model without Frictional Heating	0.1280
First Flash Temperature Model	0.1302
Second Flash Temperature Model	0.1262

Table 8.5: Average Coefficient of Friction for a Mean Piston Speed of 0.6 m/s

Data Set	Friction Coefficient
Experimental Measurements	0.1237
Model without Frictional Heating	0.1235
First Flash Temperature Model	0.1280
Second Flash Temperature Model	0.1244

On the surface, it appears that the models that do not adjust for frictional heat generation provide the best fit to the measurements. In fact, for the faster average piston speed the predicted average friction coefficient across all cases almost matches that of the experiments. Tables 8.6 and 8.7 compare the average rms error of the 3 models and how frequently each was closest to the experimental means.

Table 8.6: Average RMS Error Relative to the Experiments for a Mean Piston Speed of 0.3 m/s

Model	RMS error	Frequency That Model was Closest to Experimental Average
No Adjustments for Frictional Heating	0.0014866	6 cases
First Flash Temperature Model	0.0018159	4 cases
Second Flash Temperature Model	0.0027476	2 cases

Table 8.7: Average RMS Error Relative to the Experiments for a Mean Piston Speed of 0.6 m/s

Model	RMS error	Frequency That Model was Closest to Experimental Average
No Adjustments for Frictional Heating	0.0011368	7 cases
First Flash Temperature Model	0.0021501	3 cases
Second Flash Temperature Model	0.0028841	2 cases

Based on these results, the adjustments for flash temperature do not improve the model comparison. While they work well for specific cases as seen in Figures 8.34 and 8.35, they perform poorly at the baseline temperature of 30°C. This is likely because the flash temperature adjustments decrease the viscosity by the largest amount (see Figure 3.2). The decreased load carrying capacity of the lubricant means that more load (and friction) is carried by asperity contact, and the predicted friction coefficient increases.

CHAPTER 9

CONCLUSTIONS AND NEXT STEPS

9.1 Conclusions

This work presents three slightly different mixed lubrication and solid contact models of a piston ring-cylinder liner interface. The first model does not account for temperature changes at all due to frictional heating. The other two models increase the temperature due to the frictional force and account for that in different ways. One of those models decreases the solid friction coefficient due to metal softening with increasing temperature using Equations 8.1-8.2. This effect becomes more pronounced as the base temperature increases because the heating pushes the system towards the melting temperature. The models overall display good agreement with experimental measurements performed over a wide range of operating conditions, but larger discrepancies exist for low or high temperatures and high loads and speeds. Partially this can be attributed to the shear thinning fit not working as well farther from the temperature from which it was found. The models predict an increase in friction coefficient as temperature increases or load or speed decreases. However, they do not predict as large an increase at high temperature and low load, the condition under which

the largest friction coefficients were measured. Overall, these models can be used to design or evaluate friction reduction technologies such as better lubricants or surface textures.

9.2 Future Work

The next immediate step would be to alter the values used in Equation 3.58 (which would potentially be temperature dependent). This has already been done with a few cases shown in Figures 9.1-9.3.

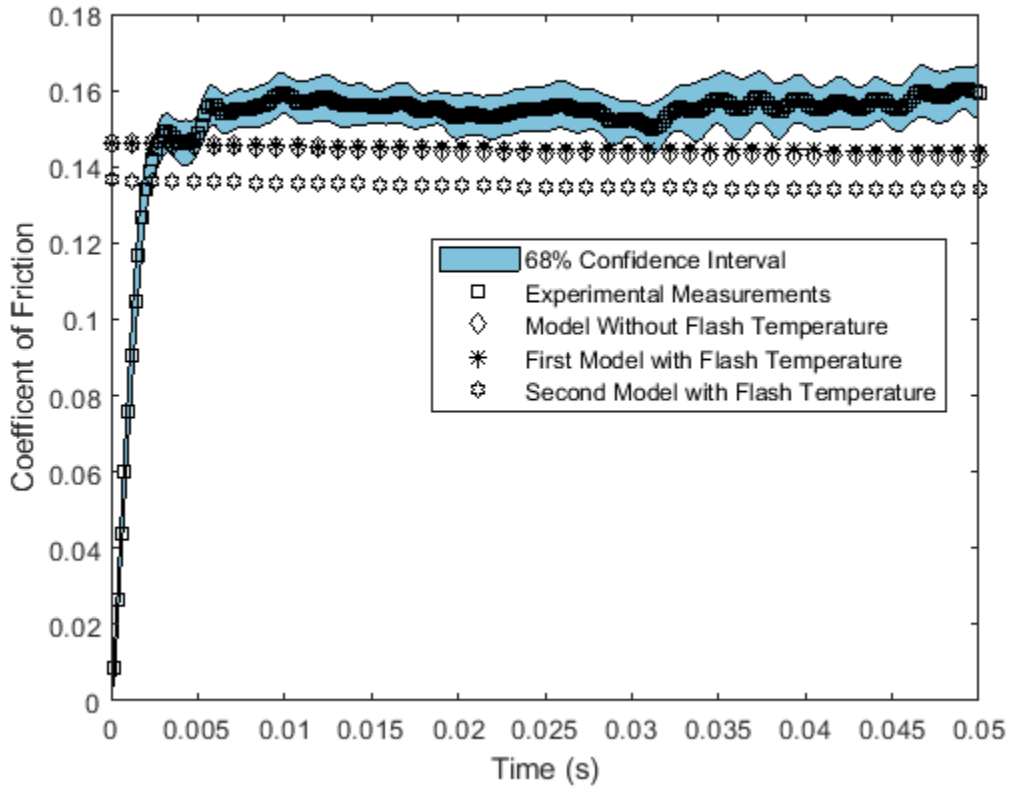

Figure 9.1: Model Comparisons to Experiments, Average Speed 0.3 m/s, Base Temperature 120 °C, 50 N Load, Dry Friction Equation $\mu = 0.163 - 0.3F_n^*$

The model still underestimated the friction coefficient (though this was the temperature/load combination for which the model underestimates the friction coefficient by the most), so further refinements were made as shown in Figures 9.2-9.3.

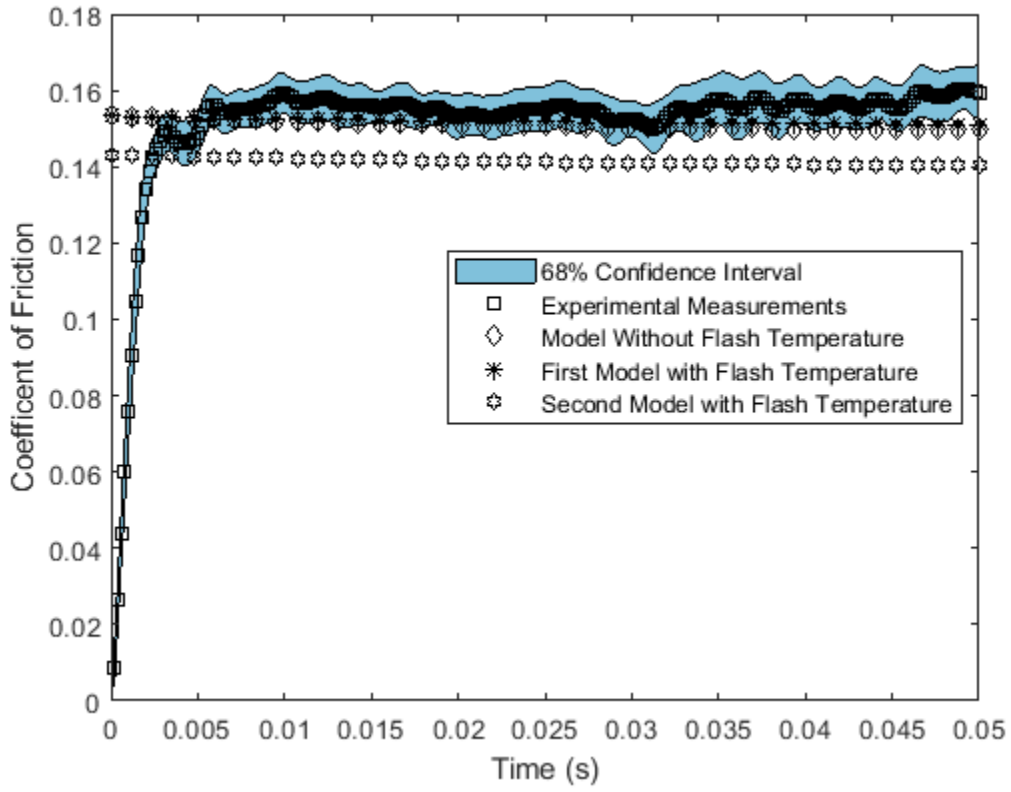

Figure 9.2: Model Comparisons to Experiments, Average Speed 0.3 m/s, Base Temperature 120 °C, 50 N Load, Dry Friction Equation $\mu = 0.170 - 0.3F_n^*$

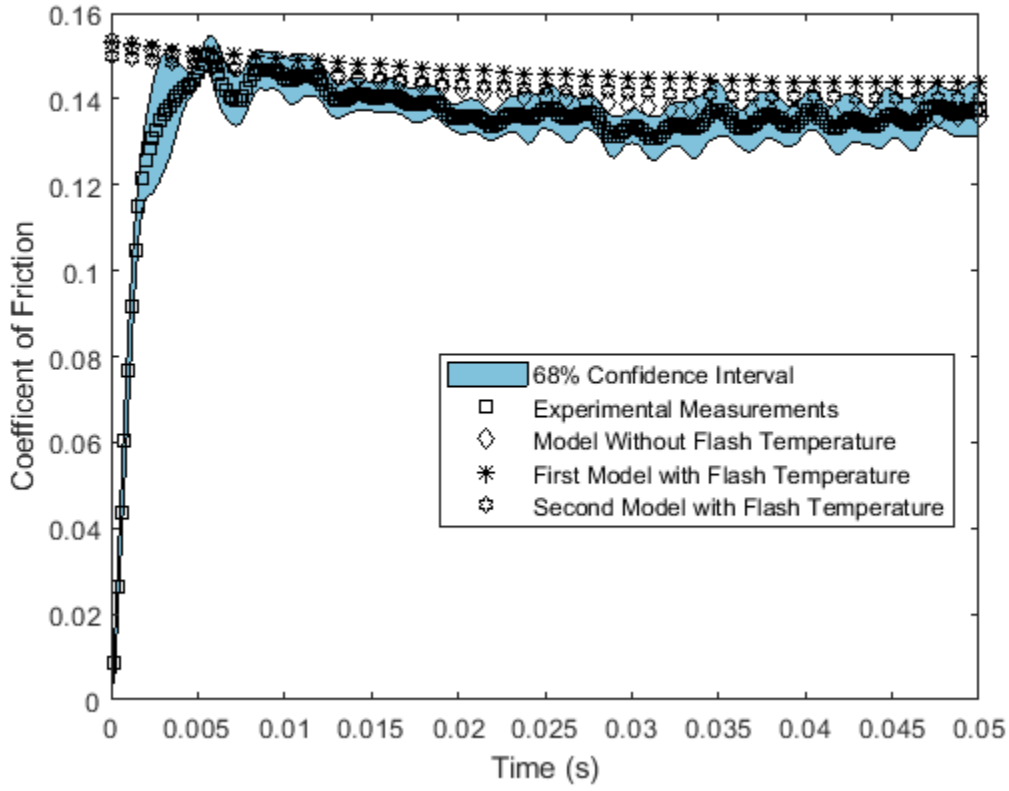

Figure 9.3: Model Comparisons to Experiments, Average Speed 0.3 m/s, Base Temperature 50 °C, 50 N Load, Dry Friction Equation $\mu = 0.170 - 0.3F_n^*$

With the second modification to the dry friction equation, the model matches the experimental measurements more closely for the higher temperature. However, it would be inferior at other temperature/speed/load combinations where the friction coefficient was lower. The next step would likely introduce a temperature dependence to the equation.

The flash temperature models could be rerun with convection from the lubricant included (which would decrease the temperature rise) and/or thermal deformations of the

ring and the liner. More likely (depending on the results of altering Equation 3.58) the flash temperature models would be discarded because there would be no appreciable effect.

Once the baseline model has been refined, the model could subsequently be compared to the other piston ring-cylinder liner combinations tested in Chapter 5. Figure 9.4 shows the stresses experienced by the ring.

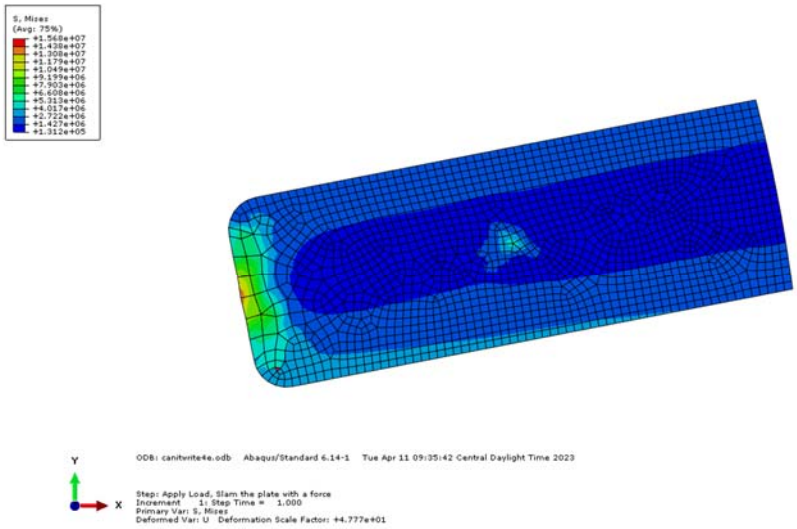

Figure 9.4: Sample Stress Applied to Piston Ring

These stresses can then be used to predict coating failure.

The model could also be expanded from an axisymmetric model to a full 3D model, which would be more computationally expensive to run. The time needed to predict the friction coefficient would determine whether such a model is worth the time.

REFERENCES

[1] Tung, S. C., M. L. McMillan. Automotive Tribology Overview of Current Advances and Challenges for the Future. Tribol. Int. 2004, 37, 517-536.

[2] Holmberg, K., P. Andersson, A. Erdemir. Global Energy Consumption Due to Friction in Passenger Cars. Tribol. Int. 2012, 47, 221–234.

[3] Söderfjäll, M, H. M. Herbst, R. Larsson, A. Almqvist. Influence on Friction from Piston Ring Design, Cylinder Liner Roughness and Lubricant Properties. Tribol. Int. 2017, 116, 272–284.

[4] IEA (2022), Electric Vehicles, IEA, Paris https://www.iea.org/reports/electric-vehicles

[5] Rahmani, R., H. Rahnejat, B. Fitzsimons, D. Dowson. The Effect of Cylinder Liner Operating Temperature on Frictional Loss and Engine Emissions in Piston Ring Conjunction. Appl. Energy 2017, 191, 568–581.

[6] Patir, N., H.S. Cheng. An average flow model for determining effects of three-dimensional roughness on partial hydrodynamic lubrication. ASME J. Tribol 1978; 100: 12–17.

[7] Locker, A., R. L. Jackson, A. Gangopadhyay, H. Ghaednia. Flow Factor Modeling of Combustion Engine Ring and Cylinder Components in Mixed Hydrodynamic Lubrication. Proc. IMechE Part J. 2022.

[8] Chu, N., R. L. Jackson, X. Wang, A. Gangopadhyay, H. Ghaednia. Evaluating Elastic-Plastic Wavy and Spherical Asperity-Based Statistical and Multi-Scale Rough Surface Contact Models with Deterministic Results. Materials, 2021, 14(14), 3864.

[9] Furuhama, S., T. Sumi. A Dynamic Theory of Piston-Ring Lubrication: 3rd Report, Measurement of Oil Film Thickness. Bull. JSME 1961 (4), 744–752.

[10] Ma, M.-T., I. Sherrington, E. H. Smith. Analysis of Lubrication and Friction for a Complete Piston-Ring Pack with an Improved Oil Availability Model: Part 1: Circumferentially Uniform Film. Proc. Inst. Mech. Eng. Part J J. Eng. Tribol. 1997, 211, 1–15.

[11] Alakin, O., G.M. Newaz. Piston Ring-Cylinder Bore Friction Modeling in Mixed Lubrication Regime: Part I—Analytical Results. J. Trib. 2001, 123, 211–218.

[12] Jeng, Y.-R. Theoretical Analysis of Piston-Ring Lubrication Part II—Starved Lubrication and Its Application to a Complete Ring Pack. Tribol. Trans. 1992, 35, 707–714.

[13] Furuhama, S., S. Sasaki. New Device for the Measurement of Piston Frictional Forces in Small Engines. SAE Trans. 1983, 92, 781–792.

[14] Tian, T. Dynamic Behaviours of Piston Rings and Their Practical Impact. Part 2: Oil Transport, Friction and Wear of Ring/Liner Interface and the Effects of Piston

and Ring Dynamics. Proc. Inst. Mech. Eng. Part J J. Eng. Tribol. 2002, 216, 229–248.

[15] Morris, N., M. Mohammadpour, R. Rahmani, H. Rahnejad. Optimisation of the Piston Compression Ring for Improved Energy Efficiency of High Performance Race Engines. Proc. Inst. Mech. Eng. Part D J. Automob. Eng. 2017, 231, 1806–1817.

[16] Bewsher, S. R., M. Leighton, M. Mohammadpour, H. Rahnejat, G. Offner, O. Knaus. Atomic Force Microscopic Measurement of a Used Cylinder Liner for Prediction of Boundary Friction. Proc. Inst. Mech. Eng. Part. D J. Automob. Eng. 2019, 233, 1879–1889.

[17] Howell-Smith, S., H. Rahnejad, P.D., King, D. Dowson. Reducing In-Cylinder Parasitic Losses through Surface Modification and Coating. Proc. Inst. Mech. Eng. Part D J. Automob. Eng. 2014, 228, 391–402.

[18] Li, C. D., M. Jin, F.-M. Du, W.-W. Wang, Y. Shen, J.-J. Xu. Wear Behavior of Al-Si Alloy Cylinder Liner Prepared by Laser Finishing. Proc. Inst. Mech. Eng. Part D J. Automob. Eng. 2018, 232, 1944–1949.

[19] Senatore, A., G. Risitano, L. Scappaticci, D. D'Andrea. Investigation of the Tribological Properties of Different Textured Lead Bronze Coatings under Severe Load Conditions. Lubricants 2021, 9, 34.

[20] Wang, X., W. Liu, F. Zhou, D. Zhu. Preliminary Investigation of the Effect of Dimple Size on Friction in Line Contacts. Tribol. Int. 2009, 42, 1118–1123.

[21] Kilgerman, Y., I. Etsion, A. Shinkarenko. Improving Tribological Performance of Piston Rings by Partial Surface Texturing. J. Trib. 2005, 127, 632–638.

[22] Spencer, A. Optimizing Surface Texture for Combustion Engine Cylinder Liners. Ph.D. Thesis, Luleåtekniska Universitet, Luleå, Sweden, 2010.

[23] Lu, P., R.J.K. Wood. Tribological Performance of Surface Texturing in Mechanical Applications—A Review. Surf. Topogr. Metrol. Prop. 2020, 8, 43001.

[24] Abril, S.O., M.D.S. Fonseca-Vigoya, J. Pabón-León. CFD Analysis of the Effect of Dimples and Cylinder Liner Honing Groove on the Tribological Characteristics of a Low Displacement Engine. Lubricants 2022, 10(4), 61.

[25] Greenwood, J.A. and J.B.P. Williamson, Contact of Nominally Flat Surfaces. Prol. R. Soc. Lond. A, 1966(295): p. 300-319.

[26] Chang, W.R., I. Etsion, and D.B. Bogy, An Elastic-Plastic Model for the Contact of Rough Surfaces. ASME J. Tribol., 1987. 109(2): p. 257-263.

[27] Jackson, R. L. and I. Green, A Statistical model of Elastic-Plastic Asperity Contact between Rough Surfaces. Trib. Int., 2006. 39(9): p. 906-914.

[28] Kogut, L. and I. Etsion, A Finite Element Based Elastic-Plastic Model for the Contact of Rough Surfaces. Tribology Transaction, 2003. 46(3): p. 383-390.

[29] Majumdar, A. and B. Bhushan, Fractal Model of Elastic-plastic Contact Between Rough Surfaces. ASME J. of Tribol., 1991, 113(1): p. 1-11.

[30] Jackson, R.L. and J.L. Streator, A multi-scale model for contact between rough surfaces. Wear, 2006. 261(11-12): p. 1337-1347.

[31] Liu, G., Q. Wang; C. Lin. A Survey of Current Models for Simulating the Contact between Rough Surfaces. *Tribol. Trans.* **1999**, *42*, 581–591.

[32] Johnson, K.L., *Contact Mechanics*. 1985, Cambridge, U.K.: Cambridge University Press. 452.

[33] Wadwalkar, S.S., R.L. Jackson, L. Kogut, A Study of the Elastic-Plastic Deformation of Heavily Deformed Spherical Contacts. Proc. IMechE Vol. 224 Part J., p. 1091-1102.

[34] Bush, A.W., R.D. Gibson, T.R. Thomas, The Elastic Contact of a Rough Surface. Wear, 19 (1975), 163-168.

[35] Ciavarella, M., J.A. Greenwood, and M. Paggi, Inclusion of Interaction in the Greenwood and Williamson Contact Theory. Wear,2008. 265 (5-6), p. 729-734.

[36] Afferrante, L., G. Carbone, G. Demelio, Interacting and Coalescing Hertzian Asperities: A New Multiasperity Contact Model. Wear 2012 (278), 28-33.

[37] Vakis, A.I., Asperity Interaction and Substrate Deformation in Statistical Summation Models of Contact Between Rough Surfaces. Journal of Applied Mechanics, 81 (4) 041012.

[38] Ciavarella, M., G. Demelio, et al., Linear Elastic Contact of the Weierstrass Profile. Proc. R. Soc. Lond. A., 2000(456): 387-405.

[39] Westergaard, H.M. Bearing Pressures and Cracks. J. Appl. Mech. Trans. ASME, 6 (1939), 49-53.

[40] Morag, Y., and I. Etsion. "Resolving the contradiction of asperities plastic to elastic mode transition in current contact models of fractal rough surfaces." Wear 262.5-6 (2007): 624-629.

[41] Candela, T., et al., Characterization of Fault Roughness at Various Scales: Implications of Three-Dimensional High Resolution Topography Measurements. Pure and Applied Geophysics, 2009. 166(10-11): p. 1817-1851.

[42] Pavelescu, D. and A. Tudor, On the Roughness Fractal Character, the Tribological Parameters and the Error Factors. Proc. Romanian Acad., 2004. 5(2): p. 1-6.

[43] Wu, J.-J., Characterization of fractal surfaces. Wear, 2000. 239: p. 36-47.

[44] Wu, J.-J., Spectral Analysis for the Effects of Stylus Tip Curvature on Measuring Fractal Profiles. Meas. Sci. Technol., 2000. 11(9): p. 1369-1376.

[45] Zhang, X., Y. Xu, and R.L. Jackson, An analysis of generated fractal and measured rough surfaces in regards to their multi-scale structure and fractal dimension. Tribology International, 2017. 105: p. 94-101.

[46] Zhang, X. and R.L. Jackson, An analysis of the multiscale structure of surfaces with various finishes. Tribology Transactions, 2017. 60(1): p. 121-134.

[47] Whitehouse, D., Fractal or fiction. Wear, 2001. 249(5-6): p. 345-353.

[48] Jackson, R.L., An Analytical Solution to an Archard-type Fractal Rough Surface Contact Model. Trib. Trans., 2010. 53(4): p. 543 - 553.

[49] Archard, J.F., Elastic Deformation and the Laws of Friction. Proc. R. Soc.Lond. A., 1957(243): p. 190-205.

[50] Johnson, K.L., J.A. Greenwood, and J.G. Higginson, The Contact of Elastic Regular Wavy Surfaces. Int. J. Mech. Sci., 1985. 27(6): p. 383-396.

[51] Krithivasan, V. and R.L. Jackson, An Analysis of Three-Dimensional Elasto-Plastic Sinusoidal Contact. Tribology Letters, 2007. 27(1): p. 31-43.

[52] A. Chen, Z., and I. Etsion. "The elastic-plastic contact behavior of rough surfaces with hard coatings." Tribology International 134 (2019): 435-442.

[53] Song, H., et al. "Statistical model of rough surface contact accounting for size-dependent plasticity and asperity interaction." Journal of the Mechanics and Physics of Solids 106 (2017): 1-14.

[54] Li, L., I. Etsion, and F. E. Talke. "Contact area and static friction of rough surfaces with high plasticity index." Journal of Tribology 132.3 (2010).

[55] Wang, X., et al. "The effect of resolution on the deterministic finite element elastic-plastic rough surface contact under combined normal and tangential loading." Tribology International 144 (2020): 106141.

[56] Zhang, H., and I. Etsion. "A Coupled Eulerian–Lagrangian Model for Sliding Inception of Elastic–Plastic Spherical Contact." Journal of Tribology 143.1 (2021): 014501.

[57] Zhang, H., and I. Etsion. "Evolution of adhesive wear and friction in elastic-plastic spherical contact." Wear (2021): 203915.

[58] Jackson, R. L., S. Saha, and Y. Xu, The Influence of Single Asperity Models on Predicting Contact Between Elastic Rough Surfaces Using Statistical Methods, STLE Tribology Frontiers Conference, Denver, CO, Oct. 25-27, 2015.

[59] Liu, G., J. Zhu, L.Yu, Q.J. Wang, Elasto-Plastic Contact of Rough Surfaces. Tribol. Trans. 2001, 44, 437–443.

[60] Jacq, C.; D. Ne´lias, G. Lormand, D. Girodin, Development of a Three-Dimensional Semi-Analytical Elastic-Plastic Contact Code. J. Tribol. 2002, 124, 653–667.

[61] Sainsot, P., C. Jacq, D. Nélias, A Numerical Model for Elastoplastic Rough Contact. Comput. Modeling Eng. Sci. 2002, 3, 497–506.

[62] Wang, Z.; W. Wang, Y. Hu, H. Wang, A Simplified Numerical Elastic-Plastic Contact Model for Rough Surfaces. Adv. Tribol. 2009, 53, 159–166.

[63] Pei, L., S. Hyun, J.F. Molinari, M.O. Robbins, Finite Element Modeling of Elasto-Plastic Contact between Rough Surfaces. J. Mech. Phys. Solids 2005, 53, 2385–2409.

[64] Sahoo, P., N. Ghosh, Finite element contact analysis of fractal surfaces. J. Phys. D Appl. Phys. 2007, 40, 4245–4252.

[65] Liu, H., D. Leray, S. Colin, P. Pons, A. Broué, Finite Element Based Surface Roughness Study for Ohmic Contact of Microswitches. In Proceedings of the IEEE 58th Holm Conference on Electrical Contacts (Holm), Portland, OR, USA, 23–26 September 2012; pp. 1–10.

[66] Thompson, M.K., J.M. Thompson, Considerations for the incorporation of measured surfaces in finite element models. Scanning 2010, 32, 183–198.

[67] Thompson, M.K., A Comparion of Methods to Evaluate the Behavior of Finite Element Models with Rough Surfaces. Scanning 2011, 33, 353–369.

[68] Megalingam, A., M.M. Mayuram, Comparative Contact Analysis Study of Finite Element Method Based Deterministic, Simplified Multi-Asperity and Modified Statistical Contact Models. J. Tribol. 2012, 134, 014503.

[69] Wang, X., Y. Xu, R.L. Jackson, Theoretical and Finite Element Analysis of Static Friction Between Multi-Scale Rough Surfaces. Tribology Letters 66, 146 (2018).

[70] An, B., X. Wang, Y. Xu, R.L. Jackson, Deterministic Elastic-Plastic Modelling of Rough Surface Contact Including Spectral Interpolation and Comparison to Theoretical Models. Tribol. Int. 2019, 135, 246–258.

[71] Khonsari, M. M., E. R. Booser, *Applied Tribology: Bearing Design and Lubrication.* 2008, Chichester, England: John Wiley & Sons Ltd, 566.

[72] Ng, C. W., C.H.T. Pan, A Linearized Turbulent Lubrication Theory. Journal of Basic Engineering, Transactions ASME 1965, 87, 675.

[73] Peiran, Y., W. Shizhu, A Generalized Reynolds Equation for Non-Newtonian Thermal Elastohydrodynamic Lubrication. J. Tribol. 1990, 112(4), 631-636.

[74] Mitsuya, Y., T. Ohkubo, H. Ota, Average Reynlds Equation Extended to Gas Lubrication Possessing Surface Roughness in the Slip Flow Regime: Approximate Method and Confirmation Experiments. J. Tribol. 1989, 111(3), 495-503.

[75] Wu., L., D. Bogy, New First and Second Order Slip Models for the Compressible Reynolds Equation. J. Tribol. 2003, 125(3), 558-561.

[76] S. a. Technologies, "Tribological properties and applications of alumina," in *https://substech.com/dokuwiki/doku.php?id=tribological_properties_and_applications_of_alumina*, ed, 2016.

[77] Jackson, R. L., The Wear and Thermo-Elastohydrodynamic Behavior of Thrust Washer Bearings Under Non-Axisymmetric Loads. Doctor of Philosophy in Mechanical Engineering, Woodruff School of Mechanical Engineering, Georgia Institute of Technology, 2004.

[78] Peklenik, J., Paper 24: New Developments in Surface Characterization and Measurements by Means of Random Process Analysis. Proceedings of the Institution of Mechanical Engineers, Conference Proceedings, Sage Publications 182(11): 108-126.

[79] Wilson, W.R.D., N. Marsault, Partial Hydrodynamic Lubrication with Large Fractional Contact Areas. J. Tribol. 1998, 120(1), 16-20.

[80] Peeken, H.J., et. al., On the Numerical Determination of Flow Factors. J. Tribol. 1997 119(2), 259-264.

[81] Hu, Y., L. Zheng. Some Aspects of Determining the Flow Factors. J. Tribol. 1989 111(3), 525-531.

[82] Morales-Espejel, G.E., Flow Factors for Non-Gaussian Roughness in Hydrodynamic Lubrication: an Analytical Interpolation. Proc. Inst. Mech. Eng., Part C: J. Mech. Eng. Sci. 2009, 223, 1433-1441.

[83] Sahlin, F., et. al., A Mixed Lubrication Model Incorporating Measured Surface Topography Part 1: Theory of Flow Factors. Proc. Inst. Mech. Eng., Part J: J. Eng. Tribol. 2010, 224, 335-351.

[84] Tripp, J., Surface Roughness Effects in Hydrodynamic Lubrication: the Flow Factor Method. J. Lubr. Technol. 1983 (105), 458-463.

[85] Elrod, H., A General Theory for Laminar Lubrication with Reynolds Roughness. J. Lubr. Technol. 1979, 101, 8-14.

[86] Lunde, L., K. Tonder, Pressure and Shear Flow in a Rough Hydrodynamic Bearing, Flow Factor Calculation. J. Tribol. 1997, 119(3), 549-555.

[87] Leighton, M., R. Rahmani, H. Rahnejat, Surface-specific flow factors for prediction of friction of cross-hatched surfaces. Surf Topography: Metrology and Properties, 2016; 4: 025002.

[88] Tzeng, S. T., E. Saibel, Surface Roughness Effect of Slider Bearing Lubrication. ASLE Transactions, 1967, 10(3), 334-348.

[89] Patir, N. , H. S. Cheng, Application of Average Flow Model to Lubrication Between Rough Sliding Surfaces. J. Tribol. 1979, 101(2), 220-229.

[90] McCool, J. I., Comparison of Models for the Contact of Rough Surfaces. Wear, 1986. 107(1), 37-60.

[91] Chu, N. The Effect of Asperity Geometry on Elastic-Plastic Statistical and Multi-Scale Rough Surface Contact Models. Master of Science (Thesis), Mechanical Engineering, Auburn University, 2018.

[92] Kalin, M., A. Pogačnik, I. Etsion, B. Raeymaekers, Comparing Surface Topography Parameters of Rough Surfaces Obtained with Spectral Moments and Deterministic Methods. Tribology International 93 (2016) 137-141.

[93] Jackson, R. L., S. Saha, Y. Xu, The Influence of Single Asperity Models on Predicting Contact Between Elastic Rough Surfaces Using Statistical Methods. STLE Tribology Frontiers Conference, Denver, CO, Oct. 25-27, 2015.

[94] Ghaednia, H., X. Wang, S. Saha, Y. Xu, A. Sharma, R. L. Jackson, A Review of Elastic-Plastic Contact Mechanics. Appl. Mech. 2017, 69(6), 060804.

[95] Rostami, A., R.L. Jackson, Predictions of the average surface separation and stiffness between contacting elastic and elastic-plastic sinusoidal surfaces. J. of Eng. Trib. (2013). 227(12), 1376-1385.

[96] Jang, J. Y., M. M. Khonsari, S. Bair, Correction Factor Formula to Predict the Central and Minimum Film Thickness for Shear-Thinning Fluids in EHL. J. Tribol. 2008, 130(2), 024541.

[97] Cohen, D. Y. Kligerman, I. Etsion, A Model for Contact and Static Friction of Nominally Flat Rough Surfaces Under Full Stick Contact Condition. J. Tribol. 2008, 130(3), 031401.

[98] Li, L., I. Etsion, F. E. Talke, Contact Area and Static Friciton of Rough Surfaces with High Plasticity Index. J. Tribol, 2010, 132(3), 031401.

[99] Wang, X., Y. Xu, R. L. Jackson, Theoretical and Finite Element Analysis of Static Friction Between Multi-Scale Rough Surfaces. Tribology Letters 66, 146 (2018).

[100] Ibrahim Dickey, R., R.L. Jackson, G.T. Flowers, Measurement of Static Friction Coefficients and Comparison to Theoretical Models. 2011, J. of Tribol., Trans. ASME, 133, 031408.

[101] Tian, X., F. E. Kennedy, Jr., Maximum and Average Flash Temperatures in Sliding Contacts. J. Tribol. 1994, 116(1), 167-174.

[102] Papazafeiropoulos, G., M. Muñiz-Calvente, E. Martínez-Pañeda. Abaqus2Matlab: A suitable tool for finite element post-processing. Adv. Eng. Softw. 2017, 105, 9–16. https://doi.org/10.1016/j.advengsoft.2017.01.006.

[103] Kamps, T., J. Walker, R. Wood, P. Lee, A. Plint. Reproducing automotive engine scuffing using a lubricated reciprocating contact. Wear 2015, 332–333, 1193–1199. https://doi.org/10.1016/j.wear.2014.12.045.

[104] ASTM-G0133-22; Standard Test Method for Linearly Reciprocating Ball-on-Flat Sliding Wear, G-133. 2016.

[105] Phoenix Tribology, TE 77 High Frequency Friction Machine. http://www.phoenix-tribology.com/at2/leaflet/te77

[106] Blok, H., The Flash Temperature Concept. Wear 6.6 (1963), 483-494.

[107] Suzuki, S., F. E. Kennedy, The Detection of Flash Temperatures in a Sliding Contact by the Method of Tribo-Induced Thermoluminescence. J. Tribol. Jan 1991, 113(1): 120-127.

[108] Johnson, G.R., W.H. Cook, Fracture Characteristics of Three Metals Subjected to Various Strains, Strain Rates, Temperatures, and Pressures. Engineering Fracture Mechanics 21(1): 31-48.

APPENDIX

Friction Measurements of a Production Ring on a Cast Iron Liner

The following Appendix contains all of the experimental measurements of a production ring on a cast iron liner.

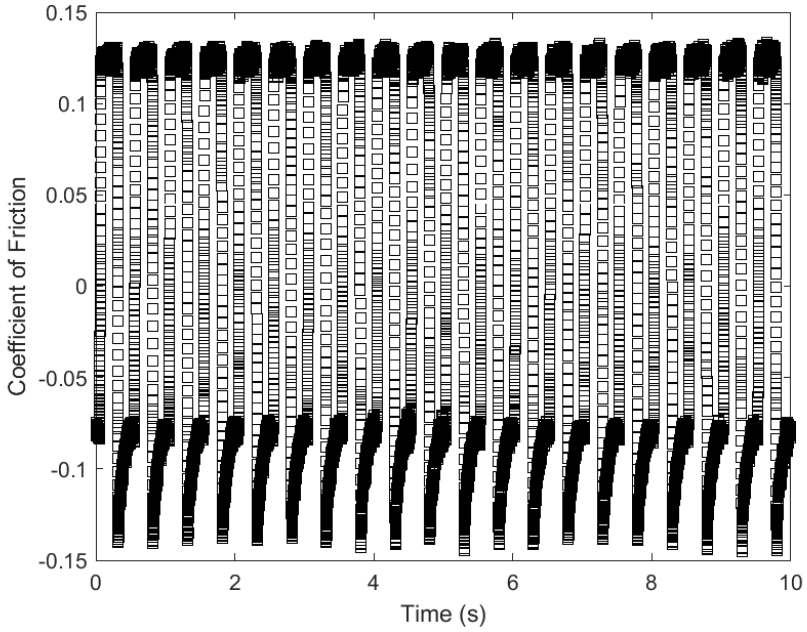

Figure A.1: First Set of Data, Sliding Frequency 2 Hz, Applied Load 50 N, Lubricant Temperature 30 °C

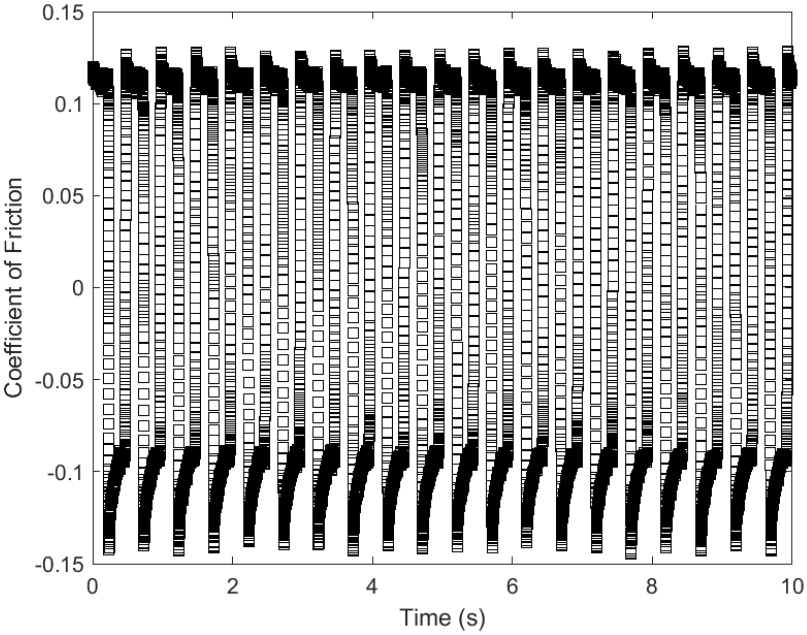

Figure A.2: First Set of Data, Sliding Frequency 2 Hz, Applied Load 100 N, Lubricant Temperature 30 °C

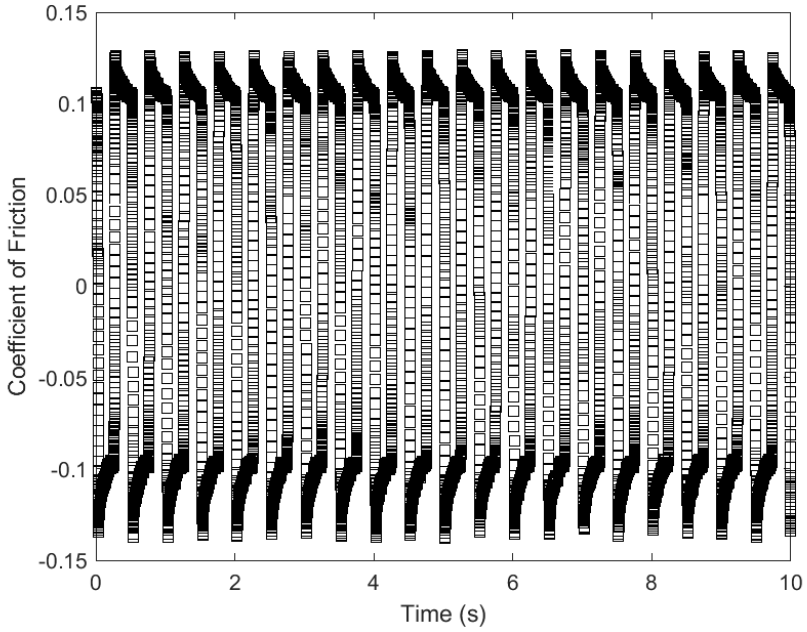

Figure A.3: First Set of Data, Sliding Frequency 2 Hz, Applied Load 150 N, Lubricant Temperature 30 °C

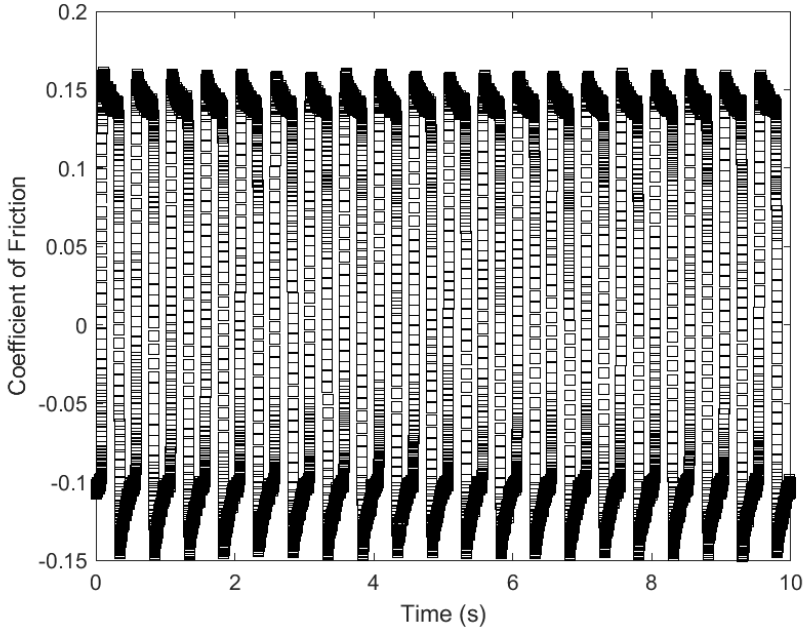

Figure A.4: First Set of Data, Sliding Frequency 2 Hz, Applied Load 50 N, Lubricant Temperature 50 °C

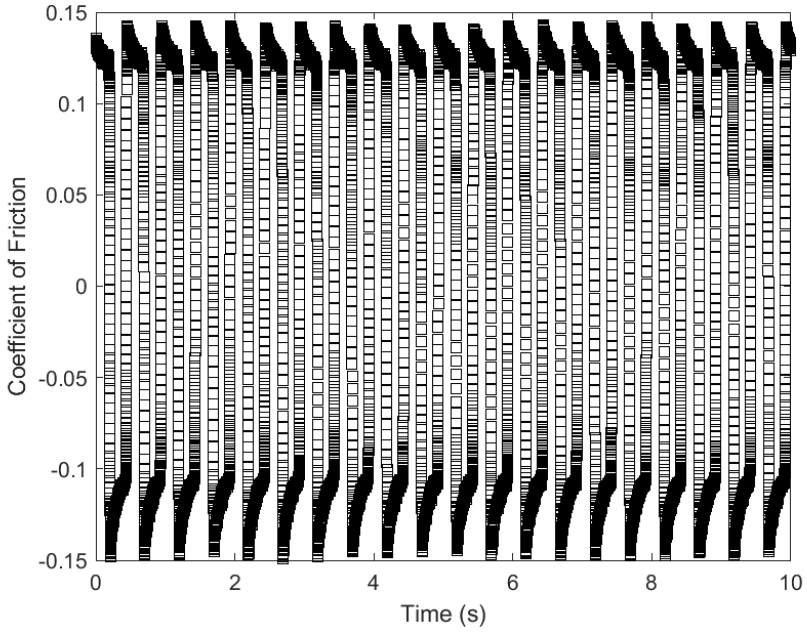

Figure A.5: First Set of Data, Sliding Frequency 2 Hz, Applied Load 100 N, Lubricant Temperature 50 °C

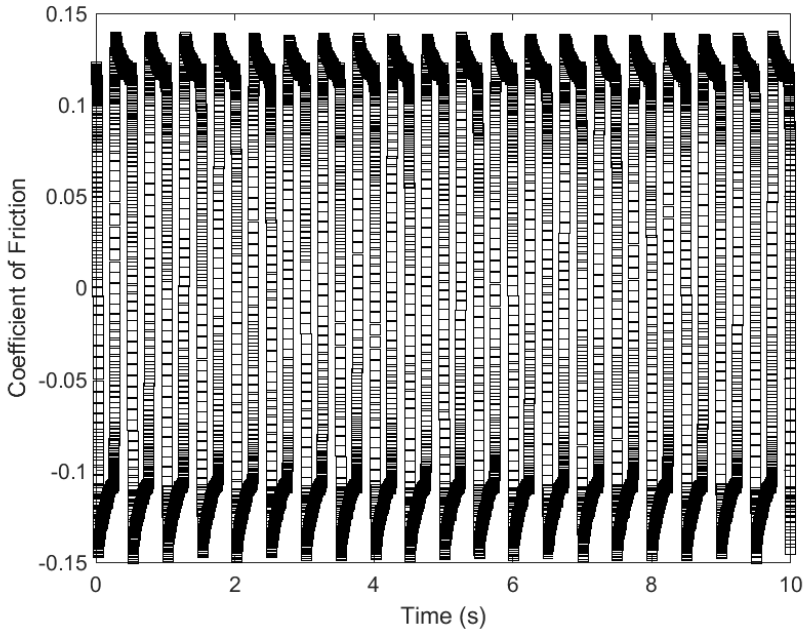

Figure A.6: First Set of Data, Sliding Frequency 2 Hz, Applied Load 150 N, Lubricant Temperature 50 °C

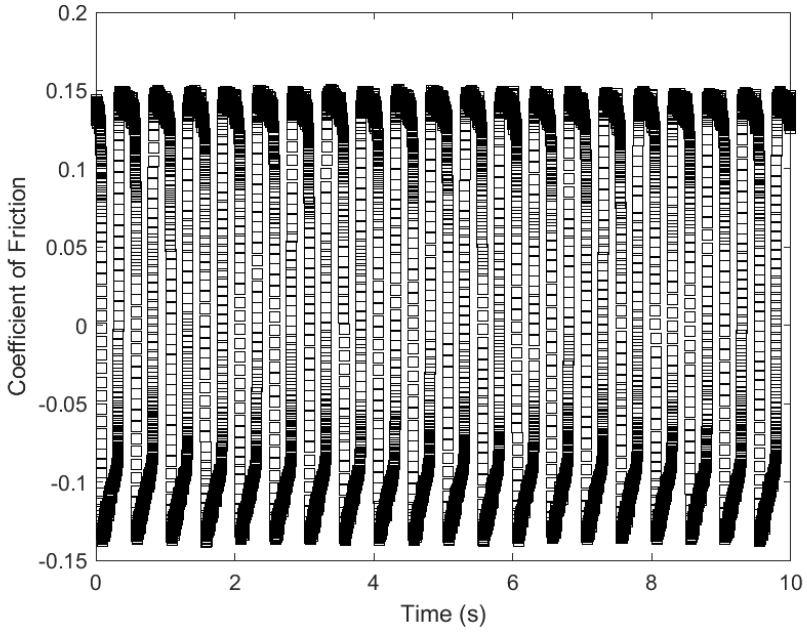

Figure A.7: First Set of Data, Sliding Frequency 2 Hz, Applied Load 50 N, Lubricant Temperature 80 °C

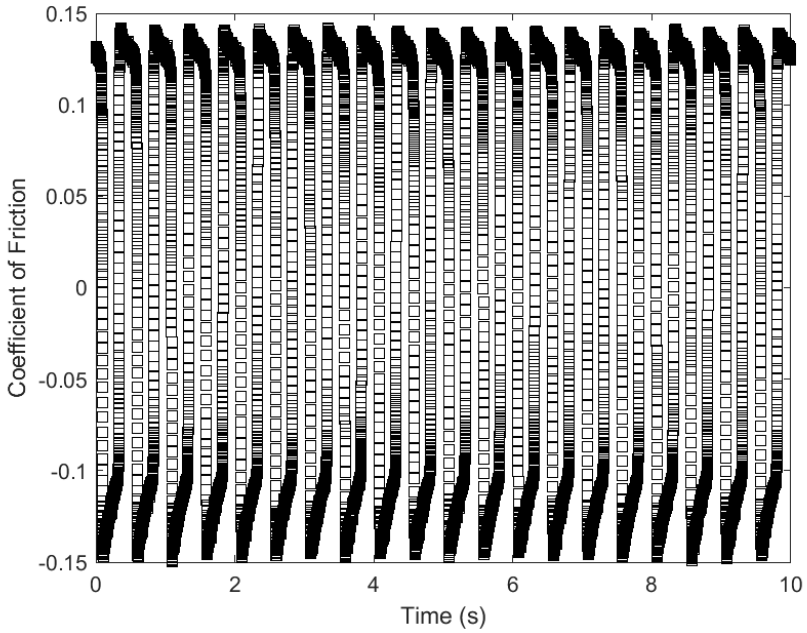

Figure A.8: First Set of Data, Sliding Frequency 2 Hz, Applied Load 100 N, Lubricant Temperature 80 °C

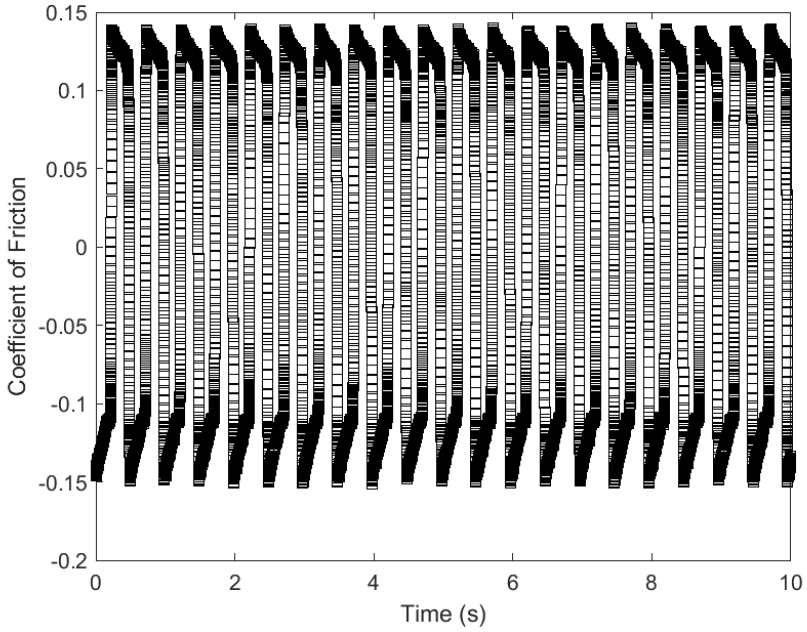

Figure A.9: First Set of Data, Sliding Frequency 2 Hz, Applied Load 150 N, Lubricant Temperature 80 °C

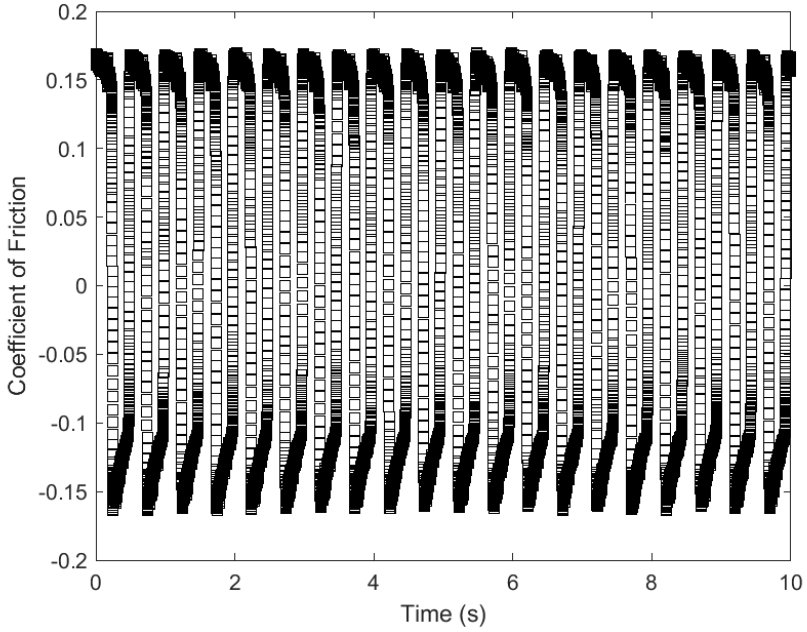

Figure A.10: First Set of Data, Sliding Frequency 2 Hz, Applied Load 50 N, Lubricant Temperature 120 °C

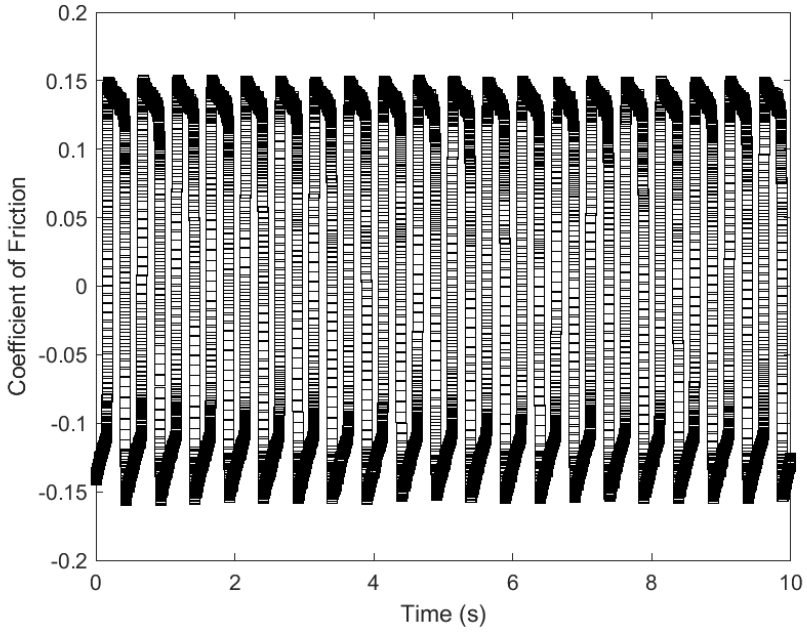

Figure A.11: First Set of Data, Sliding Frequency 2 Hz, Applied Load 100 N, Lubricant Temperature 120 °C

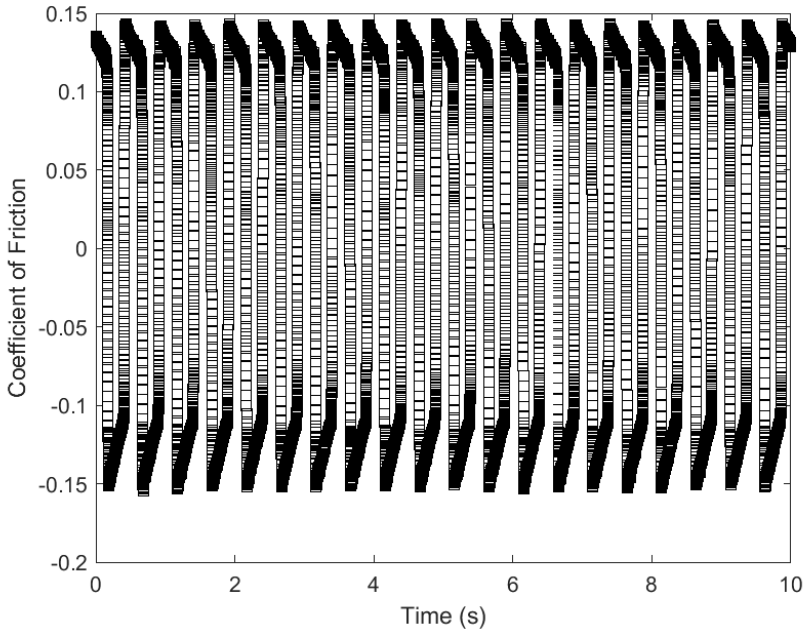

Figure A.12: First Set of Data, Sliding Frequency 2 Hz, Applied Load 150 N, Lubricant Temperature 120 °C

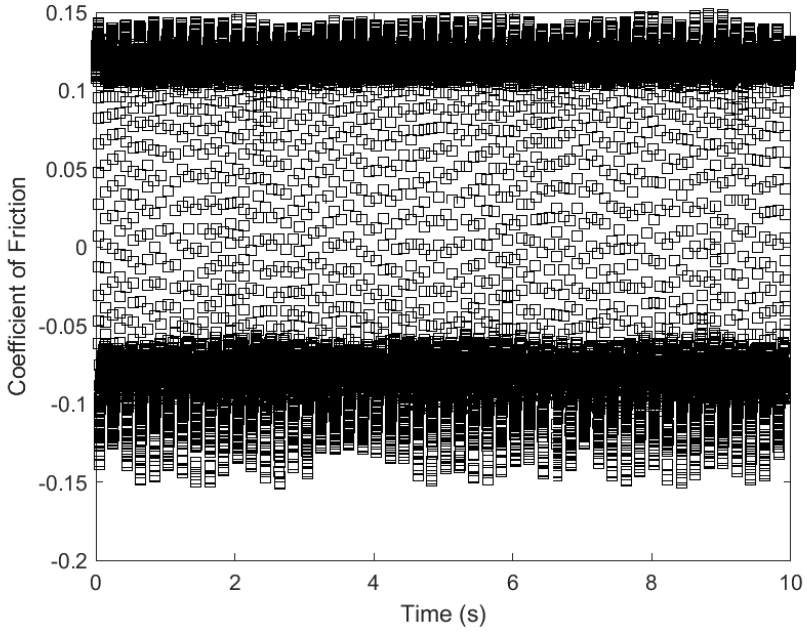

Figure A.13: First Set of Data, Sliding Frequency 5 Hz, Applied Load 50 N, Lubricant Temperature 30 °C

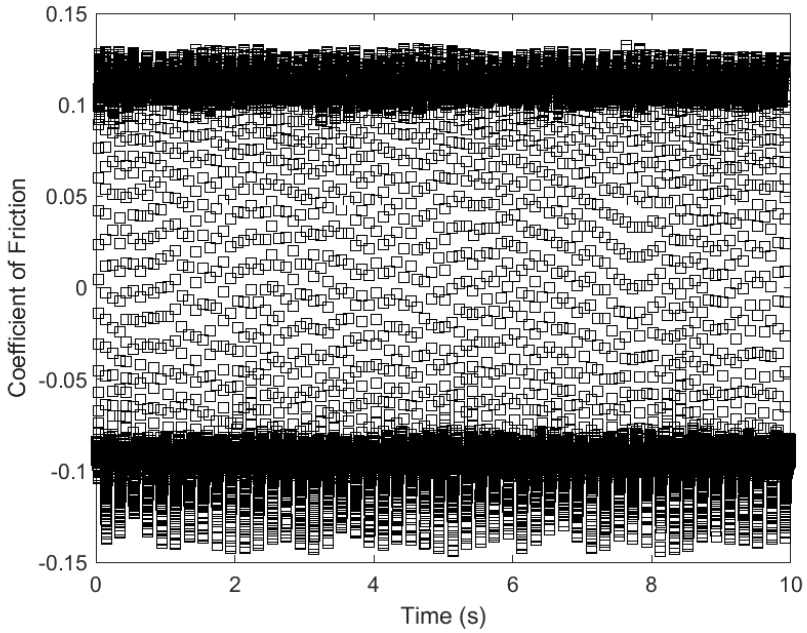

Figure A.14: First Set of Data, Sliding Frequency 5 Hz, Applied Load 100 N, Lubricant Temperature 30 °C

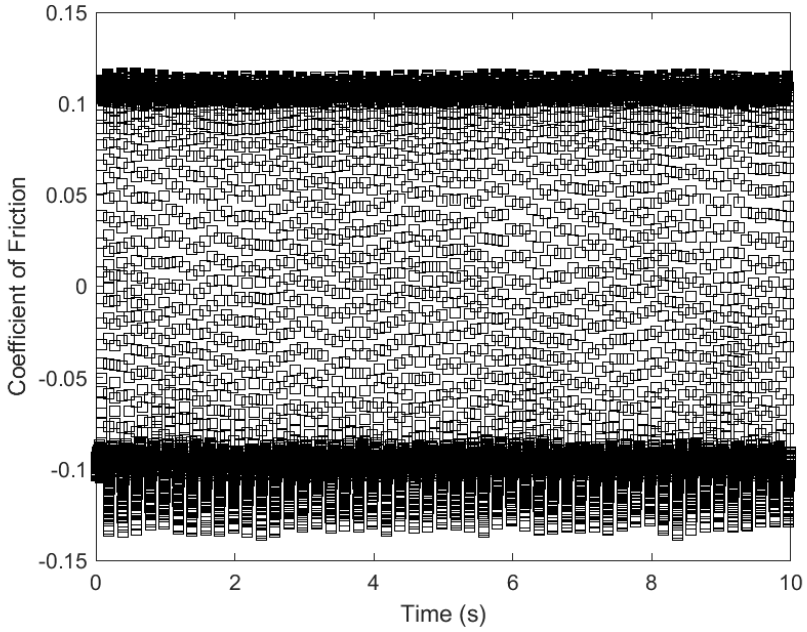

Figure A.15: First Set of Data, Sliding Frequency 5 Hz, Applied Load 150 N, Lubricant Temperature 30 °C

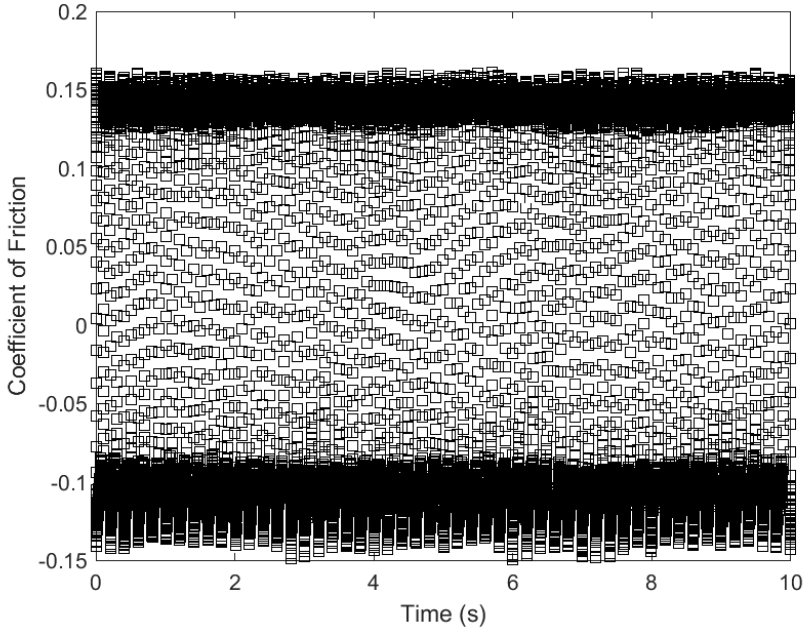

Figure A.16: First Set of Data, Sliding Frequency 5 Hz, Applied Load 50 N, Lubricant Temperature 50 °C

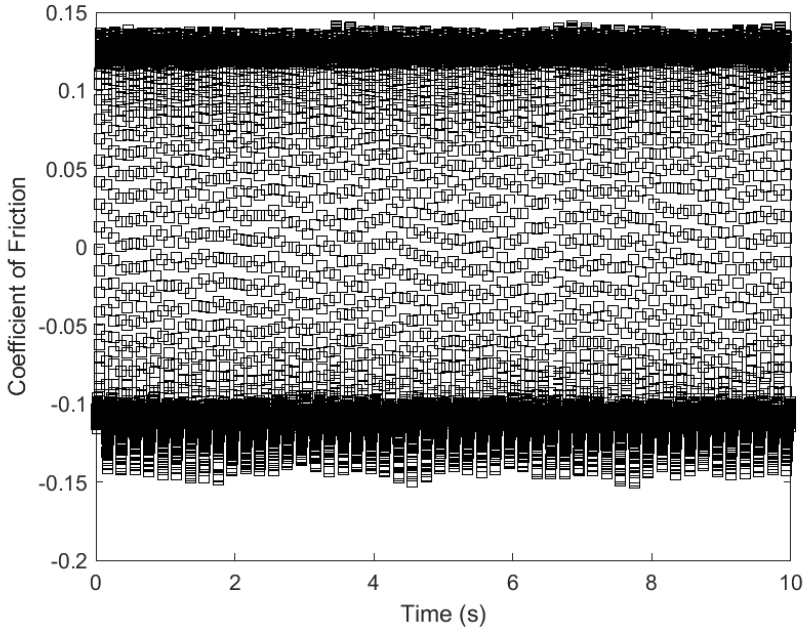

Figure A.17: First Set of Data, Sliding Frequency 5 Hz, Applied Load 100 N, Lubricant Temperature 50 °C

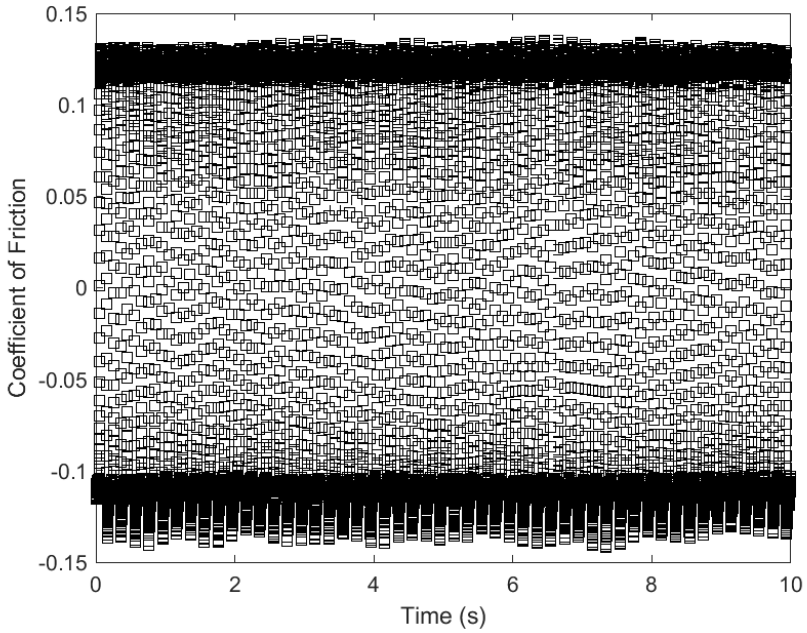

Figure A.18: First Set of Data, Sliding Frequency 5 Hz, Applied Load 150 N, Lubricant Temperature 50 °C

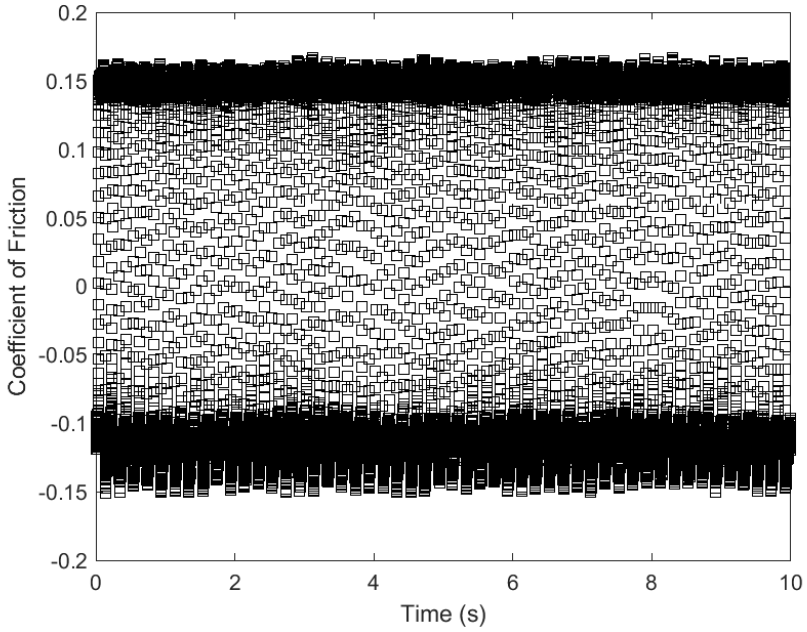

Figure A.19: First Set of Data, Sliding Frequency 5 Hz, Applied Load 50 N, Lubricant Temperature 80 °C

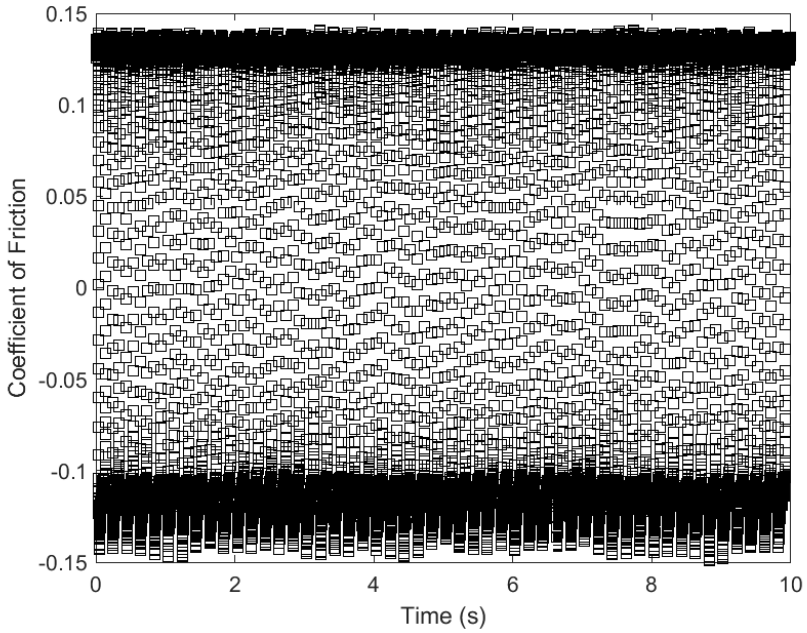

Figure A.20: First Set of Data, Sliding Frequency 5 Hz, Applied Load 100 N, Lubricant Temperature 80 °C

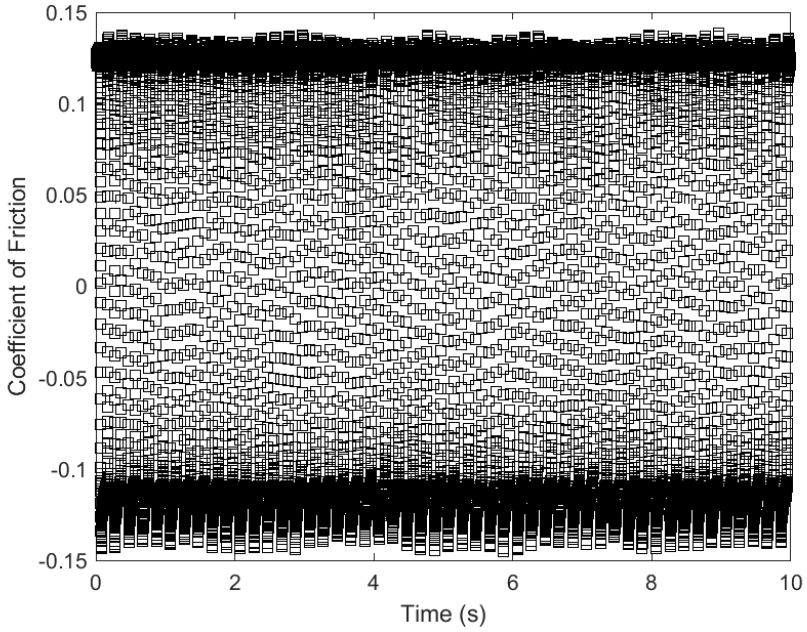

Figure A.21: First Set of Data, Sliding Frequency 5 Hz, Applied Load 150 N, Lubricant Temperature 80 °C

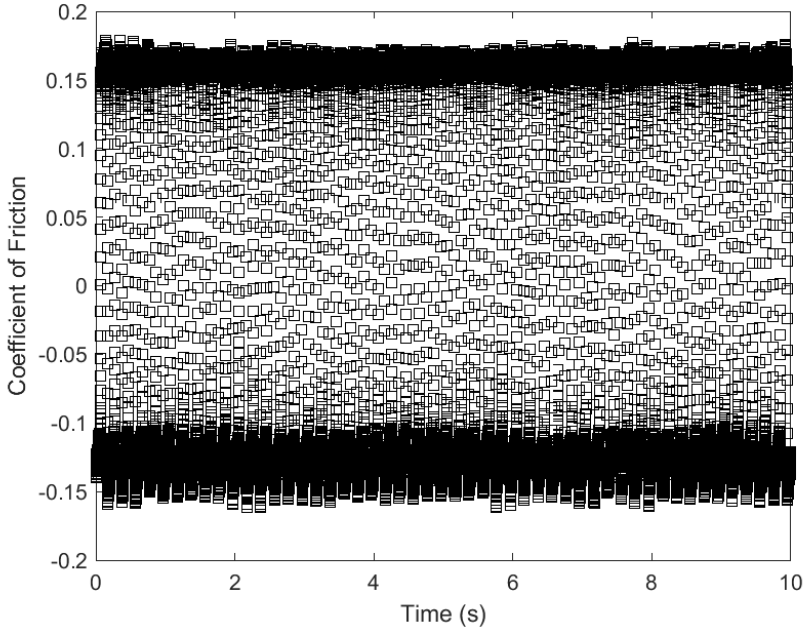

Figure A.22: First Set of Data, Sliding Frequency 5 Hz, Applied Load 50 N, Lubricant Temperature 120 °C

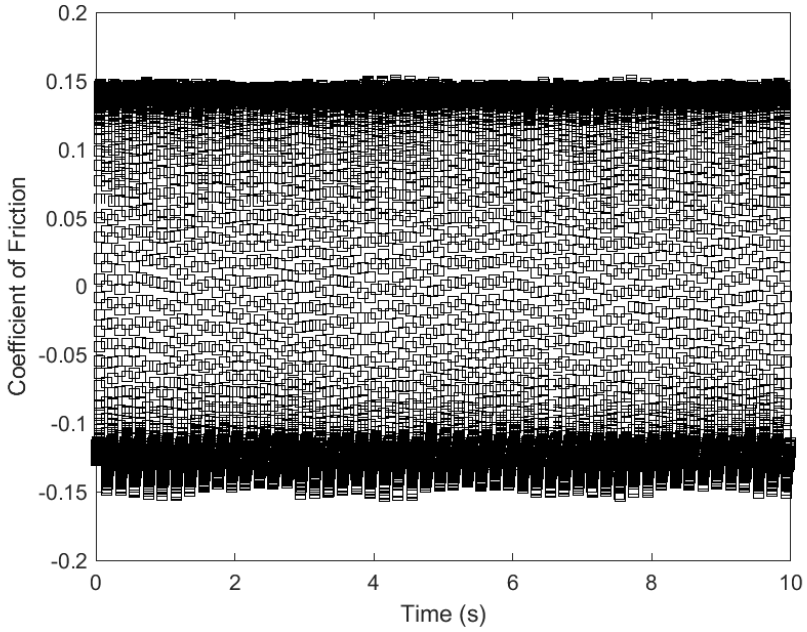

Figure A.23: First Set of Data, Sliding Frequency 5 Hz, Applied Load 100 N, Lubricant Temperature 120 °C

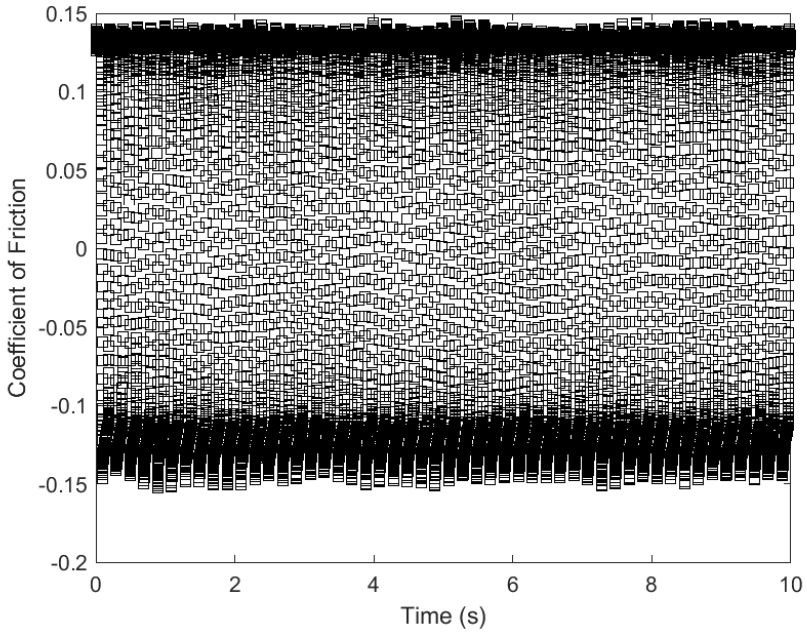

Figure A.24: First Set of Data, Sliding Frequency 5 Hz, Applied Load 150 N, Lubricant Temperature 120 °C

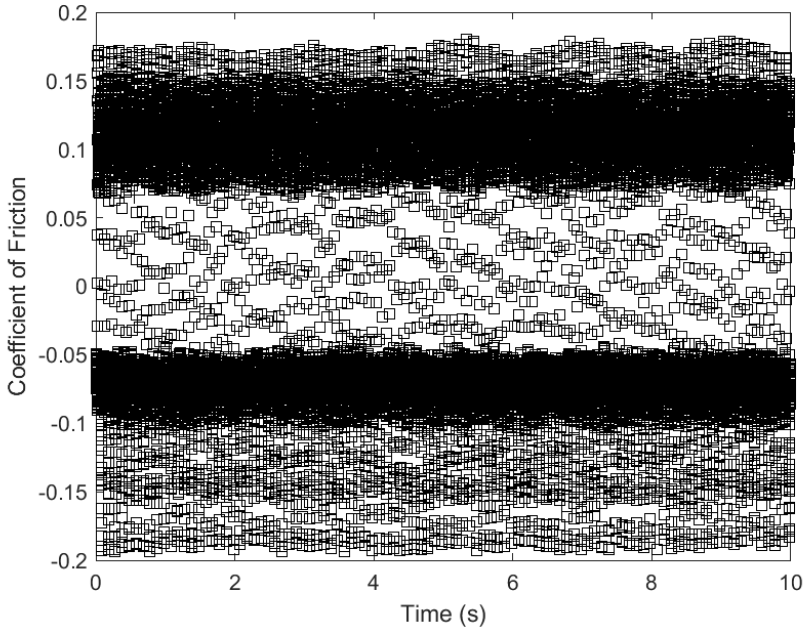

Figure A.25: First Set of Data, Sliding Frequency 10 Hz, Applied Load 50 N, Lubricant Temperature 30 °C

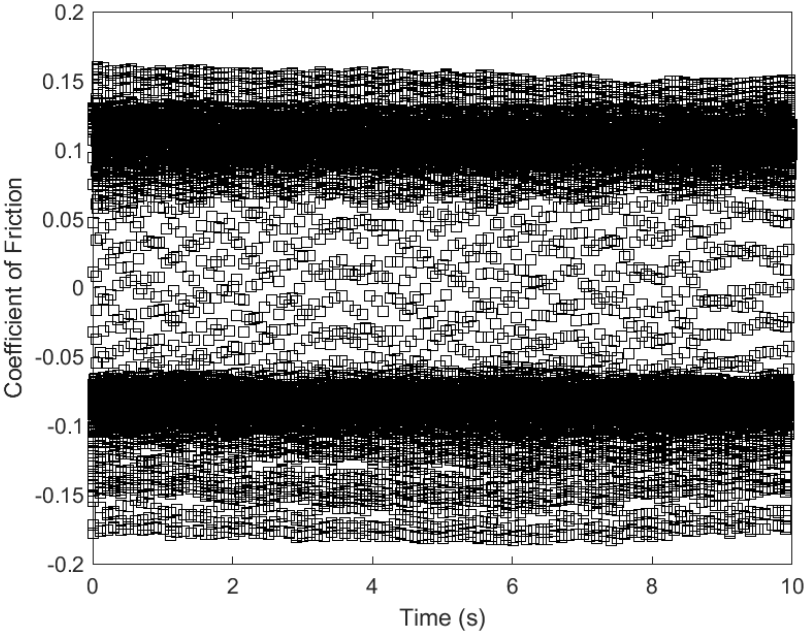

Figure A.26: First Set of Data, Sliding Frequency 10 Hz, Applied Load 100 N, Lubricant Temperature 30 °C

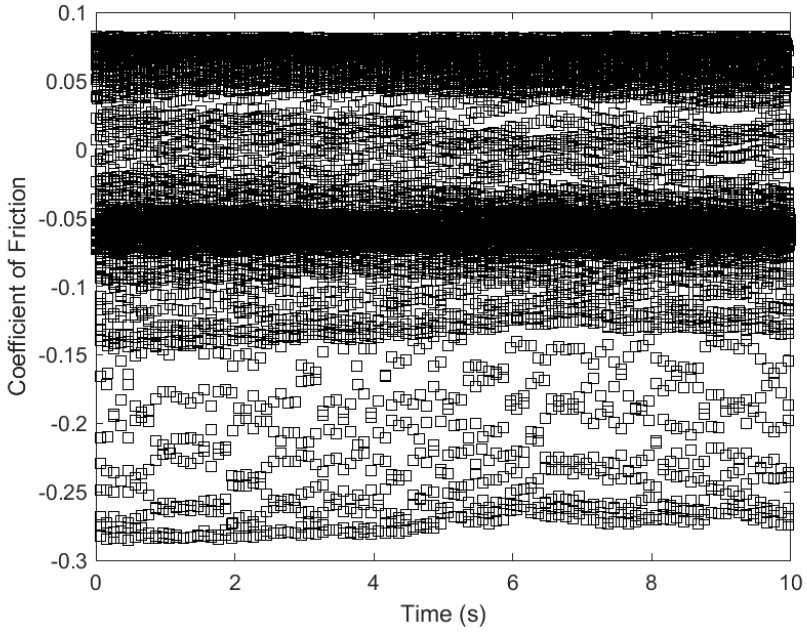

Figure A.27: First Set of Data, Sliding Frequency 10 Hz, Applied Load 150 N, Lubricant Temperature 30 °C

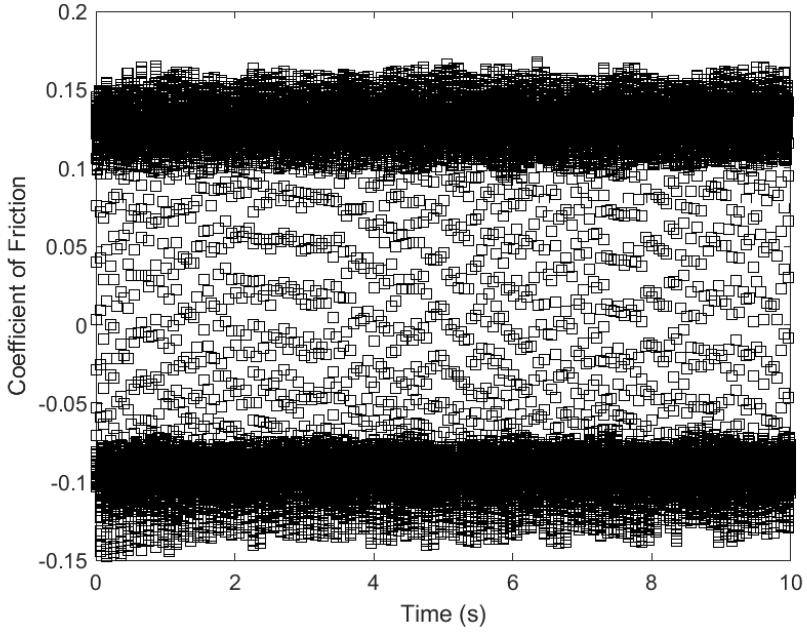

Figure A.28: First Set of Data, Sliding Frequency 10 Hz, Applied Load 50 N, Lubricant Temperature 50 °C

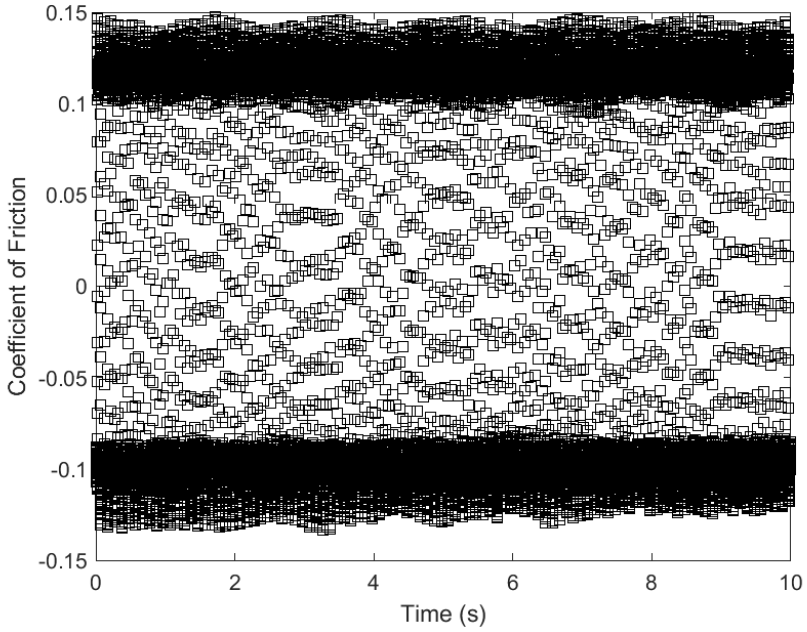

Figure A.29: First Set of Data, Sliding Frequency 10 Hz, Applied Load 100 N, Lubricant Temperature 50 °C

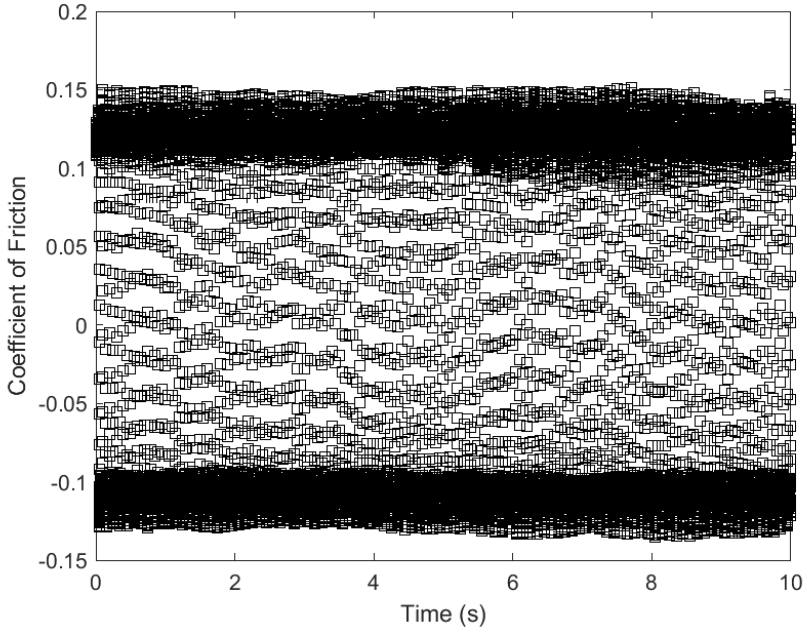

Figure A.30: First Set of Data, Sliding Frequency 10 Hz, Applied Load 150 N, Lubricant Temperature 50 °C

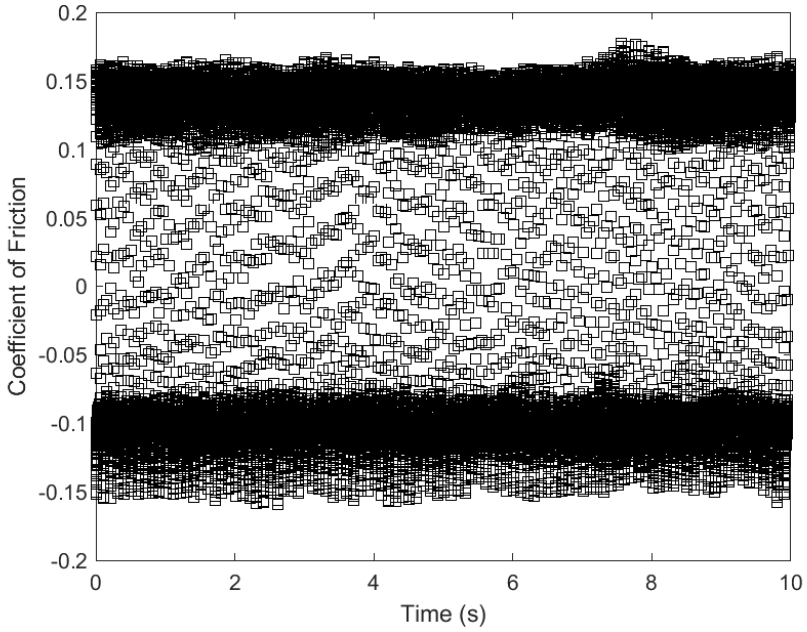

Figure A.31: First Set of Data, Sliding Frequency 10 Hz, Applied Load 50 N, Lubricant Temperature 80 °C

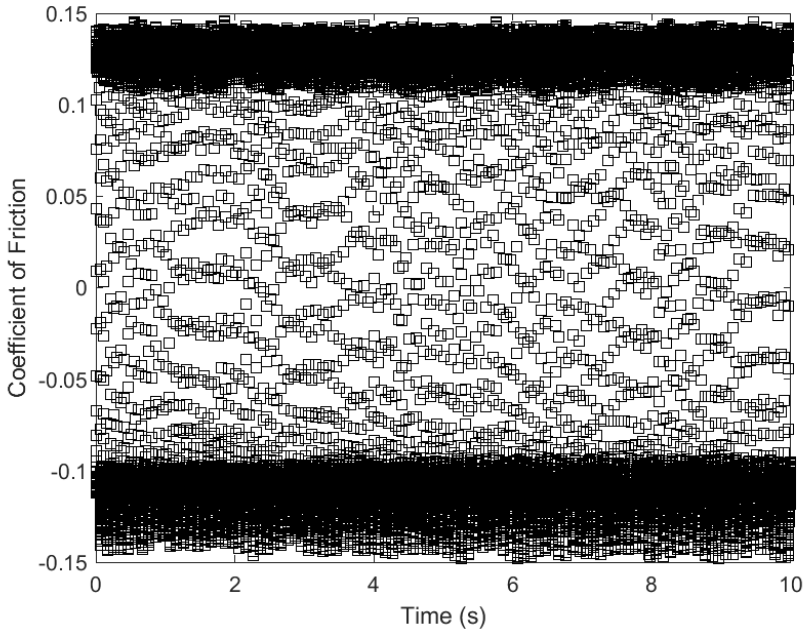

Figure A.32: First Set of Data, Sliding Frequency 10 Hz, Applied Load 100 N, Lubricant Temperature 80 °C

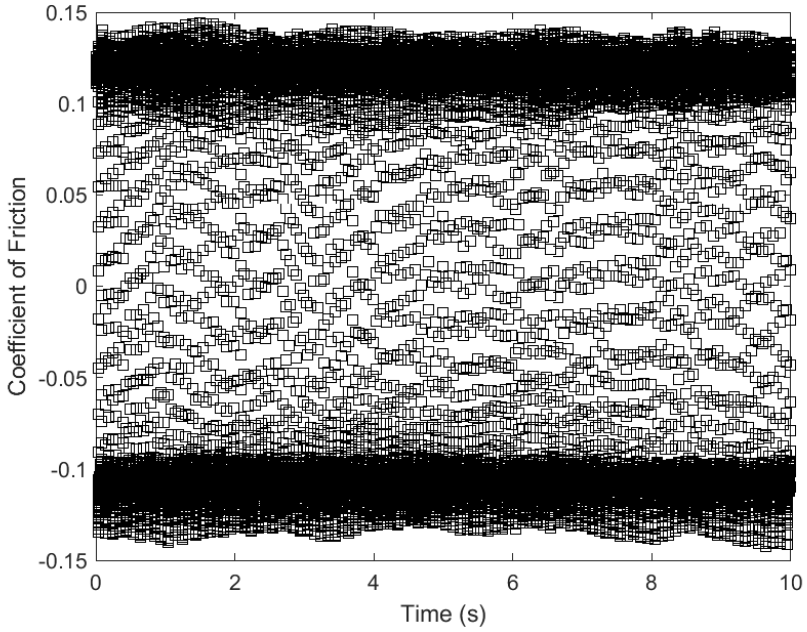

Figure A.33: First Set of Data, Sliding Frequency 10 Hz, Applied Load 150 N, Lubricant Temperature 80 °C

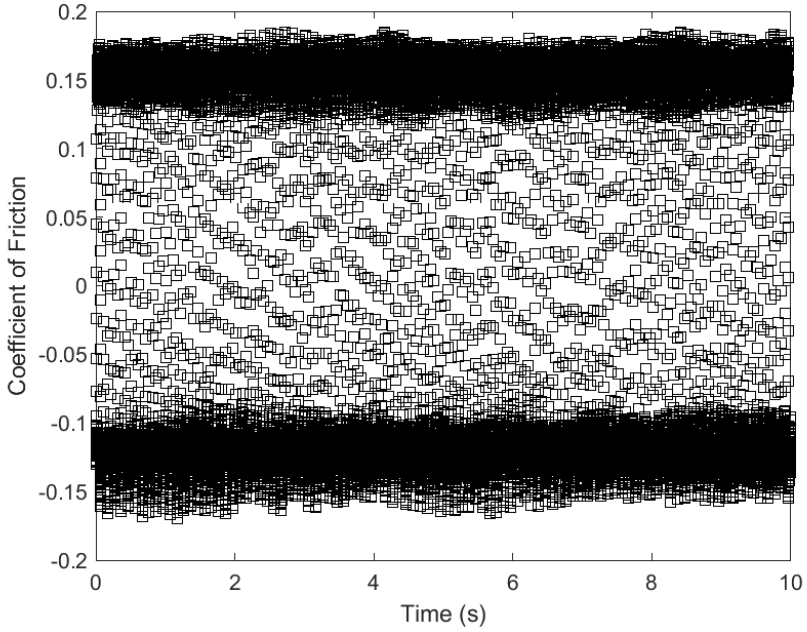

Figure A.34: First Set of Data, Sliding Frequency 10 Hz, Applied Load 50 N, Lubricant Temperature 120 °C

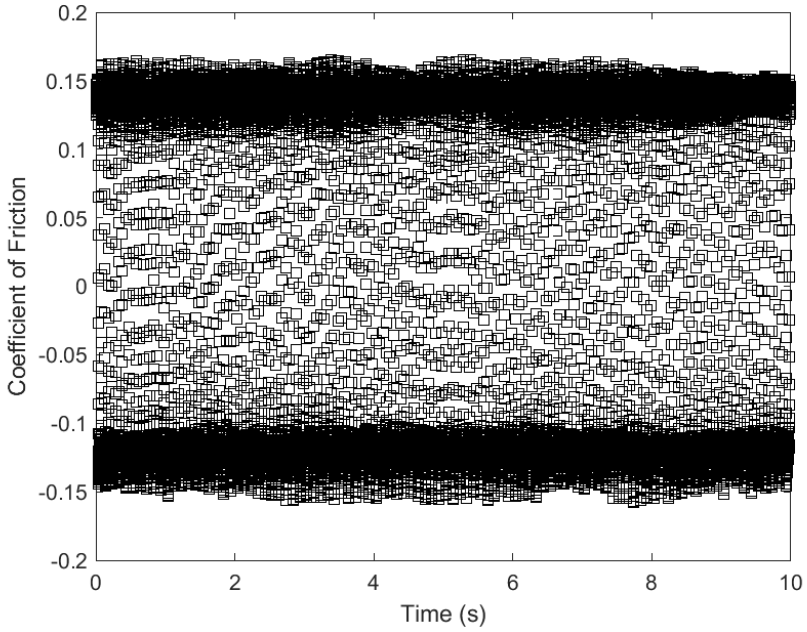

Figure A.35: First Set of Data, Sliding Frequency 10 Hz, Applied Load 100 N, Lubricant Temperature 120 °C

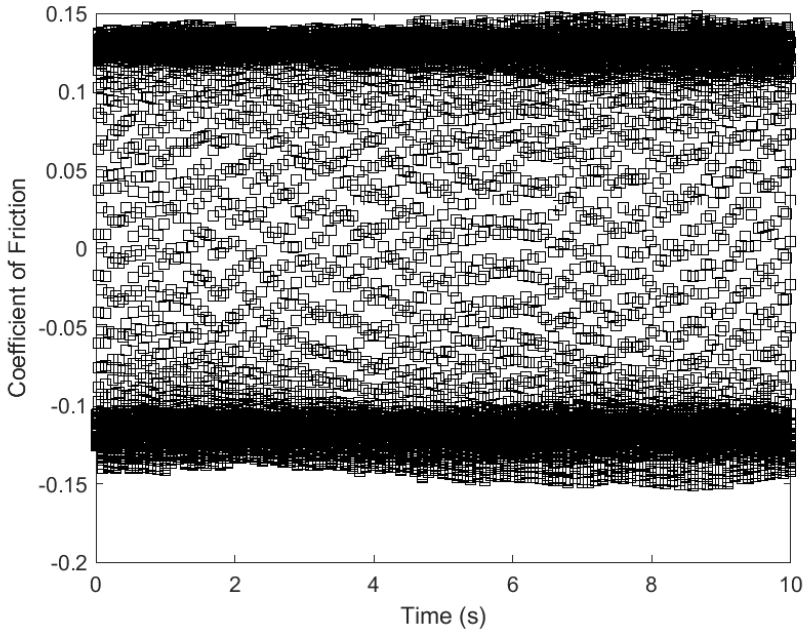

Figure A.36: First Set of Data, Sliding Frequency 10 Hz, Applied Load 150 N, Lubricant Temperature 120 °C

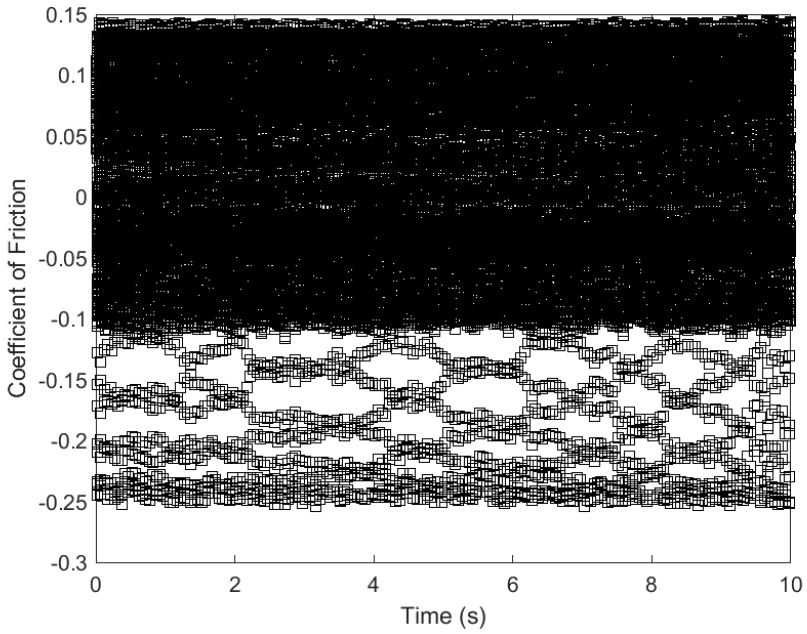

Figure A.37: First Set of Data, Sliding Frequency 20 Hz, Applied Load 50 N, Lubricant Temperature 30 °C

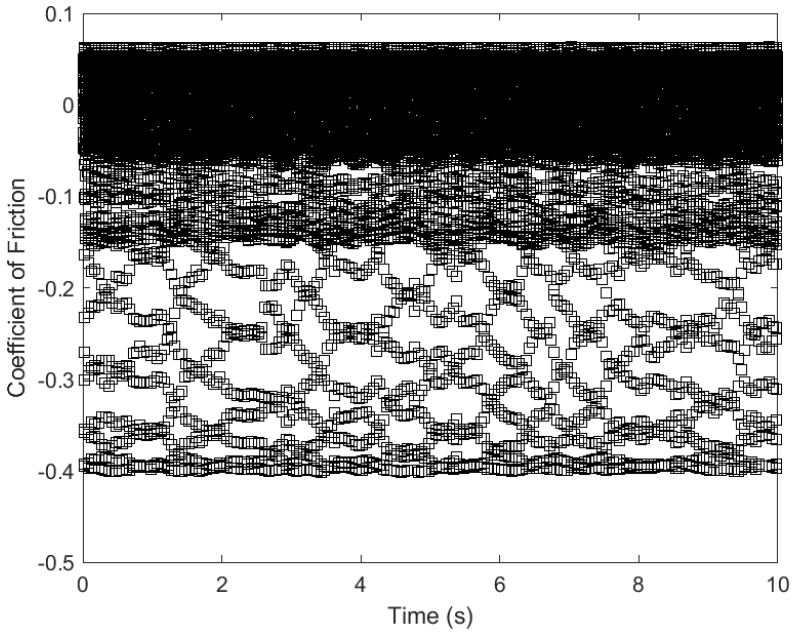

Figure A.38: First Set of Data, Sliding Frequency 20 Hz, Applied Load 100 N, Lubricant Temperature 30 °C

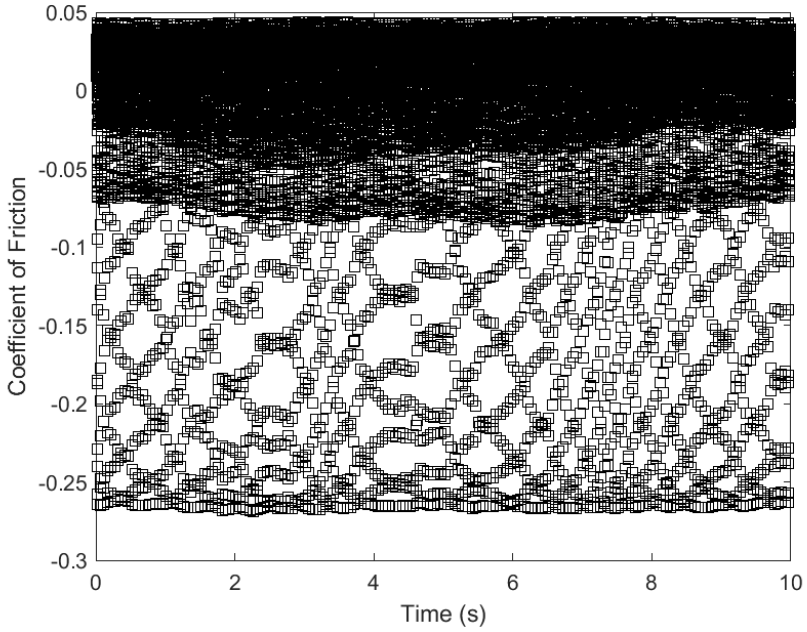

Figure A.39: First Set of Data, Sliding Frequency 20 Hz, Applied Load 150 N, Lubricant Temperature 30 °C

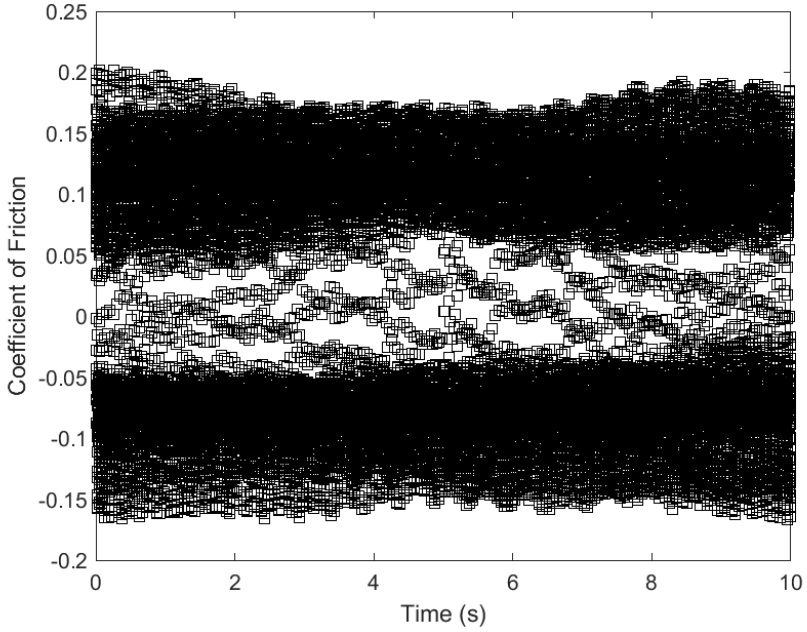

Figure A.40: First Set of Data, Sliding Frequency 20 Hz, Applied Load 50 N, Lubricant Temperature 50 °C

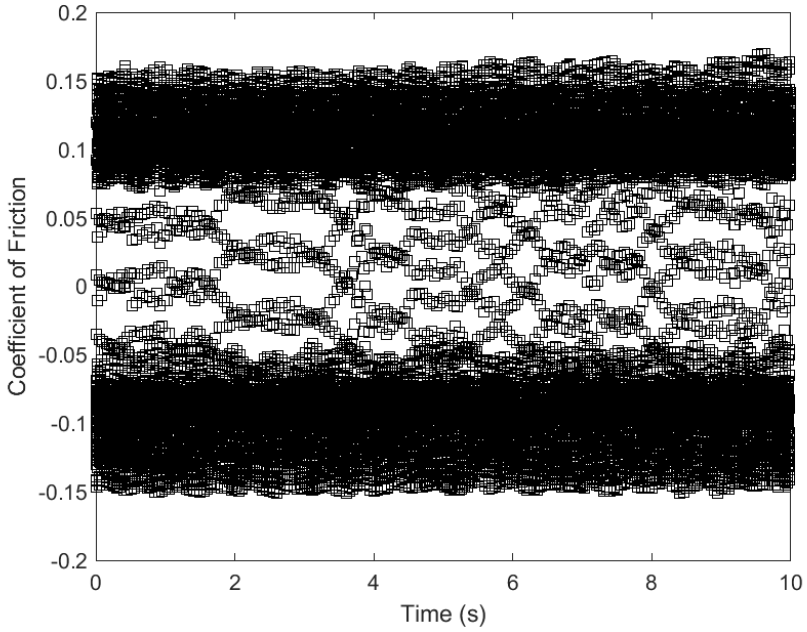

Figure A.41: First Set of Data, Sliding Frequency 20 Hz, Applied Load 100 N, Lubricant Temperature 50 °C

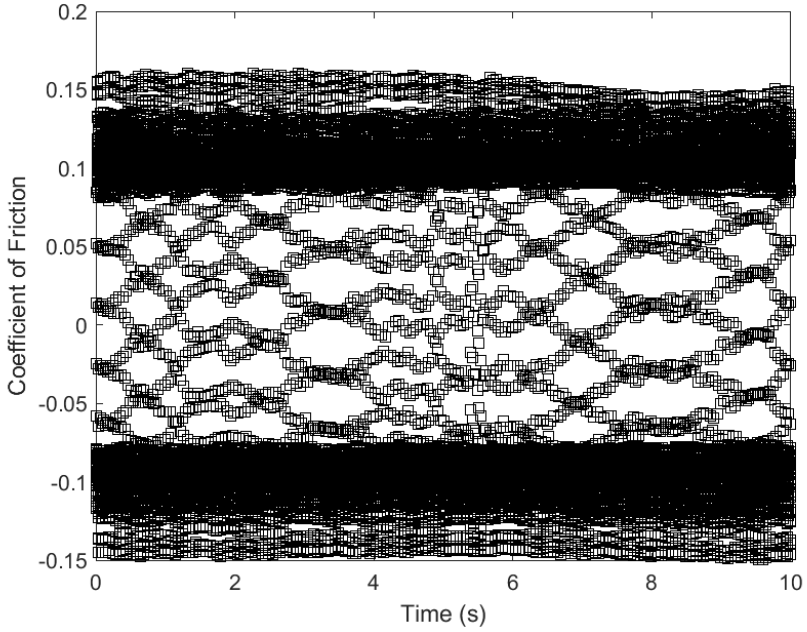

Figure A.42: First Set of Data, Sliding Frequency 20 Hz, Applied Load 150 N, Lubricant Temperature 50 °C

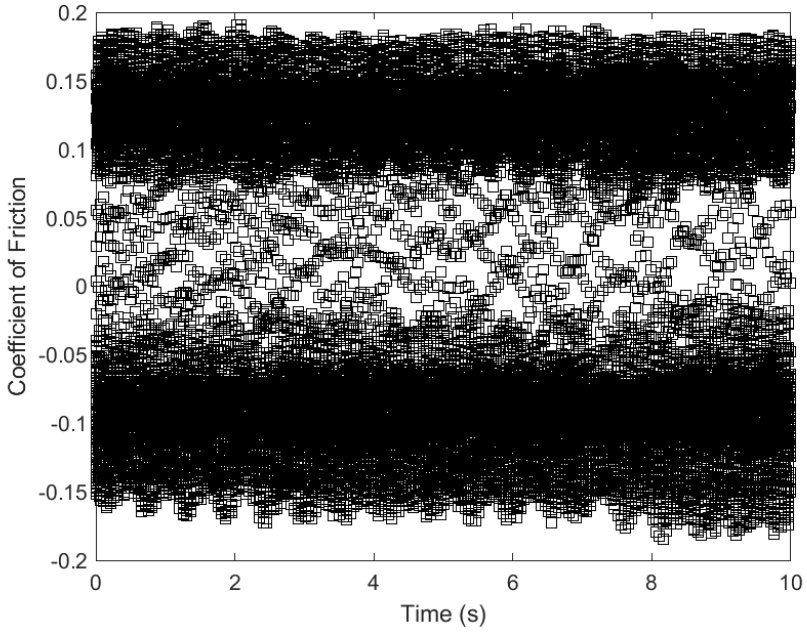

Figure A.43: First Set of Data, Sliding Frequency 20 Hz, Applied Load 50 N, Lubricant Temperature 80 °C

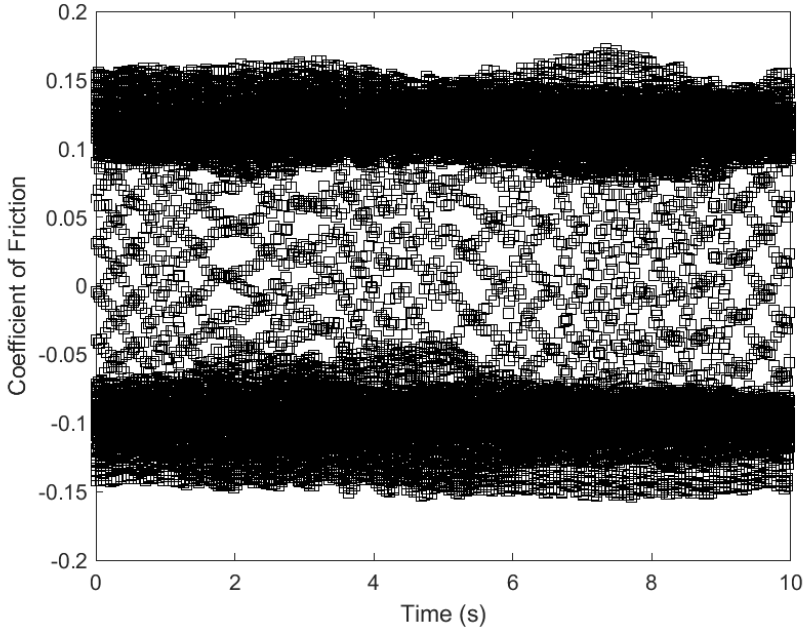

Figure A.44: First Set of Data, Sliding Frequency 20 Hz, Applied Load 100 N, Lubricant Temperature 80 °C

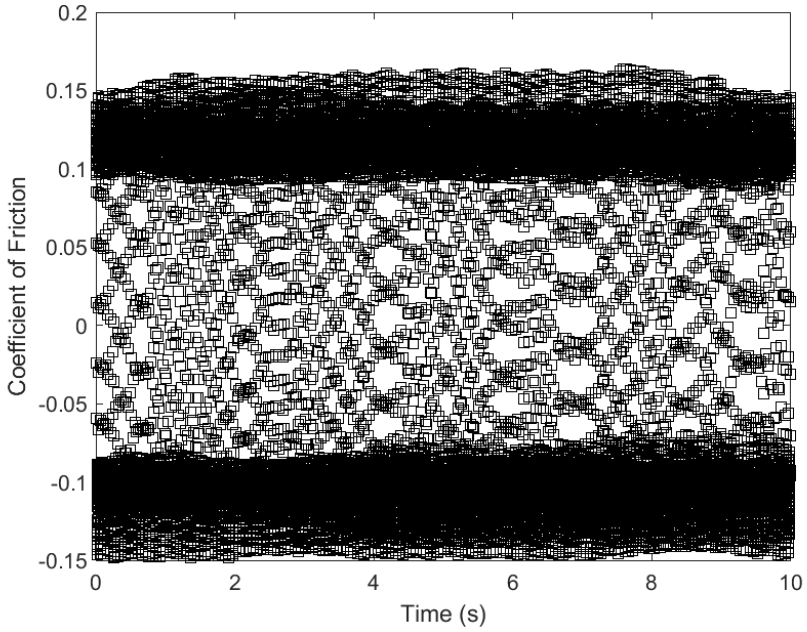

Figure A.45: First Set of Data, Sliding Frequency 20 Hz, Applied Load 150 N, Lubricant Temperature 80 °C

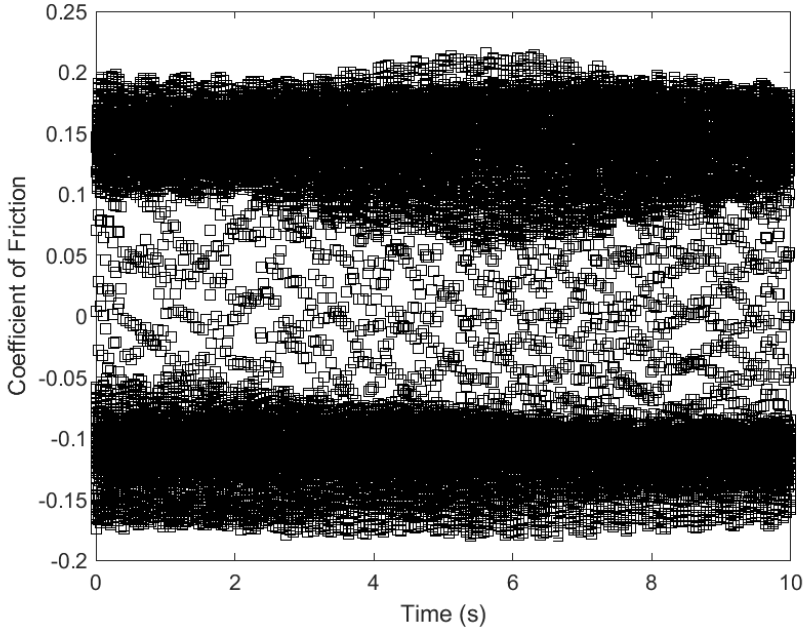

Figure A.46: First Set of Data, Sliding Frequency 20 Hz, Applied Load 50 N, Lubricant Temperature 120 °C

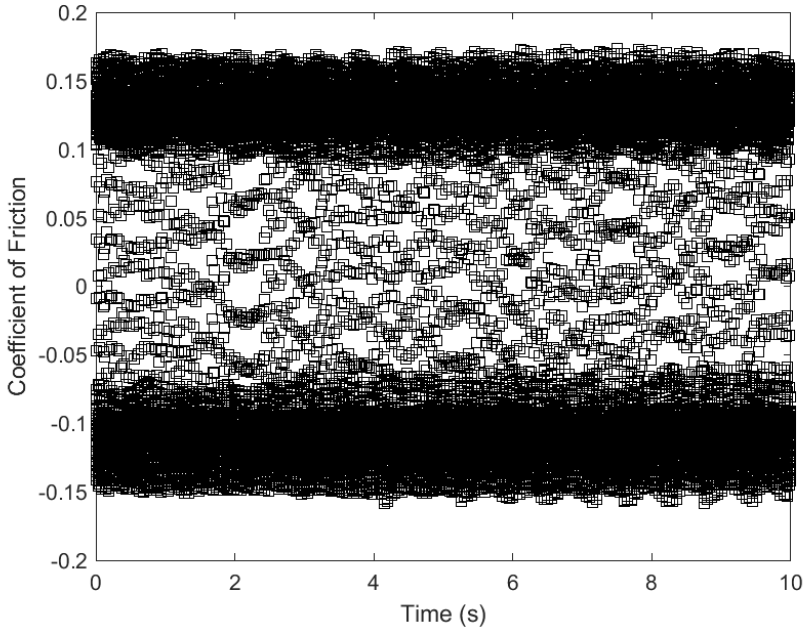

Figure A.47: First Set of Data, Sliding Frequency 20 Hz, Applied Load 100 N, Lubricant Temperature 120 °C

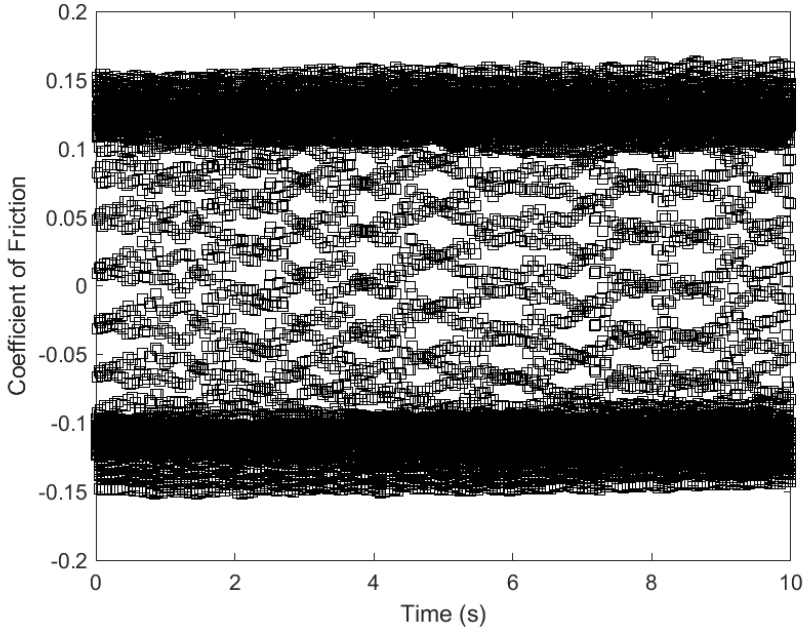

Figure A.48: First Set of Data, Sliding Frequency 20 Hz, Applied Load 150 N, Lubricant Temperature 120 °C

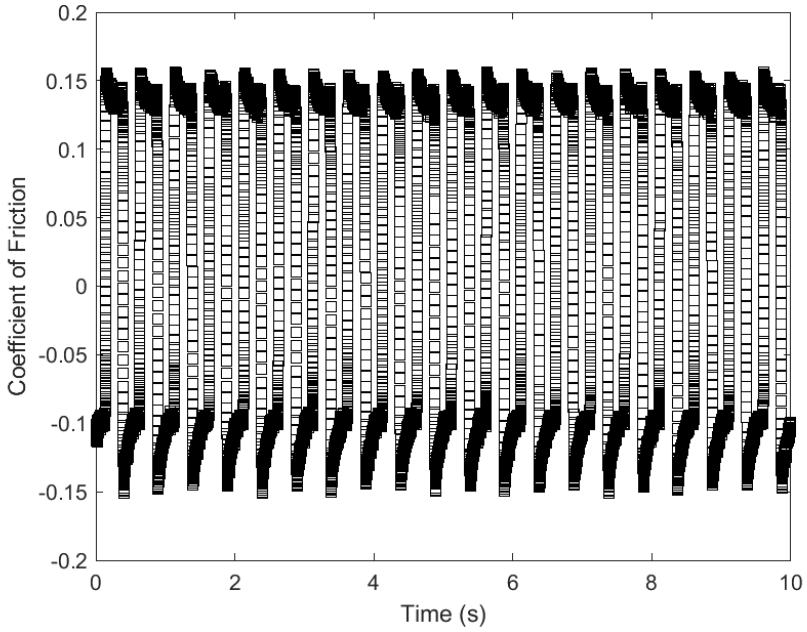

Figure A.49: Second Set of Data, Sliding Frequency 2 Hz, Applied Load 50 N, Lubricant Temperature 30 °C

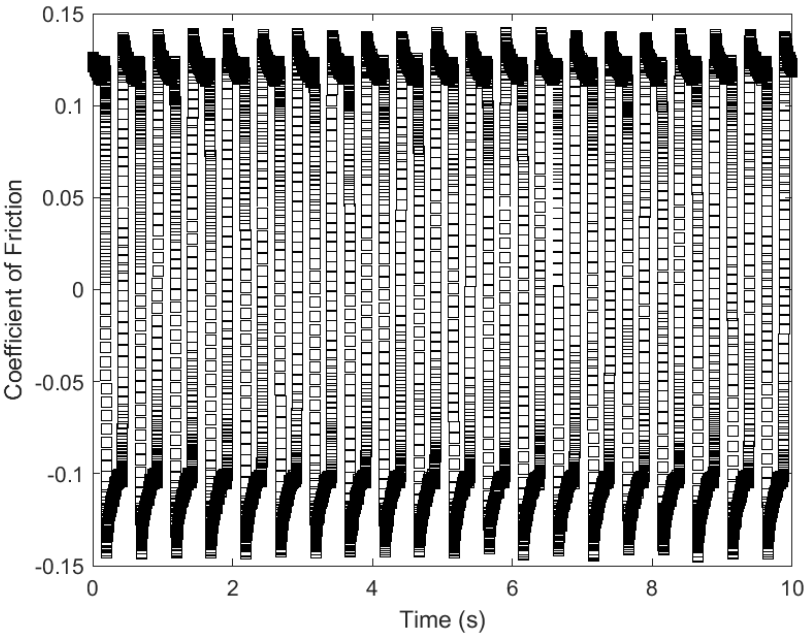

Figure A.50: Second Set of Data, Sliding Frequency 2 Hz, Applied Load 100 N, Lubricant Temperature 30 °C

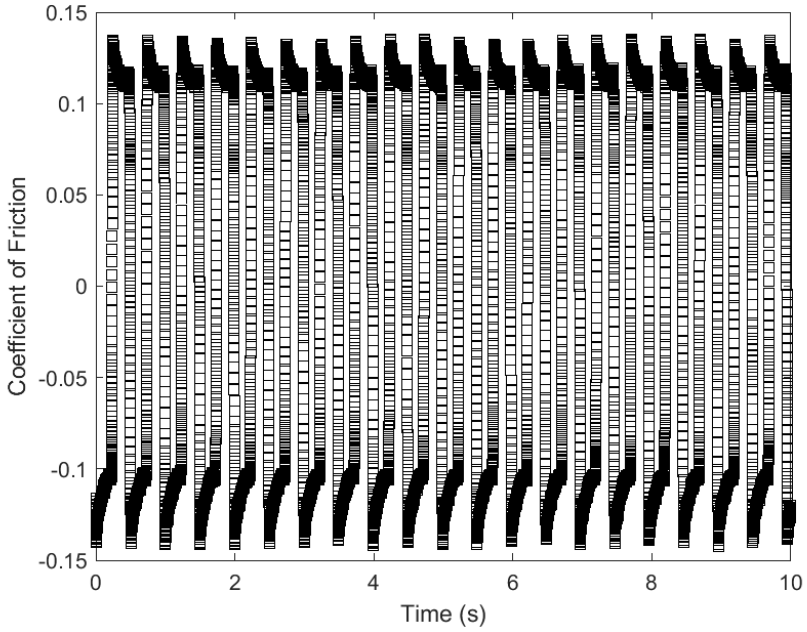

Figure A.51: Second Set of Data, Sliding Frequency 2 Hz, Applied Load 150 N, Lubricant Temperature 30 °C

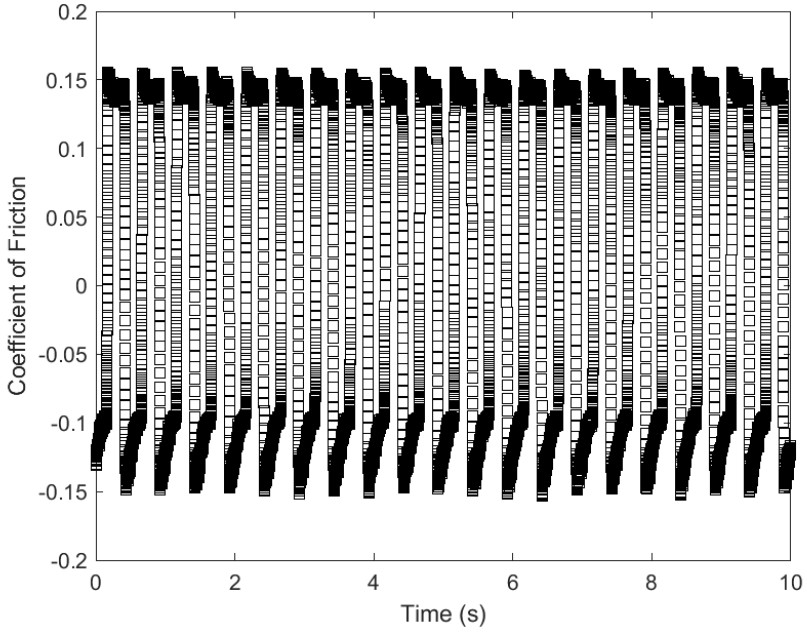

Figure A.52: Second Set of Data, Sliding Frequency 2 Hz, Applied Load 50 N, Lubricant Temperature 50 °C

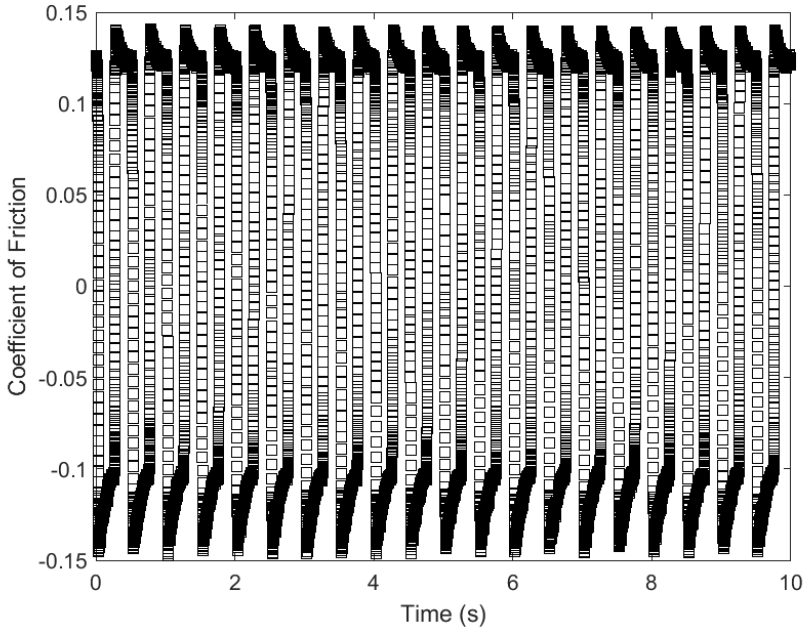

Figure A.53: Second Set of Data, Sliding Frequency 2 Hz, Applied Load 100 N, Lubricant Temperature 50 °C

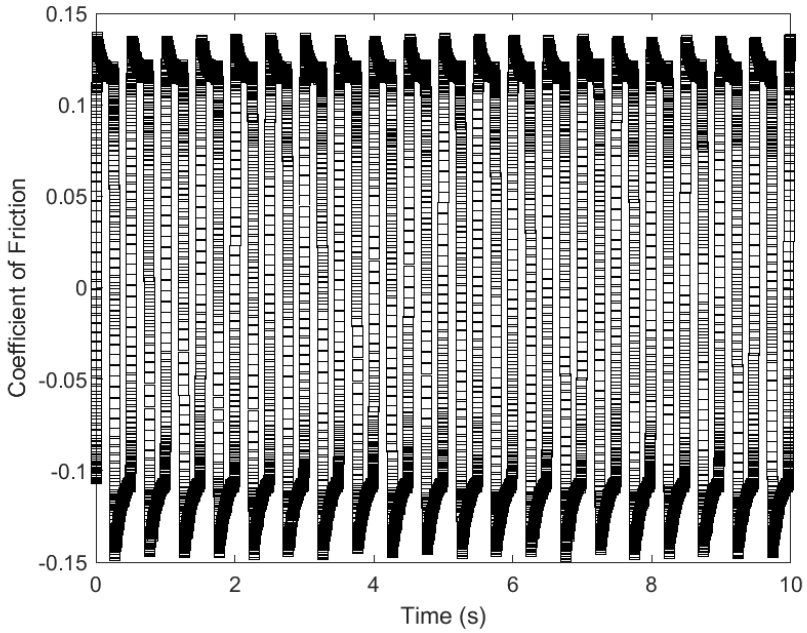

Figure A.54: Second Set of Data, Sliding Frequency 2 Hz, Applied Load 150 N, Lubricant Temperature 50 °C

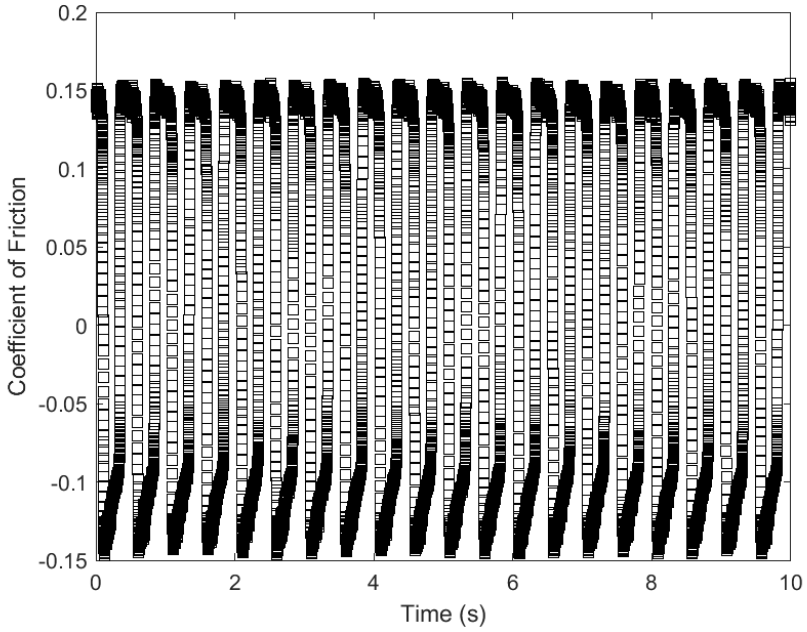

Figure A.55: Second Set of Data, Sliding Frequency 2 Hz, Applied Load 50 N, Lubricant Temperature 80 °C

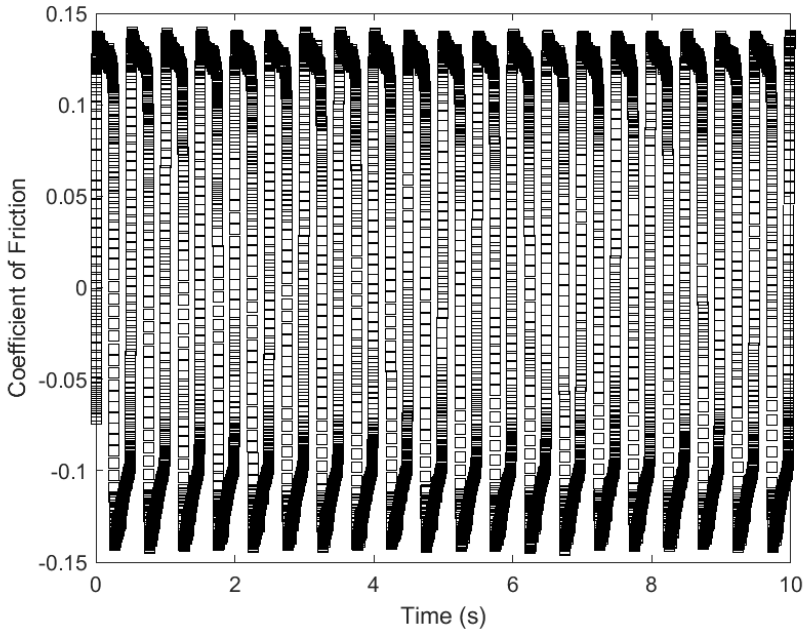

Figure A.56: Second Set of Data, Sliding Frequency 2 Hz, Applied Load 100 N, Lubricant Temperature 80 °C

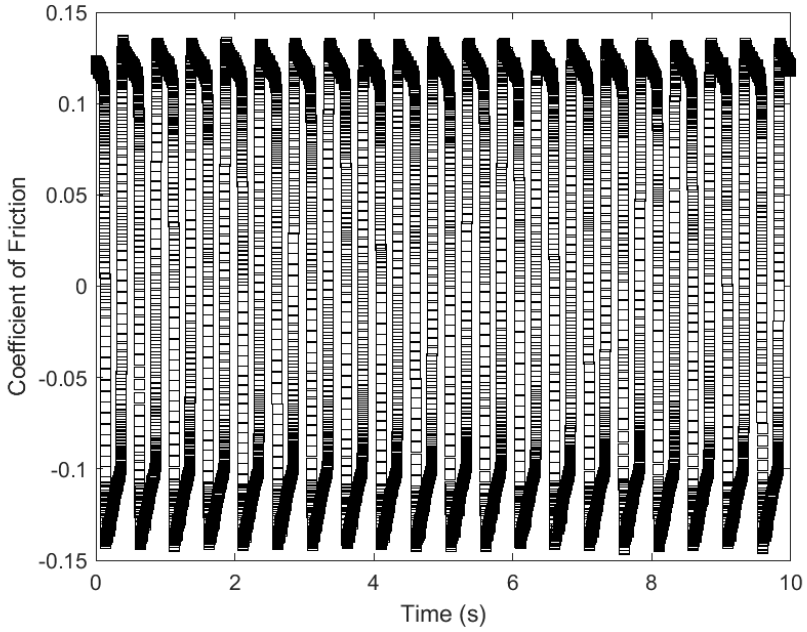

Figure A.57: Second Set of Data, Sliding Frequency 2 Hz, Applied Load 150 N, Lubricant Temperature 80 °C

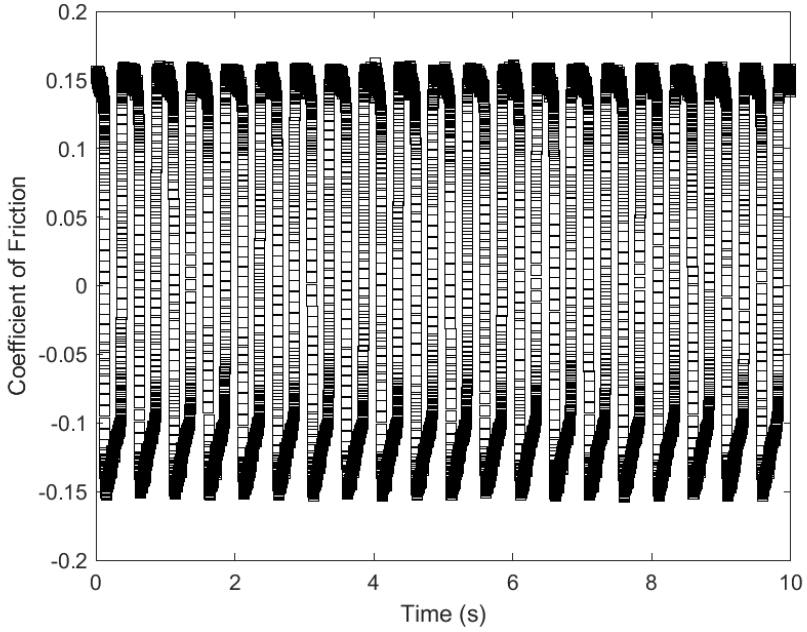

Figure A.58: Second Set of Data, Sliding Frequency 2 Hz, Applied Load 50 N, Lubricant Temperature 120 °C

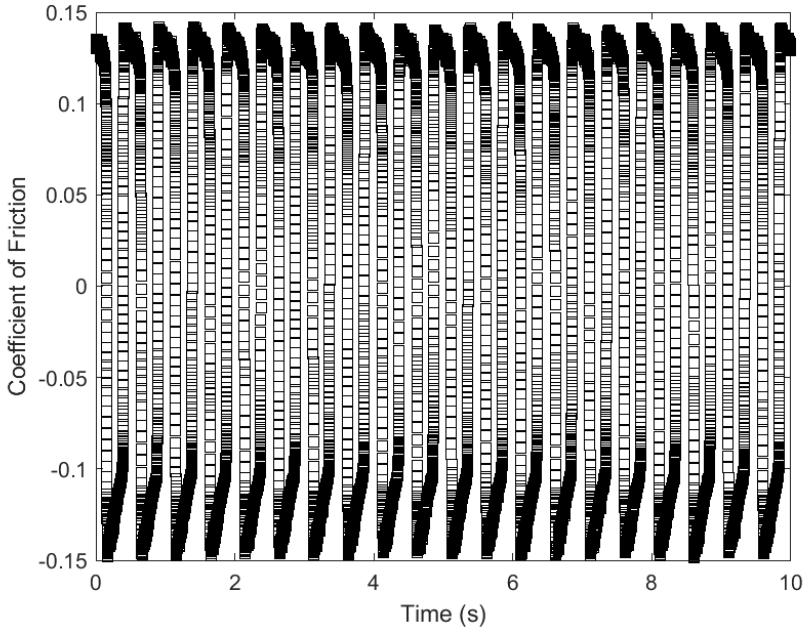

Figure A.59: Second Set of Data, Sliding Frequency 2 Hz, Applied Load 100 N, Lubricant Temperature 120 °C

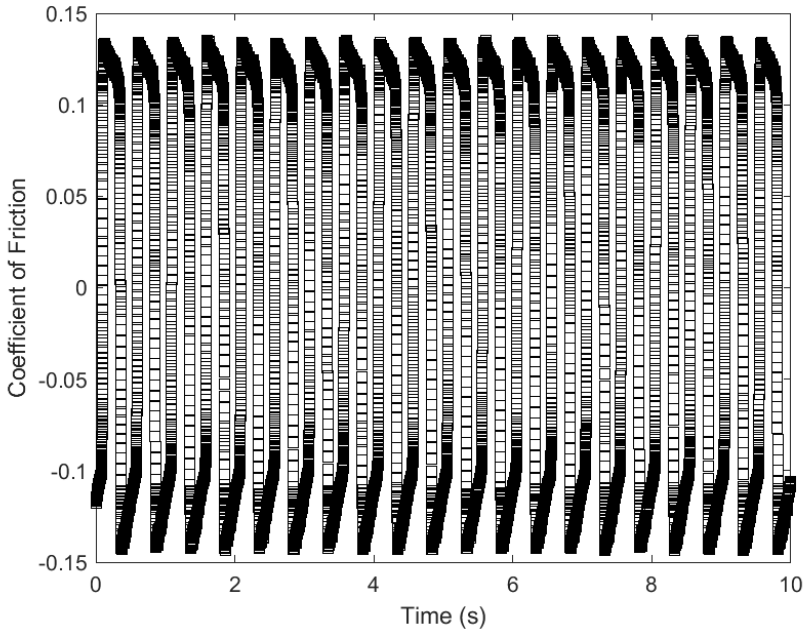

Figure A.60: Second Set of Data, Sliding Frequency 2 Hz, Applied Load 150 N, Lubricant Temperature 120 °C

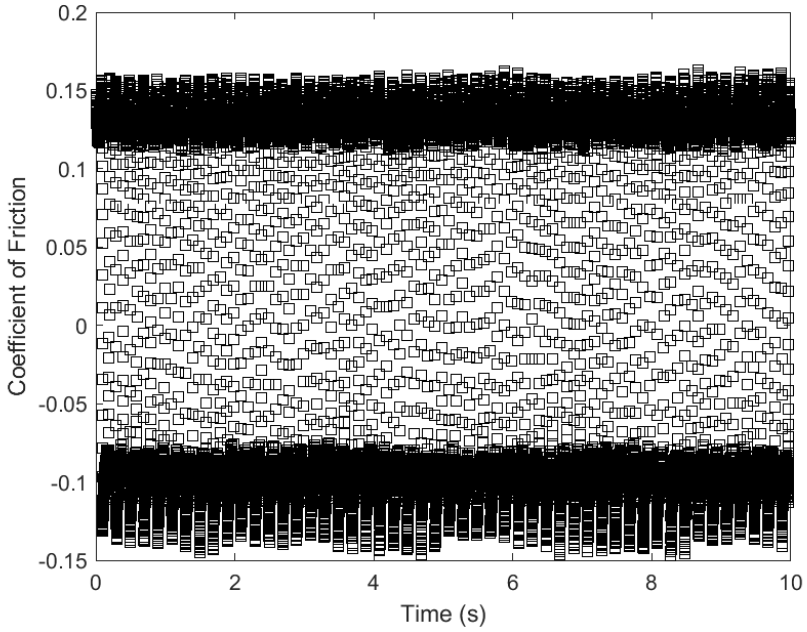

Figure A.61: Second Set of Data, Sliding Frequency 5 Hz, Applied Load 50 N, Lubricant Temperature 30 °C

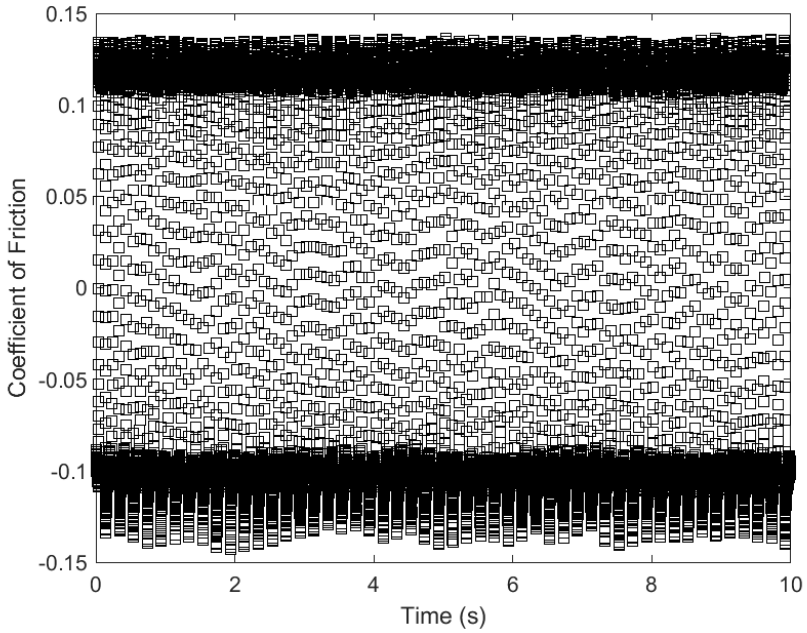

Figure A.62: Second Set of Data, Sliding Frequency 5 Hz, Applied Load 100 N, Lubricant Temperature 30 °C

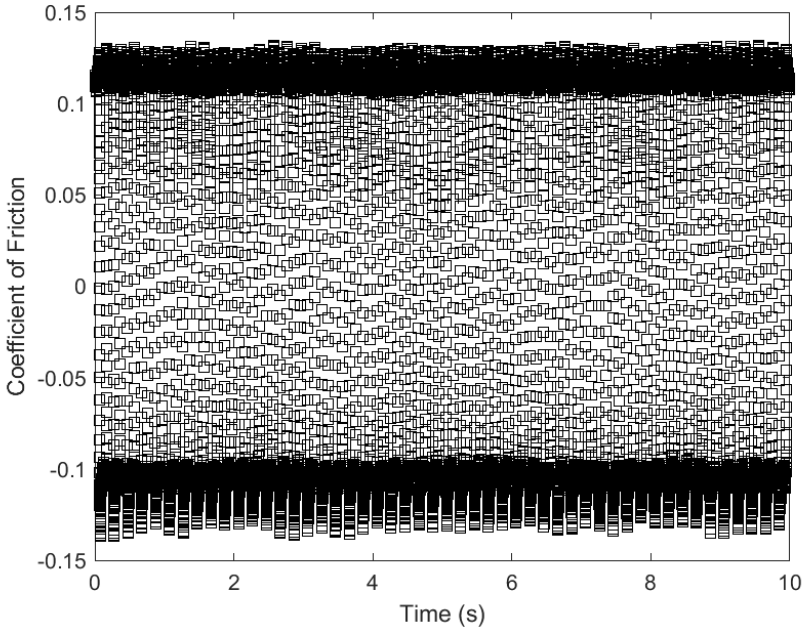

.5

Figure A.63: Second Set of Data, Sliding Frequency 5 Hz, Applied Load 150 N, Lubricant Temperature 30 °C

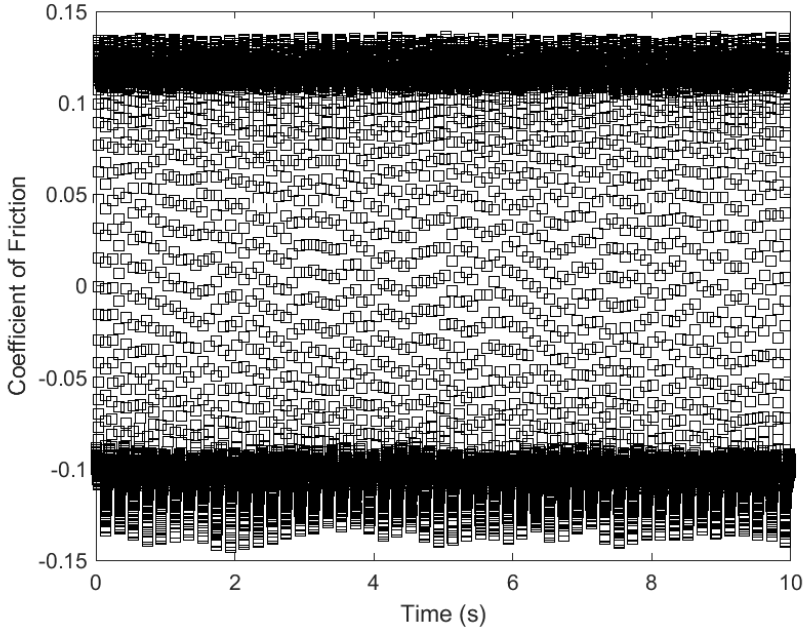

Figure A.64: Second Set of Data, Sliding Frequency 5 Hz, Applied Load 50 N, Lubricant Temperature 50 °C

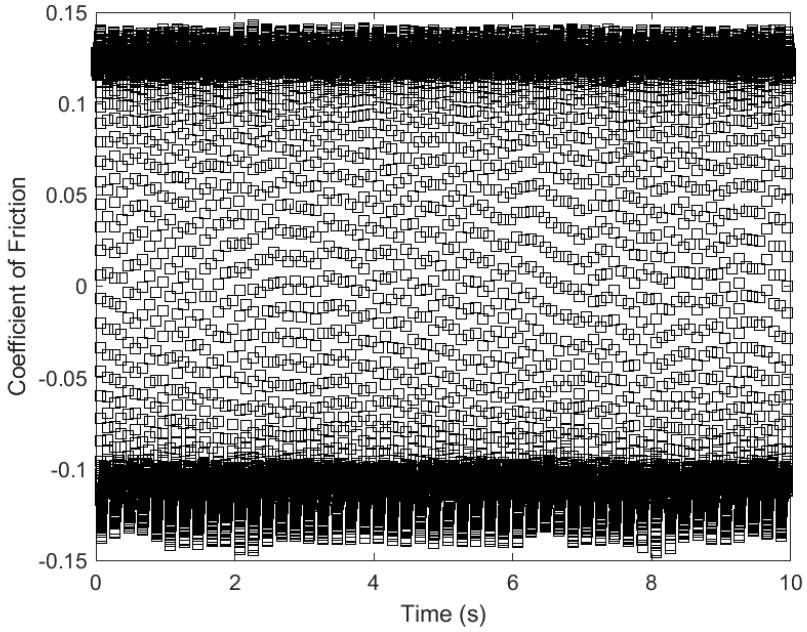

Figure A.65: Second Set of Data, Sliding Frequency 5 Hz, Applied Load 100 N, Lubricant Temperature 50 °C

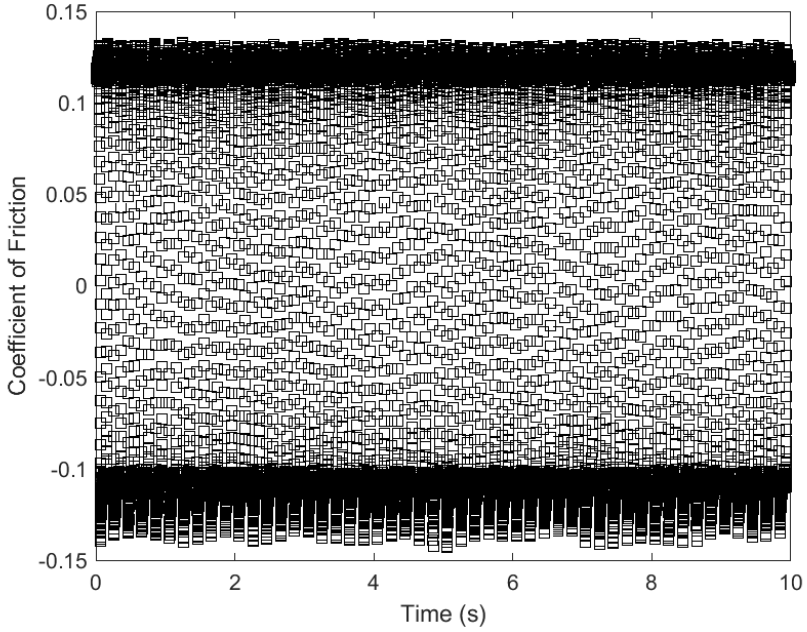

Figure A.66: Second Set of Data, Sliding Frequency 5 Hz, Applied Load 150 N, Lubricant Temperature 50 °C

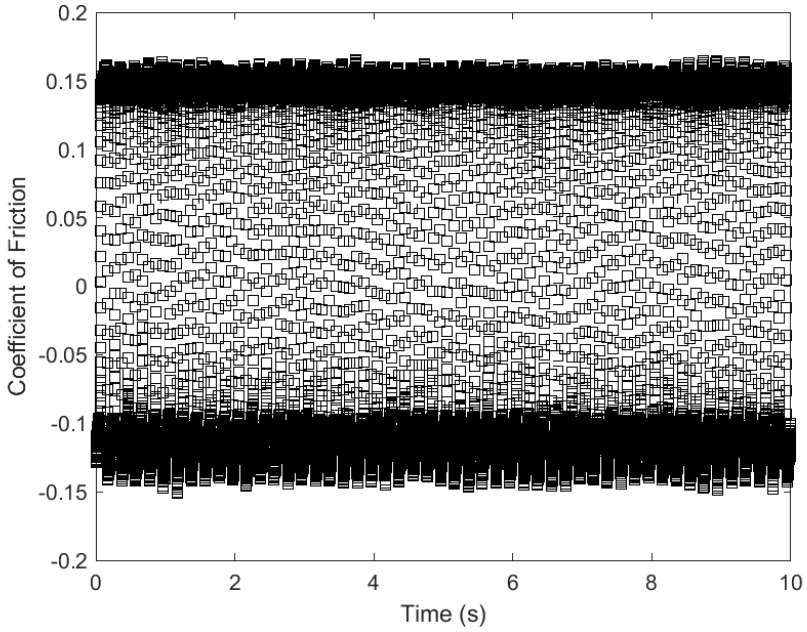

Figure A.67: Second Set of Data, Sliding Frequency 5 Hz, Applied Load 50 N, Lubricant Temperature 80 °C

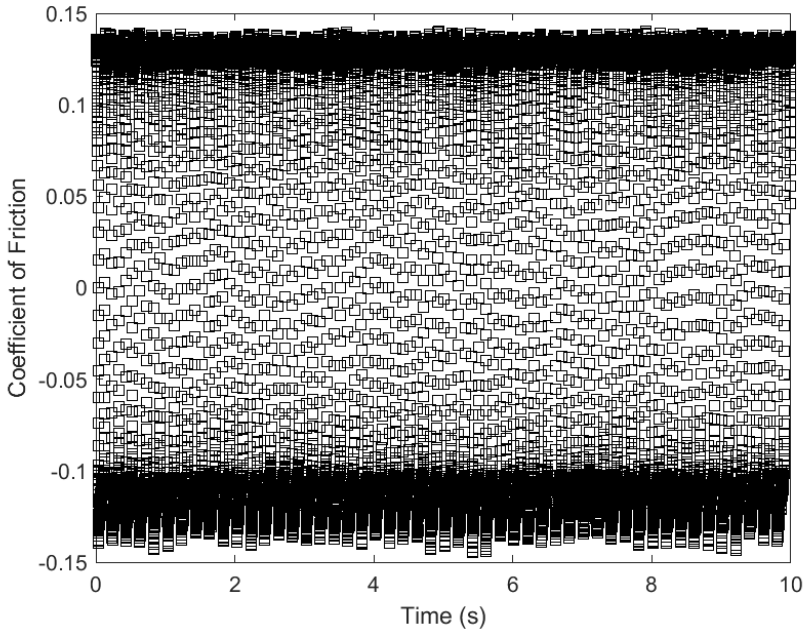

Figure A.68: Second Set of Data, Sliding Frequency 5 Hz, Applied Load 100 N, Lubricant Temperature 80 °C

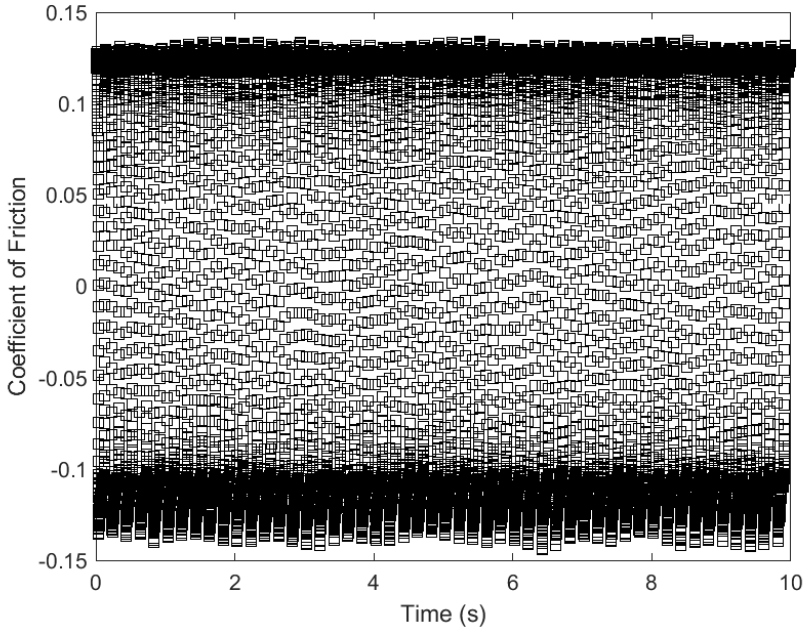

Figure A.69: Second Set of Data, Sliding Frequency 5 Hz, Applied Load 150 N, Lubricant Temperature 80 °C

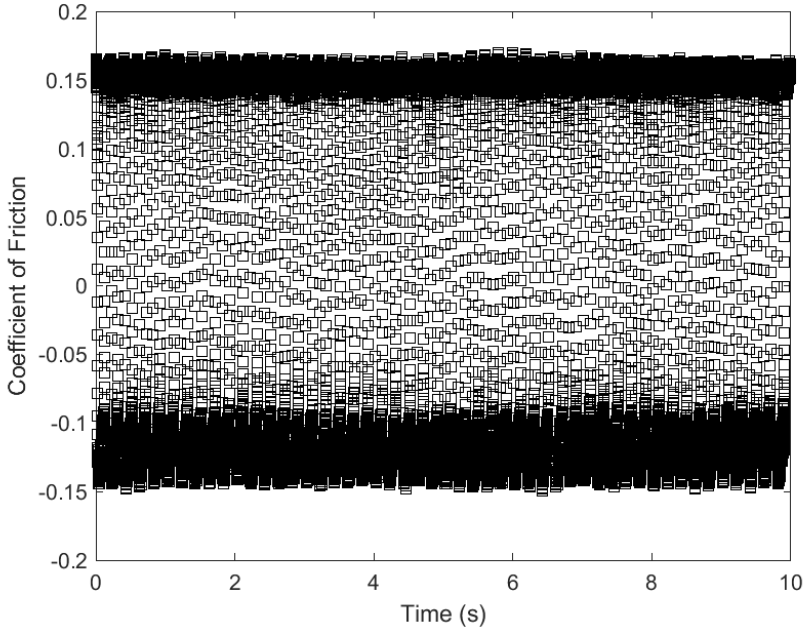

Figure A.70: Second Set of Data, Sliding Frequency 5 Hz, Applied Load 50 N, Lubricant Temperature 120 °C

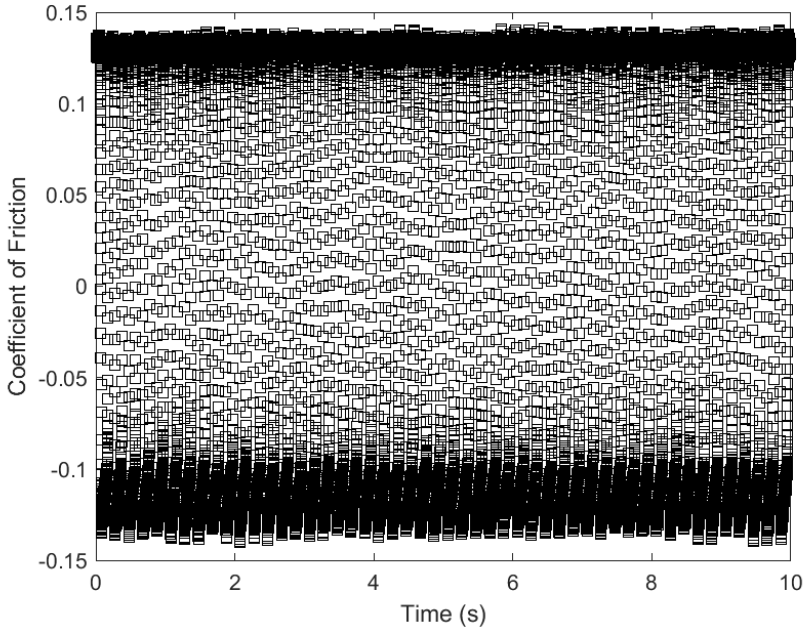

Figure A.71: Second Set of Data, Sliding Frequency 5 Hz, Applied Load 100 N, Lubricant Temperature 120 °C

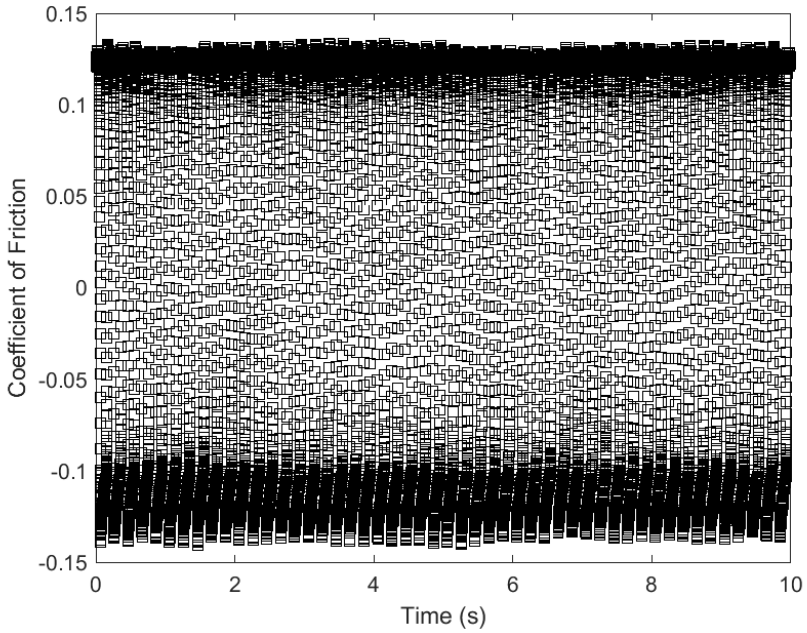

Figure A.72: Second Set of Data, Sliding Frequency 5 Hz, Applied Load 150 N, Lubricant Temperature 120 °C

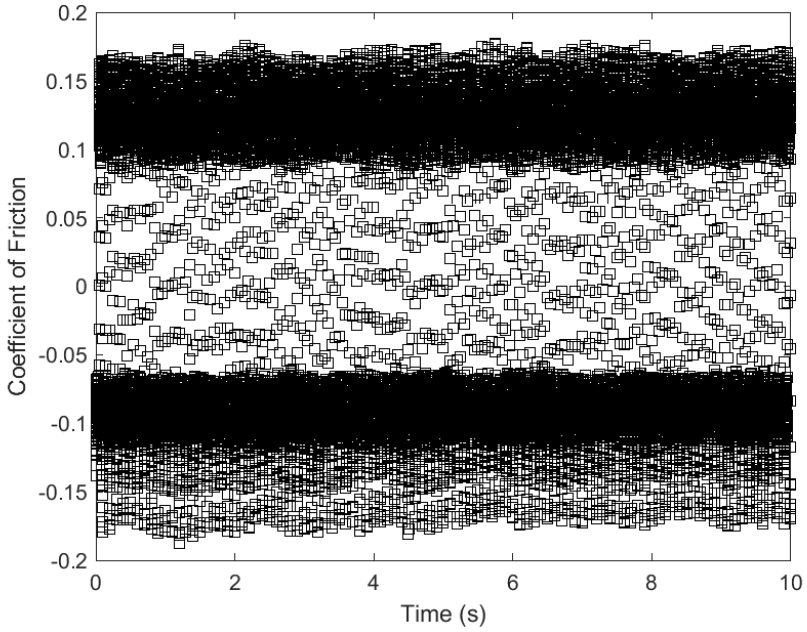

Figure A.73: Second Set of Data, Sliding Frequency 10 Hz, Applied Load 50 N, Lubricant Temperature 30 °C

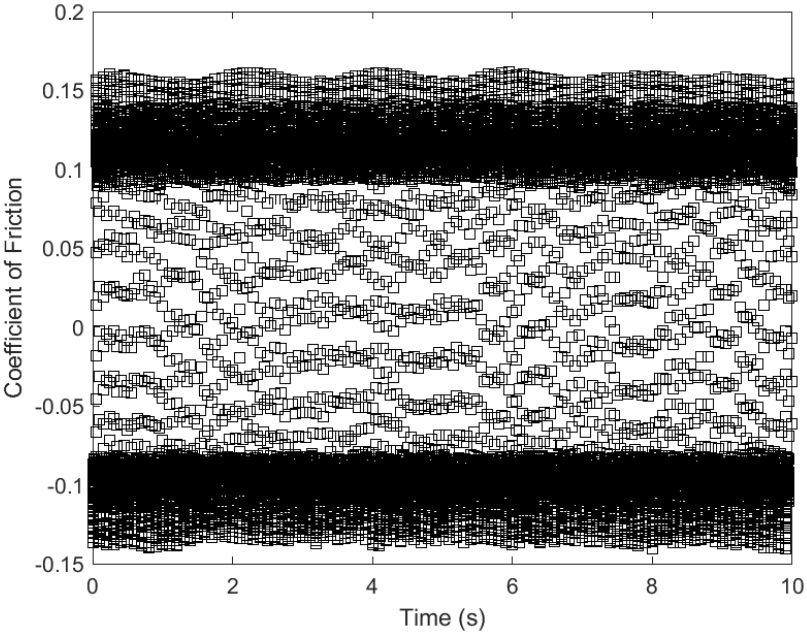

Figure A.74: Second Set of Data, Sliding Frequency 10 Hz, Applied Load 100 N, Lubricant Temperature 30 °C

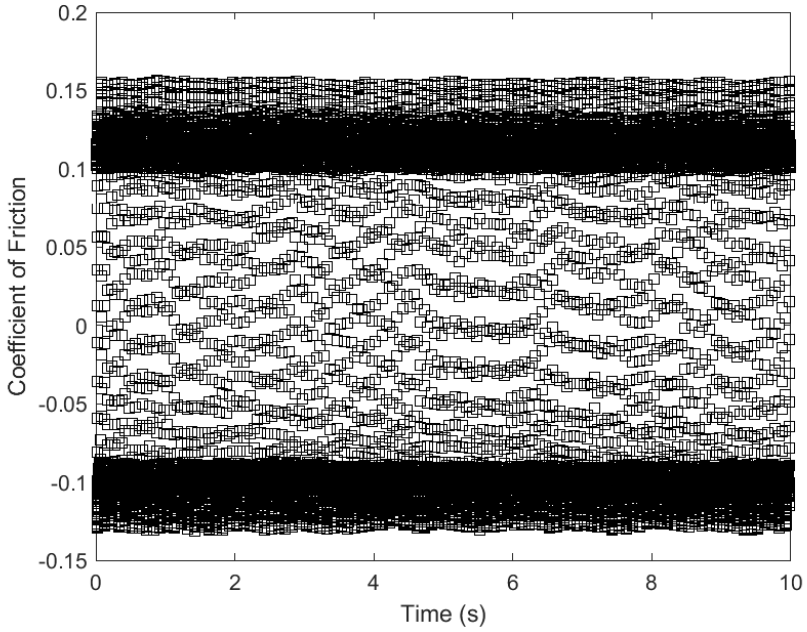

Figure A.75: Second Set of Data, Sliding Frequency 10 Hz, Applied Load 150 N, Lubricant Temperature 30 °C

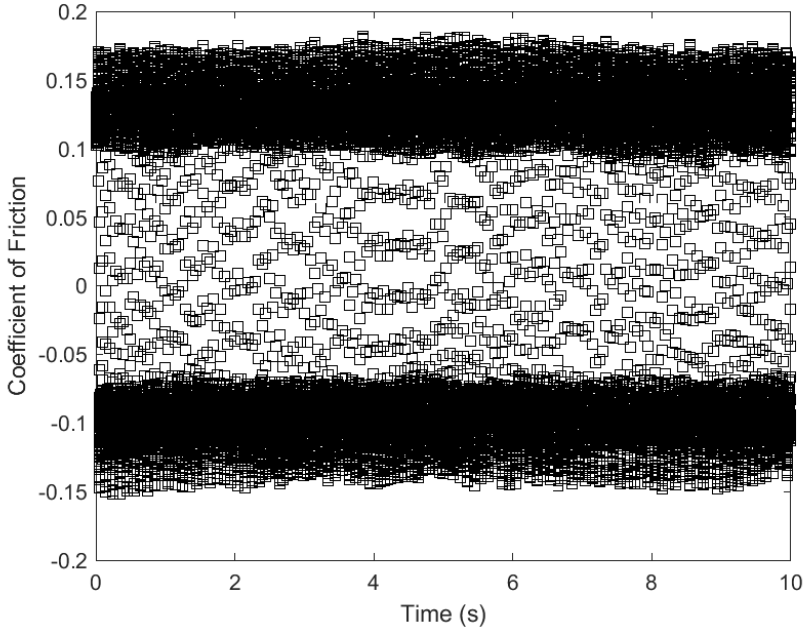

Figure A.76: Second Set of Data, Sliding Frequency 10 Hz, Applied Load 50 N, Lubricant Temperature 50 °C

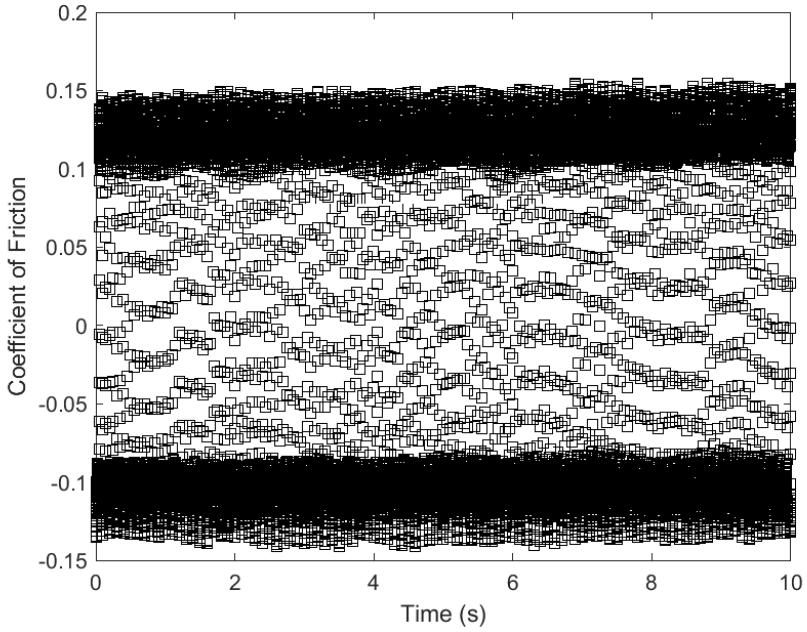

Figure A.77: Second Set of Data, Sliding Frequency 10 Hz, Applied Load 100 N, Lubricant Temperature 50 °C

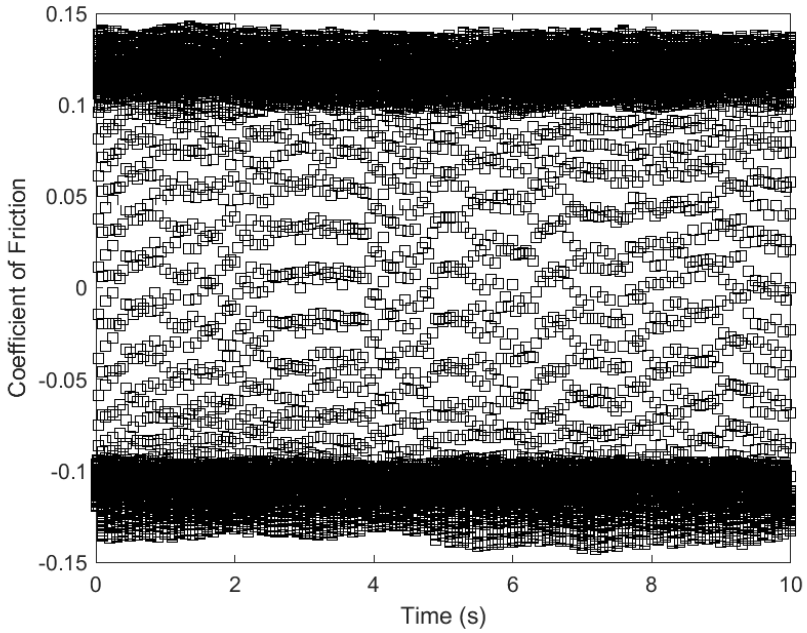

Figure A.78: Second Set of Data, Sliding Frequency 10 Hz, Applied Load 150 N, Lubricant Temperature 50 °C

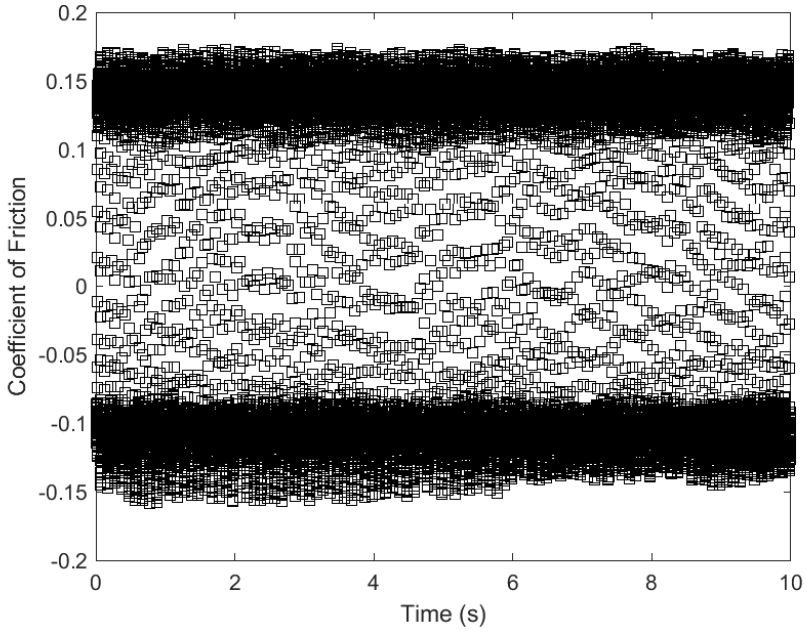

Figure A.79: Second Set of Data, Sliding Frequency 10 Hz, Applied Load 50 N, Lubricant Temperature 80 °C

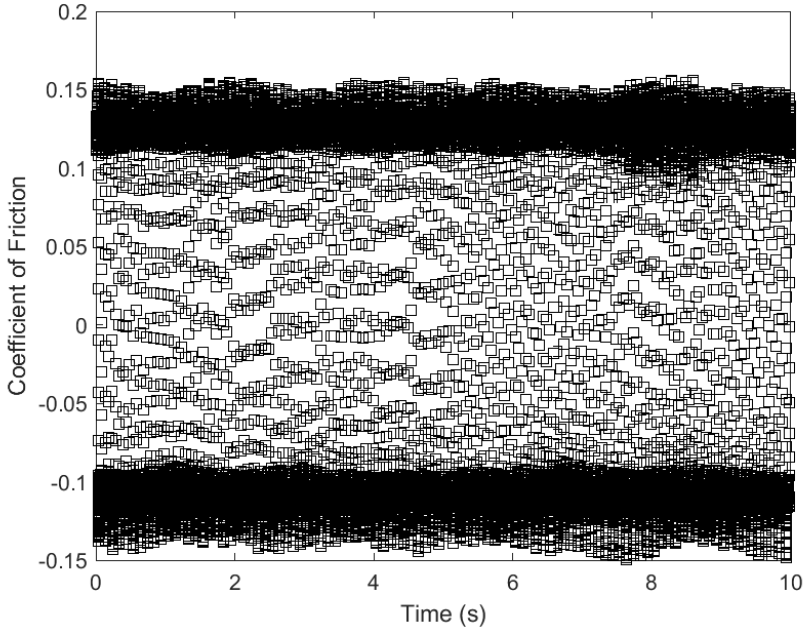

Figure A.80: Second Set of Data, Sliding Frequency 10 Hz, Applied Load 100 N, Lubricant Temperature 80 °C

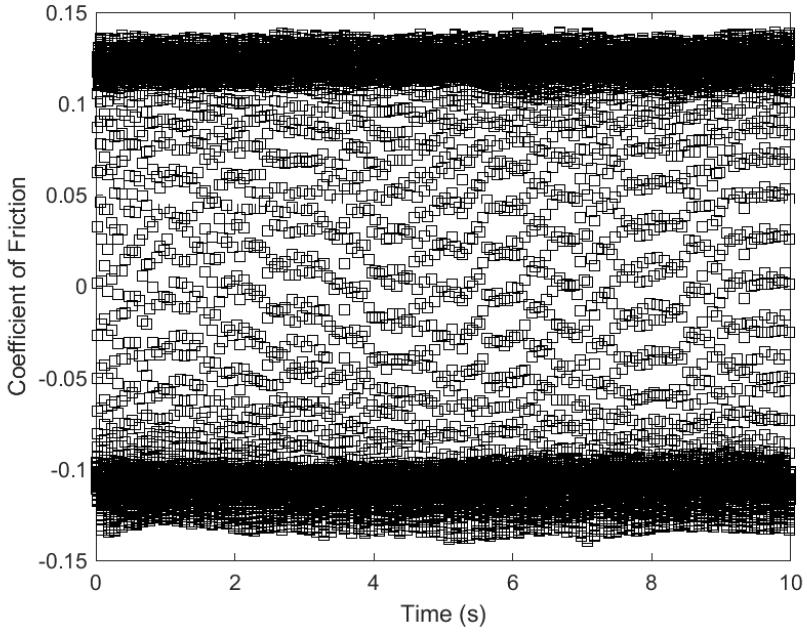

Figure A.81: Second Set of Data, Sliding Frequency 10 Hz, Applied Load 150 N, Lubricant Temperature 80 °C

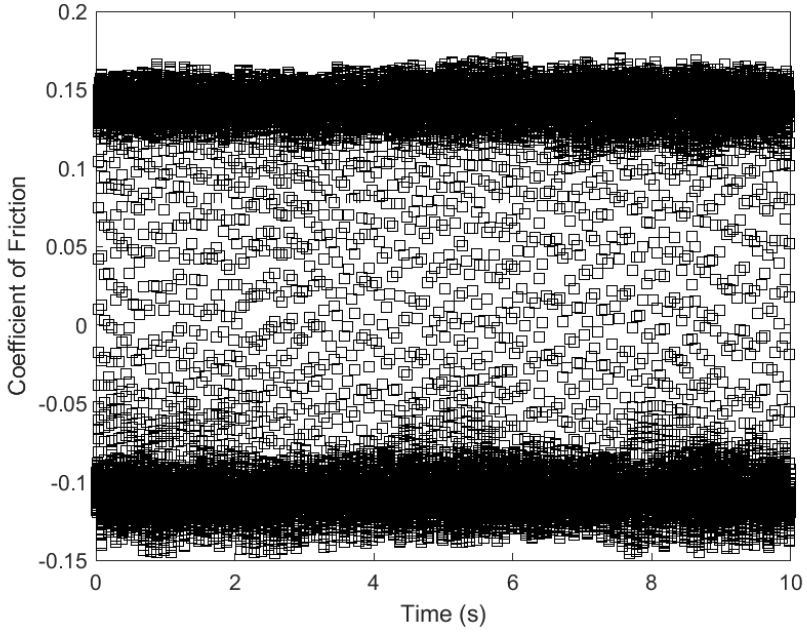

Figure A.82: Second Set of Data, Sliding Frequency 10 Hz, Applied Load 50 N, Lubricant Temperature 120 °C

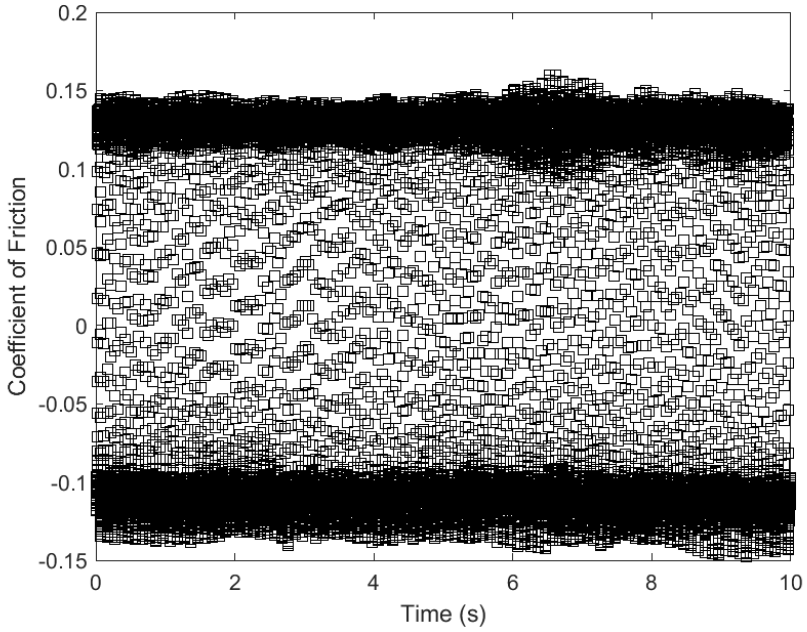

Figure A.83: Second Set of Data, Sliding Frequency 10 Hz, Applied Load 100 N, Lubricant Temperature 120 °C

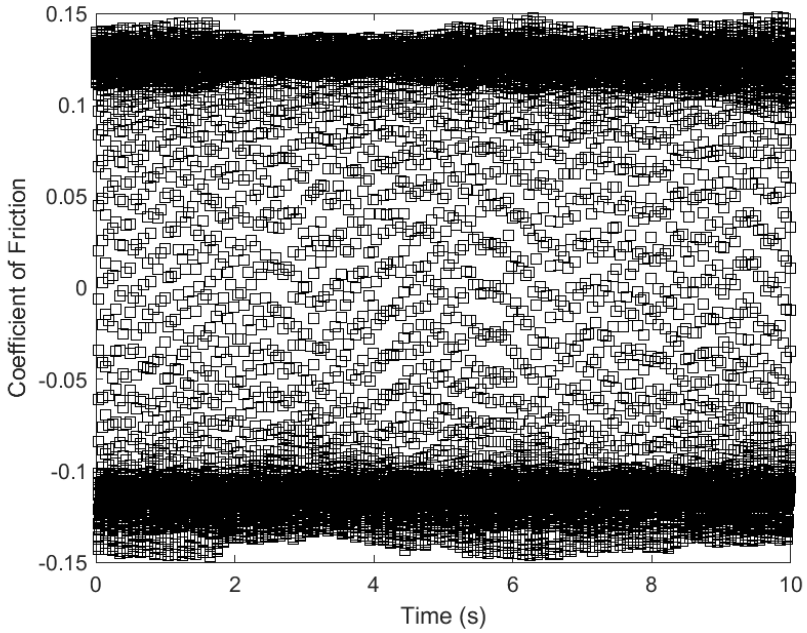

Figure A.84: Second Set of Data, Sliding Frequency 10 Hz, Applied Load 150 N, Lubricant Temperature 120 °C

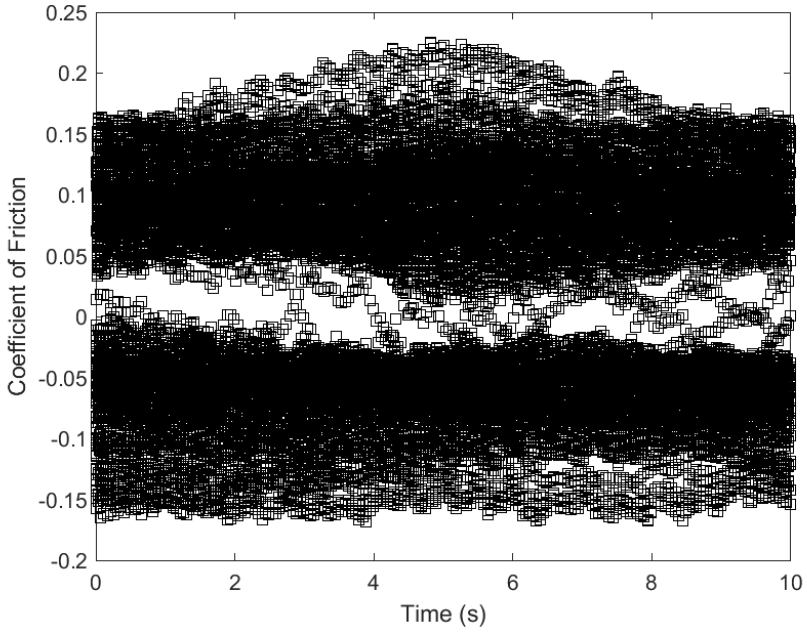

Figure A.85: Second Set of Data, Sliding Frequency 20 Hz, Applied Load 50 N, Lubricant Temperature 30 °C

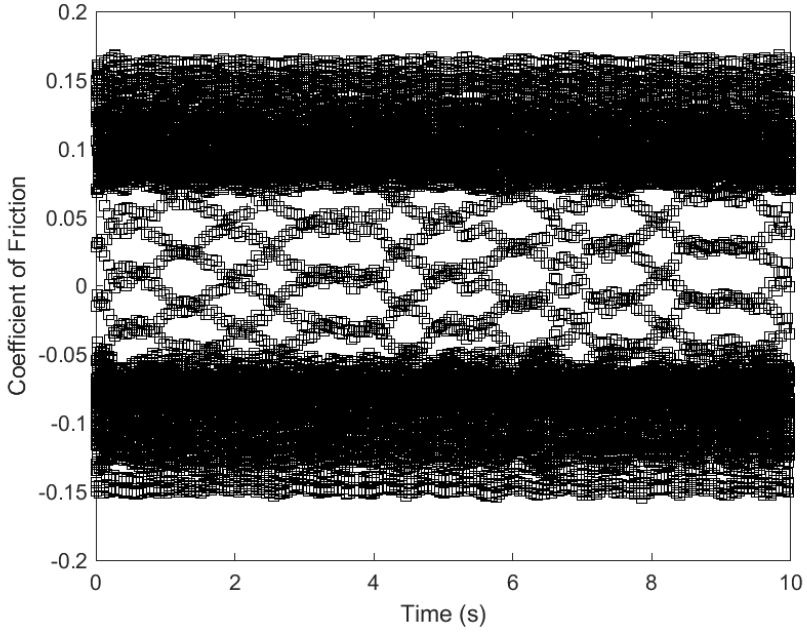

Figure A.86: Second Set of Data, Sliding Frequency 20 Hz, Applied Load 100 N, Lubricant Temperature 30 °C

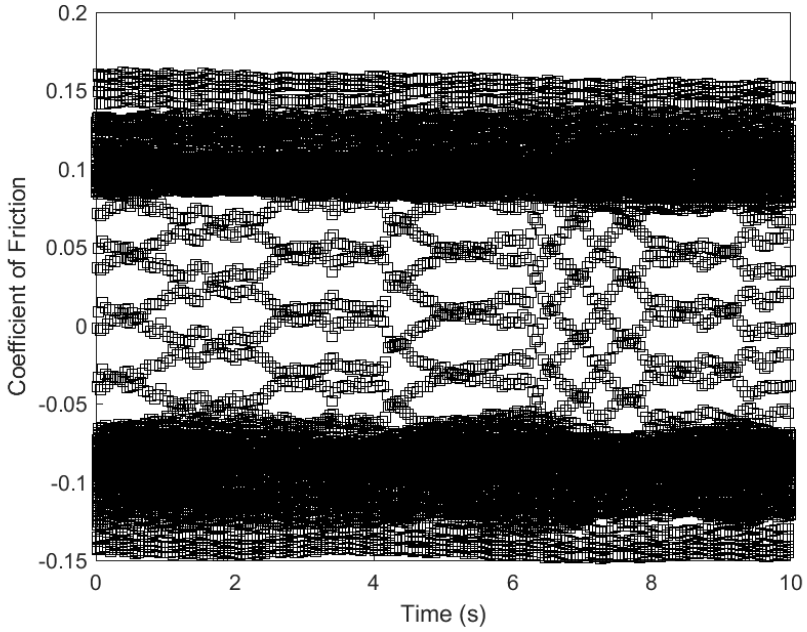

Figure A.87: Second Set of Data, Sliding Frequency 20 Hz, Applied Load 150 N, Lubricant Temperature 30 °C

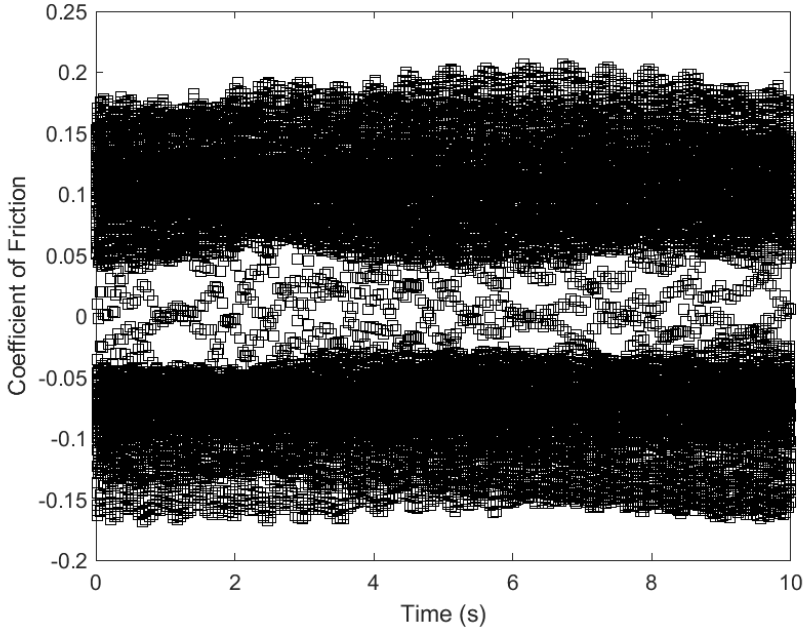

Figure A.88: Second Set of Data, Sliding Frequency 20 Hz, Applied Load 50 N, Lubricant Temperature 50 °C

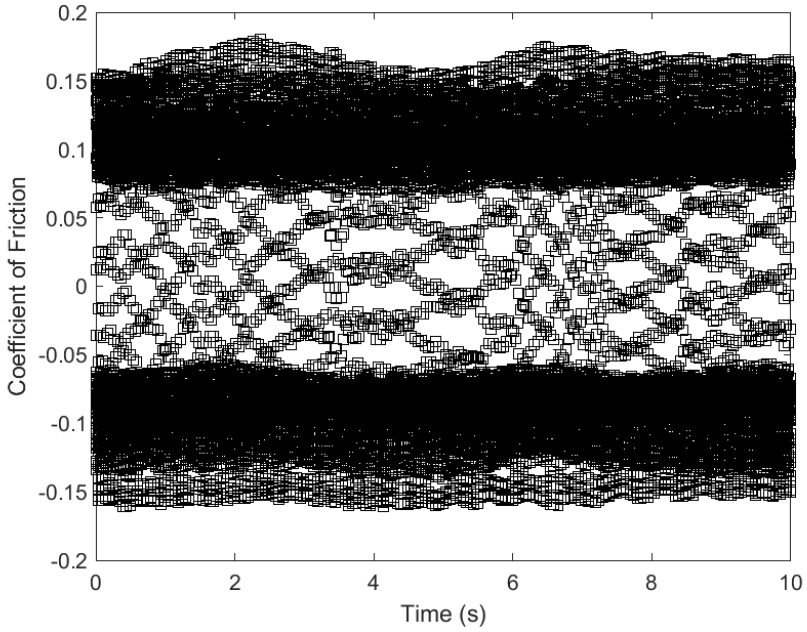

Figure A.89: Second Set of Data, Sliding Frequency 20 Hz, Applied Load 100 N, Lubricant Temperature 50 °C

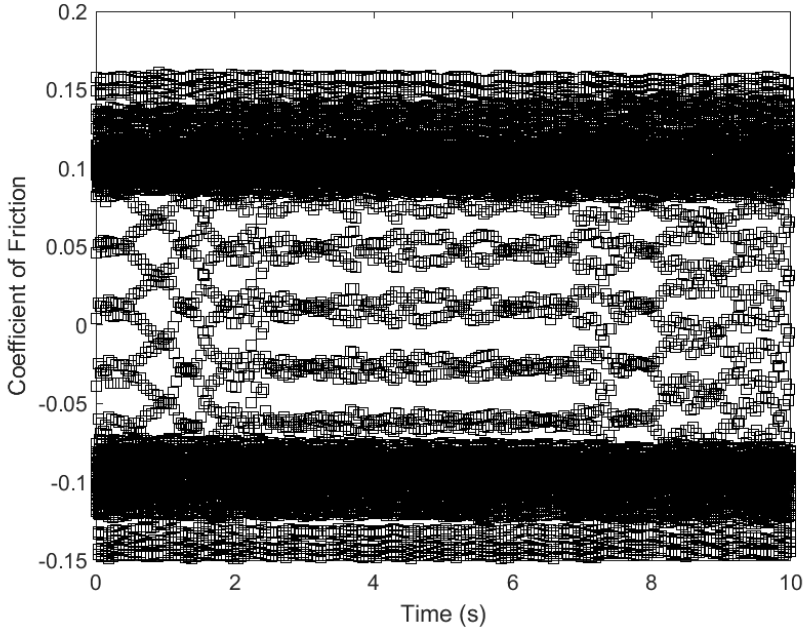

Figure A.90: Second Set of Data, Sliding Frequency 20 Hz, Applied Load 150 N, Lubricant Temperature 50 °C

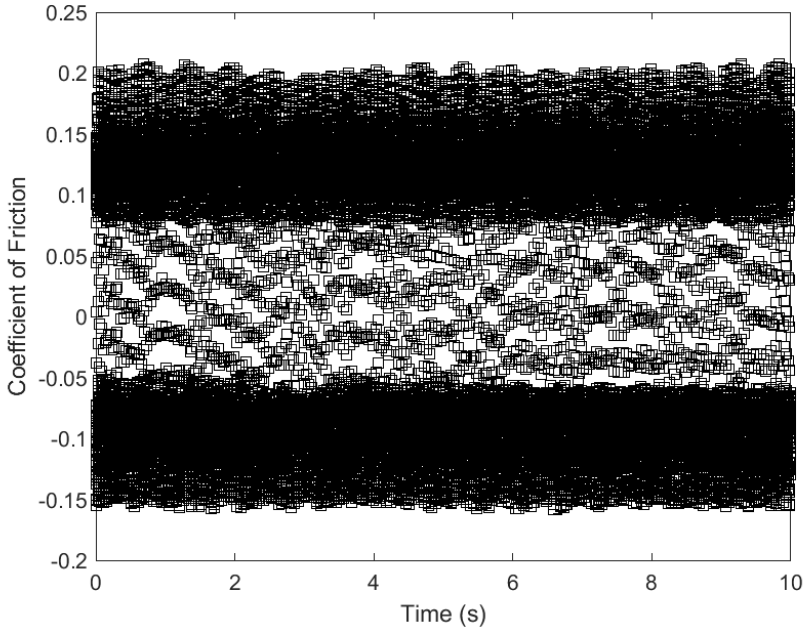

Figure A.91: Second Set of Data, Sliding Frequency 20 Hz, Applied Load 50 N, Lubricant Temperature 80 °C

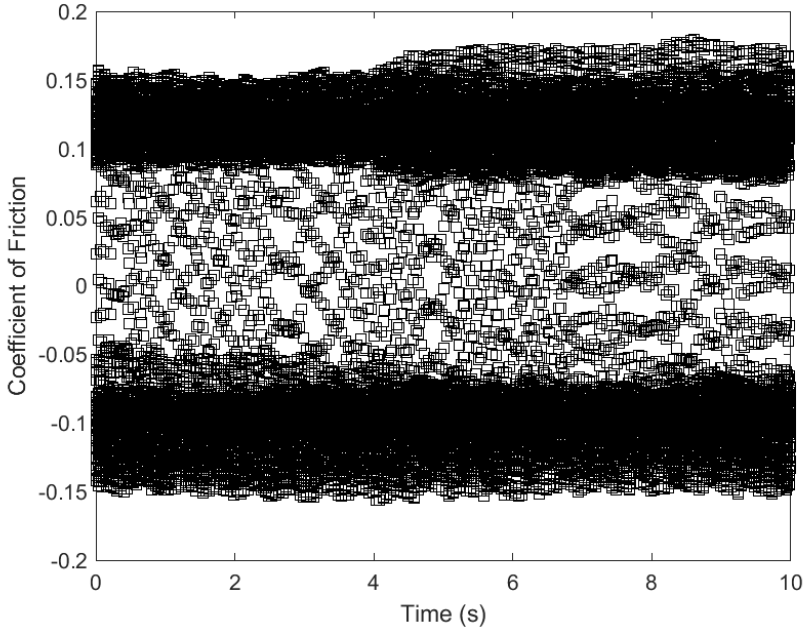

Figure A.92: Second Set of Data, Sliding Frequency 20 Hz, Applied Load 100 N, Lubricant Temperature 80 °C

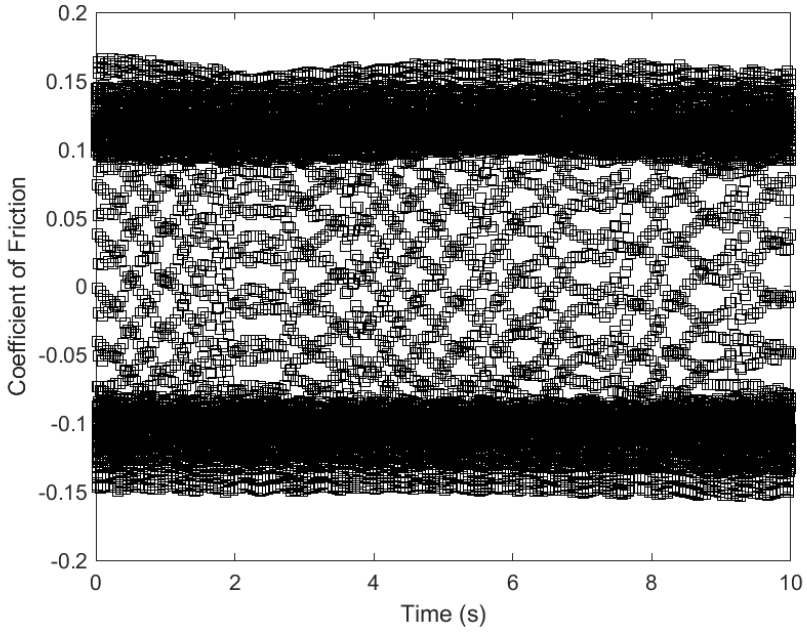

Figure A.93: Second Set of Data, Sliding Frequency 20 Hz, Applied Load 150 N, Lubricant Temperature 80 °C

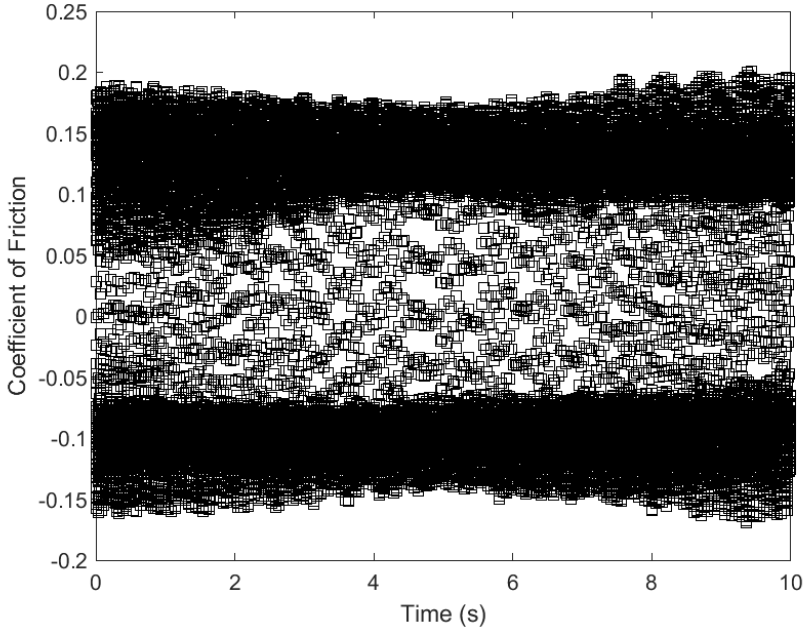

Figure A.94: Second Set of Data, Sliding Frequency 20 Hz, Applied Load 50 N, Lubricant Temperature 120 °C

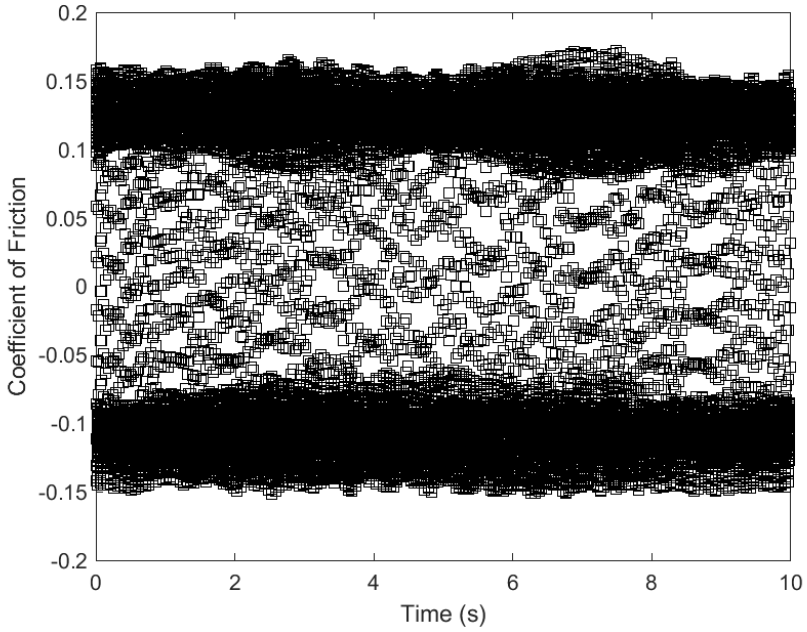

Figure A.95: Second Set of Data, Sliding Frequency 20 Hz, Applied Load 100 N, Lubricant Temperature 120 °C

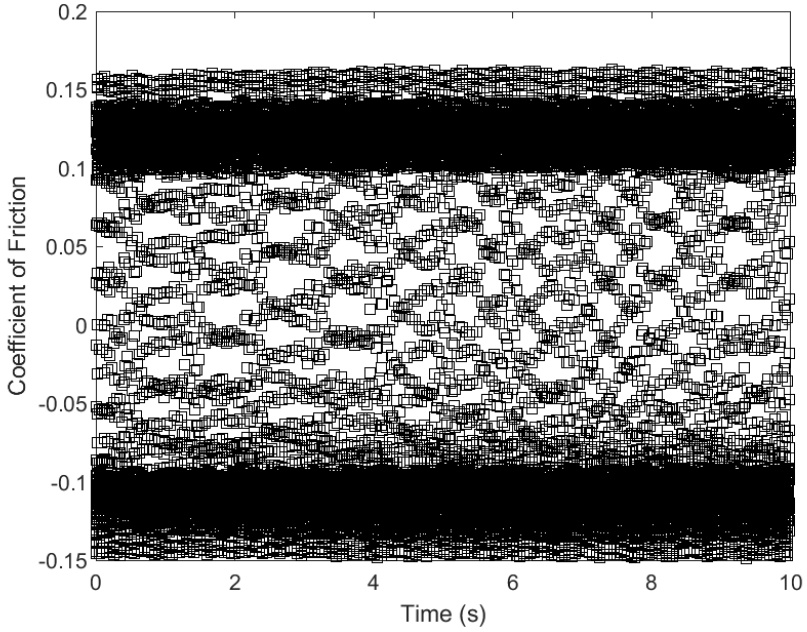

Figure A.96: Second Set of Data, Sliding Frequency 20 Hz, Applied Load 150 N, Lubricant Temperature 120 °C

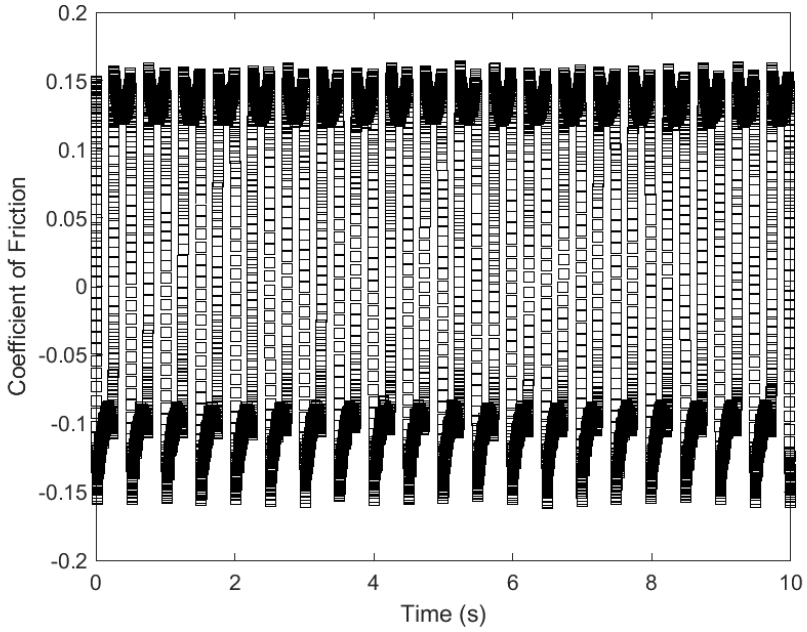

Figure A.97: Third Set of Data, Sliding Frequency 2 Hz, Applied Load 50 N, Lubricant Temperature 30 °C

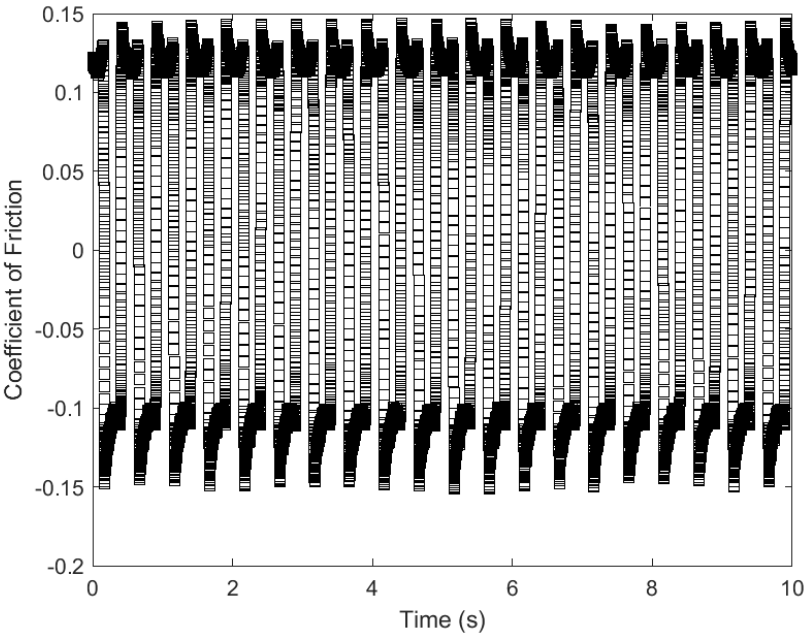

Figure A.98: Third Set of Data, Sliding Frequency 2 Hz, Applied Load 100 N, Lubricant Temperature 30 °C

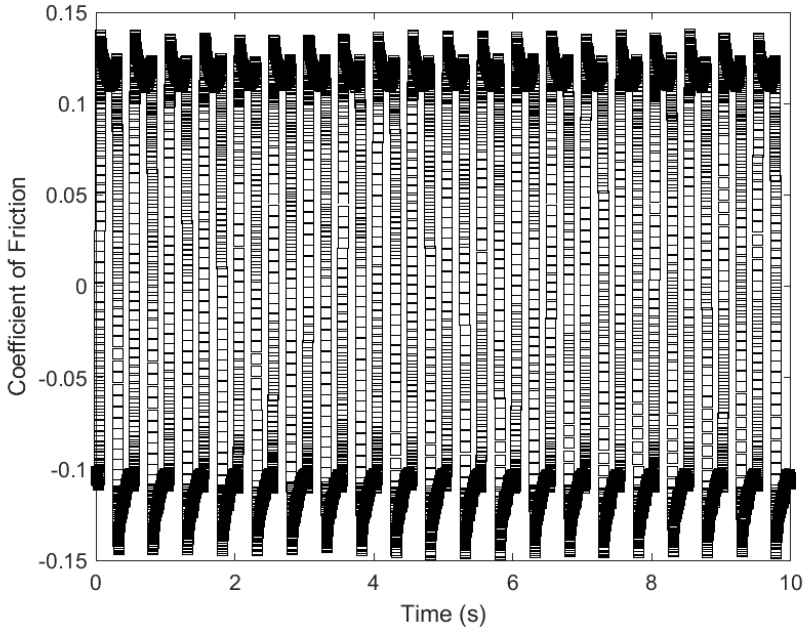

Figure A.99: Third Set of Data, Sliding Frequency 2 Hz, Applied Load 150 N, Lubricant Temperature 30 °C

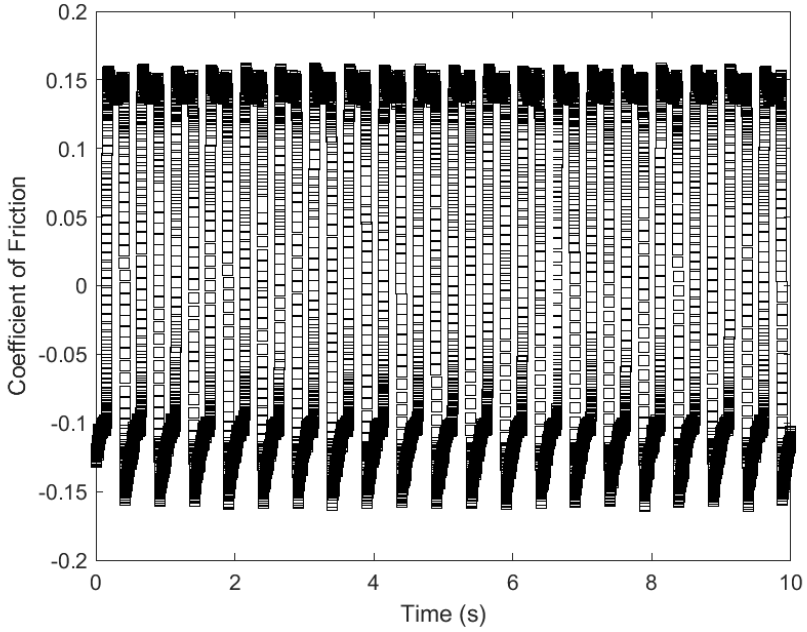

Figure A.100: Third Set of Data, Sliding Frequency 2 Hz, Applied Load 50 N, Lubricant Temperature 50 °C

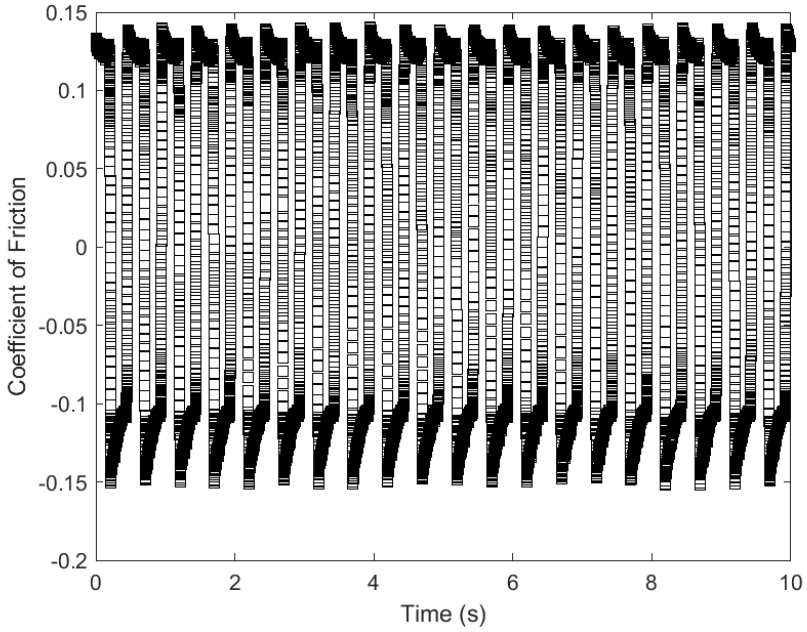

Figure A.101: Third Set of Data, Sliding Frequency 2 Hz, Applied Load 100 N, Lubricant Temperature 50 °C

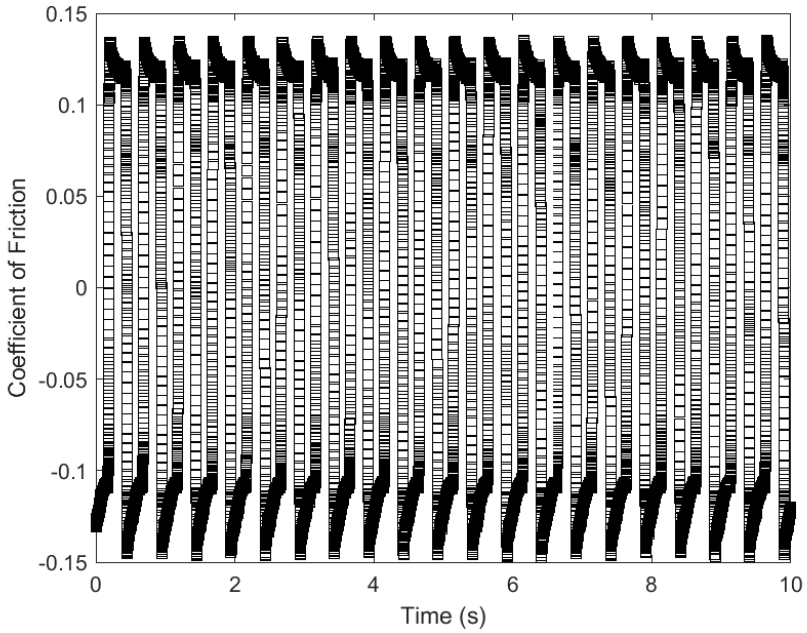

Figure A.102: Third Set of Data, Sliding Frequency 2 Hz, Applied Load 150 N, Lubricant Temperature 50 °C

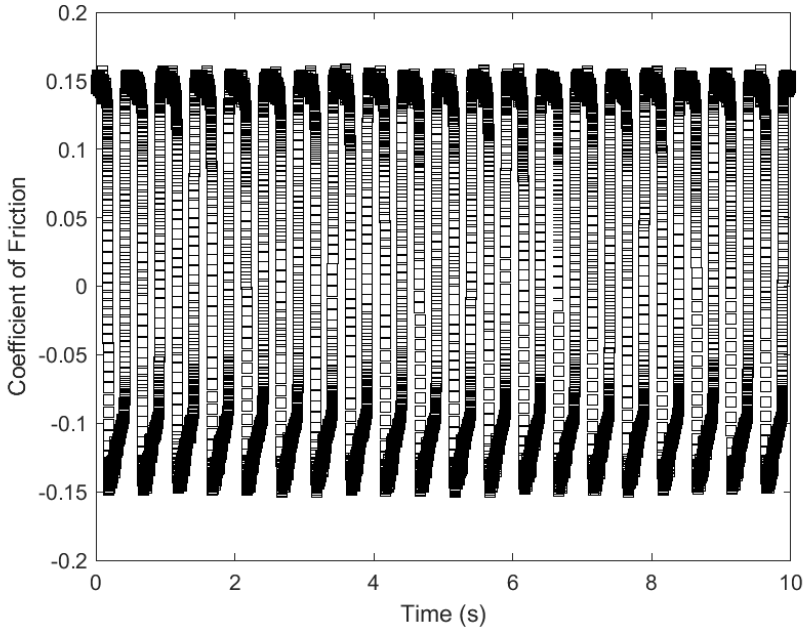

Figure A.103: Third Set of Data, Sliding Frequency 2 Hz, Applied Load 50 N, Lubricant Temperature 80 °C

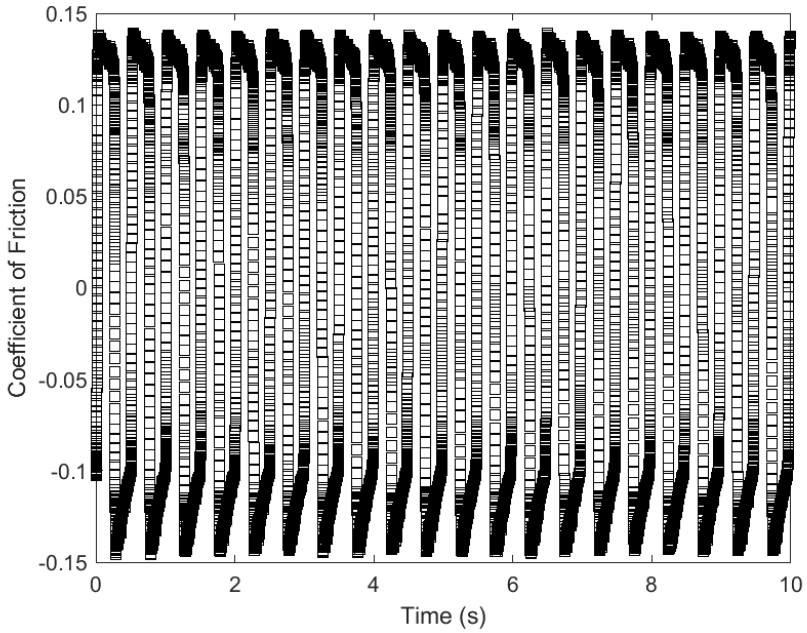

Figure A.104: Third Set of Data, Sliding Frequency 2 Hz, Applied Load 100 N, Lubricant Temperature 80 °C

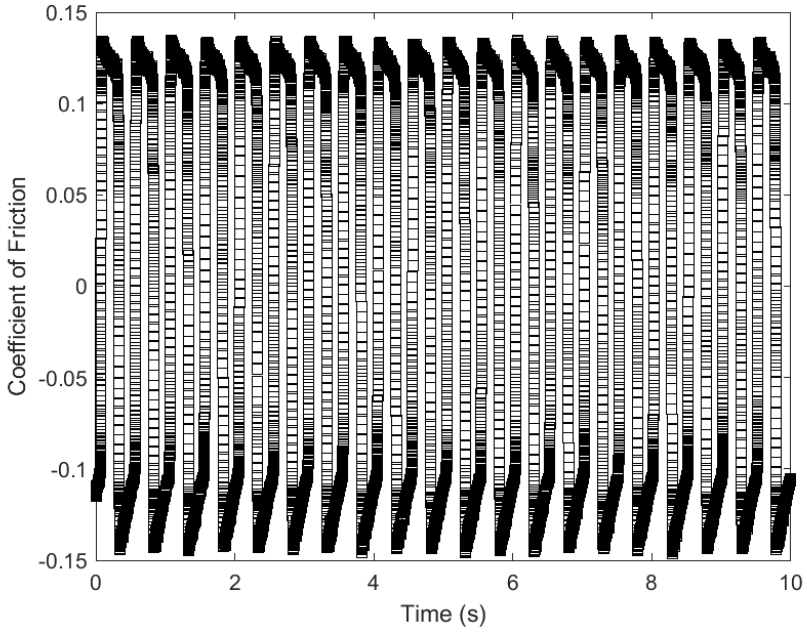

Figure A.105: Third Set of Data, Sliding Frequency 2 Hz, Applied Load 150 N, Lubricant Temperature 80 °C

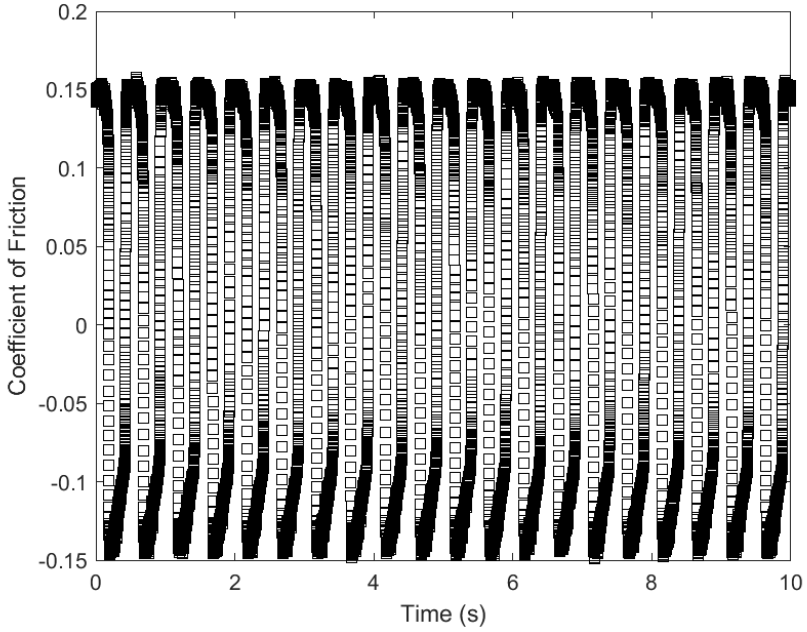

Figure A.106: Third Set of Data, Sliding Frequency 2 Hz, Applied Load 50 N, Lubricant Temperature 120 °C

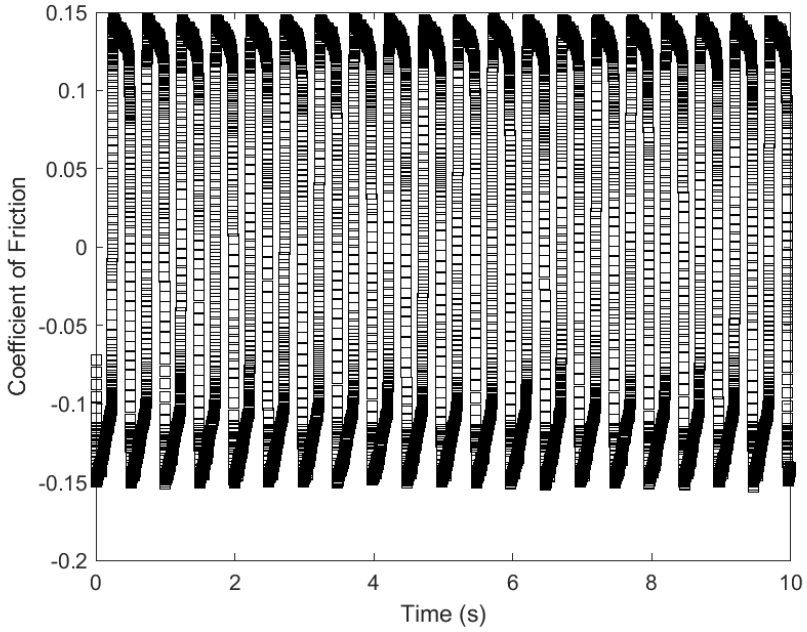

Figure A.107: Third Set of Data, Sliding Frequency 2 Hz, Applied Load 100 N, Lubricant Temperature 120 °C

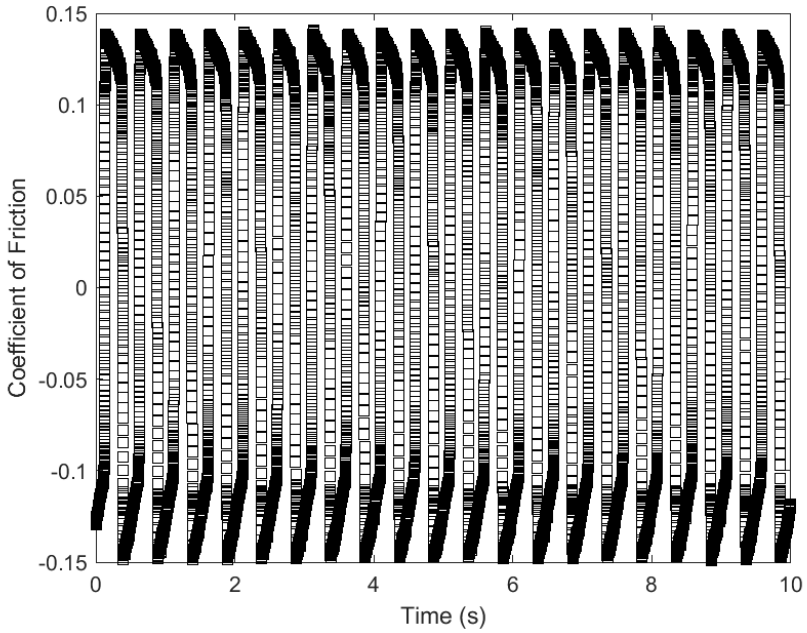

Figure A.108: Third Set of Data, Sliding Frequency 2 Hz, Applied Load 150 N, Lubricant Temperature 120 °C

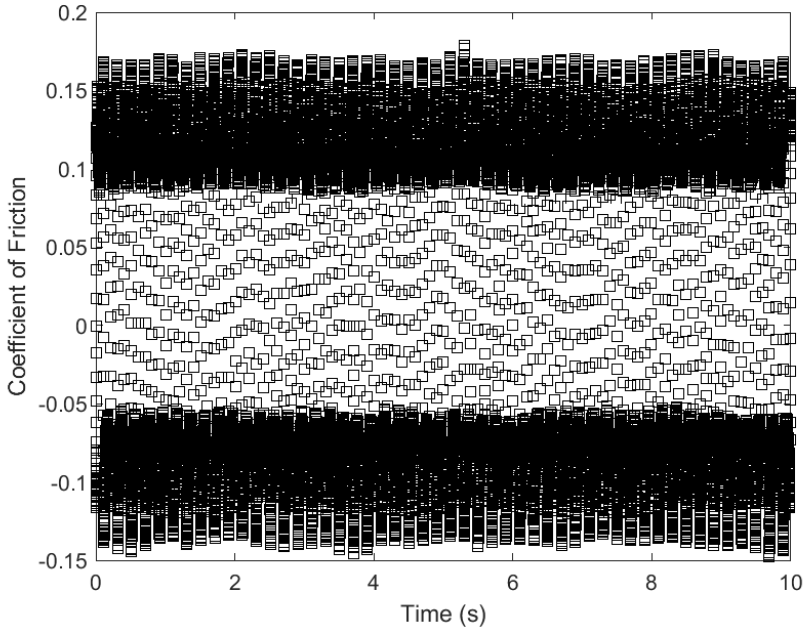

Figure A.109: Third Set of Data, Sliding Frequency 5 Hz, Applied Load 50 N, Lubricant Temperature 30 °C

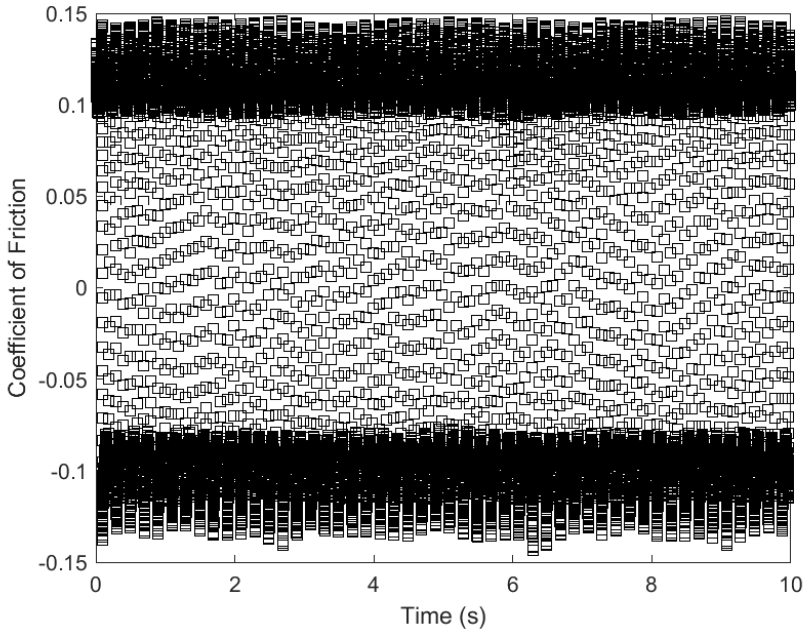

Figure A.110: Third Set of Data, Sliding Frequency 5 Hz, Applied Load 100 N, Lubricant Temperature 30 °C

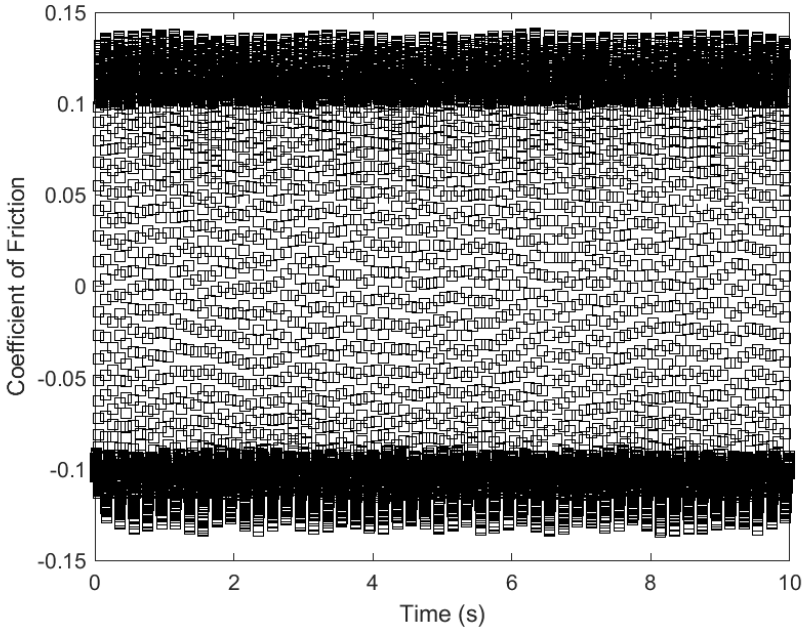

.5

Figure A.111: Third Set of Data, Sliding Frequency 5 Hz, Applied Load 150 N, Lubricant Temperature 30 °C

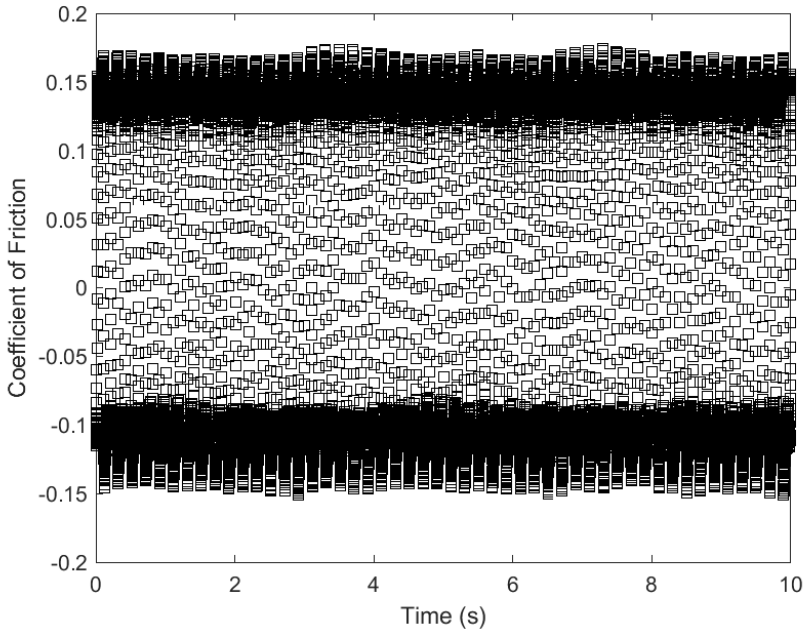

Figure A.112: Third Set of Data, Sliding Frequency 5 Hz, Applied Load 50 N, Lubricant Temperature 50 °C

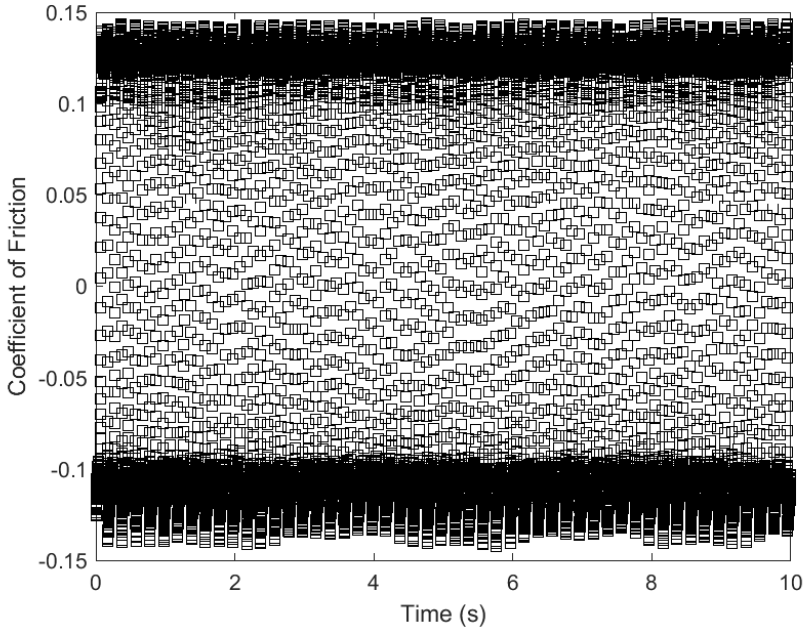

Figure A.113: Third Set of Data, Sliding Frequency 5 Hz, Applied Load 100 N, Lubricant Temperature 50 °C

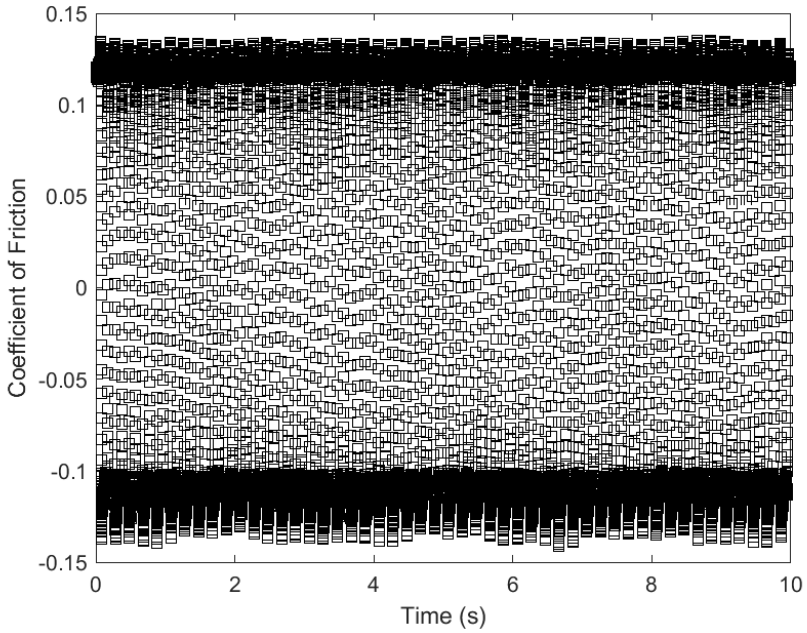

Figure A.114: Third Set of Data, Sliding Frequency 5 Hz, Applied Load 150 N, Lubricant Temperature 50 °C

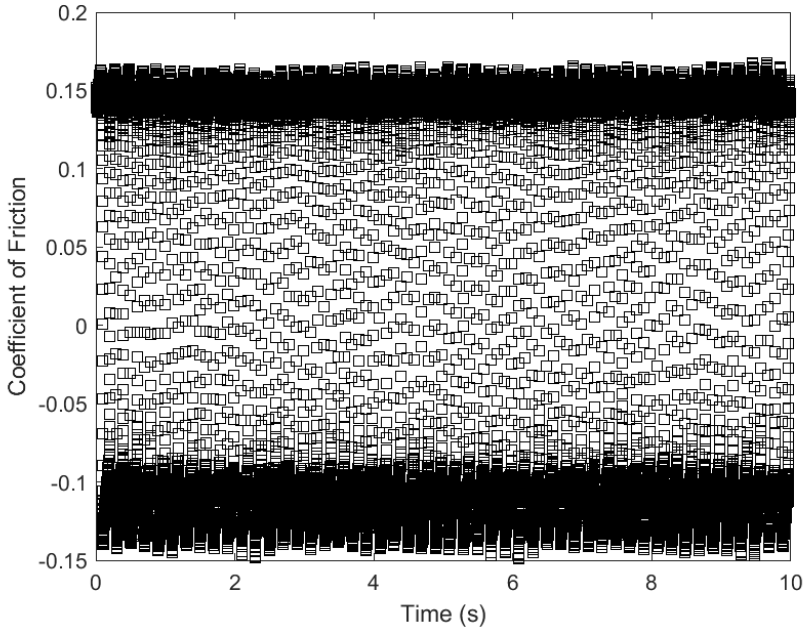

Figure A.115: Third Set of Data, Sliding Frequency 5 Hz, Applied Load 50 N, Lubricant Temperature 80 °C

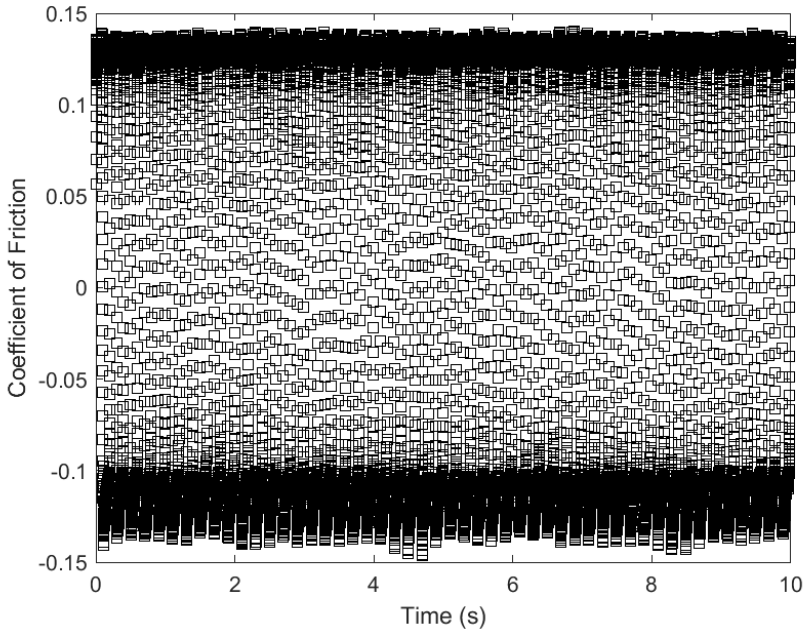

Figure A.116: Third Set of Data, Sliding Frequency 5 Hz, Applied Load 100 N, Lubricant Temperature 80 °C

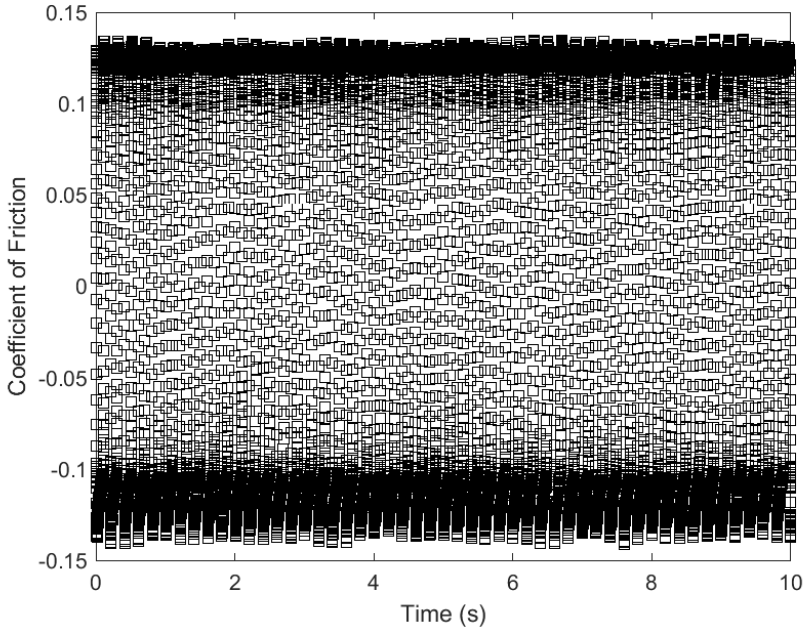

Figure A.117: Third Set of Data, Sliding Frequency 5 Hz, Applied Load 150 N, Lubricant Temperature 80 °C

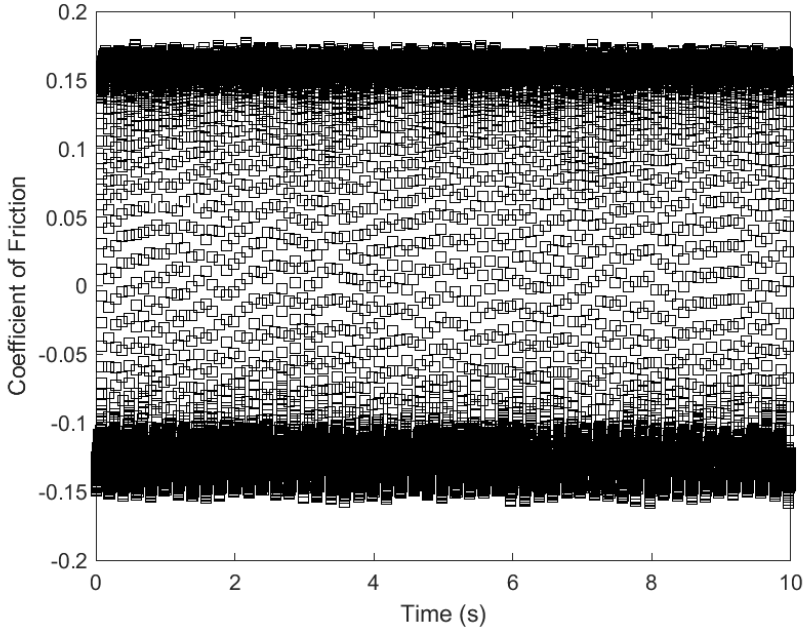

Figure A.118: Third Set of Data, Sliding Frequency 5 Hz, Applied Load 50 N, Lubricant Temperature 120 °C

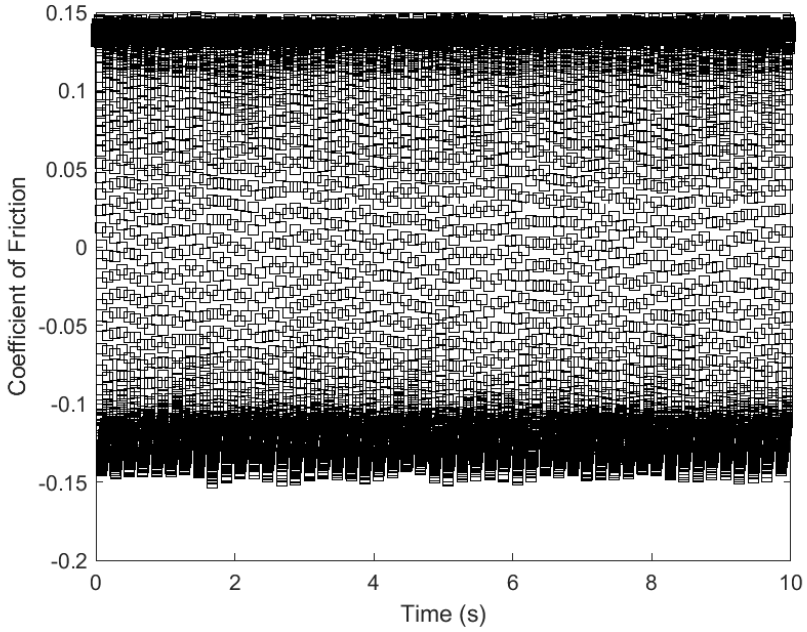

Figure A.119: Third Set of Data, Sliding Frequency 5 Hz, Applied Load 100 N, Lubricant Temperature 120 °C

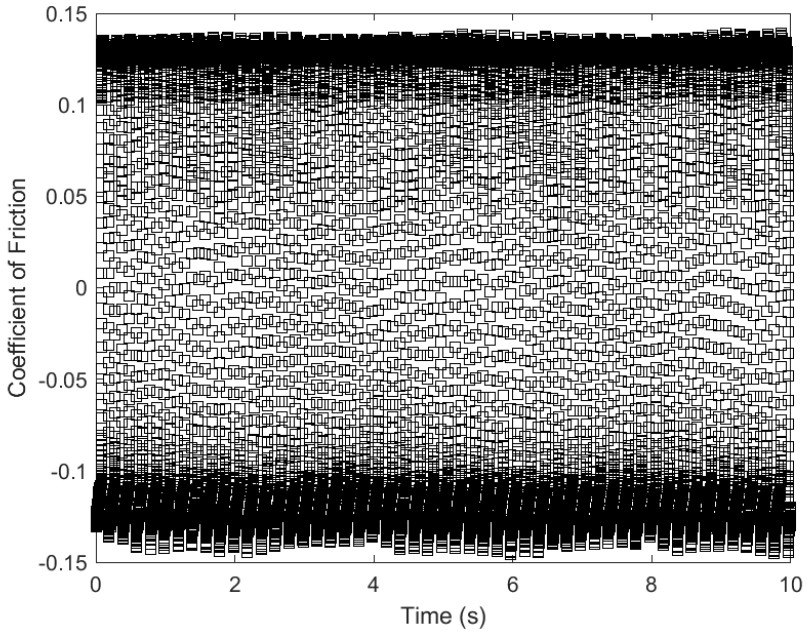

Figure A.120: Third Set of Data, Sliding Frequency 5 Hz, Applied Load 150 N, Lubricant Temperature 120 °C

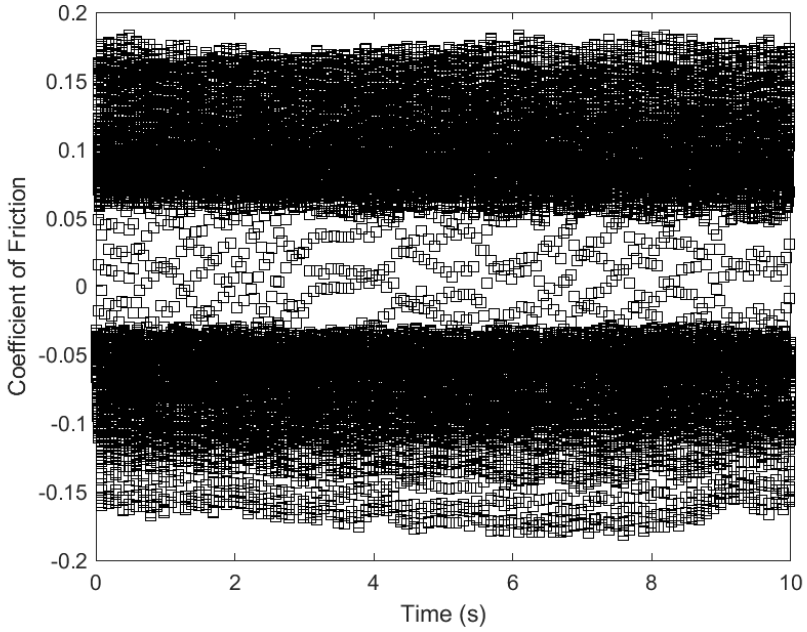

Figure A.121: Third Set of Data, Sliding Frequency 10 Hz, Applied Load 50 N, Lubricant Temperature 30 °C

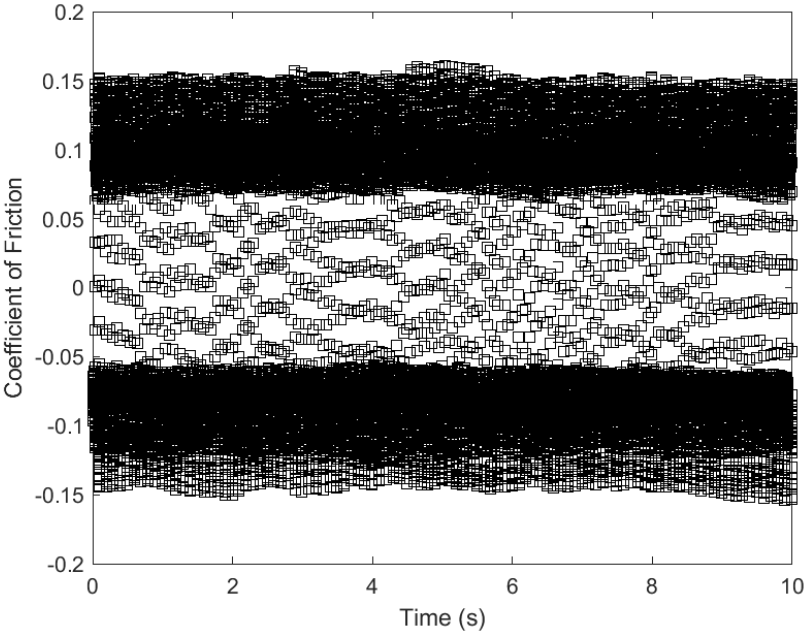

Figure A.122: Third Set of Data, Sliding Frequency 10 Hz, Applied Load 100 N, Lubricant Temperature 30 °C

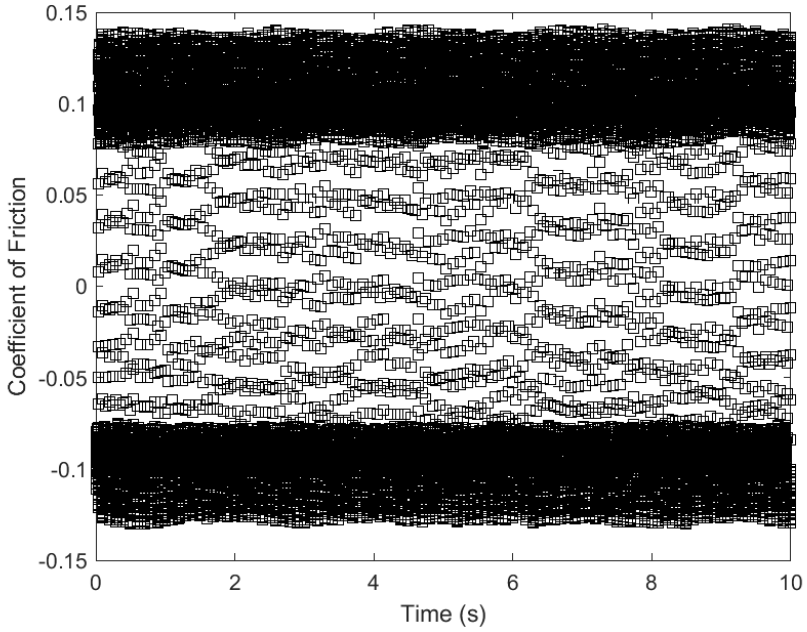

Figure A.123: Third Set of Data, Sliding Frequency 10 Hz, Applied Load 150 N, Lubricant Temperature 30 °C

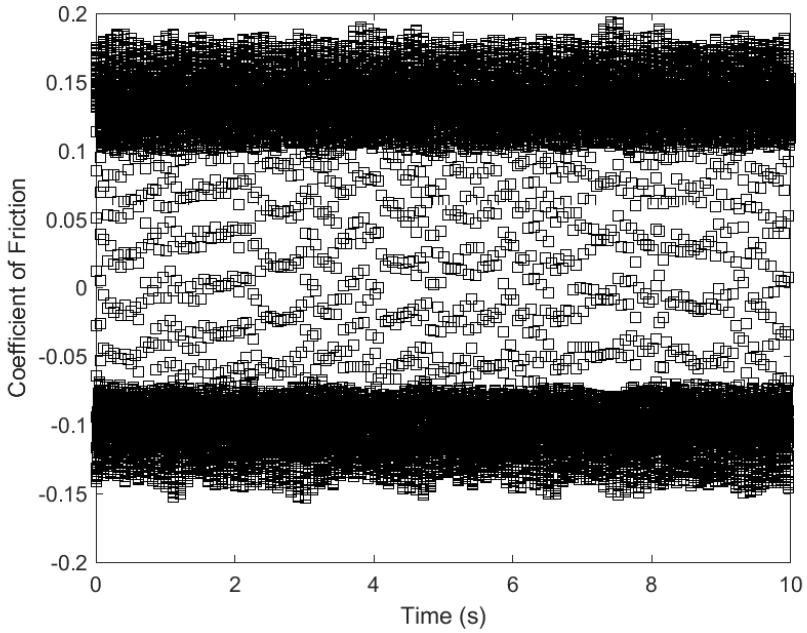

Figure A.124: Third Set of Data, Sliding Frequency 10 Hz, Applied Load 50 N, Lubricant Temperature 50 °C

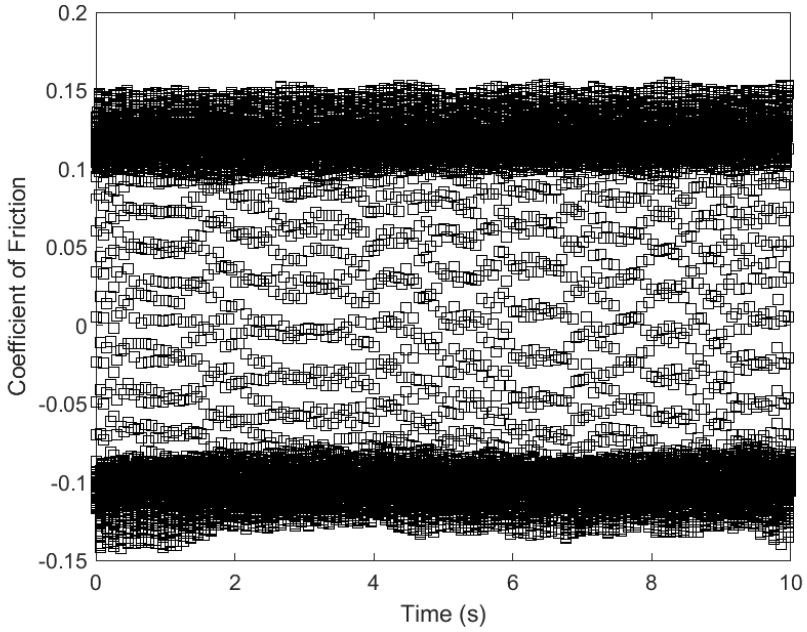

Figure A.125: Third Set of Data, Sliding Frequency 10 Hz, Applied Load 100 N, Lubricant Temperature 50 °C

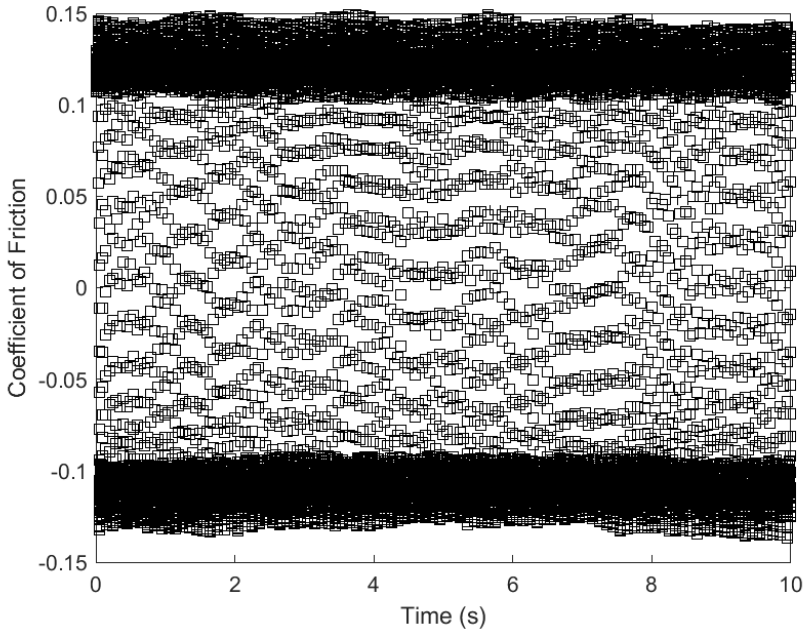

Figure A.126: Third Set of Data, Sliding Frequency 10 Hz, Applied Load 150 N, Lubricant Temperature 50 °C

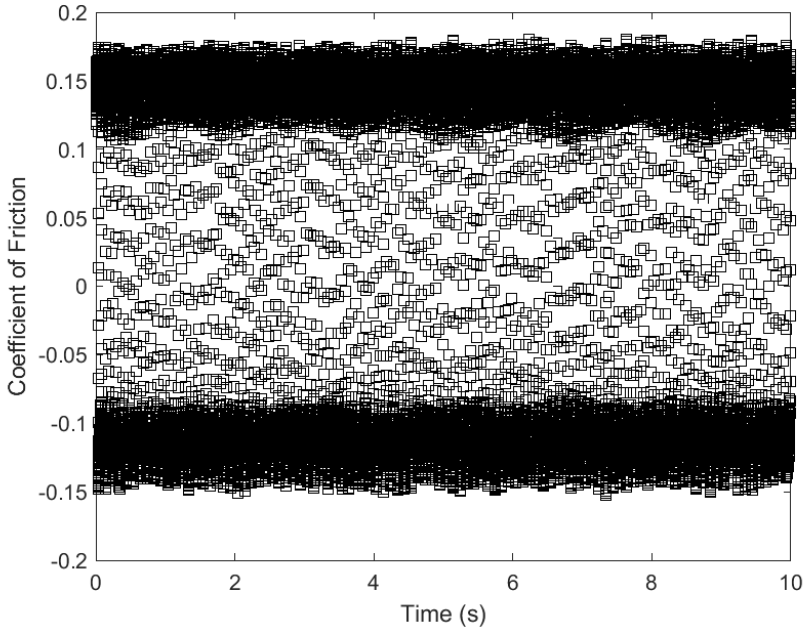

Figure A.127: Third Set of Data, Sliding Frequency 10 Hz, Applied Load 50 N, Lubricant Temperature 80 °C

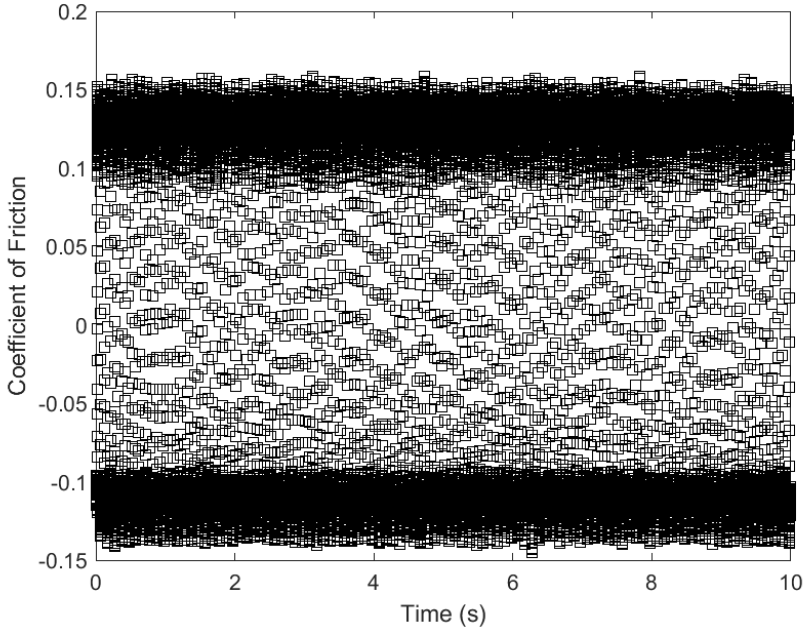

Figure A.128: Third Set of Data, Sliding Frequency 10 Hz, Applied Load 100 N, Lubricant Temperature 80 °C

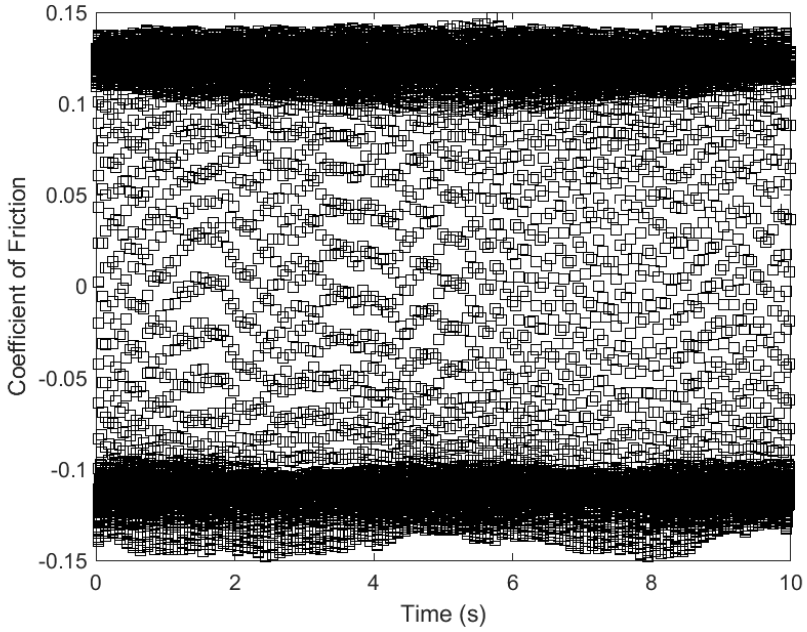

Figure A.129: Third Set of Data, Sliding Frequency 10 Hz, Applied Load 150 N, Lubricant Temperature 80 °C

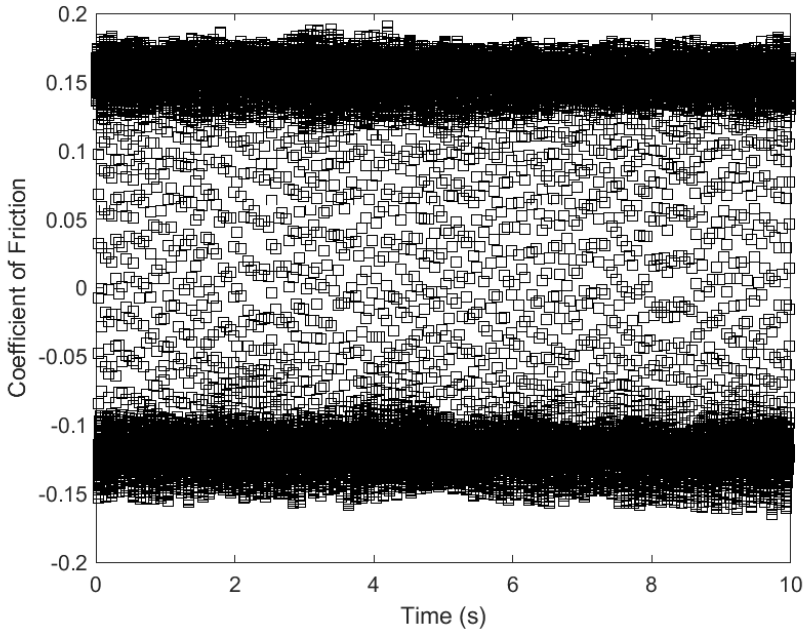

Figure A.130: Third Set of Data, Sliding Frequency 10 Hz, Applied Load 50 N, Lubricant Temperature 120 °C

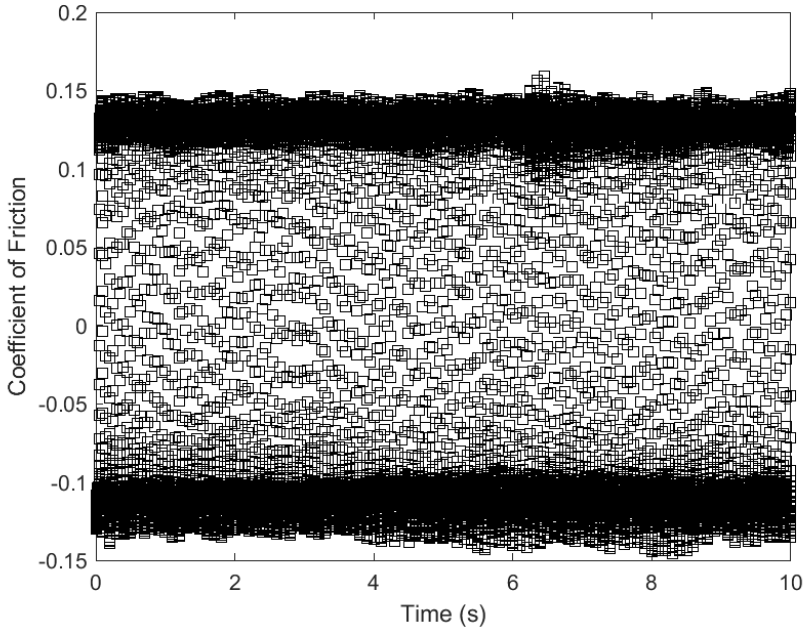

Figure A.131: Third Set of Data, Sliding Frequency 10 Hz, Applied Load 100 N, Lubricant Temperature 120 °C

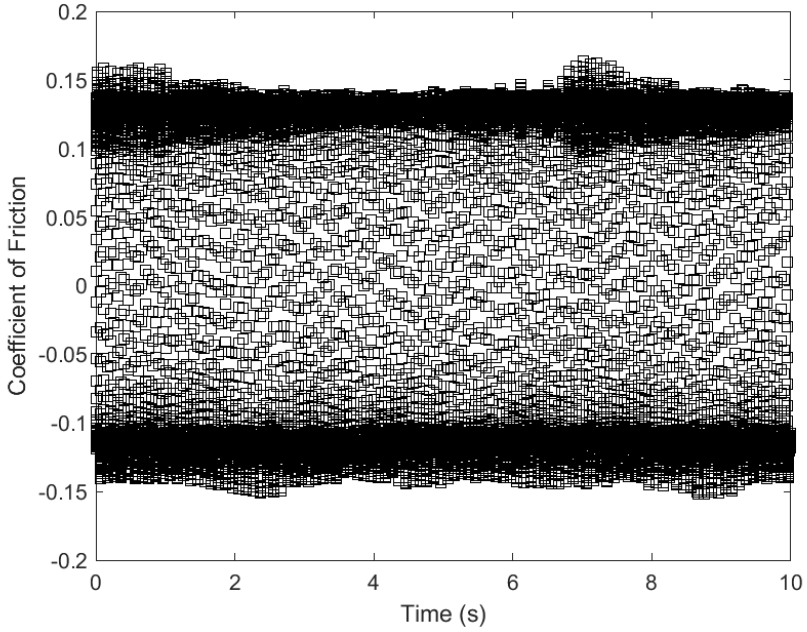

Figure A.132: Third Set of Data, Sliding Frequency 10 Hz, Applied Load 150 N, Lubricant Temperature 120 °C

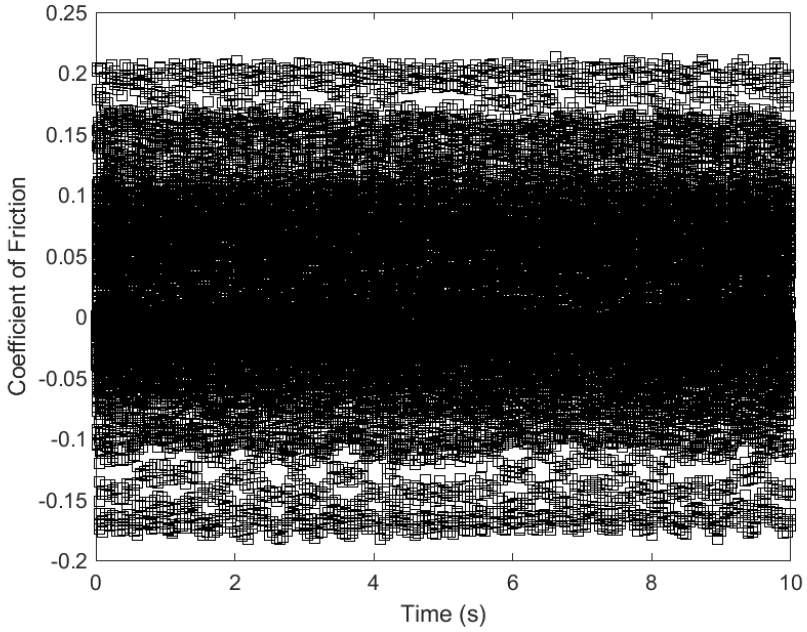

Figure A.133: Third Set of Data, Sliding Frequency 20 Hz, Applied Load 50 N, Lubricant Temperature 30 °C

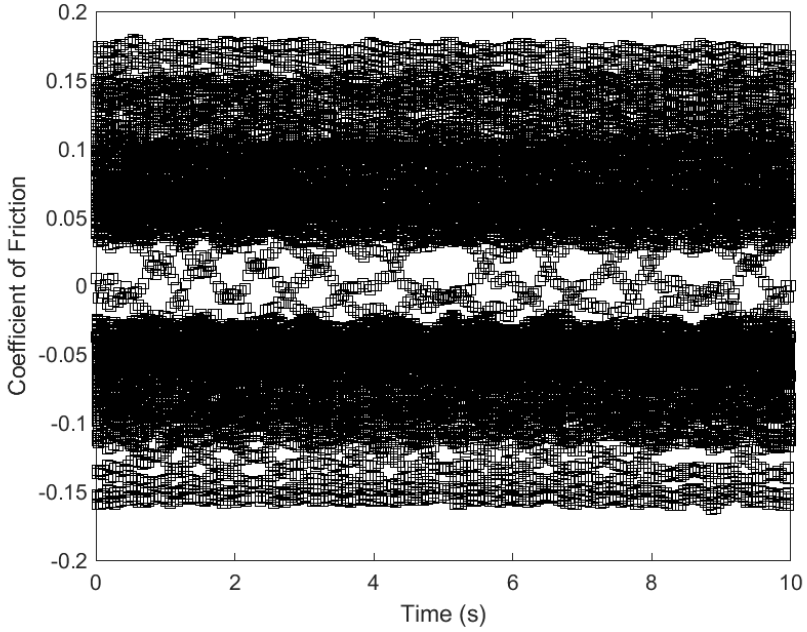

Figure A.134: Third Set of Data, Sliding Frequency 20 Hz, Applied Load 100 N, Lubricant Temperature 30 °C

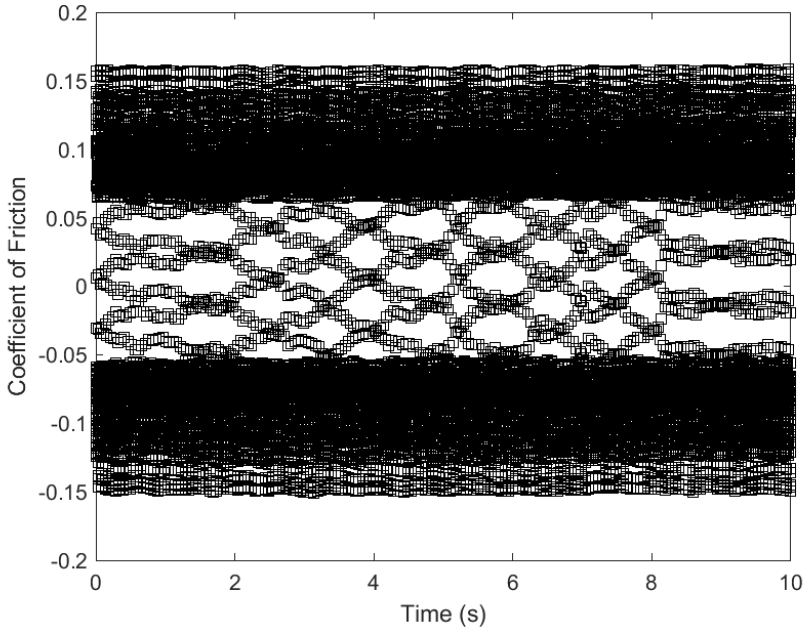

Figure A.135: Third Set of Data, Sliding Frequency 20 Hz, Applied Load 150 N, Lubricant Temperature 30 °C

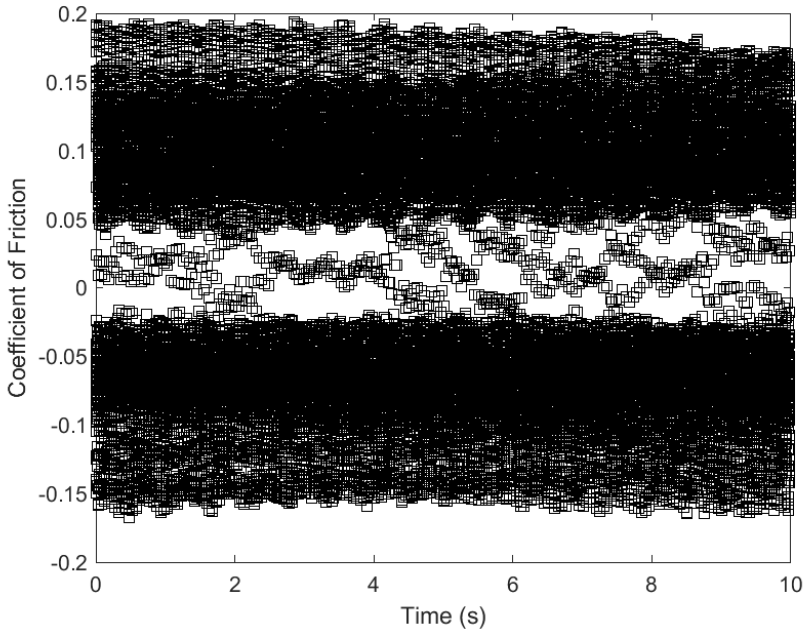

Figure A.136: Third Set of Data, Sliding Frequency 20 Hz, Applied Load 50 N, Lubricant Temperature 50 °C

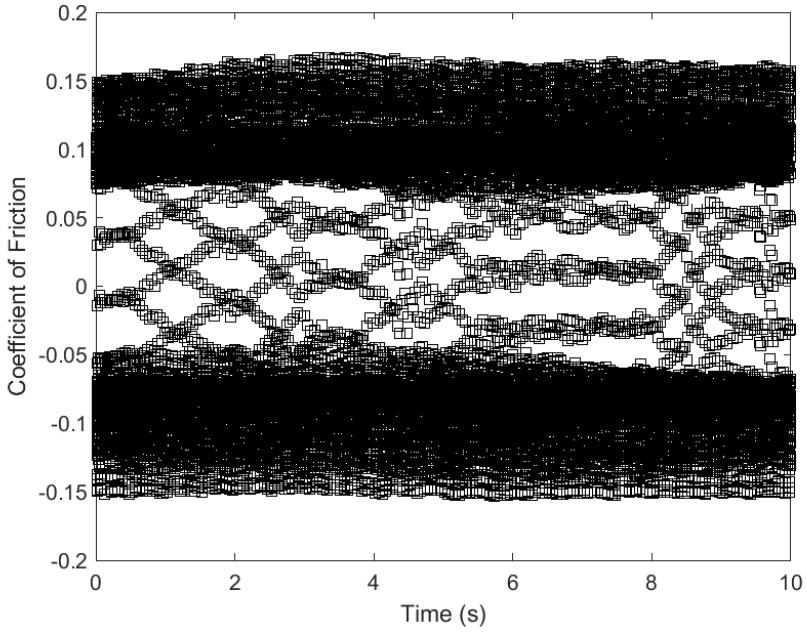

Figure A.137: Third Set of Data, Sliding Frequency 20 Hz, Applied Load 100 N, Lubricant Temperature 50 °C

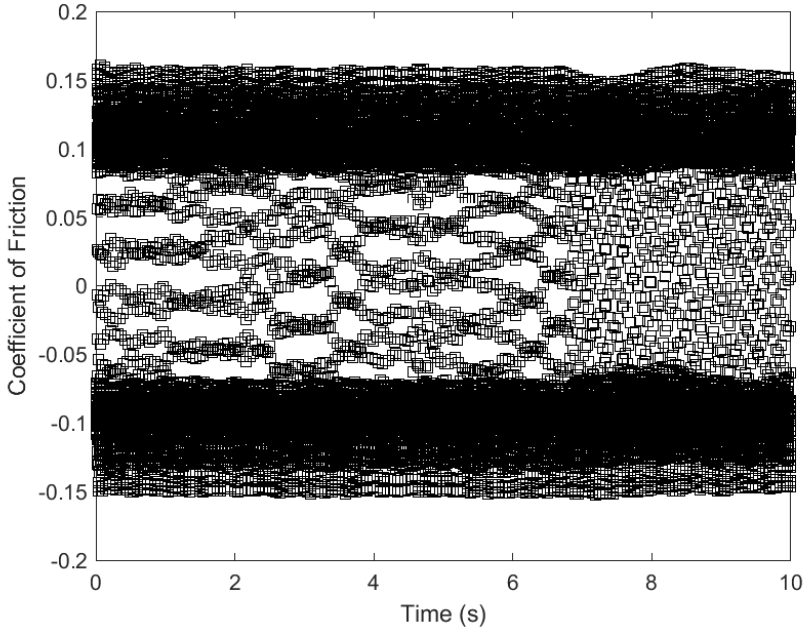

Figure A.138: Third Set of Data, Sliding Frequency 20 Hz, Applied Load 150 N, Lubricant Temperature 50 °C

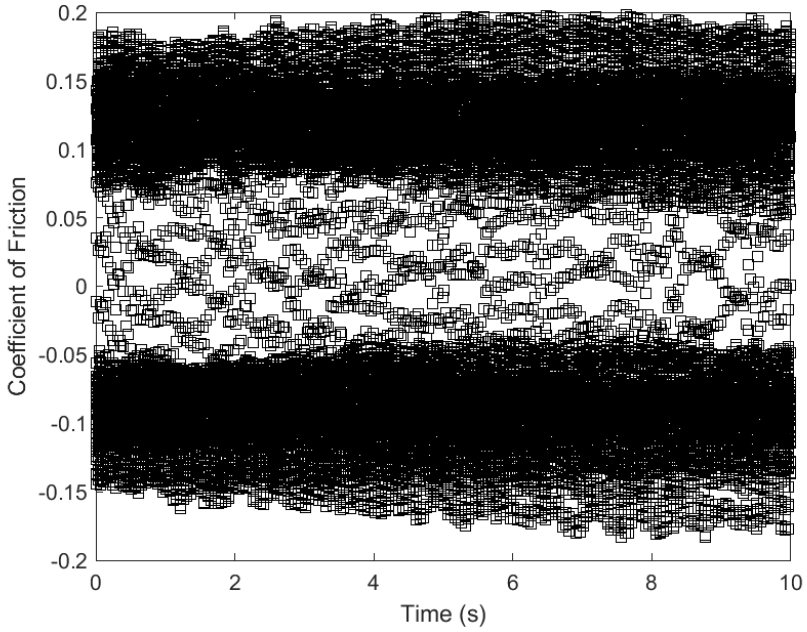

Figure A.139: Third Set of Data, Sliding Frequency 20 Hz, Applied Load 50 N, Lubricant Temperature 80 °C

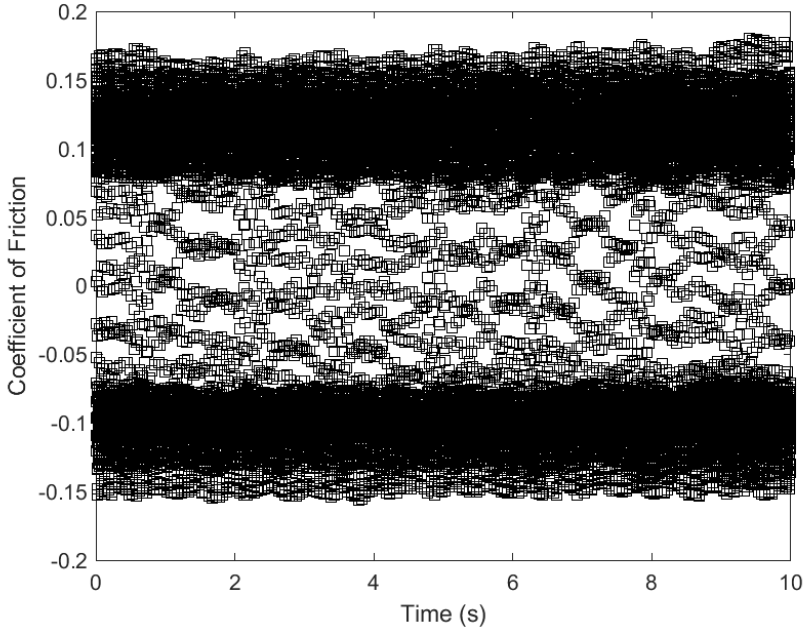

Figure A.140: Third Set of Data, Sliding Frequency 20 Hz, Applied Load 100 N, Lubricant Temperature 80 °C

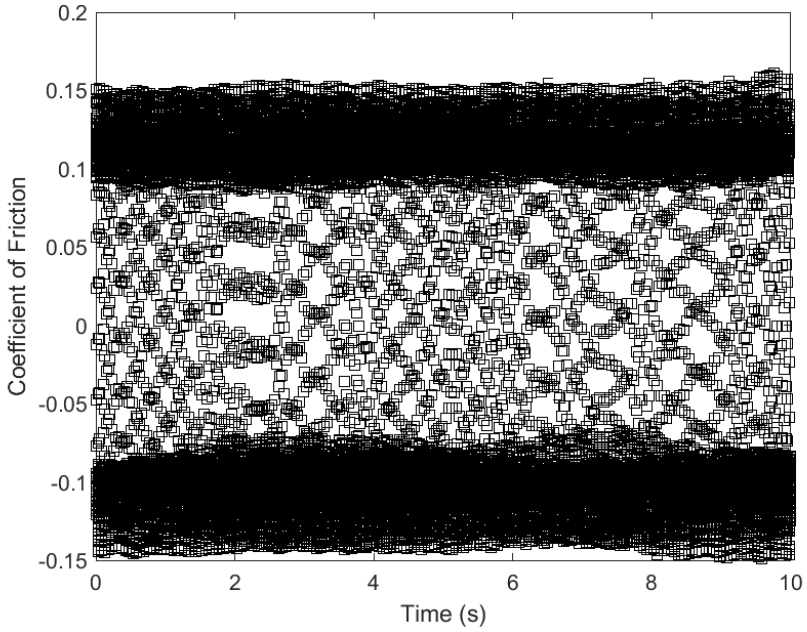

Figure A.141: Third Set of Data, Sliding Frequency 20 Hz, Applied Load 150 N, Lubricant Temperature 80 °C

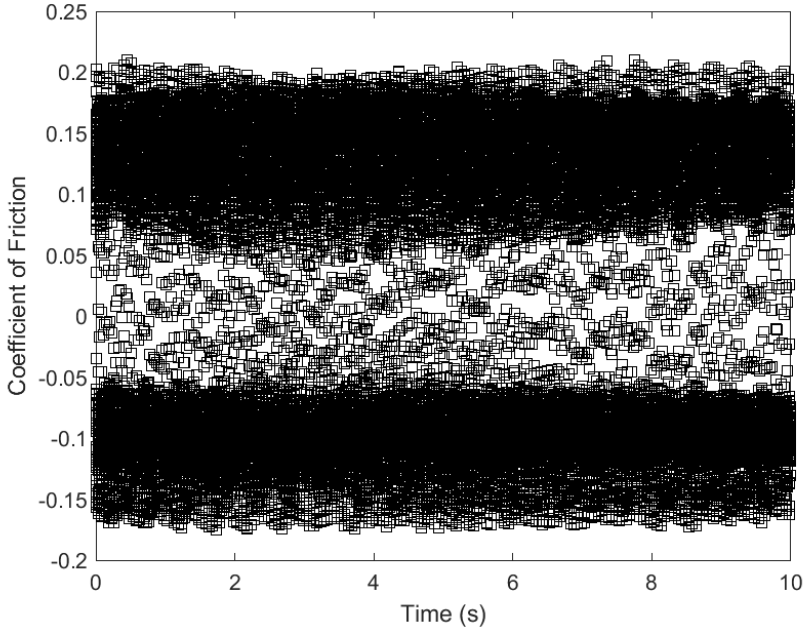

Figure A.142: Third Set of Data, Sliding Frequency 20 Hz, Applied Load 50 N, Lubricant Temperature 120 °C

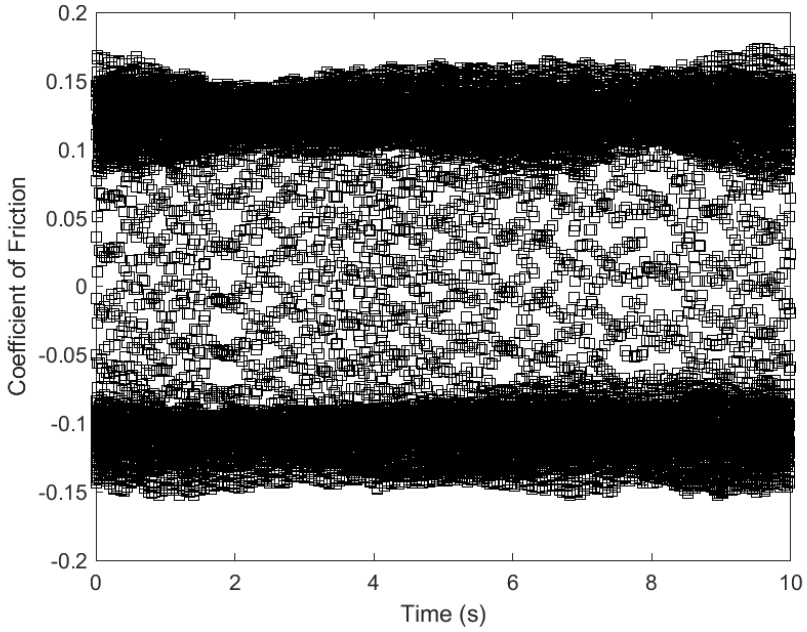

Figure A.143: Third Set of Data, Sliding Frequency 20 Hz, Applied Load 100 N, Lubricant Temperature 120 °C

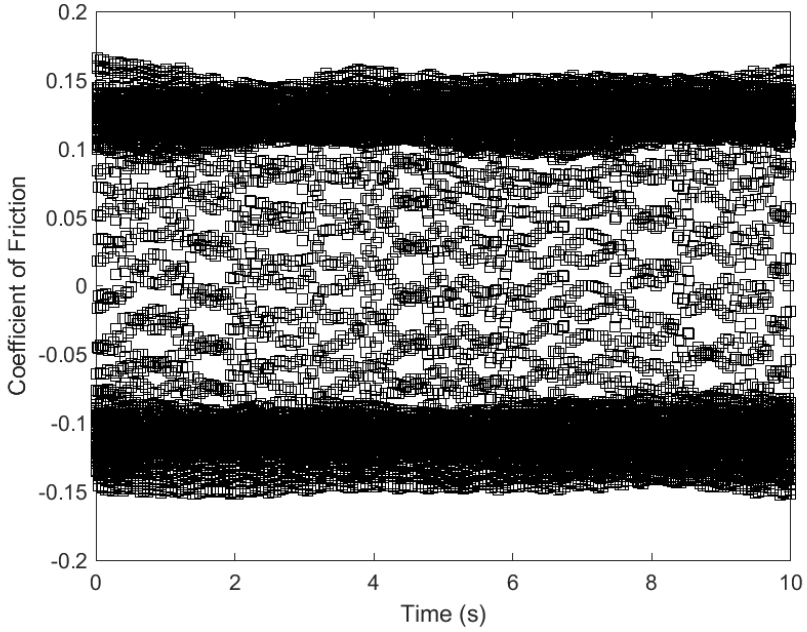

Figure A.144: Third Set of Data, Sliding Frequency 20 Hz, Applied Load 150 N, Lubricant Temperature 120 °C